

The University of Sheffield



**Electro-thermal optimisation of a 50kW
synchronous permanent magnet generator
for aerospace application**

By

Maurice Orwen Patrick Shortte

A thesis submitted for the degree of
doctor of philosophy in the department of
Electronic and Electrical Engineering at
the University of Sheffield.

January 2016

ABSTRACT

This thesis describes an in-depth series of investigations into electromagnetic and thermal behaviour of a brushless permanent-magnet electrical generator and technologies that would provide additional power density. It has a particular focus on a 50kW generator operating at speeds up to 17,000rpm which is coupled to an uncontrolled diode rectifier for DC power generation for a ‘more electric’ Rolls-Royce model 250 turbine engine. To be competitive for this application, an active power density target of 15kW/kg was set.

An electromagnetic design study has been carried out on a 15-slot, 10-pole surface-mounted permanent magnet topology. The design is optimised in order to maximise output power at the uncontrolled rectifier terminals and to limit the current density to a thermally sustainable level, ultimately operating near its electromagnetic limit.

Having established a baseline design, a prototype generator was constructed and tested both in its normal operating mode of power generation and statically using DC currents for precise thermal characterisation of the cooling strategy. The scope to further increase the power density is explored drawing on analysis of several novel features: additively manufactured coils, aluminium winding design variant, and current waveform optimisation.

ACKNOWLEDGEMENT

I would like to express my sincere gratitude to professor Geraint Jewell for his invaluable supervision, support and guidance throughout the entirety of this research work and the publishing of this thesis.

I would like to thank the EPSRC and Rolls-Royce for the award of a Dorothy Hodgkin's Postgraduate Award. I would also like to thank the staff at Rolls-Royce EPACS and SRC, particularly Ellis Chong for his enthusiasm and support.

Many thanks are also due to the technical staff in the Electrical and Machines and Drives Group for their assistance in constructing the prototype generator and test rig. To my colleagues in the Rolls-Royce University Technology Centre and the wider EMD group, who provided a great working environment and good humour, thank you.

Lastly, I would like to thank my father, Ishmael Shortte, for paving the way, my wife, Abigail, for her encouragement, my family and friends for their support and the good times throughout the course of this PhD.

TABLE OF CONTENTS

The University of Sheffield	i
Abstract	ii
Acknowledgement	iii
Table of Contents.....	iv
List of figures	ix
Nomenclature	xviii
Chapter 1 Introduction	1
1.1 The ‘more electric aircraft’	1
1.2 High performance electrical machines	4
1.3 Summary of thesis scope	9
Chapter 2 Electromagnetic design of 50kW low pressure shaft generator for an unmanned aerial vehicle	11
2.1 Introduction	11
2.1.1 Air-Cooled 50kW low pressure shaft generator.....	13
2.1.2 Design Specifications of the Liquid-cooled 50kW LP shaft generator	16
2.2 Stator electromagnetic optimisation of 50kW Liquid-cooled Generator	18
2.2.1 Calculation of key generator parameters.....	22
2.2.2 Stator geometry design optimisation.....	26
2.2.3 Selection of Slot-pitch to tooth-pitch ratio.....	29
2.2.4 Selection of number of turns and axial length	31

2.3	Rotor magnet containment stress analysis.....	34
2.4	Rotor magnet eddy-current losses & Magnet segmentation.....	38
2.5	Steady state analysis of the optimised design at the 50kW operating point	45
2.5.1	2D Finite Element Simulated performance characteristics	46
2.5.2	Electrical Losses at 50kW Operating Point	51
2.5.3	Mass of active components and power density.....	53
2.6	Selection of cooling strategy	54
2.6.1	Spiral-Jacket cooling.....	55
2.6.2	Flooded stator.....	60
2.7	Conclusion.....	63
Chapter 3 Construction, Testing and Analysis of Prototype Generator		64
3.1	Introduction	64
3.2	Rotor Construction	64
3.3	Stator Construction.....	69
3.4	Flood cooling design	73
3.5	Experimental testing of the prototype generator	77
3.5.1	Measurement of machine parameters.....	77
3.5.2	Experimental No-load back emf test.....	80
3.5.3	On-Load testing with diode bridge rectifier.....	88
3.6	Thermal monitoring during testing and Analysis.....	91
3.6.1	Thermal steady-state test results	95

3.6.2	Prediction of coil temperatures at high current densities	101
Chapter 4 Thermal Characterisation of stator flood cooling method..		102
4.1	Introduction	102
4.2	Estimation of winding temperatures using Motor-CAD	106
4.3	Thermal testing using DC excitation.....	110
4.4	Experimental results	113
4.5	Comparison of experimental and predicted temperatures	117
4.6	Conclusions	119
Chapter 5 Comparative analysis of Copper and Aluminum Windings for high power density electrical machines		120
5.1	Introduction	120
5.2	Aluminum and Copper Conductors.....	120
5.2.1	Oxidation of Aluminium Conductors.....	122
5.3	Machine design options using aluminum windings	122
5.3.1	Al design with increased axial length to maintain equivalent mass...	124
5.4	Performance of aluminum versus copper winding design	126
5.5	Conclusions	129
Chapter 6 Novel coil winding methodology using additive manufacturing		130
6.1	Introduction	130
6.2	Novel coil features enabled by additive manufacturing	131
6.3	Additive manufacturing process.....	138

6.3.1	Copper powder properties	138
6.3.2	EBM machine specifications.....	139
6.3.3	Procedure for optimising process parameters	140
6.3.4	Build temperature conditions	143
6.3.5	Pre-heat conditions.....	144
6.3.6	Melting conditions	145
6.3.7	Trial results.....	146
6.3.8	Conclusions of the Additive manufacturing process	155
6.4	AC losses in additive manufactured coils	155
6.5	Packing Factor in Additive Manufactured Coils.....	168
6.5.1	Reference Coil Design	168
6.5.2	Minimum coil requirements.....	169
6.6	Conclusion.....	171
Chapter 7 Current waveform optimisation for enhancing power density		
.....		172
7.1	Introduction	172
7.2	Predicted performance of the demonstrator design with a fully controller converter and sinusoidal current.....	172
7.3	Operation with arbitrary controlled waveforms	173
7.3.1	Optimisation Algorithm	174
7.4	Optimisation studies	176
7.4.1	Verification of the optimisation algorithm.....	176

7.5	Optimisation of current waveform for the demonstrator design	177
7.6	Interior Permanent Magnet Machines	179
7.6.1	Rotor geometry and torque production	179
7.6.2	Reference IPM design	181
7.7	Single phase optimisation.....	182
7.7.1	Torque pre-characterisation	182
7.8	Three phase optimisation.....	190
7.8.2	Optimisation algorithm	191
Chapter 8 General Conclusion.....		198
8.1	Scope for future work.....	201
References.....		202
Appendix A: Constructing prototype		206
Appendix B: Prototype Testing		214
Appendix C: Current optimisation.....		215

LIST OF FIGURES

Figure 1 MEA programmes over the years [3]	2
Figure 2 CAD drawing of gas turbine engine with electrical components to be integrated [3]	3
Figure 3 Rolls-Royce Model 250 Engine.....	8
Figure 4 Demonstration system architecture.....	9
Figure 5 Typical application of the Rolls-Royce Model 250 engine – UAV helicopter [Source – Rolls-Royce]	9
Figure 6 System architecture.....	12
Figure 7 Predicted IV curve of the air-cooled LP generator	14
Figure 8 Cross-section through air-cooled LP shaft generator FE model.....	15
Figure 9 Preliminary FE model of oil-cooled LP shaft generator.....	17
Figure 10 FE model coupled with diode bridge rectifier circuit.....	20
Figure 11 PM air-gap flux density distribution for various magnet height.....	21
Figure 12 Uncontrolled rectifier output voltage versus current characteristics of initial stator geometry design (as detailed in Table 3) at 17,000 rpm.....	22
Figure 13 – 3D FEA predicted inductance for varying axial length	24
Figure 14 Comparison of the BH curves of soft magnetic material	25
Figure 15 BH curve of Vacomax-225 grade samarium cobalt magnets [Source: Vacuumschmelze].....	26
Figure 16 Stator geometry dimensions	27
Figure 17 – The variation in current density with tooth width of the designs listed in Table 4.....	28
Figure 18 IV characteristics for designs on varying stator geometric cross-sections at 17000 RPM	29

Figure 19 Uncontrolled rectifier output IV Characteristics at 17000 RPM with various slot to tooth pitch ratios30

Figure 20 IV Curves analysing the effects of the number of turns and axial length on the output power at 17000 rpm33

Figure 21: Finite element stress distribution in the regions of the rotor at 17000rpm (Rotor temperature of 120°C; carbon fibre thickness of 2mm; 450MPa compressive stress at standstill)36

Figure 22 Variation in localised peak stress on carbon fibre containment as a function of containment thickness (Temperature of 120°C and speed 17000rpm with a pre-compression of 450MPa)36

Figure 23 Variation in electromagnetic performance as a function of airgap length 37

Figure 24 The magnet eddy-current losses of a single segment per pole of design 4 at the rated 50kW at 17,000 rpm41

Figure 25 Magnet eddy-current losses as a function of current density at 17000 rpm42

Figure 26 Instantaneous snapshot of the eddy-current distribution in a magnet pole of 12 radial segments43

Figure 27 Instantaneous snapshot of the eddy-current distribution in a magnet pole of 24 segments44

Figure 28 Finalised generator cross-section.....45

Figure 29 Finite element No-load open-circuit Back-EMF at 17,000 rpm.....47

Figure 30 Phase current at the 50kW, 17000 rpm operating point – connected to diode rectifier48

Figure 31 Flux density plot at rated operating point of 50kW at 17,000rpm.....49

Figure 32 Magnetic equipotential contours at rated load and speed.....50

Figure 33: Iron loss in the stator core at rated operating point of 50kW at 17,000 rpm.	52
Figure 34 Iron loss of the stator at 30kW operating point of a 5 th of the stator	53
Figure 35 Schematic of Spiral liquid-jacket cooling arrangement	56
Figure 36 Temperature for varying flow rate at 50kW operation point.....	58
Figure 37 Simulated temperatures at various regions of the machine at a flow rate of 5l/min operating at 50kW.....	59
Figure 38 Thermal FEA of the winding operating at 50kW and a flow rate of 5l/min using Motor-CAD	60
Figure 39 Flooded stator oil cooling arrangement	61
Figure 40 Radial view of simulated temperatures at various regions of the machine at a flow rate of 5l/min operating at 50kW	62
Figure 41 Axial view of simulated temperatures at various regions of the machine at a flow rate of 5l/min operating at 50kW	63
Figure 42 Comparison of core losses using VAC process compared with standard process (Source: Vacuumschmelze)	65
Figure 43 Comparison of the flux density per field strength of the core using the VAC process and the standard process (Source: Vacuumschmelze).....	65
Figure 44 Assembly of the hub, end-plates and a temporary shaft.....	67
Figure 45 Rotor core and hub arrangements with magnet pole niches	68
Figure 46 Assembly of the rotor showing segmented magnets	68
Figure 47 Completed rotor	69
Figure 48 Stator core.....	70
Figure 49 Stator winding part-way through manufacture	72
Figure 50 Location of thermocouples	73

Figure 51	Photos of the finished PEEK air-gap sleeve	74
Figure 52	Cross-section of machine assembly	75
Figure 53	Liquid-tight electrical feedthrough connectors.....	76
Figure 54	Liquid-tight thermocouple feedthrough gland.....	76
Figure 55	Complete assembly of prototype generator	77
Figure 56	View of interconnections and star-point of completely wound stator.....	78
Figure 57	1700V/450A uncontrolled bridge rectifier	80
Figure 58	Measured line-to-line back EMF at 17,000 rpm.....	81
Figure 59	Simulated and measured line-line Back EMF at 17,000 rpm.....	82
Figure 60	Predicted variation in the Back-EMF waveform at varying magnet remanence at 10195 rpm	83
Figure 61	3D-FEA simulated back-EMF at 10195 rpm.....	84
Figure 62	Magnet segmentation with glue-line width of 0.3mm.....	85
Figure 63	The EMF for varying adhesive thickness between segments compared with measured EMF waveform over 180 degrees electrical.....	86
Figure 64	Photograph of rotor highlighting reduced width of segments at pole edge	87
Figure 65	FFT analysis of the measured and simulated emf at 10195 rpm	88
Figure 66	Comparison of the simulated and measured I-V curve of the machine at 17000 rpm	89
Figure 67	DC current and voltage, phase current and line-line voltage measurement at 30kW, 17,000 rpm operating point	90
Figure 68	Comparison of simulated and measured winding current at 30kW, 17000 rpm	91
Figure 69	Generator thermal testing rig	92

Figure 70 Temperature difference between oil inlet and outlet as a function of flow rate at a series of rms current densities	96
Figure 71 Maximum coil temperature as a function of flow rate for varying current densities (maximum taken at highest reading from the 7 thermocouples in the coils)	97
Figure 72 Measured temperatures within the machine for TR13 (see Table 14).....	98
Figure 73 Location of the coils around the stator	98
Figure 74 Coil temperature relative to flow rate at 8.9Amm^{-2}	100
Figure 75 Predicted temperature difference of oil inlet and maximum coil as a function of current density for the prototype machine.....	101
Figure 76 Liquid-cooling arrangement with cooling channels in the slot	104
Figure 77 Cooling approach proposed by [31] with channels in alternating teeth and flooded airgap (yellow regions indicates fluid zone).....	105
Figure 78 Calculated variation in HTC as a function of flow rate for the reference slot with a packing factor of 0.5 (490 conductors of 0.67mm diameter).....	108
Figure 79 Temperatures across the machine at 1000W of copper loss only and a flow rate of 1.37l/min.....	110
Figure 80 DC current switching rig	112
Figure 81 Prototype machine during testing	113
Figure 82 Winding temperatures with switching every 10s	114
Figure 83 Verification of measured oil flow rate.....	117
Figure 84 Proportions of the active mass component of the prototype.....	124
Figure 85 Simulated Current-Voltage characteristics of the various designs shown in Table 24.....	128

Figure 86 Model of AM Coils within the active region of a rectangular slot -uniform cross-section (left) and graded cross-section (right)	134
Figure 87 Cross-section through the active region of an AM coil.....	135
Figure 88 Example of an end-winding arrangement manufactured by AM	138
Figure 89 Arcam S12 EBM Unit	140
Figure 90 Schematic diagram of the Arcam EBM machine	142
Figure 91 Photo of the build area Arcam EBM machine – shown with copper powder during trials	143
Figure 92 Schematic cross-section through a component during build showing melted and partially sintered regions	144
Figure 93 Typical sample during build-up showing preheated powder for support and fully melted regions.....	145
Figure 94 Electron beam scanning parameters	146
Figure 95 (a) Specimen layout on start plate	147
Figure 96 Cube sample I and sample II manufactured using LK and Co-Cr parameters respectively.....	148
Figure 97 Sample-I and sample-II with SF of 15 and 22 respectively.....	149
Figure 98 Dimensions of the serpentine sample (depth of 4.5mm)	149
Figure 99 EBM serpentine structure with a de-laminating defect	151
Figure 100 Surface cracks developed in test sample	151
Figure 101 EBM Serpentine sample used for resistivity and conductivity measurements.....	152
Figure 102 Surface after cutting using EDM.	153
Figure 103 Surface finish from the EBM process.....	153

Figure 104 – Alternative additively manufactured conductor arrangements (one single conductor forming each successive turn of the coil) – (a) horizontal (b) vertical..... 160

Figure 105 Finite element predicted coil losses for conductor arrangement shown in Figure 104a 162

Figure 106 Finite element predicted coil losses (per phase) for conductor arrangement shown in Figure 104b..... 163

Figure 107 Representative magnetic flux density distribution demonstrating the effect of semi-magnetic slot wedges 165

Figure 108 Conductor arrangement with each series turn divides into 5 parallel paths 167

Figure 109 Predicted variation in coil losses with speed for a coil with a single conductor region per turn and a coil in which the cross-section of one turn is divided into 5 parallel paths as defined in Figure 108 167

Figure 110 Coil dimensions 169

Figure 111 3D CAD drawing of the coil..... 169

Figure 112 Cross-sectional view of coil in Figure 111, illustrating copper and insulation regions 170

Figure 113 Packing factor against insulation thickness 171

Figure 114 Flowchart of the optimisation process..... 175

Figure 115 Optimised current waveforms generated by the optimisation algorithm for torque look up tables populated from an idealised sinewave back-emf..... 177

Figure 116 Optimised current waveform generated for the prototype machine described in chapter 2 and 3..... 178

Figure 117 Torque waveform for the pure sinusoid and the optimised current at 8 Amm ⁻² when supplied to the demonstrator	179
Figure 118 Cross-section of IPM FEA model	182
Figure 119 Torque waveform for a range of DC currents at a speed of 17,000 rpm	183
Figure 120 Verification of the spline interpolation prediction.....	184
Figure 121 Comparison of optimised and sinewave current of the same RMS value of 292A _{rms}	185
Figure 122 Comparison of torque produced by phase A when excited with a sinewave current (in phase with back-EMF) and the optimised current waveform of the same RMS value.....	186
Figure 123 Percentage increase in torque produced by the optimised current waveform for a range of current densities.....	187
Figure 124 Plot of average torque for varying phase advance angle at current density of 20A/mm ²	188
Figure 125 Comparison of average torque for the same RMS current of 292 A _{rms} (20 A/mm ²).....	189
Figure 126 Optimised single phase current for a range of current densities.....	190
Figure 127 Plot of torque against phase- <i>b</i> current using FEA and gridded-interpolation for a phase- <i>a</i> current of 292A at angle 35°.....	191
Figure 128 Contour map of the torque produced by interpolation at angle 35°	192
Figure 129 Optimised current waveform at a current density of 5Amm ⁻² (73A _{rms})	193
Figure 130 Torque comparison of the optimised (Figure 129) and sinewave current of the same RMS value at a current density of 5Amm ⁻² (73A _{rms})	194

Figure 131 Optimised current waveforms at a current density of 20Amm^{-2} (292A_{rms})
..... 195

Figure 132 Torque comparison using optimised (Figure 131) and sinewave current
(no phase advance) at current density of 20Amm^{-2} (292A_{rms})..... 196

Nomenclature

Symbol	Definition	Unit
A	Cross-sectional area	m^2
ang	Angle	$^\circ$
B	Flux density	T
C_p	Specific heat capacity	J/kg.k
D	Diameter	m
f	Frequency	Hz
I_{rms}	RMS Current	A
i_q	Quadrature current	A
i_d	Direct current	A
k_w	Winding factor	
k_{ss}	Proportion of winding in the active region	
k_{ew}	Proportion of winding that are end-windings	
k_{int}	Proportion of winding that are interconnects	
L	Length	m
L_{coil}	Coil Inductance	H
L_{ax}	Axial length	m
L_{cu}	Axial length of copper winding design	m
m	mass	kg
m_{mag}	Mass of active components that scales with L_{ax}	kg
M	Mutual inductance	H
N	Number of turns	
P_{cu}	Copper loss	W
q	Power loss	W
R	Resistance	Ω
T	Torque	Nm
T	Temperature	$^\circ C$
t	Time	s
V_{cu}	Volume of copper	m^3

α	Temperature coefficient of resistance	K^{-1}
δ_{Al}	Density of Aluminium	Kg/m^3
δ_{Cu}	Density of copper	Kg/m^3
ρ	Resistivity	Ωm
φ	Flux	Wb
ψ	Flux linkage	Wb
μ_r	Relative permeability	H/m

Chapter 1 INTRODUCTION

1.1 THE 'MORE ELECTRIC AIRCRAFT'

The many ancillary systems on an aircraft, i.e. those that do not provide the main propulsion, are usually powered from the main aircraft engine via various mechanism in the form of either mechanical, hydraulic, pneumatic or electrical power. Aircraft systems which are driven from electrical power have become increasingly competitive in terms of functionality, controllability, energy efficiency, reliability and maintenance costs. This is due to continued advancements in the reliability and power density of power electronics and electrical machines in recent years.

With the increased use of electrical systems, the electrical load on aircraft has increased substantially over the years. This is mainly because of the integration of more electric devices such as; electrical actuators, electrical environmental controls. In the future, electric fuel and oil pumps and other electrified systems are likely to emerge. This increasing use of electrical systems has led to the so-called 'More Electric Aircraft' (MEA) concept [1].

In the 1960's a typical large aircraft engine would be required to produce $\sim 40\text{kVA}$, whereas a modern large civil aircraft is required to produce in excess of $\sim 250\text{kVA}$ (from one remaining healthy engine under engine shut-down conditions on a twin-engined aircraft such as the Boeing 787).

Industry projections expect further increases in installed electrical generating capacity in order to meet future aircraft electrical power demand [2]. It is possible that this demand will not be met from increasing generators driven from the

accessory gearbox. The integration of larger electrical generators onto the main gas turbine shafts are being investigated.

There have been several large-scale MEA R&D programmes over recent years, as shown in Figure 1. These programmes have variously attempted to identify, optimise and validate innovative electrical aircraft equipments and systems.

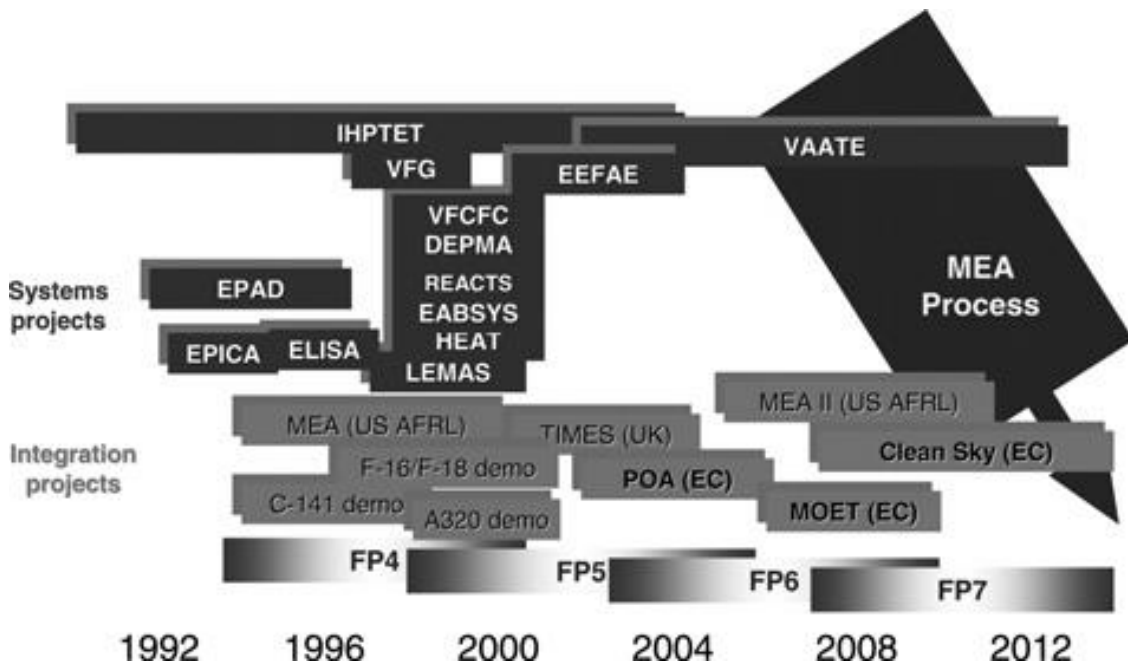


Figure 1 MEA programmes over the years [3]

The Power Optimised Aircraft (POA) technology programme, a consortium of 43 organisations in the aeronautical industry sector in Europe, contributed 100M Euros to explore technologies for reducing the power consumption of non-propulsive systems [3], including investigating the advantages of novel electrical power generation systems. Having conducted the engine system validation test using the Rolls-Royce Trent 500, it was demonstrated that each of the conventionally gearbox-driven systems could be replaced with main engine-shaft connected generator [3].

Figure 2 shows the typical electrical components of the POA engine demonstrator . The POA programme carried out the following series of demonstrations and experimental testing: Operation of novel electrical components (Fuel, oil pumps, ect.), electric start of the engine using high pressure shaft starter-generator, and the control of parallely generated power between the LP and HP generators to maintain stability of the 350V DC Bus. Although the technologies developed in the POA demonstration were seen as immature for use on aircraft systems as they stand, the project did serve to highlight several strands of research that will provide important steps in the realisation of the MEA [3].

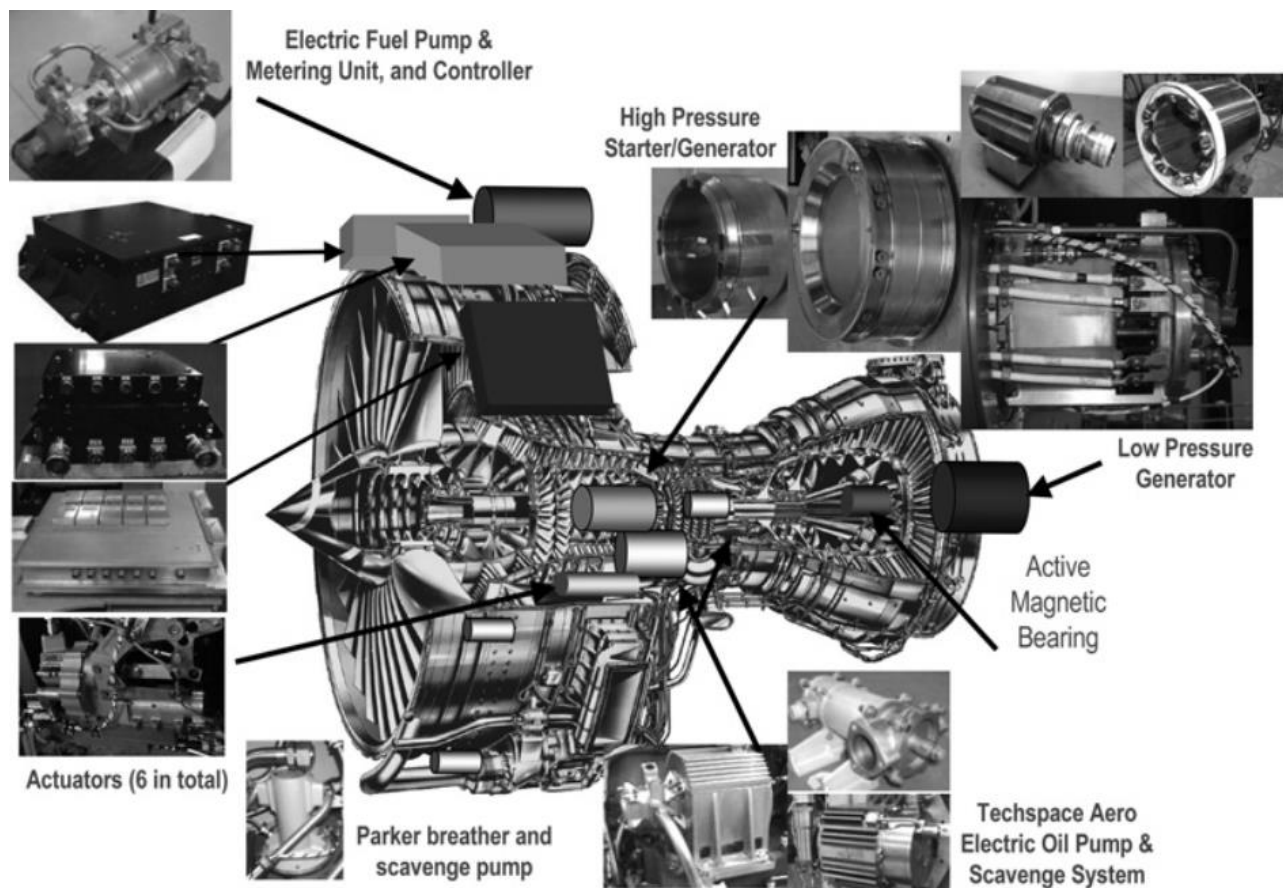


Figure 2 CAD drawing of gas turbine engine with electrical components to be integrated [3]

1.2 HIGH PERFORMANCE ELECTRICAL MACHINES

Well established electrical machine topologies, such as induction and wound-field synchronous machines are continuously being improved in terms of reliability, efficiency and power density. However, improvements are being achieved with diminishing returns. More significant advances continue to be made in more recently developed topologies such as permanent magnet (PM), switched reluctance and synchronous reluctance machines. On a true like-for-like basis, PM electrical machines are generally recognised as offering the highest power density and have received much research interest over the last 20 years or so [4]. This research effort has been directed towards applications and demands from the automotive, motorsport, renewable and aerospace sectors. PM electrical machines are continually being pushed to their operating limits in these demanding applications, with designers often expected to extract ever-more power from the same size machines. In order to meet these objectives, it is necessary to address a series of technical challenges to achieve any improvement in power to weight ratio or in other application power to volume ratio. These include the adoption of new materials and manufacturing methods, the minimisation of losses through careful electromagnetic design, the management of losses in the machines and the interactions with the power electronic converter.

PM machines are often categorised based on the direction of the flux path in the magnetic circuit, with radial flux or axial flux being the most common. The selection of axial or radial flux was often decided by the geometrical constraint of the application and the operating speed range. In the past, axial flux machines received much less attention than their radial flux counterparts, because of mechanical critical aspects and manufacturing complexity. However, recently, axial flux machines have

received more attention in the automotive industry and have proven to be competitive in terms of power density [5] and a good fit to the power and speed range of automotive applications (several tens of kW at 6,000-10,000rpm). However, their major drawback in performance is their limited rotational speed for high power applications, since the rotor aspect ratio cannot be adapted to suit the combination of torque and speed. High speed axial field machines have been developed for power generation applications based on a stack of axial field stators and rotors. Although this stacking approach can offer high power density in terms of the kW/kg for very high speed applications, they do not offer such competitive power density at lower speeds.

There are many types of rotors used in radial-flux PM machines. When used in combination with appropriate stator designs these provide a range of properties and performance features. The two main categories of rotor are variants on interior permanent magnet (IPM) or surface-mounted permanent magnet (SPM).

IPM have received significant attention for use in automotive application. This is due to a particular characteristic of IPM which readily allows the constant speed power range to be extended using so-called flux weakening. IPM rotors inherently exhibit a degree of saliency due to the arrangement of the magnets on the rotor. This give rise to a torque component commonly known as reluctance torque.

Flux weakening is not usually considered for safety critical aerospace applications because of the large back-emf that can be present at the terminals if the drive fails or shuts-down.

SPM machines with non-overlapping concentrated windings are generally regarded as offering the most power dense topology, particularly for generator applications in

which machine reactance can be a limiting factor on performance. However, the resulting emf often have significant harmonic content. SPM machines can employ either distributed overlapping windings or non-overlapping concentrated [2]. Non-overlapping with concentrated windings can further sub-divided into double layer (all teeth wound) or single layer (alternate teeth wound). Non-overlapping concentrated winding provides the following advantages compared to the various other alternatives: high power density, short end-windings, high slot fill factor and fault tolerant capabilities when used with particular combination of phase and slot numbers [3, 4].

The emergence and continued development of permanent magnet materials has resulted in well-established grades of materials that combine both excellent magnetic properties (in particular remanence and coercivity) and elevated temperature capability. In the aerospace sector, the residual concerns over the long-term stability and corrosion resistance of NdFeB ensure that $\text{Sm}_2\text{Co}_{17}$ remains the preferred permanent magnet material despite its slightly inferior room temperature magnetic properties. Although airgap flux densities of 0.7-0.8T or so can be achieved with $\text{Sm}_2\text{Co}_{17}$, the main factor which facilitate high power densities is operating with high stator coil current densities, with values of 10-15 A/mm² being commonplace.

There are several challenges that arise in the design of SPM machines operating at high stator coil current densities. Losses within a high current density machine design tend to be dominated by copper loss and requires a more complex cooling approach to remove heat from the windings.

As well as the high level of stator copper losses, the high current density contributes to significant levels of eddy-current losses in the magnets thus increasing the magnet

temperature and often requires a method to minimise the magnet temperature to sustainable levels. The effect is reduced if the effective magnetic airgap is large (i.e. several mm) in order to accommodate a magnet containment sleeve. The most common and effective method of reducing the magnet eddy-current losses is by segmenting the magnets along the magnetisation direction and/or axially.

The stator copper loss can be reduced by increasing the slot fill or slot packing factor. Commonly achieved slot fill factors tend to fall within the range of 0.3 to 0.5 for in-situ wound coils and slightly higher for pre-formed coils.

This thesis investigates several approaches to increasing the power density of permanent magnet machines. In order to undertake these investigations in a systematic manner, these investigations were undertaken in the context of a 50kW generator which is driven by the low-pressure (LP) shaft of a Rolls-Royce Model 250 gas-turbine engine, a standard example of which (without a high power generator) is shown in Figure 3.

The generator is one element in a wider electrical systems demonstration rig. The system architecture is shown in Figure 4, with the LP generator highlighted within a red box. This architecture is a synthetic representation of the power generation and distribution network on a UAV platform which employs a Model 250 engine. This technology demonstration fits into a broader R&D programme ASTRAEA II (Autonomous Systems Technology Related Airborne Evaluation & Assessment) which was undertaken by a consortium including Rolls-Rolls. The objective of this wider programme is to develop and demonstrate some key technologies for the operation of autonomous vehicle safely and routinely within civil airspace over the

United Kingdom. One use of such autonomous vehicles might be fire scouting using a UAV helicopter shown in Figure 5.

The requirements for the generator are very challenging, in particular the need to achieve the highest levels of power density (full specification for the generator is described in detail in Chapter 2).

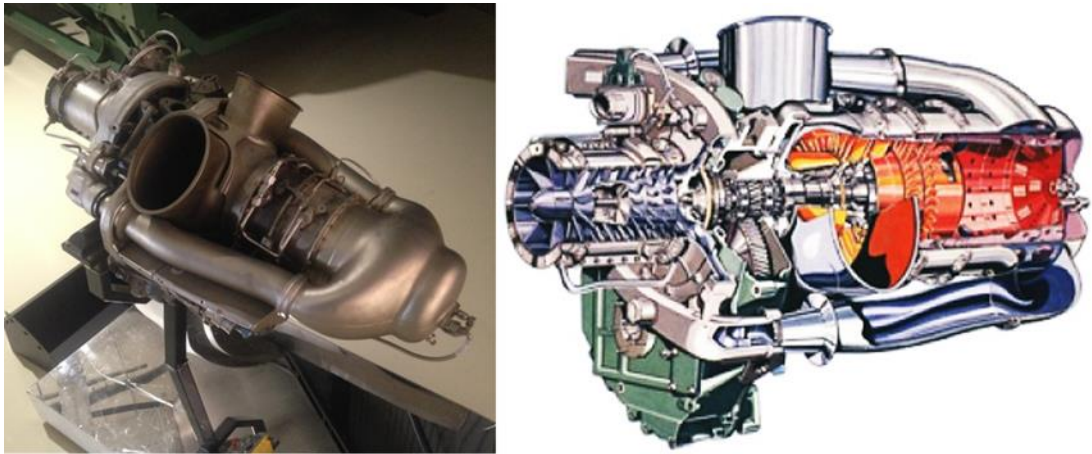


Figure 3 Rolls-Royce Model 250 Engine

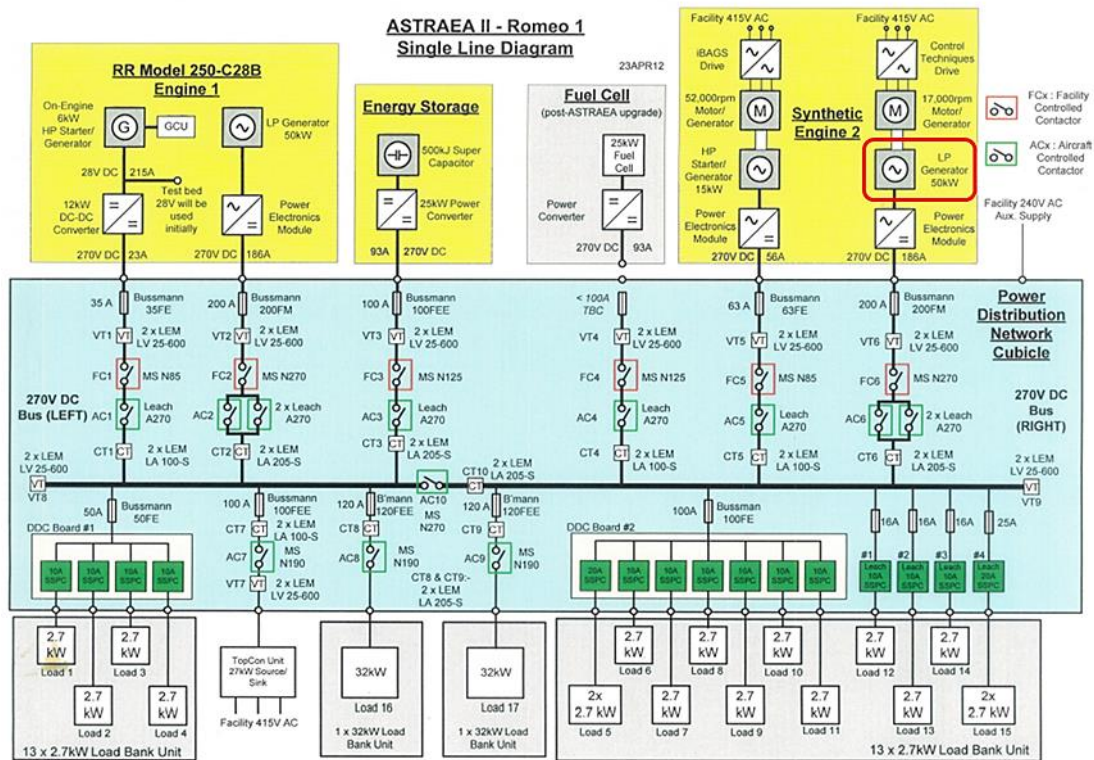


Figure 4 Demonstration system architecture



Figure 5 Typical application of the Rolls-Royce Model 250 engine – UAV helicopter [Source – Rolls-Royce]

1.3 SUMMARY OF THESIS SCOPE

This thesis reports on a series of design studies and investigations into features and technologies, which can be exploited to enhance the power density of a high speed permanent magnet generator. These include investigations into electromagnetic, thermal and control aspects of performance with a view to progressively enhancing the performance of a baseline reference design established in chapter 2.

The thesis is arranged into a series of chapters, which address the following aspects of high power density design and technologies:

Chapter 2 – The electromagnetic design optimisation of a 50kW PM generator for an uncontrolled rectifier was described. This design establishes the

baseline power density using the best materials and technologies currently available.

Chapter 3 – This chapter provides a detailed description of the construction, testing and analysis of the prototype design outlined in chapter 2.

Chapter 4 – This chapter investigated several thermal liquid cooling methods and characterise the flooded stator cooling approach employed in the prototype. The performance of the cooling method could provide flexibility to operate at a higher current density and thus further increase power density.

Chapter 5 – This chapter compares the use of aluminium conductors with copper in order to reduce weight of windings and hence increase power density. A significant proportion of the active mass of the design outlined in chapter 2 is contributed by the windings.

Chapter 6 – A novel coil manufacturing method using additive manufacturing (AM) was investigated in this chapter. AM allows novel intricate features to be integrated into the coils to improve in the performance.

Chapter 7 – This chapter outlines a current waveform optimisation technique to increase the maximum torque per amp by profiling the current waveform.

Chapter 8 – This chapter provides a summary of chapter 2-7, outline novel contributions and scope of future work.

Chapter 2 ELECTROMAGNETIC DESIGN OF 50kW LOW PRESSURE SHAFT GENERATOR FOR AN UNMANNED AERIAL VEHICLE

2.1 INTRODUCTION

An integral component of the ASTRAEA (Autonomous Systems Technology Related Airborne Evaluation & Assessment) demonstration rig is a high power density liquid-cooled 50kW generator for the low pressure shaft of an unmanned aerial vehicle. A summary of the key performance specification for this generator is shown in Table 1. This chapter describes the electromagnetic design and modelling of the generator while chapter 3 describes the construction and testing of a prototype.

Table 1 Design specifications

Feature	Value
Speed range (rpm)	10,195-17,000
Output power (kW)	30-50
Stator outer diameter (mm)	160
Power converter	Uncontrolled bridge rectifier
DC bus voltage (V)	270

The generator is required to generate 30kW at 10,195rpm and 50kW at 17,000 rpm. An ambitious power density of 15kW per kg of active weight (i.e. excluding casing and shaft / hub) was the design target for the generator. This challenging target reflects the premium on mass reduction in aerospace applications. The system architecture to deliver power to a regulated 270V DC bus is shown in Figure 6.

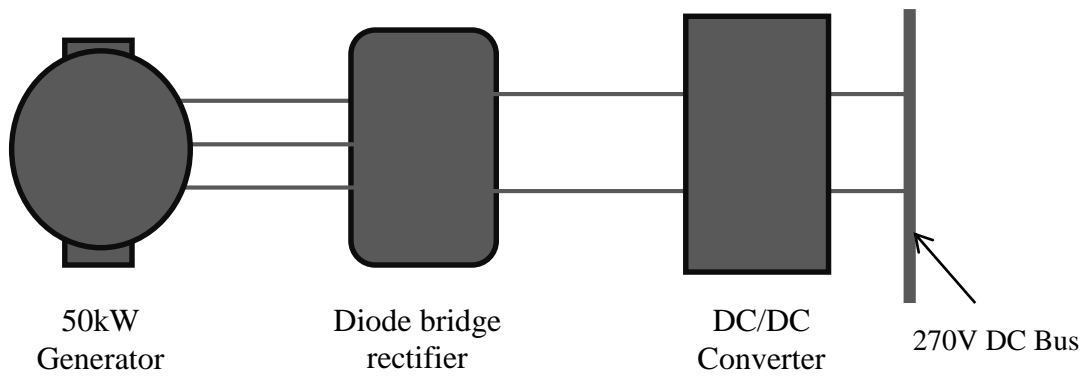


Figure 6 System architecture

The preferred machine type identified for this high power density application and specifications was a permanent magnet synchronous generator (PMSM) with a fractional-slot, concentrated winding configuration. Fractional-slot concentrated winding synchronous (FSCW) PM machines have received significant attention in recent years, with many well recognised advantages over other machine types, including high power density, high slot packing factor, short end turns (less copper), high efficiency, low cogging torque and, in some configurations, fault-tolerance capability. FSCW do however, give rise to higher induced eddy-current loss in the magnets of the rotor [4]. Therefore, design features must be included to limit these losses to an acceptable level.

From a system configuration point of view, it is crucial to understand the output power characteristics of a PM synchronous generator when coupled to an uncontrolled diode bridge rectifier. The absence of any controllability in a diode bridge rectifier means that maximum power that can be extracted from the rectifier terminals is fixed, during the machine design stage. The generator has a voltage regulation characteristic, which is governed mainly by the ratio of the permanent magnet flux to the coil inductance. For this reason, throughout the machine design

stage reported in this chapter, the performance of the machine is considered at the diode bridge rectifier DC output terminals rather than at the generator terminals.

2.1.1 AIR-COOLED 50kW LOW PRESSURE SHAFT GENERATOR

The design of this liquid-cooled LP shaft generator follows on from a previous project in which a baseline forced air-cooling LP shaft generator design was constructed for testing. This air-cooled machine was designed to operate in conjunction with the same uncontrolled diode rectifier bridge. A cross-section through this 10 pole, air-cooled design is shown in Figure 8 while its electromagnetic performance and key parameters are summarised in Table 2. Although this air-cooled variant demonstrated the required performance, its active power density was modest at 3.69 kW/kg. This was due to the limited stator current densities of 7.6A/mm² RMS and 7.3A/mm² RMS at the 30kW/10,195rpm and 50kW/17,000rpm respectively. The predicted variation in the rectifier average DC voltage versus current for this design at both 10,195rpm and 17,000rpm is shown in Figure 7. It can be seen from Figure 7 that the electromagnetic power limit of this machine is ~140kW at 17,000rpm which is well in excess of its thermal rating of 50kW.

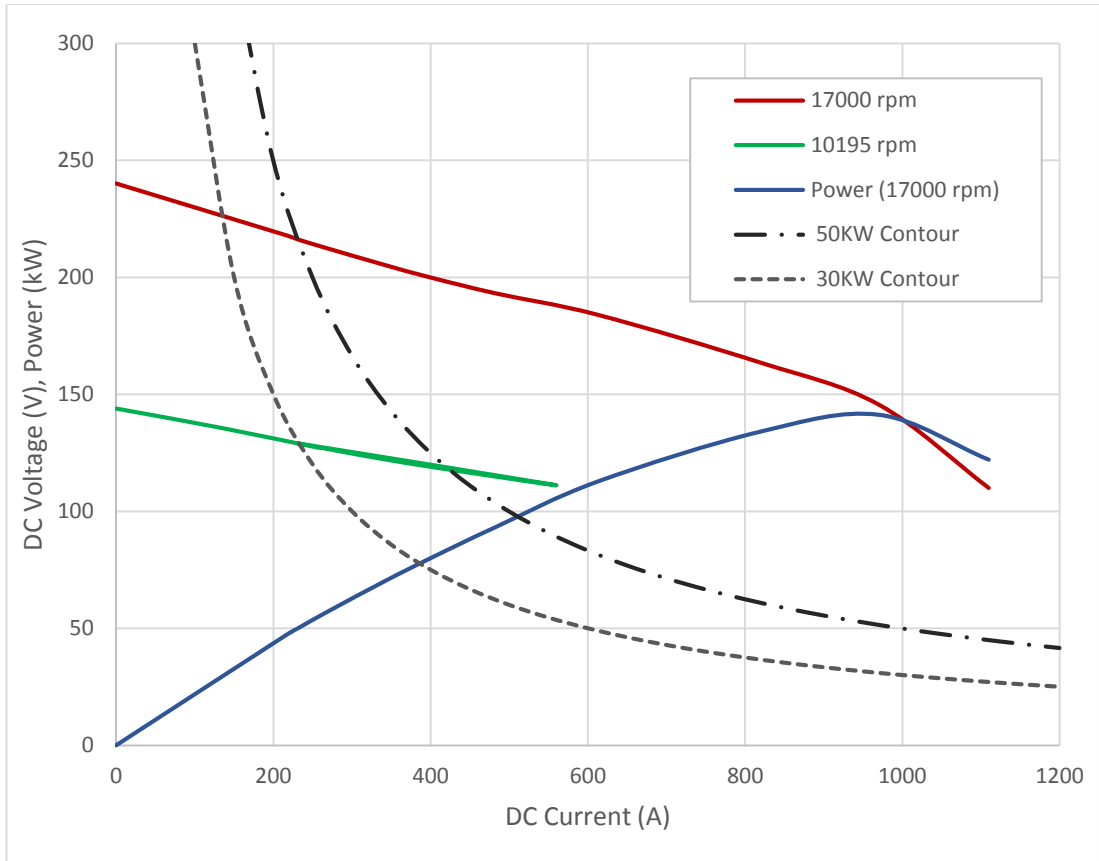


Figure 7 Predicted IV curve of the air-cooled LP generator

Table 2 Key parameters of air-cooled LP 50kW generator

Quantity	Value
Stator outer diameter (mm)	160
Stator bore diameter (mm)	122
Rotor outer diameter (mm)	116
Active length	165
Mechanical air-gap length (mm)	1
Active mass (kg)	13.6
Open circuit DC Voltage (V)	144 at 10,195rpm
	240.2 at 17,000rpm
50kW Operating point (A_{dc}, V_{dc})	230.9, 216.3
Coil packing factor	0.6
Total loss for a coil temperature of 200°C (W)	1420
Active Power Density (kW/kg)	3.69

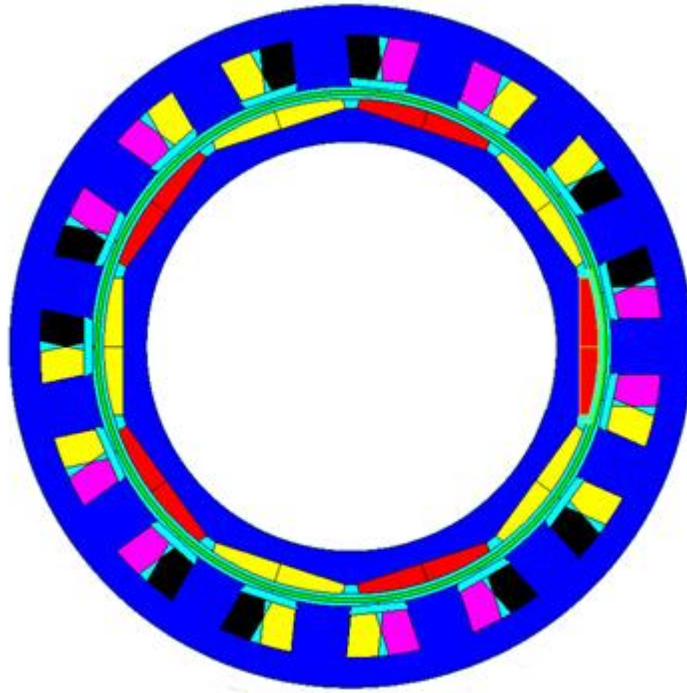


Figure 8 Cross-section through air-cooled LP shaft generator FE model

The generator design synthesis described in this chapter is targeted at a more aggressive electric loading in order to achieve a much higher power density for the same application and performance specifications. This is to be realised through a combination of using advanced cooling techniques, more aggressive electromagnetic design (i.e. to drive the core materials further into saturation) and weight reduction features.

The FSCW slot-pole configuration of 15-slots 10-poles with bread-loaf surface mounted permanent magnets was adopted from the air-cooled generator design in order to provide a more direct comparison. This slot and pole combination was previously chosen for the air-cooled version on the basis of power density from an electromagnetic point of view. However, it was never operated at its electromagnetic power limit of 140kW due to thermal considerations. High performance electrical

machines tend to operate near their electromagnetic and thermal limit simultaneously.

2.1.2 DESIGN SPECIFICATIONS OF THE LIQUID-COOLED 50kW LP SHAFT GENERATOR

The liquid-cooled 50kW generator described in this chapter, provides a baseline design incorporating the best available materials and advanced cooling technologies. Subsequent chapters will consider further improvements in power density using novel design features and advanced control strategies.

A series of top level design changes were made to the existing air-cooled design with a view to maximising the power density. Cobalt iron was chosen as the material for the rotor and stator cores (Silicon iron was used in the air-cooled LP generator). This has the highest saturation flux density limit of all bulk soft magnetic materials at 2.34T. The same permanent magnet material was chosen, viz. Samarium Cobalt ($\text{Sm}_2\text{Co}_{17}$) which has a high remanence and is not as sensitive to temperature and is more stable against corrosion than Neodymium Iron Boron ($\text{Nd}_2\text{Fe}_{14}\text{B}$). Direct oil flood cooling of the stator windings (discussed in more detail in chapter 4) was employed which allows substantial increase in RMS current density, from $\sim 7\text{Amm}^{-2}$ to $\sim 12\text{Amm}^{-2}$. A 1mm thick sleeve is required in the air-gap to prevent oil from stator from entering the void around the rotor. When combined with a magnet containment of 2mm and a 1mm mechanical clearance, the effective magnetic air-gap is increased to 4mm from the 3mm in the air-cooled generator.

The preliminary geometric design parameters established from some standard sizing and design equations are listed in Table 3. The corresponding cross-section for this design is shown in Figure 9. The stator outer diameter is retained at 160mm as was the case for the air-cooled variant. The stator bore was set by the size required to

generate 28Nm at 17,000 rpm. The initial sizing of the stator geometry was based on well-established approach of operating the core at a flux density which is near the onset of magnetic saturation. The axial length was sized to be the minimum required to achieve 50kW operating point.

Table 3 Preliminary geometric design parameters

Quantity	Value
Stator outer diameter (mm)	160
Axial length (mm)	50
Stator bore (mm)	60
Effective magnetic air-gap length (mm)	4
Magnet thickness (at centre of pole) (mm)	9

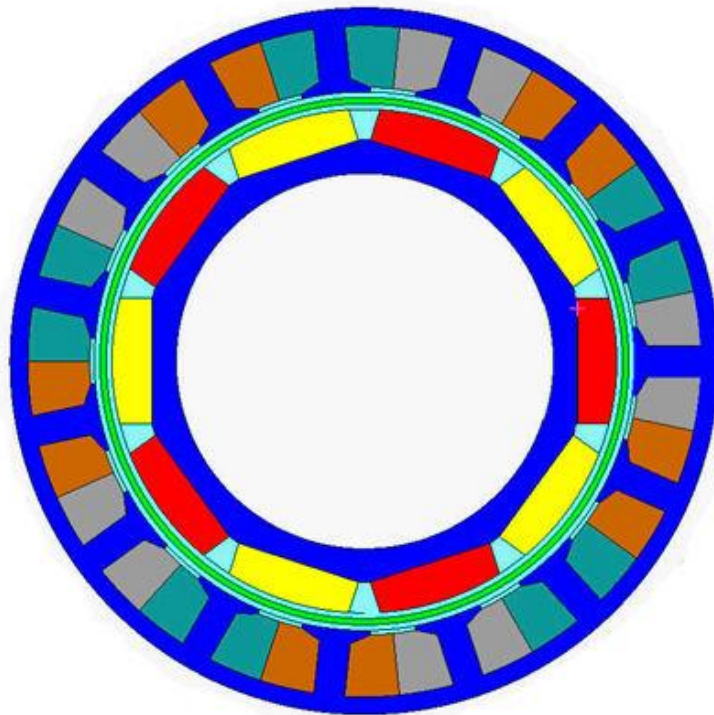


Figure 9 Preliminary FE model of oil-cooled LP shaft generator

2.2 STATOR ELECTROMAGNETIC OPTIMISATION OF 50kW LIQUID-COOLED GENERATOR

Having established an initial design using standard sizing equations a series of finite element simulations were undertaken to optimise stator geometry. By designing the machine to operate near its electromagnetic limit at 50kW, some benefits can be gained from a thermal and weight reduction. The current density was set to 12A/mm² RMS at a coil packing factor of 0.5. The coils will be wound in-situ because of the stator core having tooth-tips which limits the packing factor. This value is typical of the highest packing factor that can be achieved with an unsegmented core with tooth tips. The various designs were modelled using two-dimensional, non-linear, electric circuit-coupled finite element analysis. A schematic of this model is shown in Figure 10.

An uncontrolled rectifier topology was specified for the following reasons:

- High reliability
- High efficiency
- Simplicity with no control requirements
- Rugged
- Low maintenance

However, an uncontrolled rectifier has some drawbacks that must be considered at the generator electromagnetic design stage. Unlike its controlled counterparts, the uncontrolled rectifier has no means of compensating for the drop in voltage at its input terminals. Any increase in load current at a given speed, will result in an increase in the voltage dropped across the winding resistance and reactance, hence reducing the terminal voltage. The winding reactance is the dominant contributor to the reduction in terminal voltage. By minimising the inductance, the rate at which the terminal voltage reduces with load current can be minimised. Therefore, the

impedance must be optimised for the generator to meet its required peak output power capability at the rectifier output terminals. In addition, the current waveform from an uncontrolled rectifier has a significant harmonic content, which will contribute additional core losses and eddy-current loss in the magnets [12].

The uncontrolled diode bridge rectifier was specified as the best suitable for the system configuration and application. However, as mention above, it imposes constraints on the generator design and hence limits the system output power.

Figure 10 shows the arrangement of the generator connected to an uncontrolled diode bridge rectifier. The 1.6V sources in the bridge rectifier represent the forward diode voltage drop. The load at the output terminal was represented using a simple resistor.

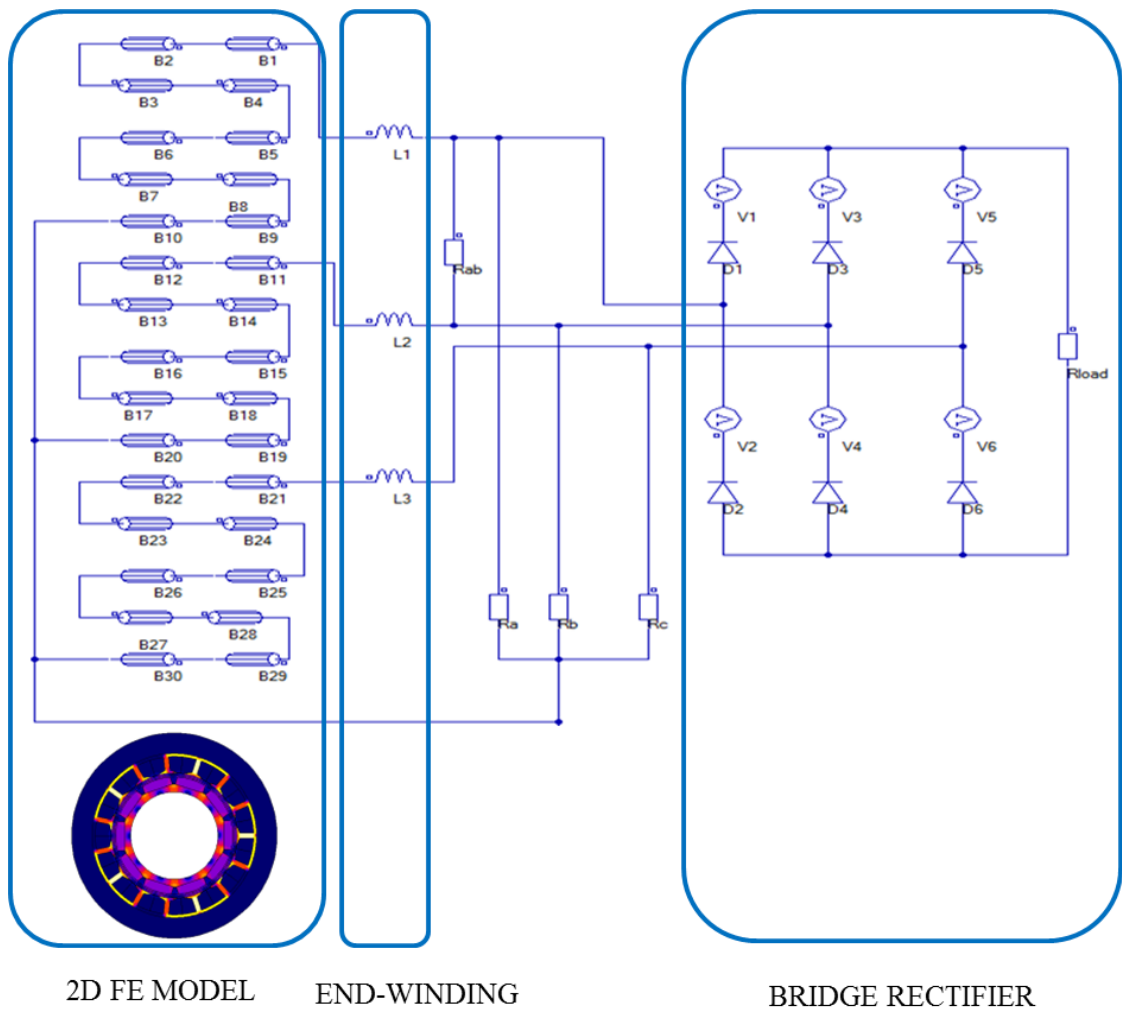


Figure 10 FE model coupled with diode bridge rectifier circuit

The generator has a large effective magnetic air-gap of 4 mm due to the need to accommodate the magnet containment, coolant sleeve and the mechanical clearance. The optimum thickness of the magnets was selected based on the analysis that is summarised in Figure 11. The increase in stress on the containment with magnet thickness was taken into consideration.

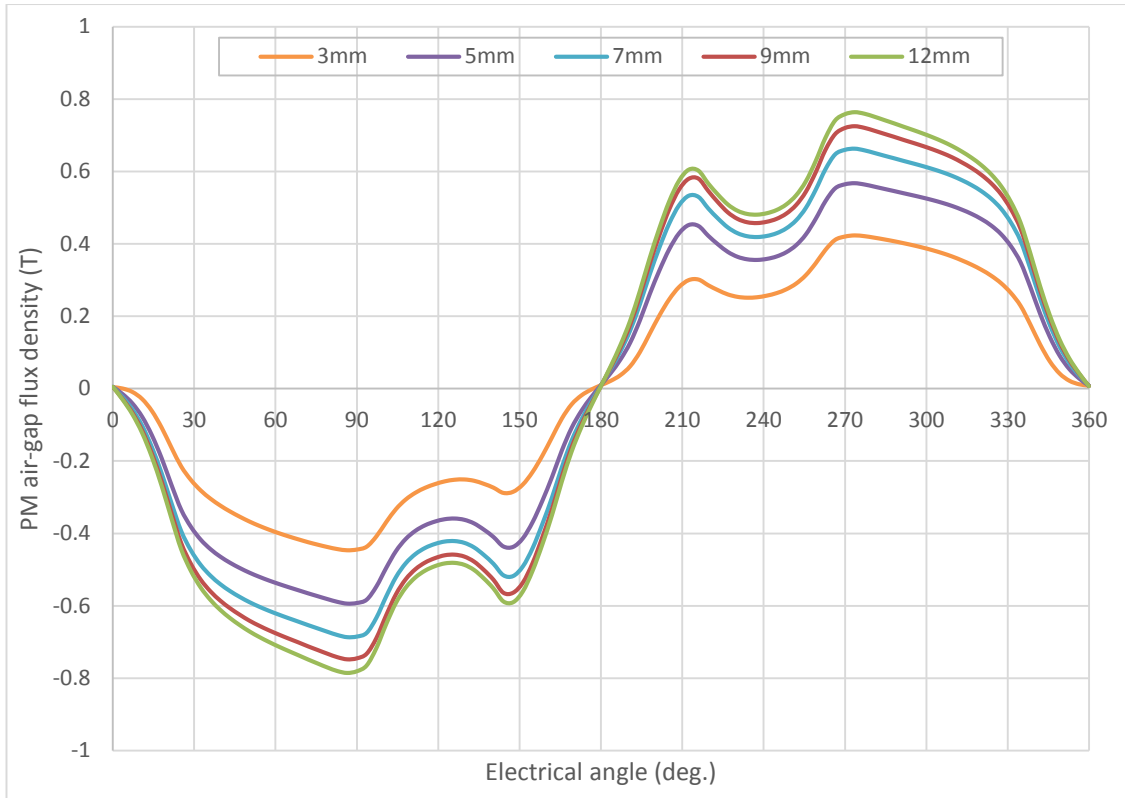


Figure 11 PM air-gap flux density distribution for various magnet height

Figure 12 shows the FE simulated DC current and DC voltage relationship (FE model shown in Figure 10) at the terminals of the diode bridge rectifier for the initial design detailed previously in Table 3. The DC/DC converter is designed to operate in a voltage step-up mode to produce a regulated 270VDC bus. Hence, there is a limit on the maximum voltage at the rectifier terminals. The open circuit dc voltage at the rectifier terminals was therefore set not to exceed 260V, which provides 10V of ‘headroom’.

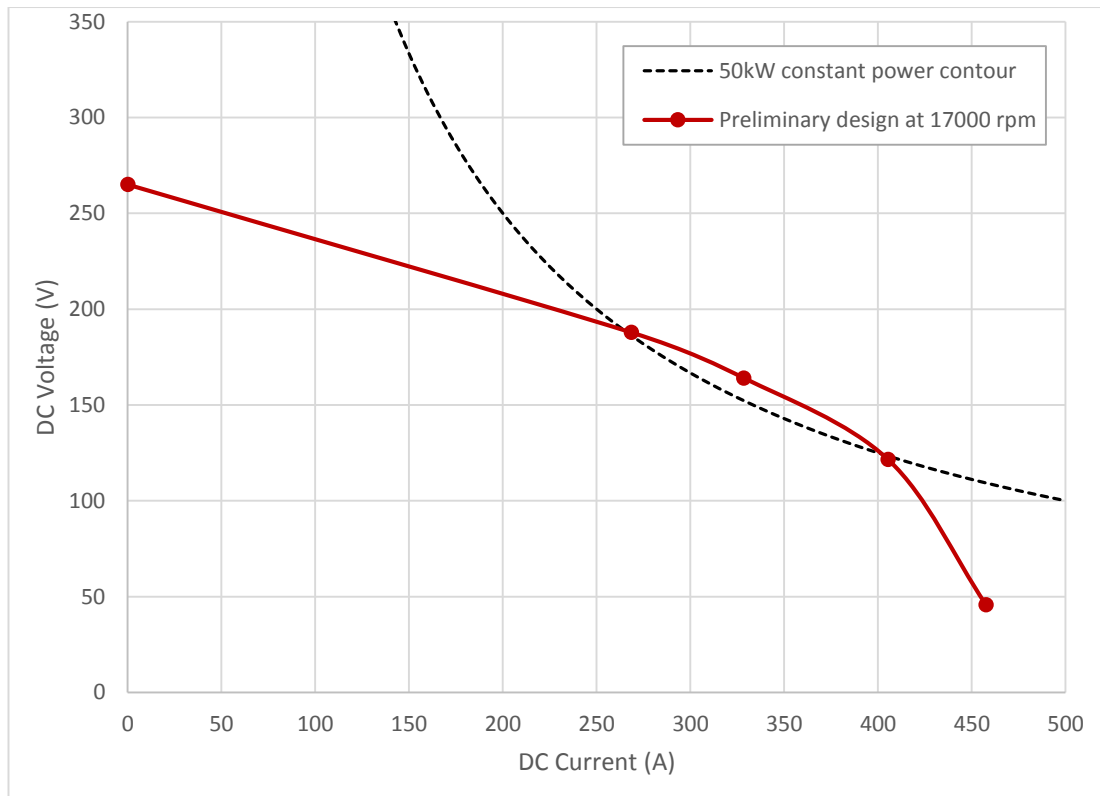


Figure 12 Uncontrolled rectifier output voltage versus current characteristics of initial stator geometry design (as detailed in Table 3) at 17,000 rpm

The rate of the drop in DC voltage with load current in Figure 12 is largely a result of the reactance of the winding. Achieving 50kW at the lowest possible current would benefit from reducing the inductance but only if this is achieved without a greater reduction in the EMF constant.

2.2.1 CALCULATION OF KEY GENERATOR PARAMETERS

Accurate calculation of the self- and mutual inductance is important in order to obtain results from the system modelled. Hence, a combination of two-dimensional and three-dimensional numerical (FE) simulations were used to predict the synchronous inductance, including the end-winding inductance. The end-winding inductance was predicted from three dimensional FE analyses in which the active region was separated out by comparison with 2D FE. This value was then added to

the circuit model as a fixed inductor, which was coupled with the two-dimensional FE model of the generator, as shown previously in Figure 10.

A fixed value of end-winding inductance (which sits outside the two-dimensional finite element region) was established using three-dimensional finite element analysis. Isolating a value of end-winding inductance was done by calculating the inductance by three-dimensional finite element analysis of a series of machines with the same cross-section but increasing axial lengths. The variation in inductance with axial length, which is an essentially linear relationship, can be extrapolated back to zero axial length. This offset or the inductance can be regarded as the value of the end-winding inductance.

Figure 13 shows the calculated values of inductance for machines up to 120mm in length, from which an end-winding value can be estimated. Although this calculation was performed for one particular cross-section, the resulting end-winding inductance can be applied for machines of the same pole number and stator diameter with limited error.

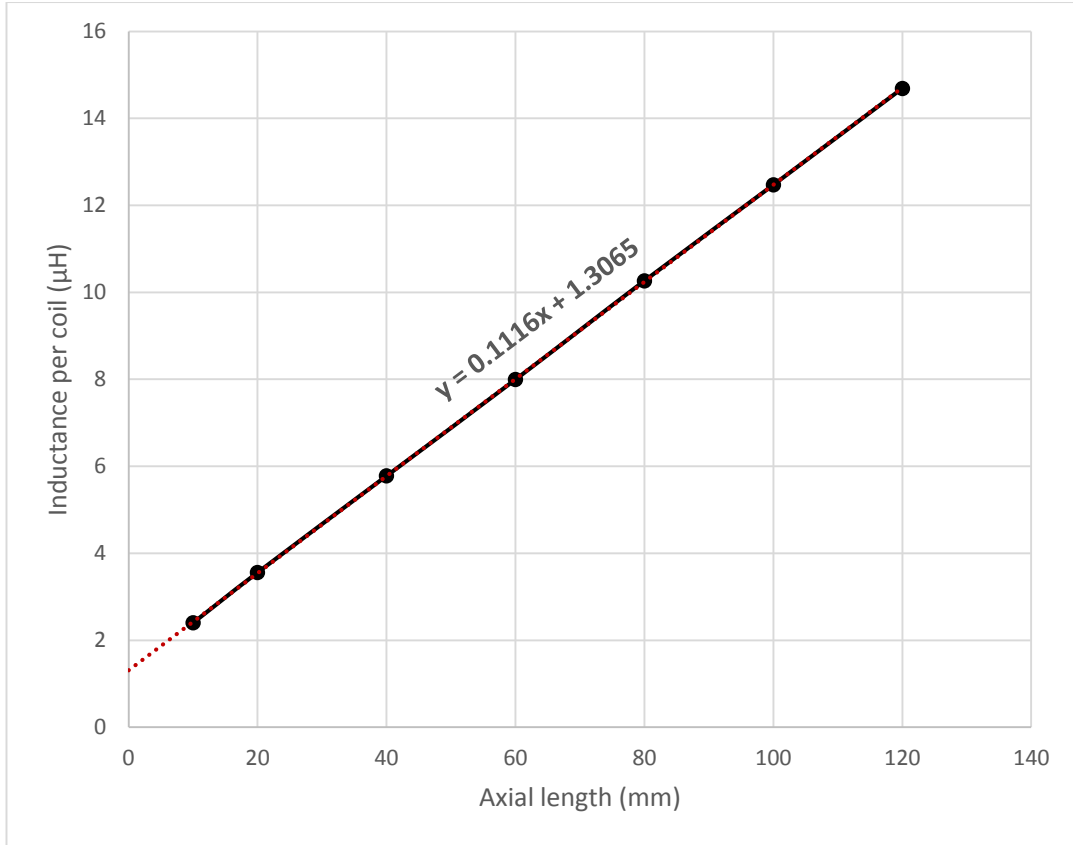


Figure 13 – 3D FEA predicted inductance for varying axial length

The resistance was calculated using the estimated length per turn, packing factor and the resistivity of the copper. The length of the turn was estimated using the geometry of the slot and the axial length. Twice the axial length, plus the circumference of two semi-circles representing the end-winding length gives the mean length per turn. The semi-circle was estimated to have a diameter that spans from the middle of a half slot, across the tooth width to the middle of the other half slot of the coil. The resistance was adjusted for temperature by using equation (1) with a copper temperature coefficient of 0.0039.

$$R_{new} = R_{old}(1 + \alpha_{cu}(T_{new} - T_{old})) \quad (1)$$

The stator and rotor core was modelled using the VacoFlux 50 Cobalt Iron data provided by the company Vacuumschmelze of which the cores would be purchased

from. VacoFlux 50 is their highest magnetic saturation grade of cobalt iron. Figure 14 show the data provided by Vacuumschmelze, which compares the BH characteristics of two grades of cobalt iron, silicon iron and iron.

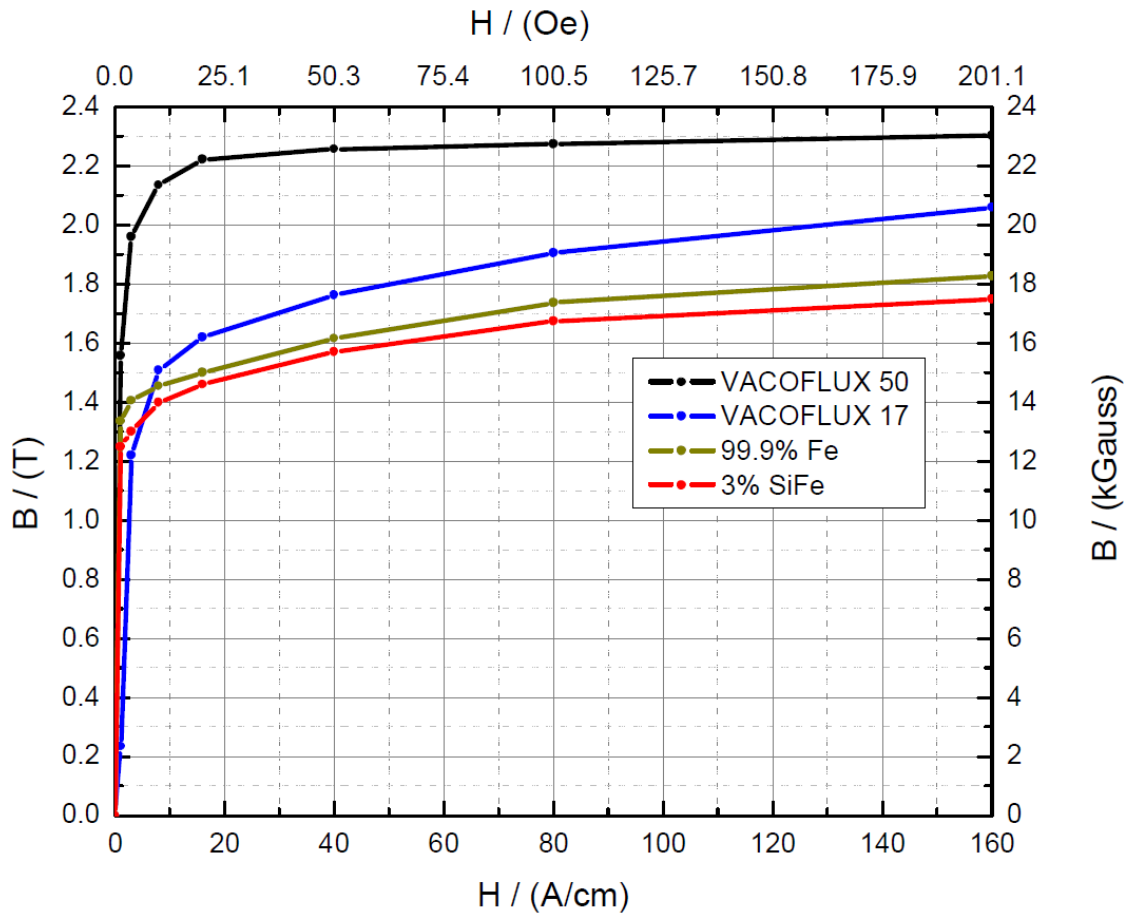


Figure 14 Comparison of the BH curves of soft magnetic material [Source: Vacuumschmelze]

Samarium cobalt ($\text{Sm}_2\text{Co}_{17}$) magnets were also simulated using data from Vacuumschmelze. Their highest grade of samarium cobalt is called Vacomax-225, which can provide up to 30 MGOe energy density with a remnant flux density of 1.08. Figure 15 shows the demagnetisation curves of Vacomax 225 for temperatures within the range of 20°C to 300°C.

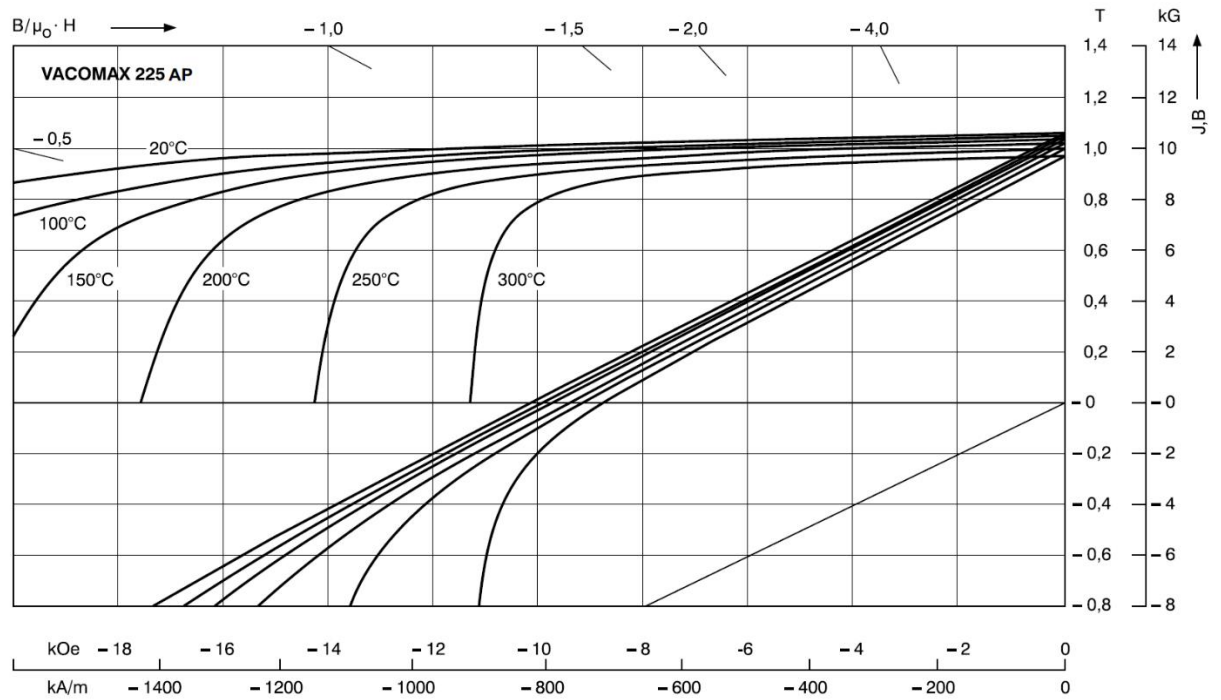


Figure 15 BH curve of Vacomax-225 grade samarium cobalt magnets [Source: Vacuumschmelze]

2.2.2 STATOR GEOMETRY DESIGN OPTIMISATION

Using the initial geometric dimensions of Table 3 as the baseline, the various key dimensions shown in Figure 16 were scaled downwards in 10% increments. For each combination of dimensions, summarised in Table 4, a series of circuit-coupled finite element simulations were performed to predict the rectifier output V-I characteristics. The output power, the inductance and the current density were the performance features considered in selecting the preferred design.

Conventionally, excessive magnetic saturation in the stator core region is usually avoided in sizing the stator core. However, in this analysis, the level of saturation was not constrained (recognising that it will increase core losses) and the output power at the bridge rectifier terminals was considered as the only figure of merit.

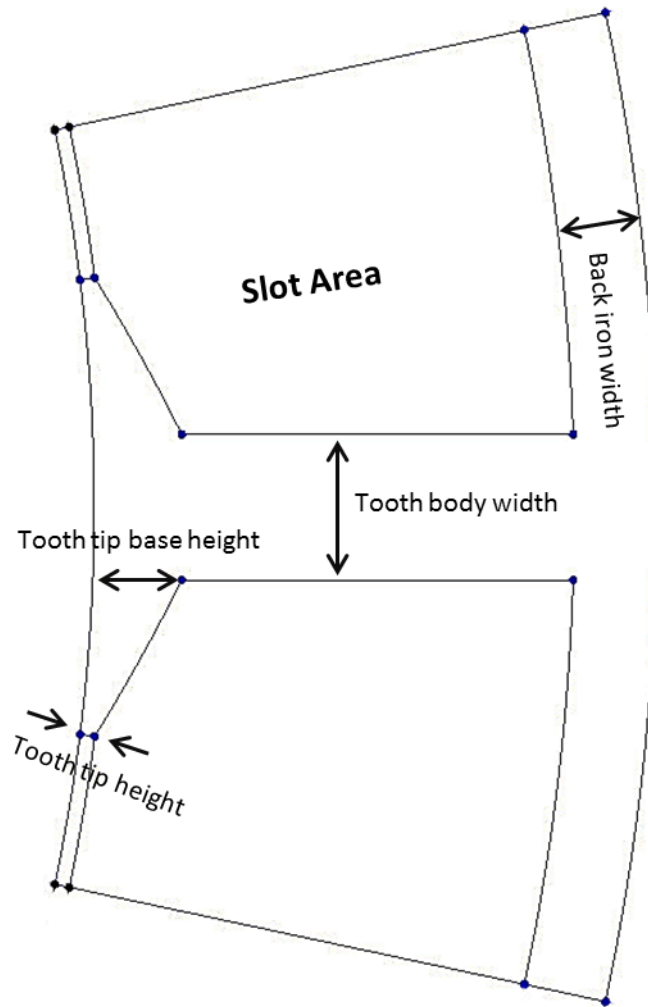


Figure 16 Stator geometry dimensions

Table 4 Stator geometry parameters of the designs

Dimensions (mm)	Design 1	Design 2	Design 3	Design 4
Tooth body width	7	6.3	5.6	4.9
Back iron width	4	3.6	3.2	2.8
Tooth tip height	0.5	0.45	0.4	0.35
Slot Area (mm ²)	154	164	174	185

A key benefit in reducing the stator core dimensions is the increased slot area and thus reduction in current density required to achieve the 50kW output requirement. This is in essence, pushing the electromagnetic design near its electromagnetic limit for the 50kW operating point. However, beyond a certain reduction in the core

dimensions, the maximum achievable output power begins to fall as the magnetic saturation starts to decrease the emf/torque constant. This can be seen in Figure 17.

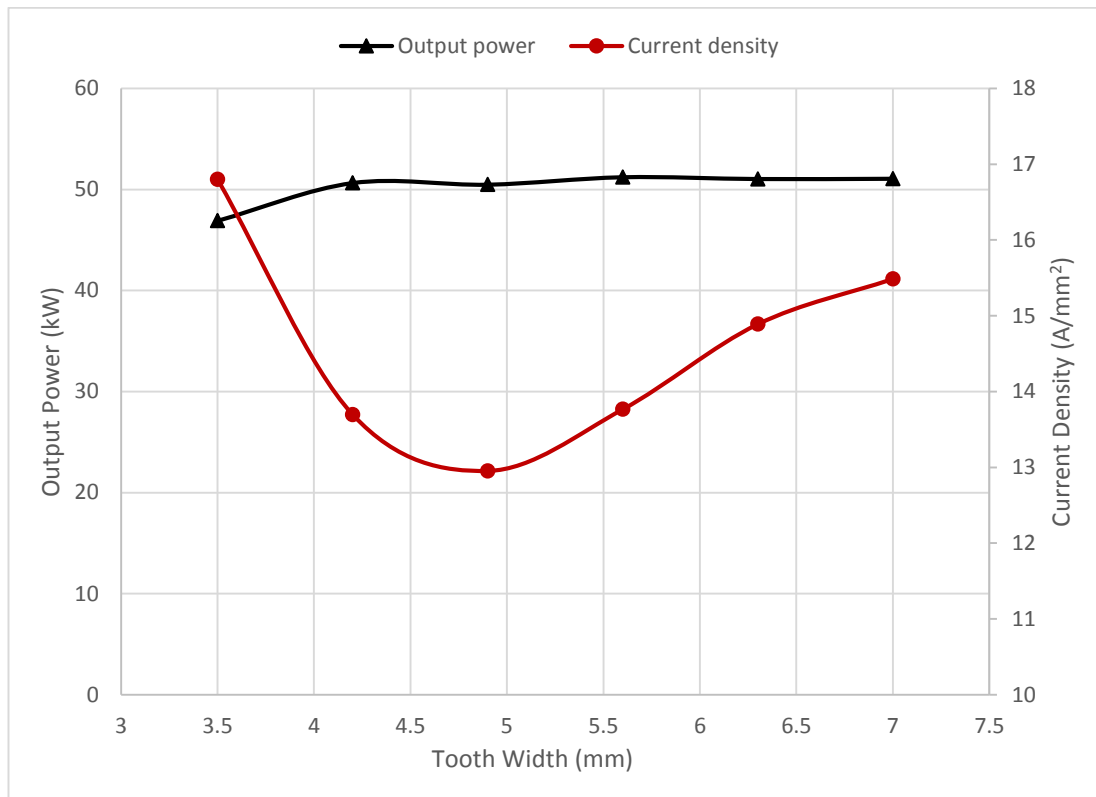


Figure 17 – The variation in current density with tooth width of the designs listed in Table 4

From the results represented in Figure 17 and Figure 18, design 4 was observed to be most suitable as it met the 50kW output power requirement at the lowest current density. This design was chosen going forwards for further analysis.

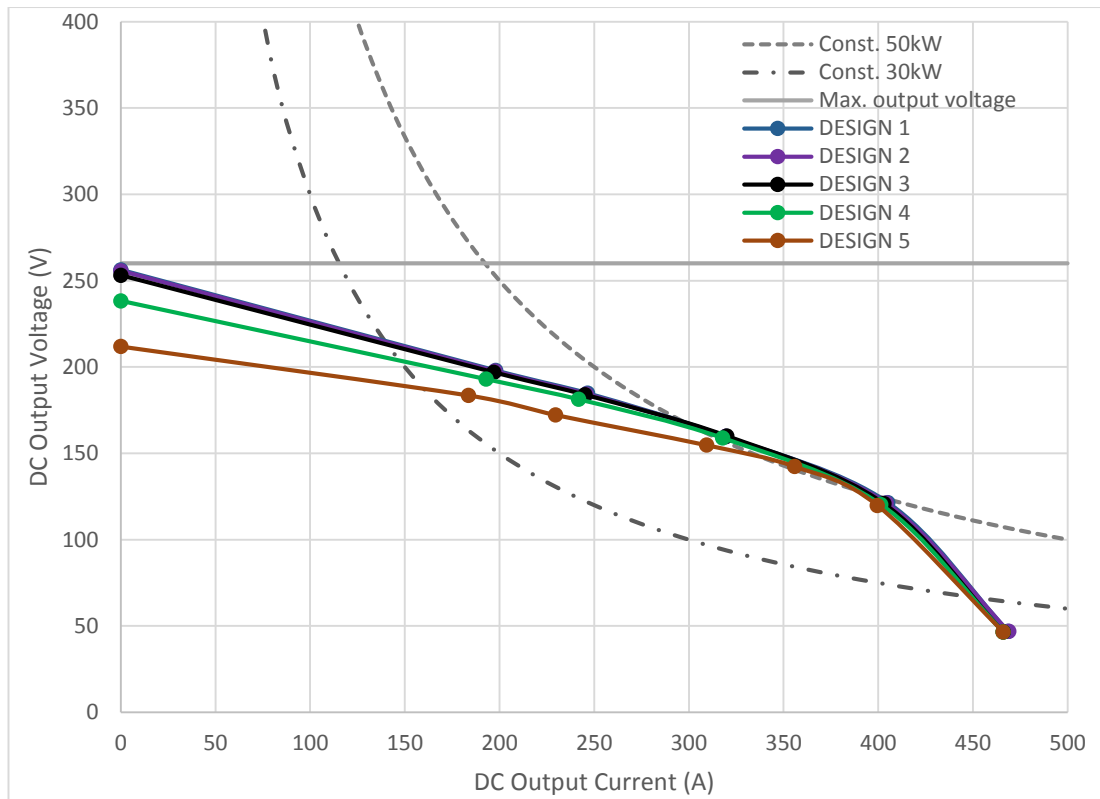


Figure 18 IV characteristics for designs on varying stator geometric cross-sections at 17000 RPM

2.2.3 SELECTION OF SLOT-PITCH TO TOOTH-PITCH RATIO

The slot-pitch to tooth-pitch (SPTP) ratio plays a major role in this design. The inductance is influenced by the SPTP ratio, tending to increase as the SPTP increases. Its impact on the output power of the preferred design established in section 2.2.1 was investigated and quantified.

A SPTP of 1 corresponds to there being no slot opening with the tooth tip of adjacent teeth in contact. The series of SPTP ratio investigated were 0.55, 0.6, 0.7, and 0.8. As the SPTP increases from 0.55 to 0.8, the peak no-load back-EMF voltage increases as would be expected given the greater peak flux-linkage captured by the wider teeth. However, the inductance also increases due to increased cross-slot leakage thus limiting the output power at the rectifier output terminals. As discussed previously in section 2.2, the DC voltage at the rectifier terminals cannot exceed 270V for reasons imposed by the DC/DC converter. Therefore, this rules out SPTP

ratios at the top end of the range for this number of turns per coil. In selecting the optimal SPTP ratio, there is a trade-off between no load back-emf voltage and inductance. The objective is to minimise the inductance for reasons discussed in section 2.0, while achieving a no load back-emf just below the 270V limit and ultimately meet the 50kW operating point. With these objectives in mind, a SPTP ratio of 0.6 was chosen based on the results shown in Figure 19.

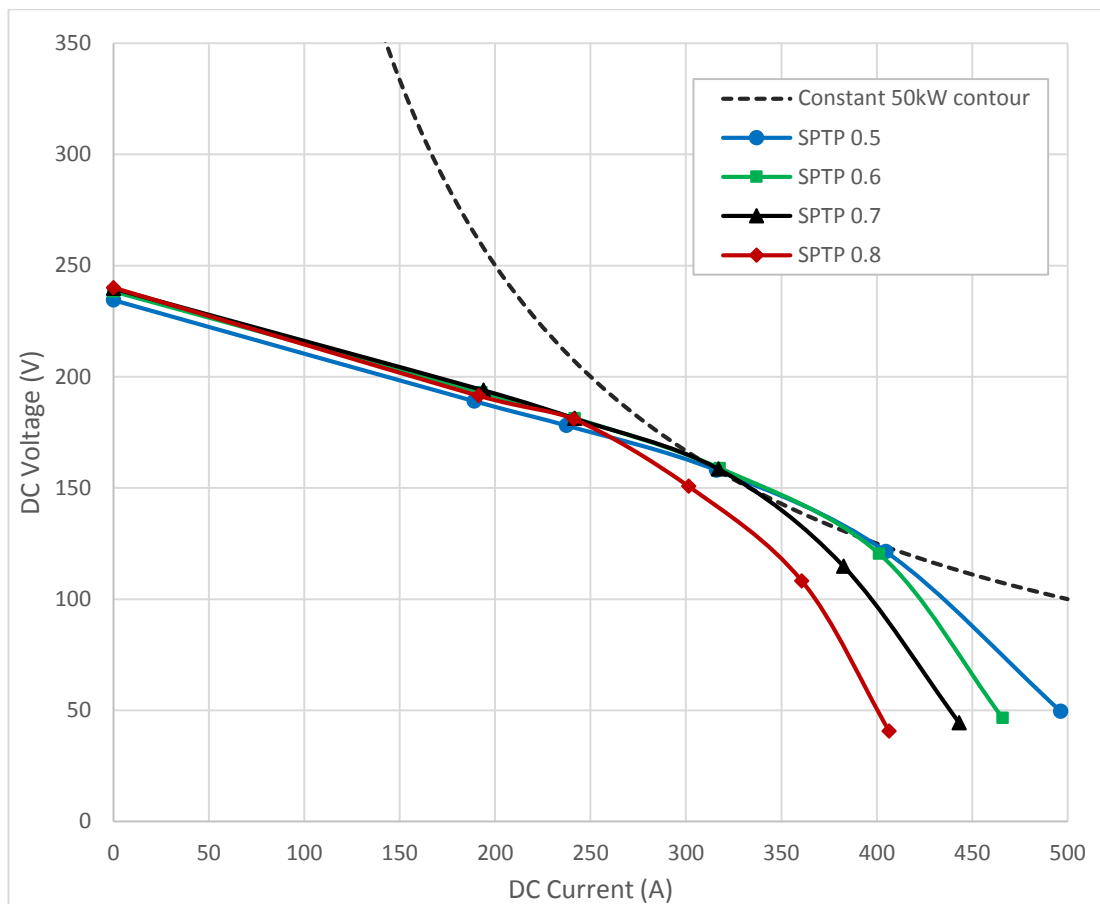


Figure 19 Uncontrolled rectifier output IV Characteristics at 17000 RPM with various slot to tooth pitch ratios

2.2.4 SELECTION OF NUMBER OF TURNS AND AXIAL LENGTH

As there is no active control over the output voltage with an uncontrolled diode rectifier, the no-load back EMF voltage needs to be selected to obtain the required power out at the design stage. The magnitude of the EMF voltage is proportional to both the number of turns and the axial length. As discussed in section 2.2.1, minimising the inductance is important at the design stage to attain the power at the rectifier terminals.

The power and hence torque increase proportional with the axial length as can be deduce from Equation (2). The drawback of increasing the axial length is that it increases the weight at the same rate as the EMF. This is because every active component, including the casing, on the rotor side and stator side would need to be increased at the same proportion. The power density (kW/kg) is the main parameter this study is looking to maximise and therefore increasing the length will reduce the power density ratio, as the power output does not necessarily increase at the same rate.

$$T = \frac{\pi}{2} B Q D^2 L \quad (2)$$

The number of turns is directly proportional to the EMF, as shown by equation (3). However, the inductance is proportional to the square of the number of turns as shown in equation (4). With this in mind, system topologies with an uncontrolled rectifier and high speed operation tend to have a low number of turns for this reason. Hence, adjusting the EMF by varying the number of turns becomes a very coarse method of matching the output voltage with such low numbers of turns per coil. However, this can be alleviated by connecting the coils per phase in parallel, since each coil is now equipped with the same number of turns as would be present in the

full phase for a series winding, and hence a finer adjustment is possible. The parallel coil connections can be quite complex to implement because of the number of terminations that must be formed in the restricted volume.

$$EMF_{rms} = 2\pi f \phi (Nk_w) \quad (3)$$

$$L_{coil} = \frac{N^2 \phi}{I} \quad (4)$$

A series of designs with 4 and 5 turns and axial length ranging between (45-55mm) were analysed. The resulting output voltage versus current characteristics derived from finite element analysis for a series of operating points are shown in Figure 20. The slope of the IV curve is influence by the inductance, which increases at higher rate with the number of turns than the axial length. The no-load output voltage (zero current) is larger for a longer axial length and higher number of turns. For the same axial length but varying number of turns, the no-load output voltage is, as expected, higher as the EMF is also a function of number of turns and as mention previously, the inductance. Moreover, a point to note is that the gradient of the 45mm/4turns is lower than the 45mm/6-turn design due to the inductance. Designs with a no-load output voltage greater than 260V are not feasible because the DC-DC converter operates in boost mode only with a design headroom of 10V to the DC link.

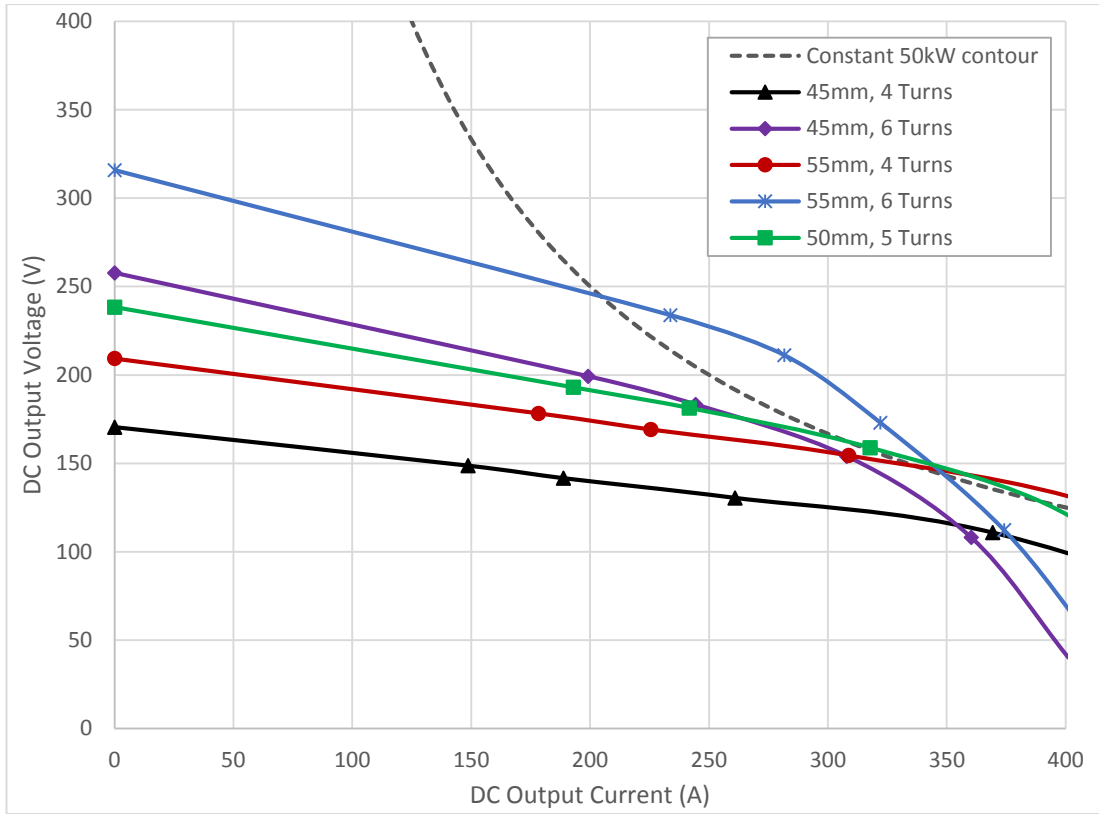


Figure 20 IV Curves analysing the effects of the number of turns and axial length on the output power at 17000 rpm

2.3 ROTOR MAGNET CONTAINMENT STRESS ANALYSIS

In order to counteract the centrifugal forces exerted on the magnets at high speed, some form of mechanical containment is required. The containment sits in the airgap and inevitably increases the effective magnetic airgap length. Consequently, this reduces the airgap flux density for a given magnet length and hence, the electromagnetic performance, notably the torque constant.

The need for containment is a well-recognised drawback of this topology of PM machines for high speed machines. Therefore, much research effort has been carried out into various types of containment materials with high strength/mass ratio. The two most commonly employed materials are Inconel sleeves and carbon fibre composite over-wraps. The electrical conductivity of the containment becomes an important factor as eddy current losses are induced which raise the temperature of the magnets. In many cases, this can rule out Inconel sleeves. In this design, carbon fibre was selected as the containment material since a number of machine features are likely to make induced eddy currents in the sleeve a particular concern:

- The high electrical frequency, i.e. 1.42kHz for 10 poles at 17,000rpm
- Concentrated winding with large slot openings that will produce pronounced spatial harmonics
- Current waveform resulting from the diode rectifier will produce significant time harmonics

The stress on the containment is temperature dependant as a result of thermal expansion mismatch between the rotor core / magnets and the carbon fibre. This tends to increase the stress with increasing temperature. The objective of the design optimisation is to select the minimum thickness of the carbon fibre that can withstand the stress with some specified safety factor. It is also important to note that the containment must apply significant pre-compression onto the magnets to ensure

that they remain in contact with the rotor core at the maximum speed [13]. This is usually achieved by pre-tensioning the fibre as it is wound onto the rotor magnets.

The stress on the carbon fibre containment was analysed numerically using the structural analysis software Ansys. The manufacture of the carbon fibre banding of the rotor was subcontracted to external company called Cobham and the properties of the epoxy and carbon fibre used by Cobham (and which are summarised in Table 5) were adopted to predict the stress levels in the containment. A pre-tension of 450MPa was adopted in the model. The predicted stress distribution in the various regions of the rotor is shown in Figure 21 for the case rated speed of 17,000 rpm, at a temperature of 120°C and a carbon fibre thickness of 2mm. As shown in Figure 22, the peak stress exerted on the carbon fibre composite increases rapidly as the containment thickness falls below 1.25mm. The structural analysis provides assurance in selecting the thickness of the carbon fibre containment.

Table 5 Table of rotor components mechanical properties

Properties	Young's Modulus (GPa)	Poisson's ratio	Density (kg/m³)	Thermal Coef. of expansion (10⁻⁶ K⁻¹)
Vacomax 225	150	0.3	8400	12
Vacoflux50	215	0.3	7640	12
Carbon Fibre	132.5	0.3	1760	0.251
Titanium 6Al-4V	114	0.34	4430	8.6
Wedge (Interpole)	1	0.4	3000	30

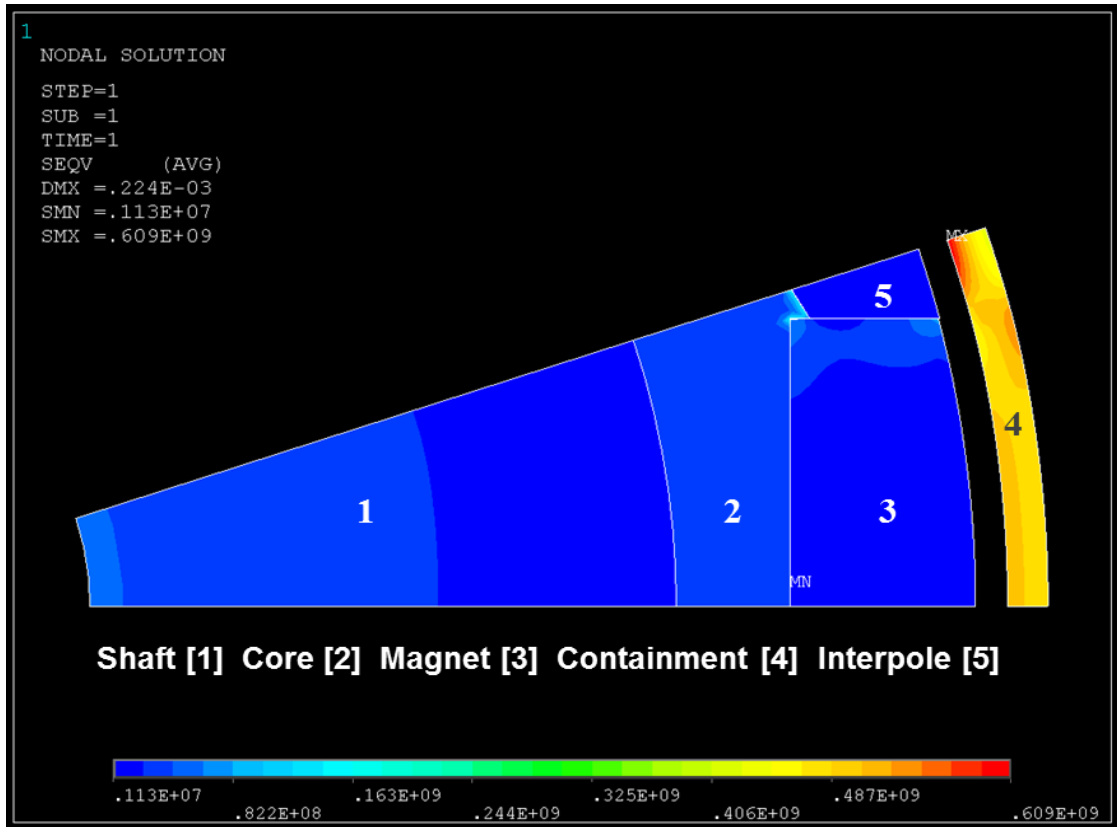


Figure 21: Finite element stress distribution in the regions of the rotor at 17000rpm (Rotor temperature of 120°C; carbon fibre thickness of 2mm; 450MPa compressive stress at standstill)

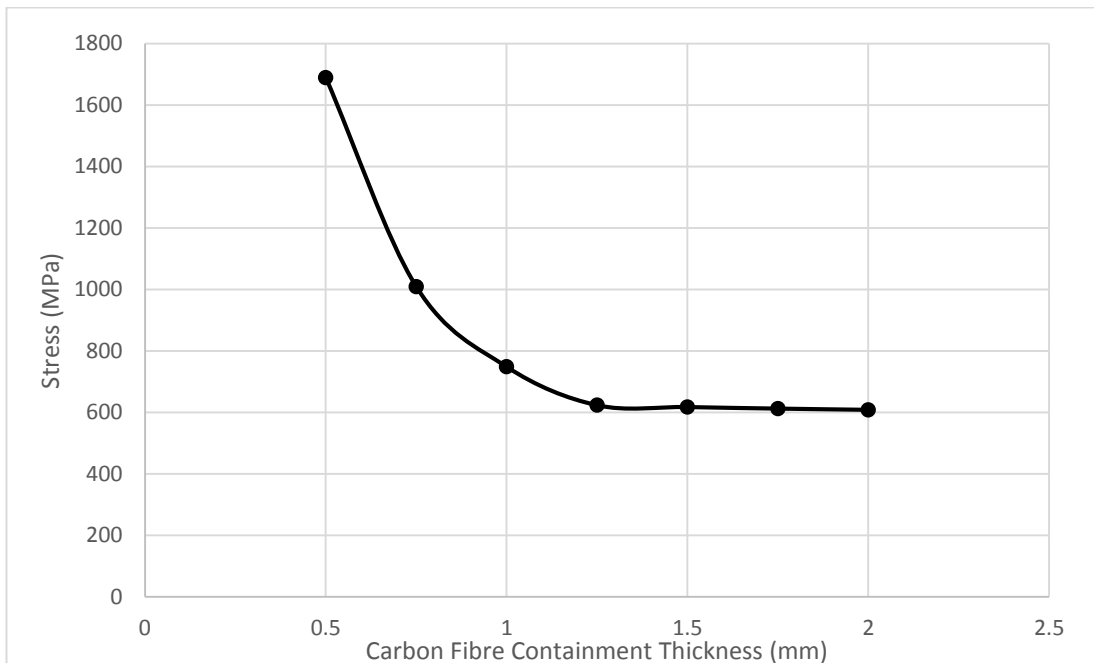


Figure 22 Variation in localised peak stress on carbon fibre containment as a function of containment thickness (Temperature of 120°C and speed 17000rpm with a pre-compression of 450MPa)

There is an electromagnetic penalty that is incurred as a result of the presence of the non-magnetic containment in the airgap. Figure 23 illustrates the variation in the generator performance (in terms of rectifier output V/I curves) for a range of different effective magnetic airgap lengths.

The thickness of carbon fibre was selected to be 2mm, which provides a reasonable trade-off with electromagnetic performance while offering headroom in mechanical stress to accommodate a degree of uncertainty in the temperature and allow for manufacturing tolerances.

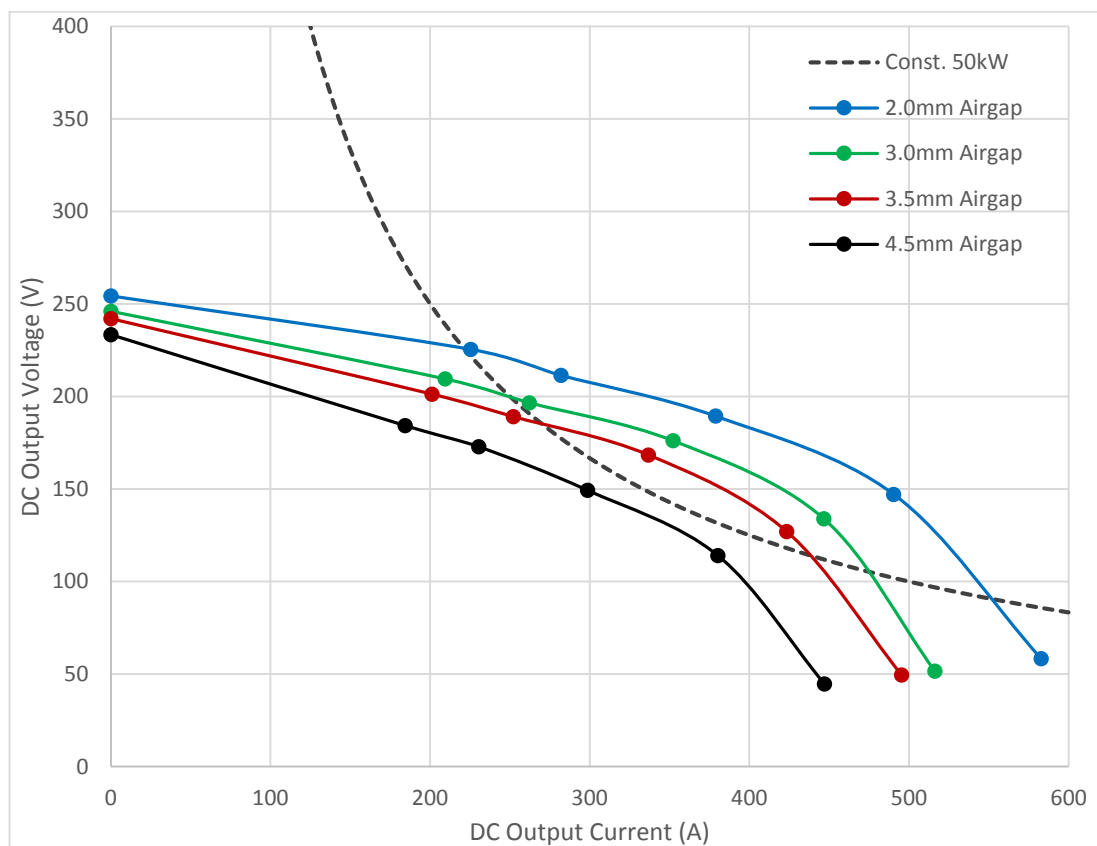


Figure 23 Variation in electromagnetic performance as a function of airgap length

2.4 ROTOR MAGNET EDDY-CURRENT LOSSES & MAGNET SEGMENTATION

As discussed in section 2.1 of this chapter, one of the drawbacks of FSCW configuration is the presence of spatial harmonics in the airgap flux density. These harmonics are responsible for inducing eddy currents in the magnets (and in the sleeve if it was electrically conducting). These are both a source of additional loss and hence reduced efficiency, but the most significant issue in most machines is the direct heating of the magnets. This will cause their magnetic properties to drop with increasing temperature and increase the risk of irreversible demagnetisation. The induced eddy-currents can be reduced by a combination of two approaches:

- Reducing the harmonic content of the airgap flux density by selection of the slot geometry and winding configuration
- Reducing the cross-sectional area of the induced current paths by segmenting each pole into a number of small magnet pieces.

High power density permanent magnet machines generally have a fractional slot-pole combination with concentrated windings and a high electric loading. This combination tends to produce an airgap MMF with relatively high harmonic content, generating magnet losses. The magnet eddy current loss produced by a machine with concentrated windings is higher than that of a comparable machine with distributed windings. In a classical integer slot winding configuration, the MMF waveform is repeated a number of times equivalent to the number of pole-pairs and its spatial harmonics are multiples of the airgap fundamental MMF. However, for a fractional-slot winding configuration, the MMF can contain parasitic MMF harmonics of orders close to the fundamental and/or sub-harmonics with longer wave lengths. The parasitic MMF harmonics in the airgap rotate at different speeds to the rotor thus exposing the magnets to a time-varying magnetic field. The three factors of the

harmonics which influences the magnet losses are; the amplitude, the relative speed with respect to the rotor and the wavelength. The influence of the parasitic harmonics wavelength and the width of the magnet pole on rotor losses was investigated in [14], which highlighted that the path taken by the eddy-current in the magnet segment is determined by the ratio of the wavelength of the harmonic order and the width of the segment. A parasitic harmonic with a relatively large wavelength compared to the magnet segment width produces a high level of magnet losses [15]. For this reason, sub-harmonics and other parasitic harmonics close to the fundamental harmonic generates the higher levels of magnet losses.

For surface-mounted PM rotors, the rotating flux density distributions imposed by the harmonics in the airgap flux density are approximately the same seen by the magnets segments because of their close proximity to the airgap. However, for IPM, the rotating flux density distribution seen by the magnets are a result of the applied in the airgap multiplied by a concentration factor [15]. The magnet losses approach a steady state level with the increase in segmentation [16].

The slot openings will also cause flux density variations in the magnet due to the modulation of the localised permeance, which causes fluctuations in the localised magnet working point, thus producing eddy-current losses in the magnets. The shape of the tooth and the slot-tooth pitch ratio will influence the magnet losses. Optimising the tooth shape to reduce magnet eddy-current losses was investigated in [7]. For applications where field weakening is required, the magnet eddy-current loss contributed by slotting effect reduces when operating in the flux weakening region (generally high speeds) because of the reduction in flux crossing stator and rotor. The effects of slot-pole combination with multiple phases (3,5,7) was investigated in

[15] which demonstrated that single layer or modular windings produce higher levels of eddy-current losses compared to a double layer.

Many approaches to reducing eddy current losses in the magnets seek to reduce the airgap mmf harmonics [6]. However, this is often achieved with some penalty paid in torque capability. This is not an immediately favourable option when power density is paramount.

It is also important to note that temperature rise and ultimately thermal irreversible demagnetisation is caused by the temperature rise in the magnets rather than losses per se. Therefore, optimising heat transfer path from the magnets to some heat-sinking element such as the shaft is also a necessary consideration.

One well-recognised method of reducing eddy currents is segmenting each magnet pole into a number smaller magnet pieces which are electrically isolated from each other. Each magnet pole can, in principle, be segmented axially, radially and circumferentially. One benefit of having a large airgap is that it acts like a "spatial filter" for high order MMF harmonics, which reduces the losses caused by high order spatial harmonics [6].

Analysis was performed to reduce the losses in the magnets by segmentation. The losses were predicted using 2D FE analysis in which each individual magnet piece was considered as an electrical conducting region in which eddy currents could be induced. The magnet region in the FE model was assigned a value of electrical conductivity for $\text{Sm}_2\text{Co}_{17}$ of 1.25 MSm^{-1} . Each solid conducting segment was connected to its own $100\text{k}\Omega$ resistor in series to constrain the eddy-current within a segment. The magnet losses calculated from this 2D model does not take the axial segmentation into consideration. Therefore, the losses calculated will tend to be an

overestimate if the magnets are to be segmented axially with dimensions comparable to the radial and circumferential dimensions.

A series of time-stepped, transient simulations at the rated speed and power were carried out in order to calculate the eddy-current magnet losses as a function of tooth pitch to slot pitch ratio. Figure 24 shows that as the slot opening decreases the losses reduce. This is to be expected given the reduced permeance fluctuation and the reduced slotting harmonics. Increasing the slot pitch to tooth pitch ratio by 10% (0.6 to 0.7), the losses reduce by 10%. As the slot pitch to tooth pitch ratio approaches unity, the benefit in reducing the losses diminishes.

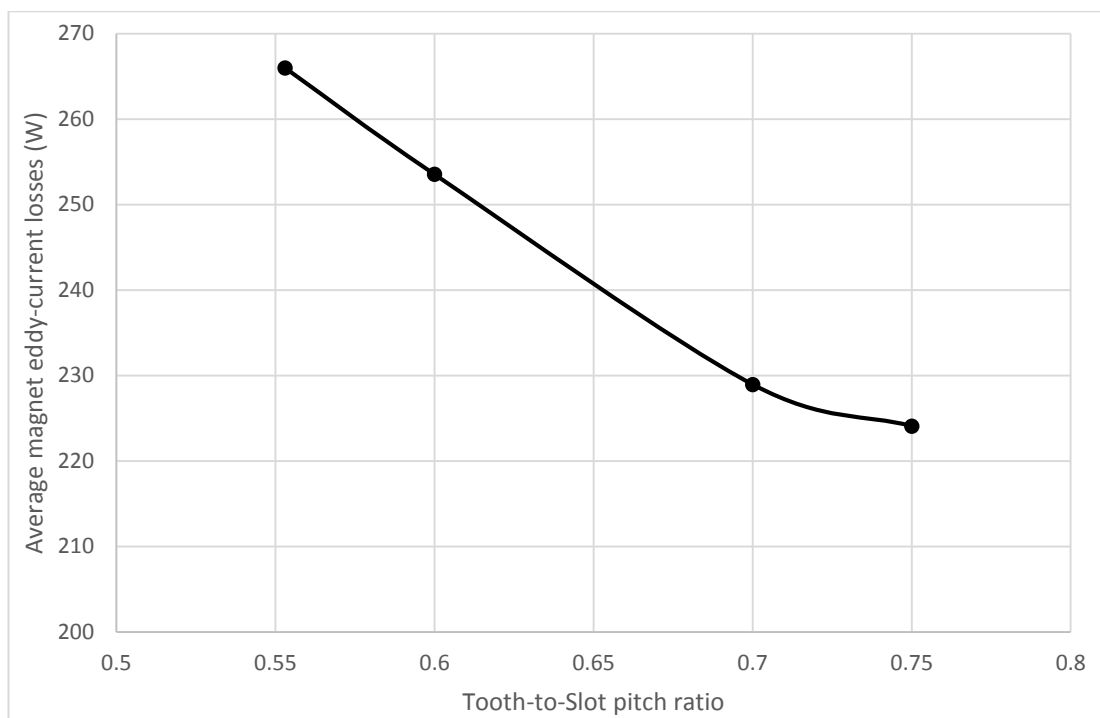


Figure 24 The magnet eddy-current losses of a single segment per pole of design 4 at the rated 50kW at 17,000 rpm

A further series of simulations considered magnet eddy-current losses as a function of the stator current loading. The simulations were carried out at a slot pitch to tooth pitch ratio of 0.6 at the rated operating point of 50kW at 17,000 rpm. Figure 25

shows that the rate at which the magnet loss increases with current density changes markedly at around 8 Amm^{-2} .

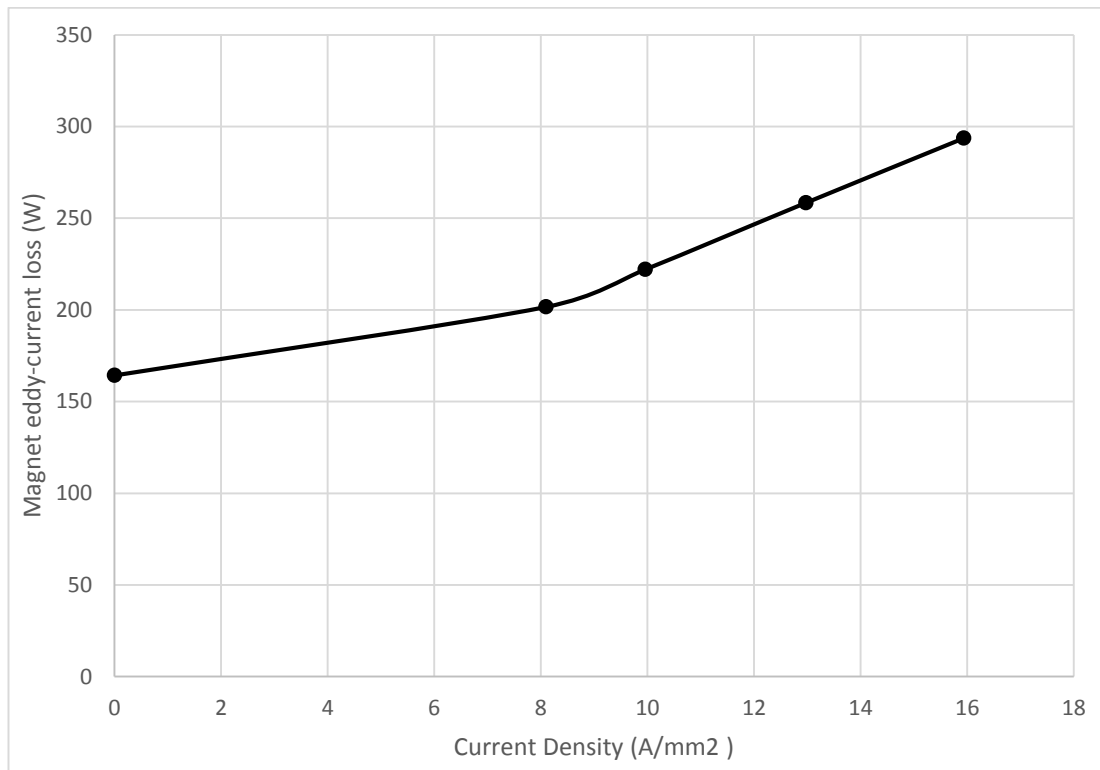


Figure 25 Magnet eddy-current losses as a function of current density at 17000 rpm

The magnet eddy-current loss was simulated for both 12 and 24 segments per pole at the 50kW at 17,000rpm operating point. The 12 segment variant was based on 12 sub-divisions circumferentially as shown in Figure 26. An instantaneous snapshot of the eddy-current loss distribution for this segmentation is shown in Figure 26.

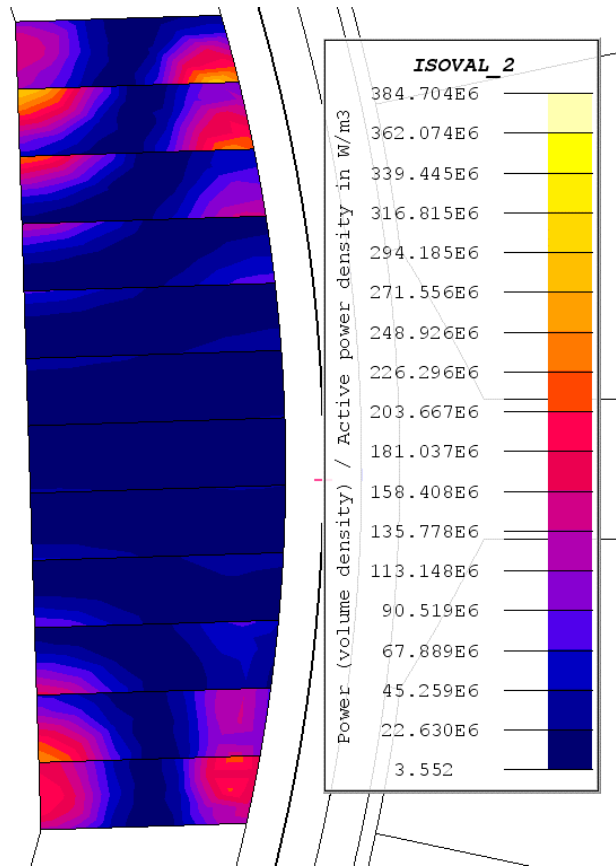


Figure 26 Instantaneous snapshot of the eddy-current distribution in a magnet pole of 12 radial segments

The 12 segments per pole was further segmented radially into 2 layers, giving a total of 24 segments per magnet pole, as shown in Figure 27. This significantly reduces the magnet eddy-current losses, as can be seen in Table 6.

Although not accounted for with a 3D FE analysis, in the final prototype machine, the magnets were segmented axially into 10mm long pieces. This will result in some further reduction in the losses shown in Table 6.

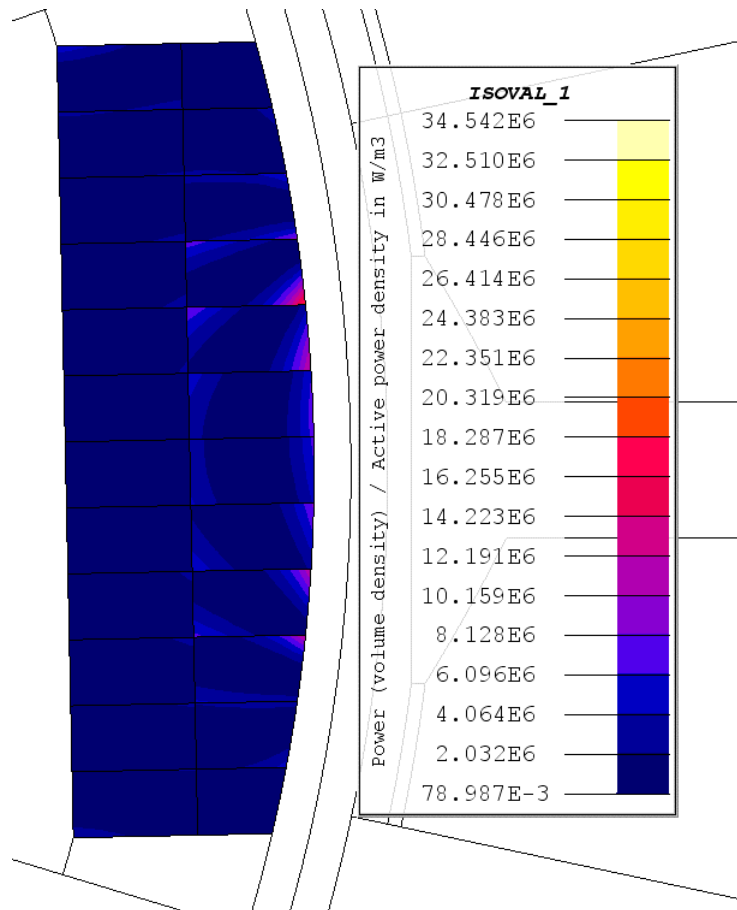


Figure 27 Instantaneous snapshot of the eddy-current distribution in a magnet pole of 24 segments

Table 6 Comparison of magnet eddy-current losses for several levels of segmentation at 50kW at 17,000 rpm operating point

No. of Segments	Magnet eddy-current loss (W)
1 Segment	1337.5
12 Segments	264.8
24 Segments	115.5

2.5 STEADY STATE ANALYSIS OF THE OPTIMISED DESIGN AT THE 50kW OPERATING POINT

Finalised design parameters were established from the analysis presented in the previous sections. The resulting machine cross-section (including the concentrated winding layout) is shown in Figure 28 and a summary of the key design parameters are contained in Table 7.

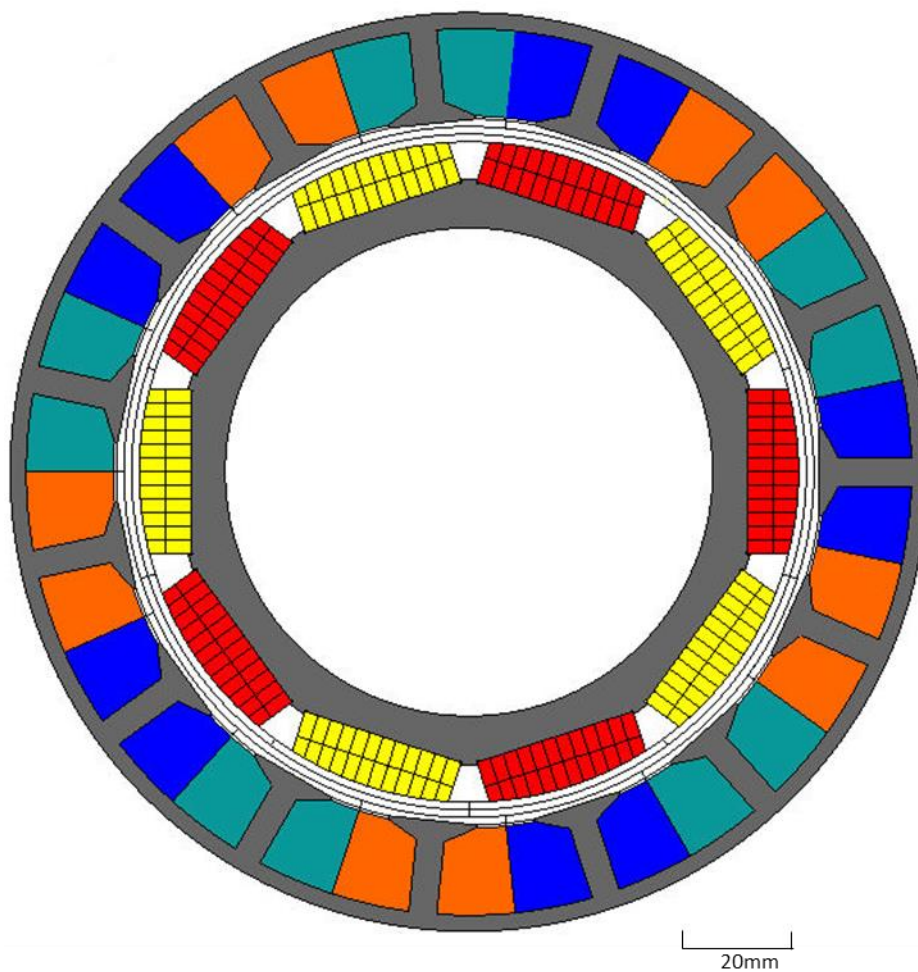


Figure 28 Finalised generator cross-section

Table 7 Design parameters of the finalised design

Stator Dimensions	Value (mm)
Number of stator slots	15
Stator outer diameter	160
Stator bore diameter	122
Effective magnetic air-gap	4.0
Stator back iron thickness	2.8
Stator bore coolant retention sleeve thickness	1.0
Tooth body width	4.9
Tooth tip height	0.5
½ Slot area (mm ²)	174
Stator slot packing factor	0.5
Turns per coil	5
Series connected coils per phase	5
Machine active length	50
Resistance per coil (mΩ)	1.38
Inductance per coil (Including End-winding)	6.97μH
Active weight (kg)	4.77
Rotor Dimensions	Value
Number of poles	10
Magnet height (from centre)	9
Containment thickness	2
Rotor outer diameter	118
Rotor inner diameter	85

2.5.1 2D FINITE ELEMENT SIMULATED PERFORMANCE CHARACTERISTICS

The generator coupled with the uncontrolled rectifier was simulated with a simple load resistor to obtain the required output power to the DC/DC converter. The load resistor does not fully represent the dynamic performance of the DC/DC converter as it is recognised that there would be some inductance and capacitance seen from the rectifier terminals.

The predicted back-EMF is shown in Figure 29. The features observed in the back-EMF at $\sim 90^\circ$ and $\sim 270^\circ$ electrical angle shown in Figure 29 are due to the large slot openings. The shape of the line-to-line emf is suited for an uncontrolled diode bridge rectifier as the emf peak occurs in the region where the diodes are conducting over a cycle. Figure 30 shows the simulated current waveform when operating at rated point of 50kW at 17000 RPM.

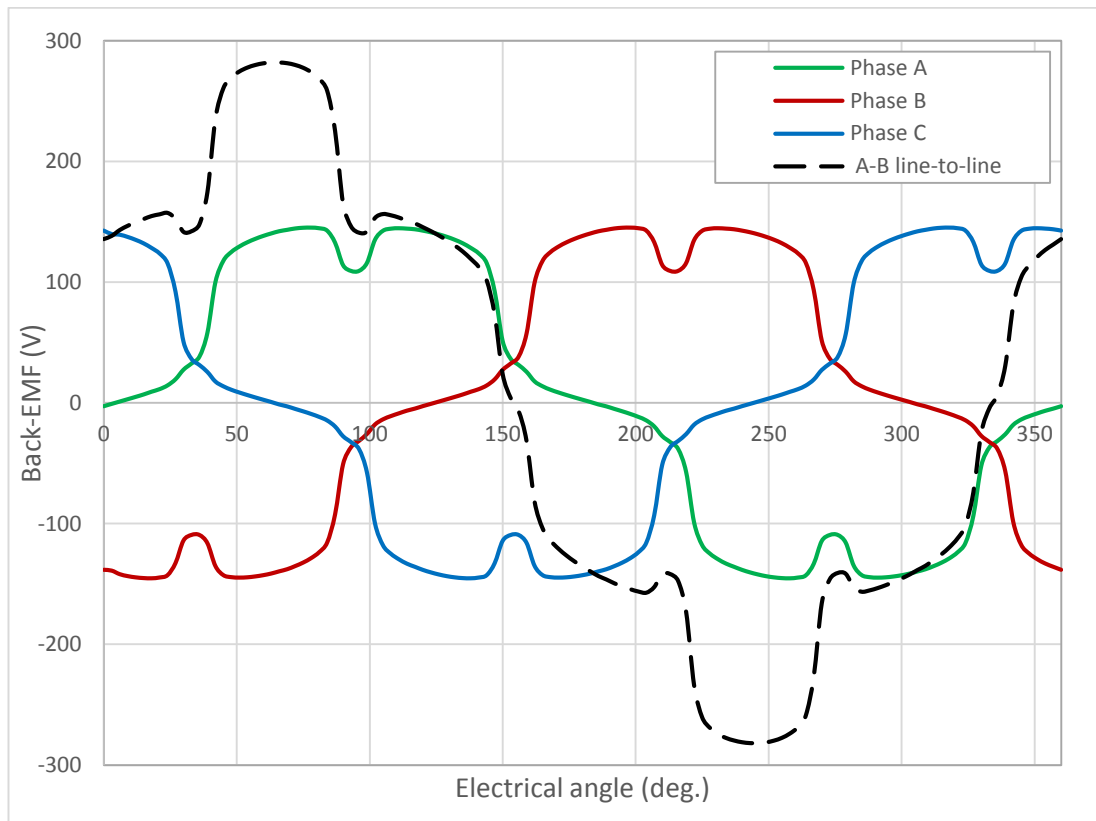


Figure 29 Finite element No-load open-circuit Back-EMF at 17,000 rpm

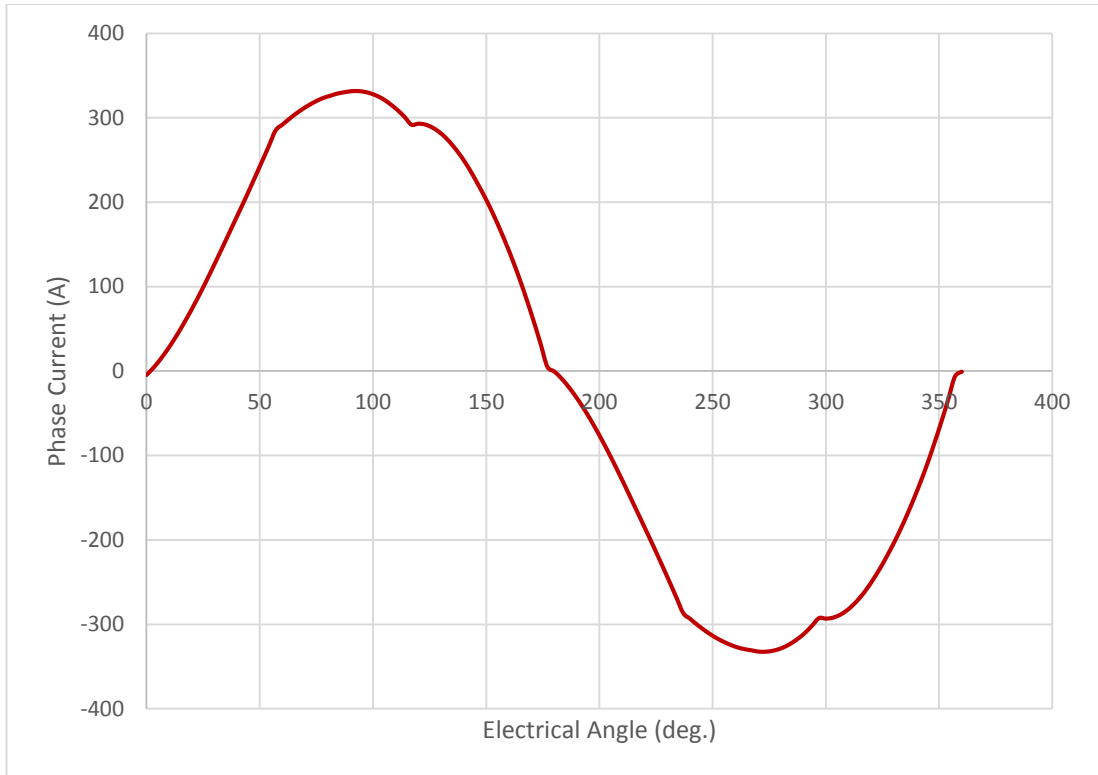


Figure 30 Phase current at the 50kW, 17000 rpm operating point – connected to diode rectifier

Figure 31 shows a representative level of saturation in the stator core at rated speed of 17,000rpm and rated power of 50kW. As mentioned previously, cobalt iron saturates at 2.3T and the flux density within the tooth and back iron approaches this value. However, operating with an appreciable level of saturation does not reduce the output power to a meaningful extent, but does give a benefit in additional slot area gained. Figure 32 shows the equipotential contours at rated load and speed of 50kW at 17,000rpm respectively.

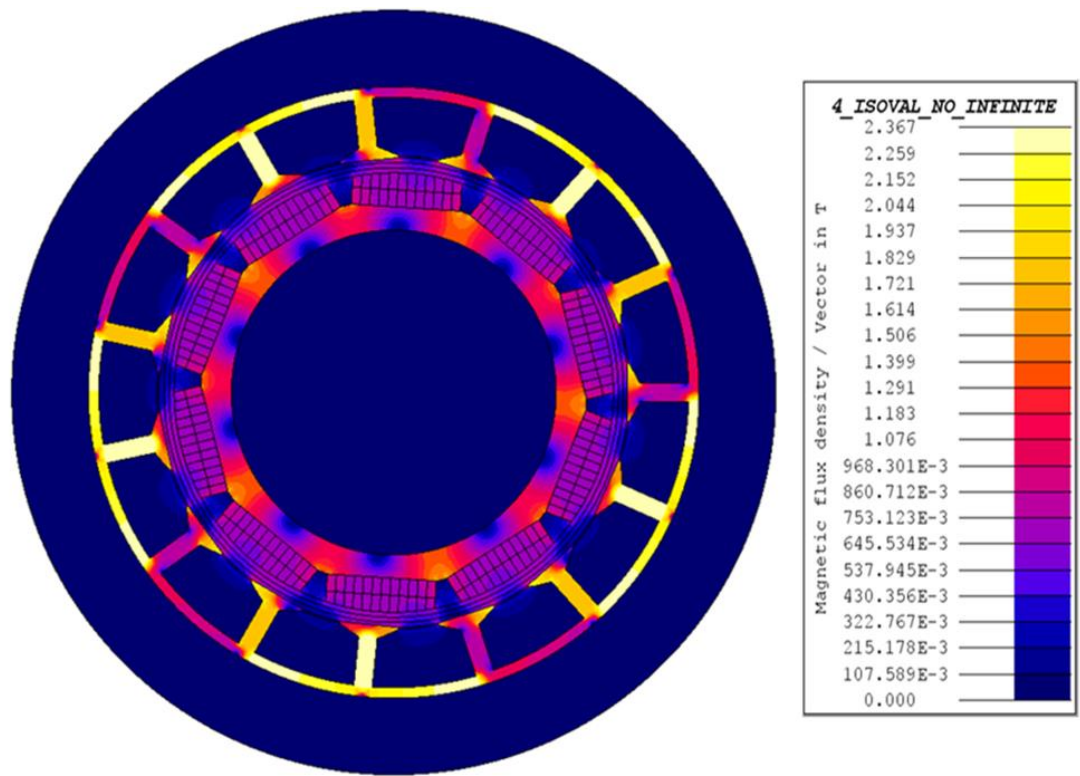


Figure 31 Flux density plot at rated operating point of 50kW at 17,000rpm

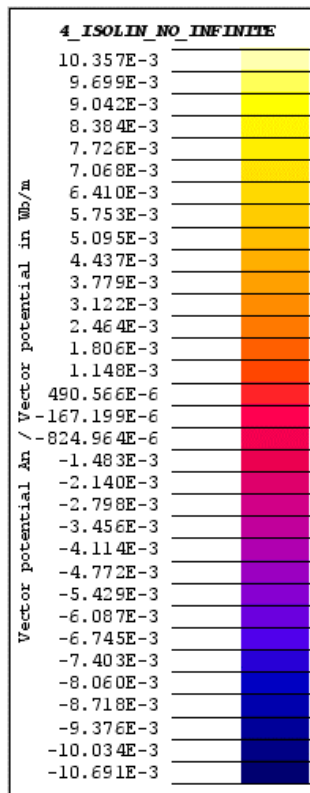
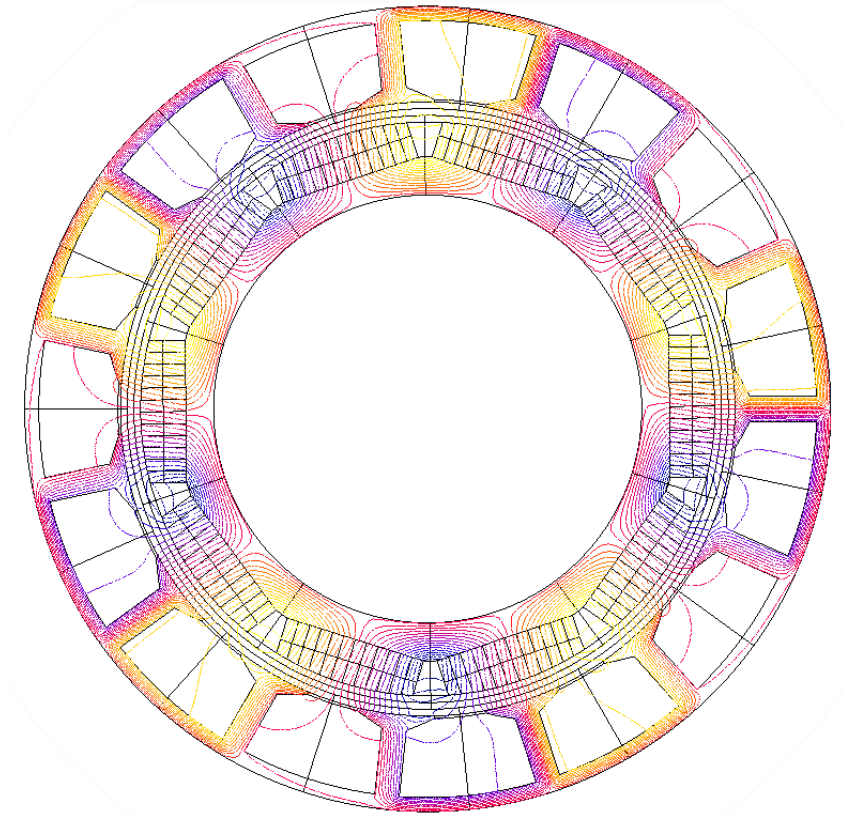


Figure 32 Magnetic equipotential contours at rated load and speed

2.5.2 ELECTRICAL LOSSES AT 50kW OPERATING POINT

Copper losses were calculated using the true RMS phase current of the winding. A typical waveform is shown in Figure 30. The losses were calculated at the worst case coil temperature of 200° C.

Each coil consists of 5 series turns formed with 49 parallel strands of 0.67mm diameter wire. The effective cross-section area of conductor 17.4mm² by paralleling 49 strands to give the equivalent area per turn, the resulting conductor bundle is flexible, and so the winding process can achieve 0.5 packing factor.

The phase resistance at 200°C was calculated to be 6.68mΩ using equation 6. The length of the conductor per turn per coil was estimated to be 158.5mm. Using Equation (7), the copper losses were calculated to be 1.2kW.

$$R = \frac{\rho L}{A} \quad (5)$$

$$R_t = R_0(1 + \alpha(T_t - T_0)) \quad (6)$$

$$P_{cu} = N_{ph} I_{rms}^2 R \quad (7)$$

The iron losses were predicted using an FE model coupled in combination with a pre-existing Matlab algorithm. The flux density information for each time step of each element of the mesh of the stator core is passed on to the Matlab algorithm which then calculates the iron losses using equation (8) along with the material data, speed, and the start/finish time of an electrical cycle.

$$P_{Fe} = \left| k_h \hat{B}_l^{a+b\hat{B}_l} f \right| + \left| \frac{\sqrt{\sigma_{Fe}}}{\delta_{Fe}} k_{exc} \frac{1}{T_t} \int \left| \frac{dB_t}{dt} \right|^{1.5} dt \right| \quad (8)$$

$$+ \left| \frac{\sigma_{fe} d_l^2}{12\delta_{Fe} T_t} \int \left| \frac{dB_l}{dt} \right|^2 dt \right|$$

A plot of the iron loss in the stator core is shown in Figure 33. The stator iron loss at 50kW operating point at 17,000 rpm was calculated to be 234W while the rotor core was only 1W.

As would be expected given the high current density and the high performance core material selected, the overall losses are dominated by copper.

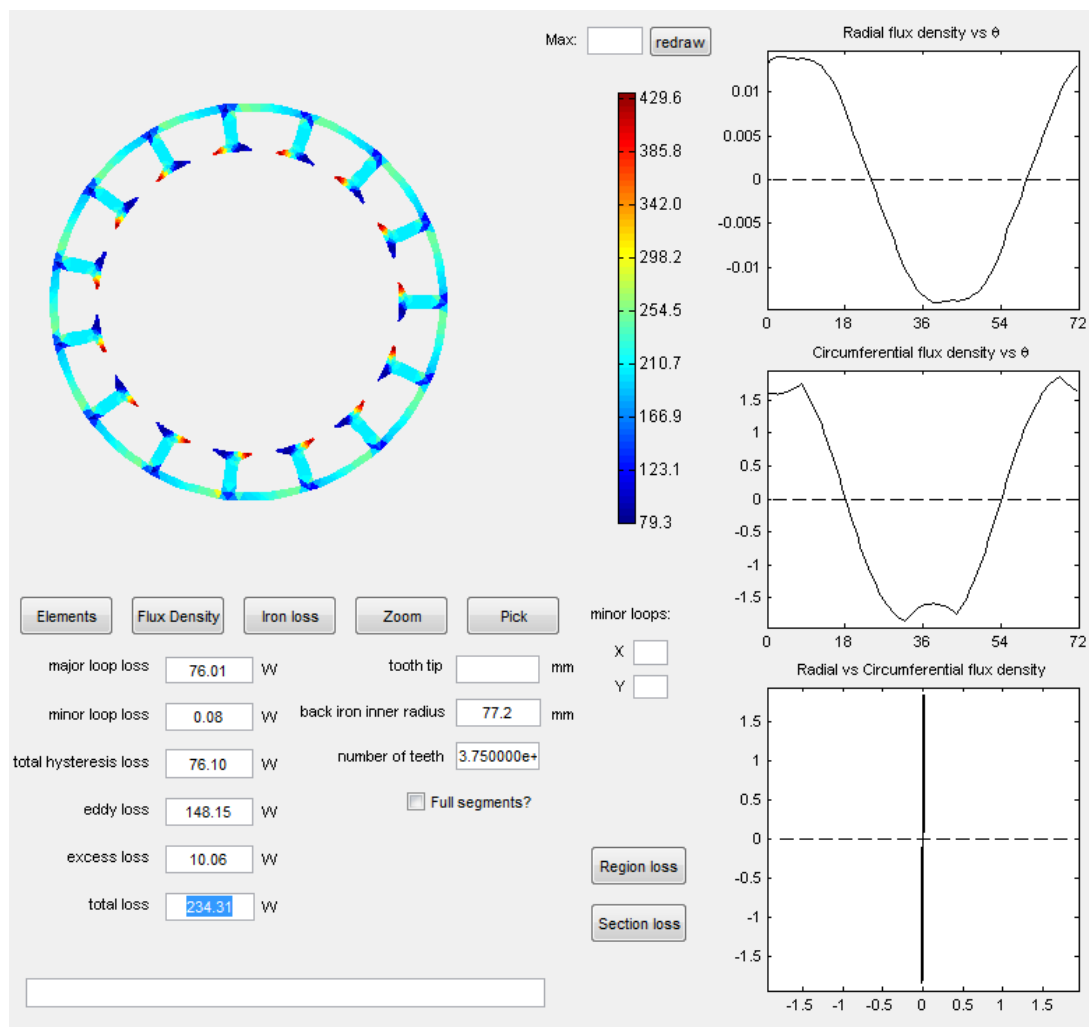


Figure 33: Iron loss in the stator core at rated operating point of 50kW at 17,000 rpm.

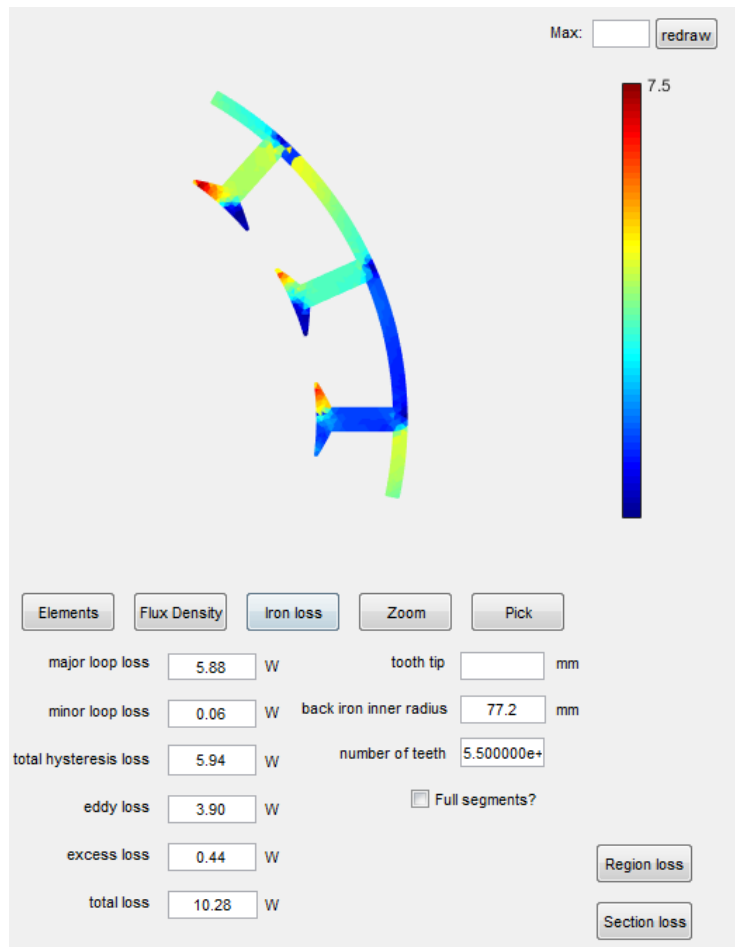


Figure 34 Iron loss of the stator at 30kW operating point of a 5th of the stator

2.5.3 MASS OF ACTIVE COMPONENTS AND POWER DENSITY

The mass of the design was critical for this application. The aim of the design was to achieve a power density of 15kW per kilogram of active weight. This means, at 50kW the active mass of the machine must be 3.33kg. The active mass refers to the components which make up the electromagnetic design which consist of the cobalt iron stator and rotor core, the copper winding and the samarium cobalt magnets. The active mass was calculated using the densities provided in the manufacturer's specifications, shown in Table 8 and the volume. Table 8 also shows the mass of the active components.

Table 8: Mass of the active components

Component	Density (kg/m³)	Mass (kg)
Stator lam	8120	1.18
Rotor lam	8120	0.75
Magnets	8400	1.00
Windings	8940	1.84
Total		4.77

The power density at the rated power was calculated to be 10.5 kW/kg. This is ~3x the value achieved by the air-cooled version. This design extends the thermal limit thus permitting the machine to operate at higher current densities and therefore the size was reduced for the same 50kW rated power.

2.6 SELECTION OF COOLING STRATEGY

The thermal behaviour of the motor was modelled for the 50kW operating point to determine a suitable cooling strategy. This was done using Motor-CAD software package which uses a majority of lumped-parameter method with some FEA analysis of the slot to identify hot spots. At a design current density of 12A/mm², a form of liquid cooling was required to maintain temperatures within a safe operating limit. Table 9 shows a summary of the losses at 50kW for a Jacket cooling and flooded stator cooling. The jacket cooling method does not require a sleeve in the airgap. Therefore the electromagnetic airgap was simulated at 3mm and 4mm for the jacket cooling and the flooded stator cooling respectively. The copper losses for the 3mm design are lower because of the increase in flux-linkage and hence, back-EMF, means that less current is required to produce the same rated power of 50kW. Subsequently, the increase in the flux-linkage also increases the iron loss but overall a reduction in the total loss.

Table 9 Summary of the losses for jacket and flooded cooling

Loss component (W)	Jacket	Flooded
Copper	814	1200
Core	329	234
Magnet	187.5	116
Windage	75.6	75.6
Total	1406	1626

2.6.1 SPIRAL-JACKET COOLING

An investigation was first carried out on a spiral liquid-jacket to check its suitability. Figure 35 shows a schematic of the arrangement. The end-winding on the non-driving end was extended by 10mm to account for interconnections between phases and the star point. A mock up stator core and winding was done to accurately estimate the end-winding length. The liquid-jacket channel dimensions were selected to be 10mm in height and 5mm in width with a flow direction from rear (non-driving end) to front.

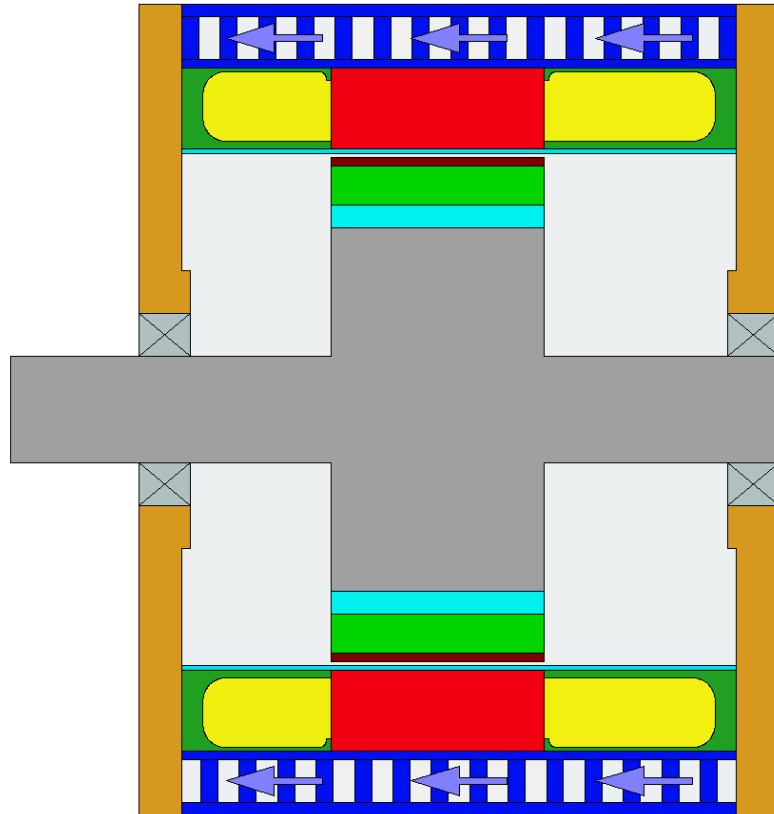


Figure 35 Schematic of Spiral liquid-jacket cooling arrangement

The end-winding region was simulated with a high thermal conductivity encapsulant, Durapot 862, which has a thermal conductivity of $0.58\text{W/m}\cdot\text{K}$ and a temperature limit of 315°C . The majority of commonly use encapsulants have a thermal conductivity of $\sim 0.23\text{W/m}\cdot\text{K}$ e.g. Epoxylite.

Table 10 shows a summary of the thermal conductivity of the other components.

Table 10 Material and thermal conductivities of the components

Component	Material	Thermal Conductivity (W/m·K)
Casing	Aluminium	168
Encapsulant	Durapot 862	0.58
Core laminations	Cobalt Iron (Vacoflux 50)	30.0
Slot liner	Nomex® 410	0.14
Magnet	Samarium Cobalt	11.0
Winding	Copper	401
Winding insulation	Polyamide	0.35
Airgap Sleeve	PEEK	0.25

A design interference fit of 0.2mm between the casing and the stator lamination stack was used. An impregnation quality of 90% was assumed. This was accounted for in the thermal conductivity of the material by a multiplier factor. A natural convection heat transfer coefficient of $6 \text{ W/m}^2\cdot\text{K}$ was used for the outer surface of the casing and an ambient temperature of 20°C . The properties of the oil used as a coolant in the model can be found in Table 11.

Table 11 Typical properties of the coolant oil

Properties	Value
Thermal Conductivity	0.149
Density	986.9
Specific heat capacity	1926
Kinematic Viscosity	3.92×10^{-5}
Dynamic Viscosity	0.0387
Prandtl Number	499.8

Simulated thermal results for the liquid-jacket cooling method

The model was simulated for a range of flow rates. Figure 36 shows how the maximum winding temperature varies with flow rate. The temperatures of the various components of the machine at 5l/min at the 50kW operating are shown in Figure 37. Also at this operating point, the temperature gradient of the slot is shown in Figure 38.

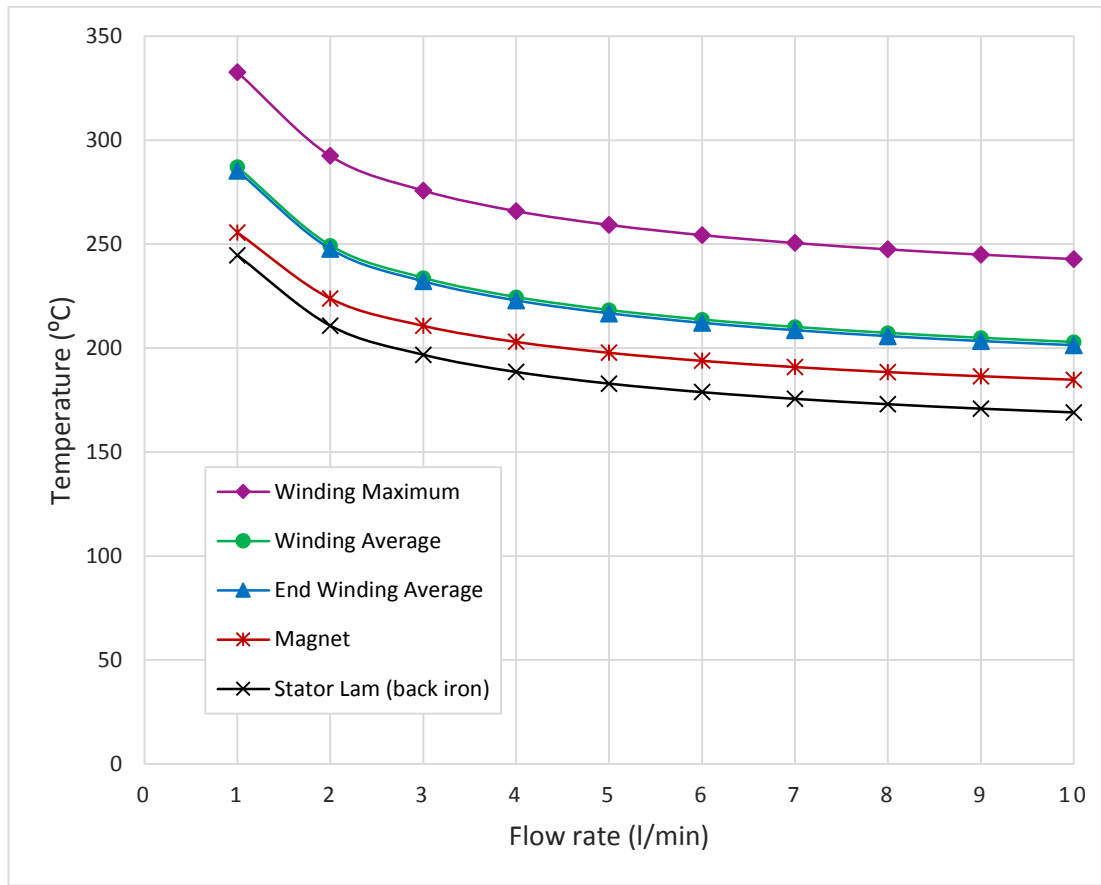


Figure 36 Temperature for varying flow rate at 50kW operation point

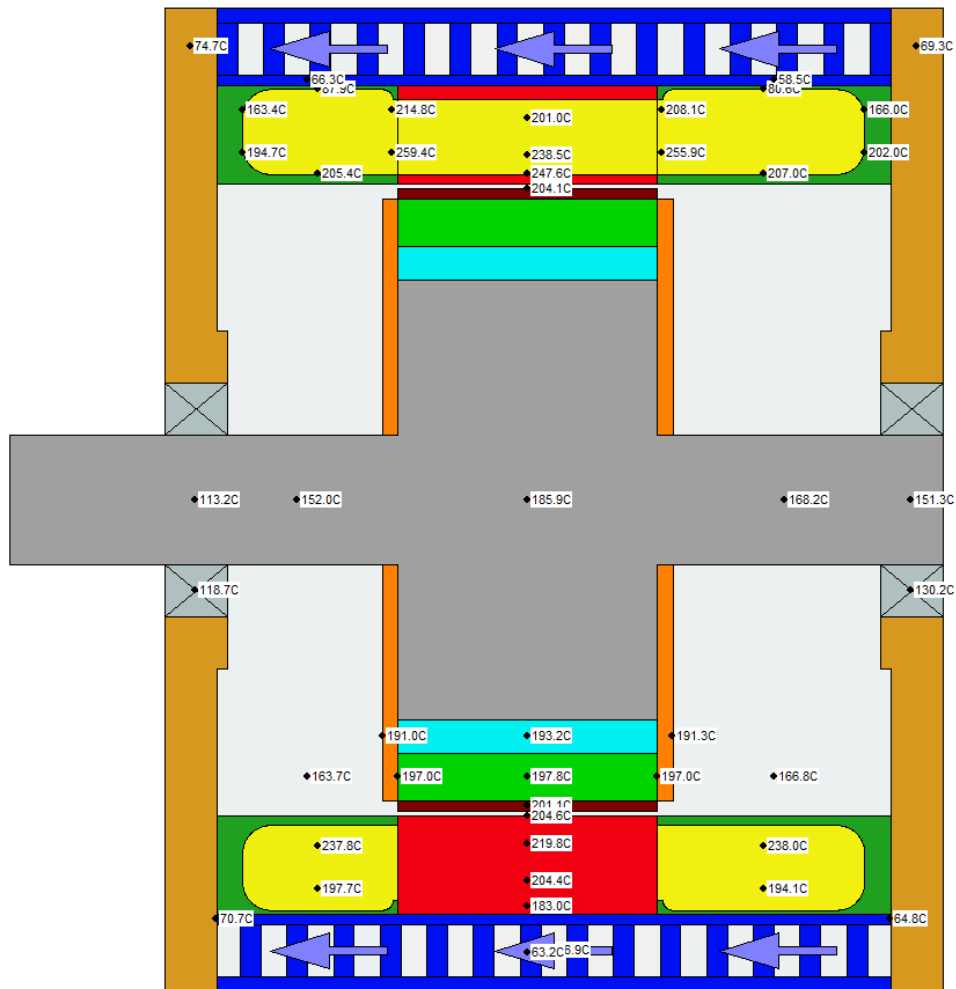


Figure 37 Simulated temperatures at various regions of the machine at a flow rate of 5l/min operating at 50kW

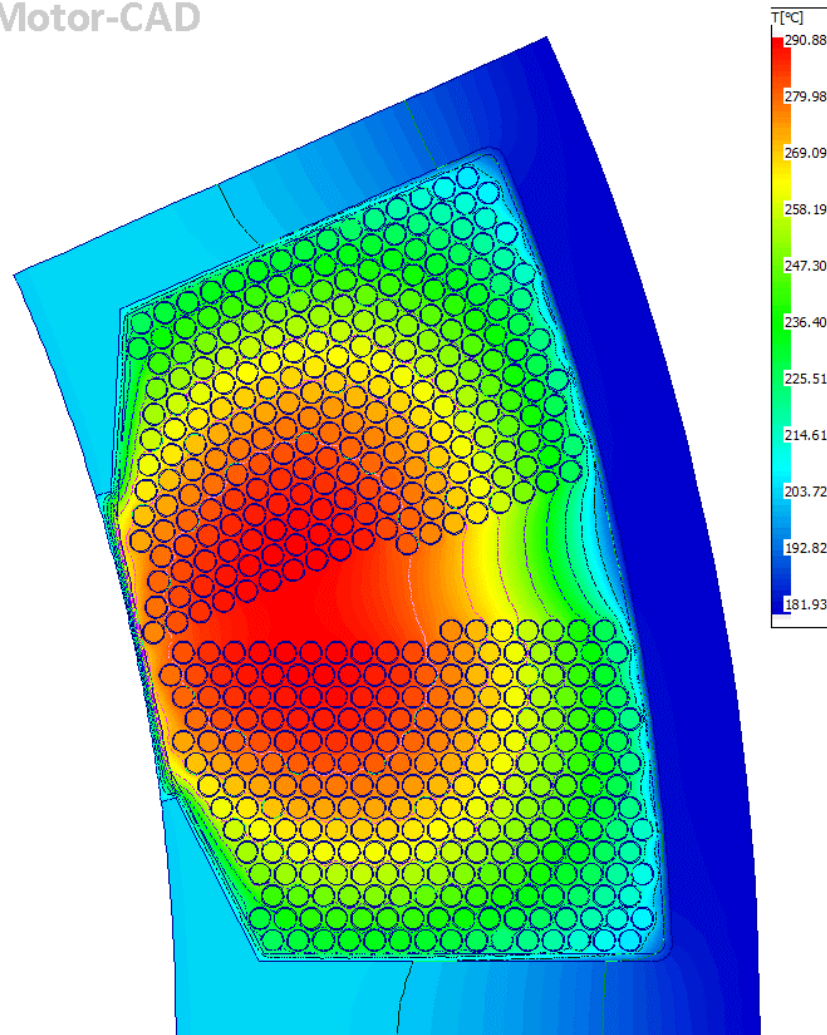


Figure 38 Thermal FEA of the winding operating at 50kW and a flow rate of 5l/min using Motor-CAD

The results suggest that a liquid-jacket cooling arrangement would not be sufficient for this design. Therefore, the flooded-stator cooling design was investigated. This was simulated using a simplified model in Motor-CAD to determine the suitability of this type of cooling.

2.6.2 FLOODED STATOR

The flooded stator arrangement allows coolant to flow between the individual conductor strands, circulating from the rear end of the machine at the six o' clock position, through the active region and exit at the front end at the twelve o' clock position. Figure 39 shows arrangement of this cooling approach.

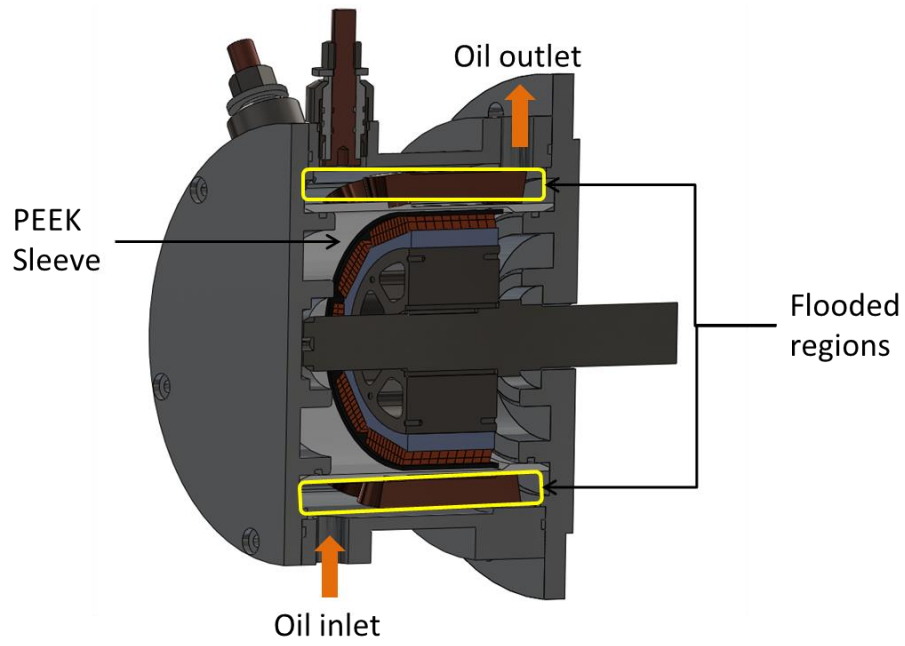


Figure 39 Flooded stator oil cooling arrangement

The model was simulated with a flow rate of 5 l/min and the losses summarised in Table 9. The resulting machine temperatures are shown in Figure 40 and Figure 41.

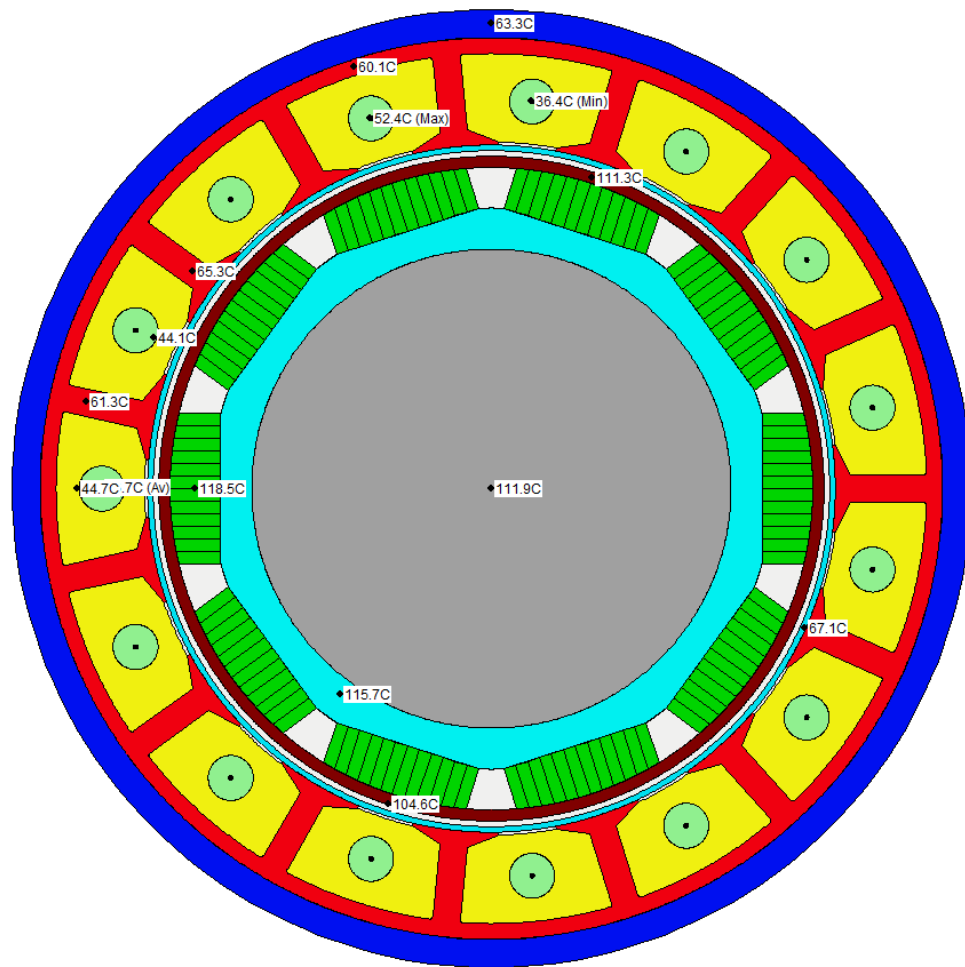


Figure 40 Radial view of simulated temperatures at various regions of the machine at a flow rate of 5l/min operating at 50kW

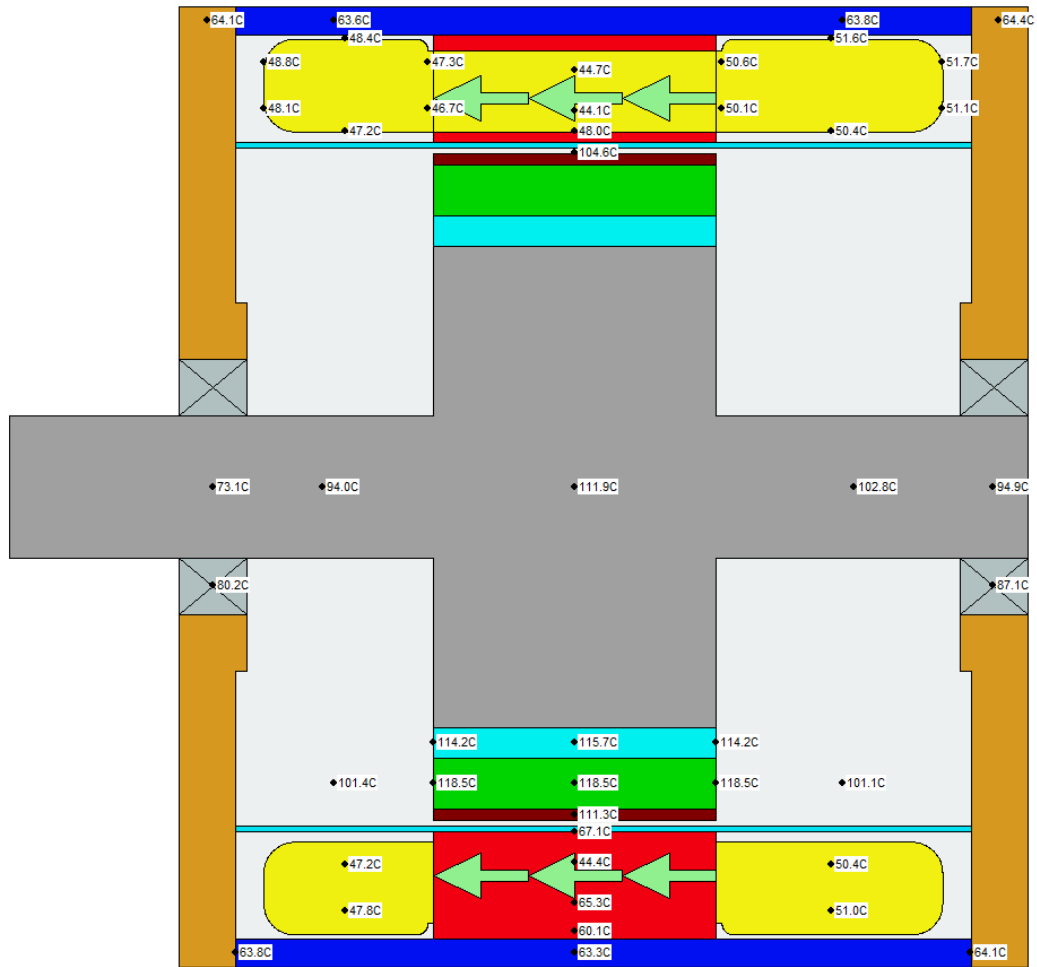


Figure 41 Axial view of simulated temperatures at various regions of the machine at a flow rate of 5l/min operating at 50kW

The results shown in Figure 40 and Figure 41 shows that this type of cooling was more than adequate for the rated operating point of 50kW at 17000 rpm.

2.7 CONCLUSION

This design outlined here sets the baseline power density (10.5 kW/kg active power density) on what can be achieved using existing technology and materials with a more complex cooling method required to maintain temperatures to a sustainable level. The following chapter (Chapter 3) will look at the construction and testing of the prototype of this design. Chapter 4 will characterise the cooling approach taken

and chapter 5 onwards will investigate strategies on improving the power density of this design.

Chapter 3 CONSTRUCTION, TESTING AND ANALYSIS OF PROTOTYPE GENERATOR

3.1 INTRODUCTION

Chapter 2 described the electromagnetic optimisation of the 50kW PM synchronous generator with the flooded stator cooling arrangement for connection to an uncontrolled diode bridge rectifier, resulting in a final optimised design. This chapter describes the construction, experimental testing and results analysis of the prototype.

3.2 ROTOR CONSTRUCTION

The manufacture of one-off stator and rotor cores is usually done by either wire based electro-discharge machining of a clamped stack of laminations or laser cutting of individual laminations. For this demonstrator machine, the stator and rotor cores were manufactured by Vacuumschmelze using their latest soft magnetic material manufacturing process, VAC Stack technology. However, in the VAC stack process, the 0.2mm thick cobalt iron lamination sheets are adhesively bonded to form a single rectangular block before being cut-out using the wire EDM. The end result in a precise adhesive bonded stack of the final geometry with a typical dimensional tolerance of 0.01mm. This process results in reduced core losses and improved magnetisation performance compared to stamping / laser cutting as shown in Figure 42 and Figure 43 respectively by Vacuumschmelze [17].

VAC Stacking Procedure: Reduction of Losses

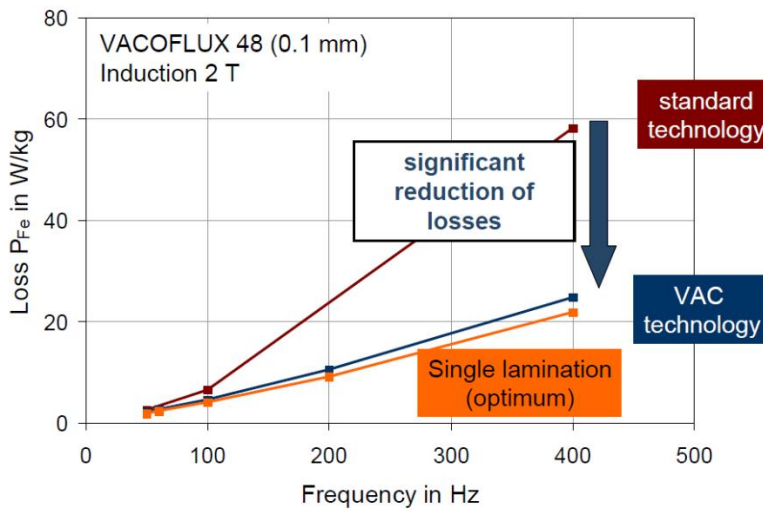


Figure 42 Comparison of core losses using VAC process compared with standard process (Source: Vacuumschmelze)

VAC Stacking Procedure: Improved Magnetic Properties

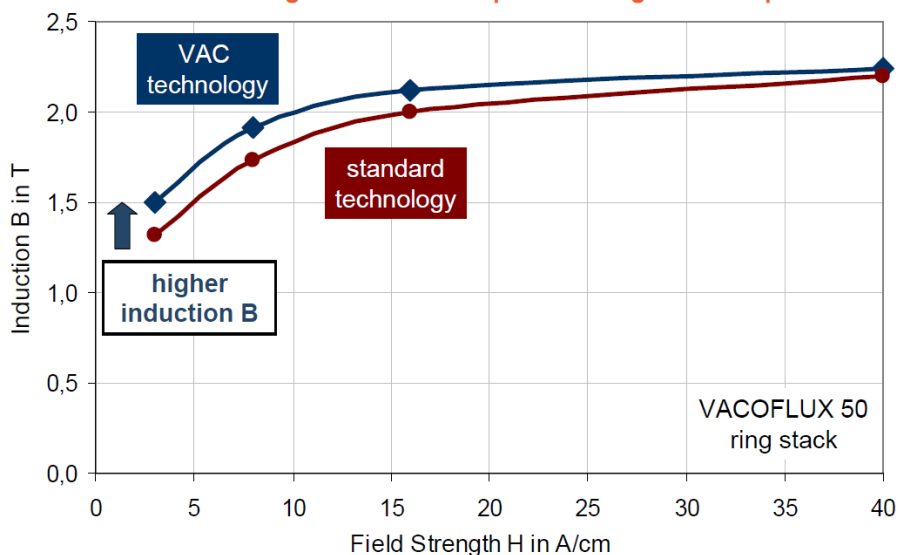


Figure 43 Comparison of the flux density per field strength of the core using the VAC process and the standard process (Source: Vacuumschmelze)

The rotor core was attached to a non-magnetic hub which was in turn connected to the rotor shaft. Keyways were used to locate both the rotor core to the hub and the hub to the shaft. The hub was manufactured from Titanium (specifically Titanium 6-4 which includes addition of 6% Al and 4% Vanadium). This material offers the following benefits as a hub material:

- A low density (4430kg/m^3) which is useful in terms of minimising overall machine mass.
- High strength (0.2% proof stress of 880MPa) to accommodate centrifugal loading imposed by high speed operation
- Coefficient of thermal expansion which is a good match with that of Cobalt iron with values of 8.8 and $9.5\mu\text{m/m.K}$ respectively.

Figure 44 shows the hub, a pair of Titanium end-plates and a dummy shaft used during the rotor assembly process. As shown, a series of apertures were created in the hub to reduce its mass without compromising on mechanical strength.

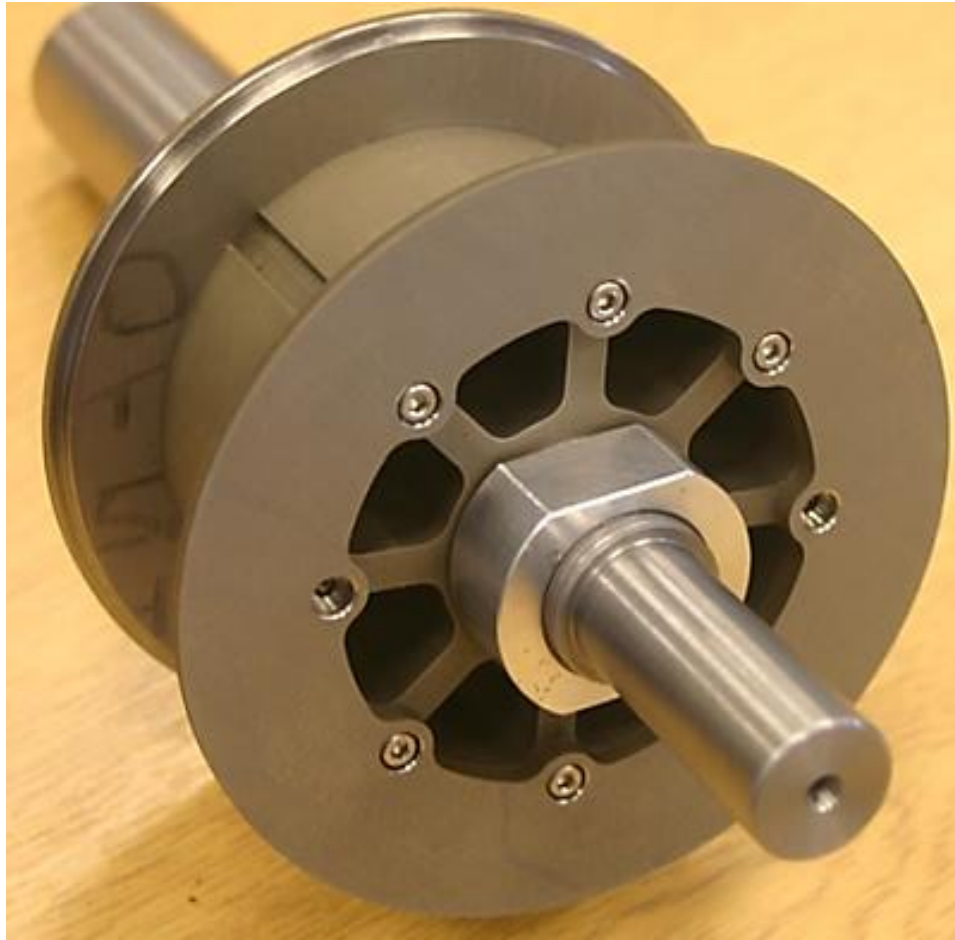


Figure 44 Assembly of the hub, end-plates and a temporary shaft

The rotor core design included a series protrusion to precisely locate and align the magnets within each pole. The detail of these protrusions is shown in Figure 45. The $\text{Sm}_2\text{Co}_{17}$ permanent magnets were cut and bonded to the rotor core by an external supplier (Cermag Ltd). As discussed in Chapter 2, the magnets were segmented to reduce eddy-current losses. Each pole is made up of 240 separate pieces of magnet (10 segments along the axial length, 2 circumferentially and 12 radially). The high degree of segmentation can be seen in Figure 46. The magnet segments are bonded together using a high temperature epoxy Duralco NM25 which can withstand temperatures up to 260°C [18]. The inter-polar regions are filled using a high temperature and high strength non-magnetic filler, Hylomar ST574 [19] which has a density of 2000 kg/m^3 and is evident as dark red regions in Figure 46.

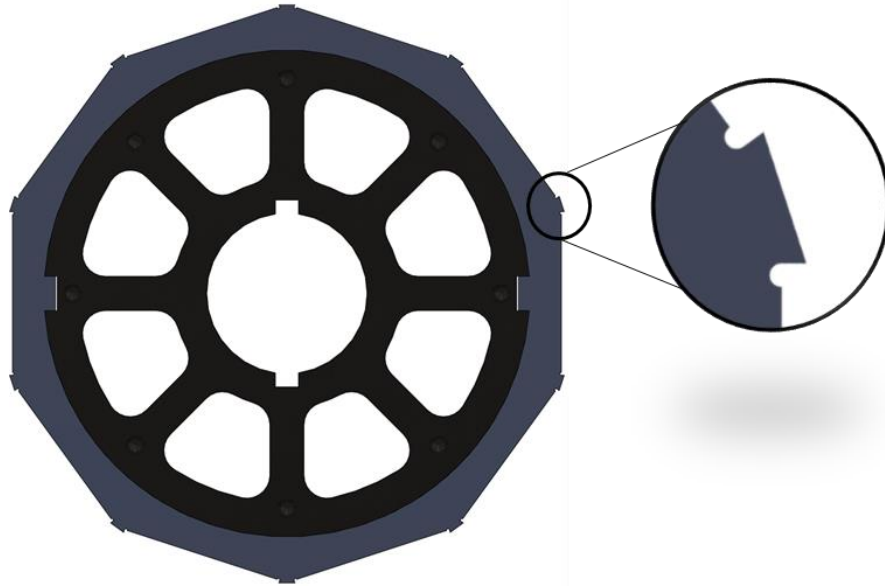


Figure 45 Rotor core and hub arrangements with magnet pole niches

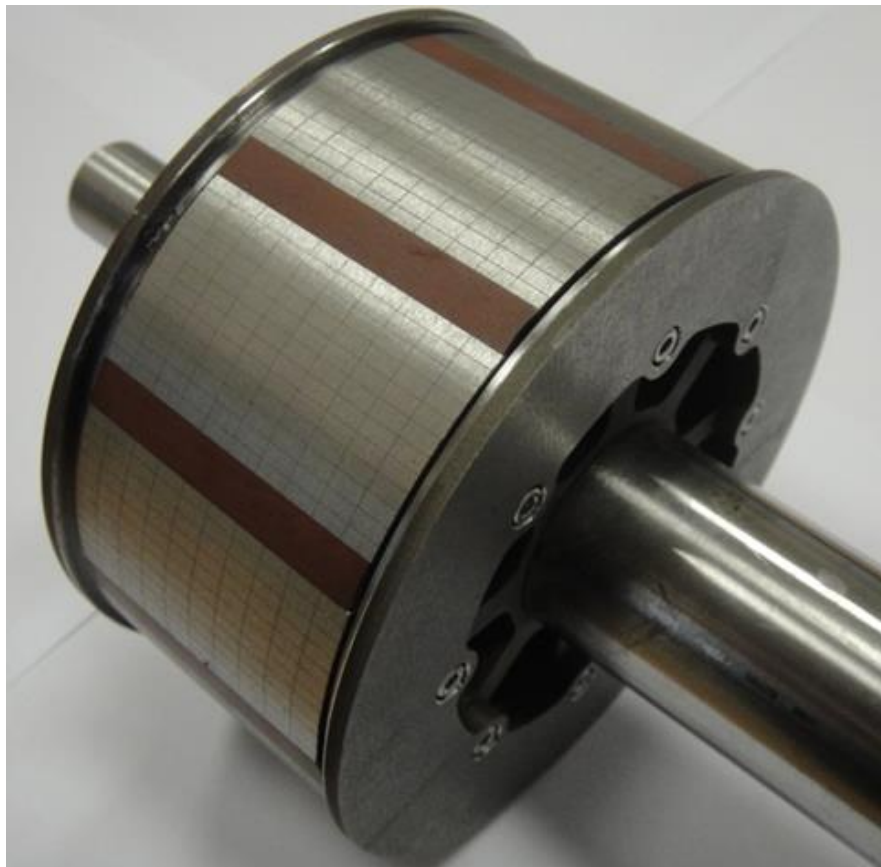


Figure 46 Assembly of the rotor showing segmented magnets

A 2mm deep groove was incorporated at the outer edge of end-plate as shown in Figure 46 in order to accommodate a 2mm thick carbon fibre composite containment

sleeve for retaining the magnets. This arrangement provides a flush finish across the surface of the rotor as shown in Figure 47. The carbon fibre banding was subcontracted to Cobham (UK) because of the need to maintain a pre-stress of 450MPa during manufacture in order to counteract the centrifugal forces at the upper end of the speed range. The rotor was two-plane balanced to better than G2.5 specification by a specialist balancing company. In order to achieve the requisite balance, material was selectively removed from the end-plates as shown in Figure 47

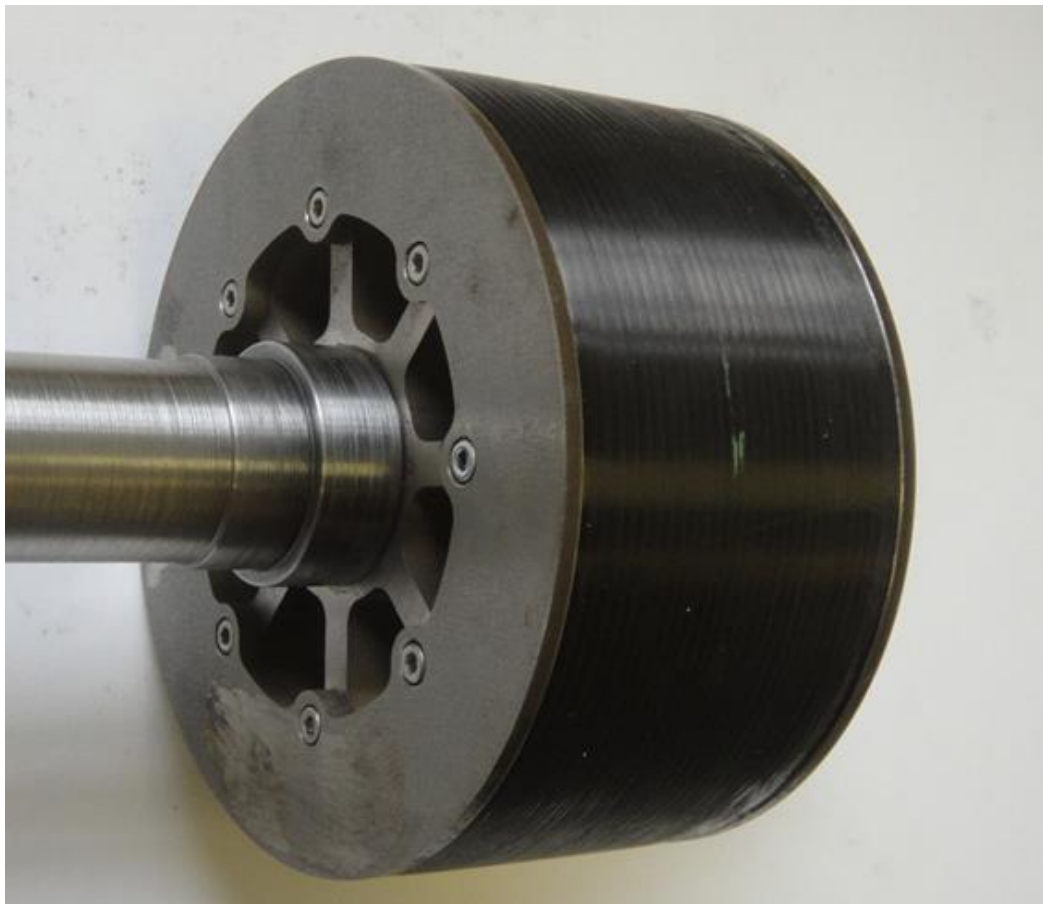


Figure 47 Completed rotor

3.3 STATOR CONSTRUCTION

The stator core was sourced and manufactured in the same manner as the rotor core using the same grade of cobalt iron (Vacoflux50) and manufactured using the same VAC Stack process. Figure 48 shows the bonded stator core prior to winding.

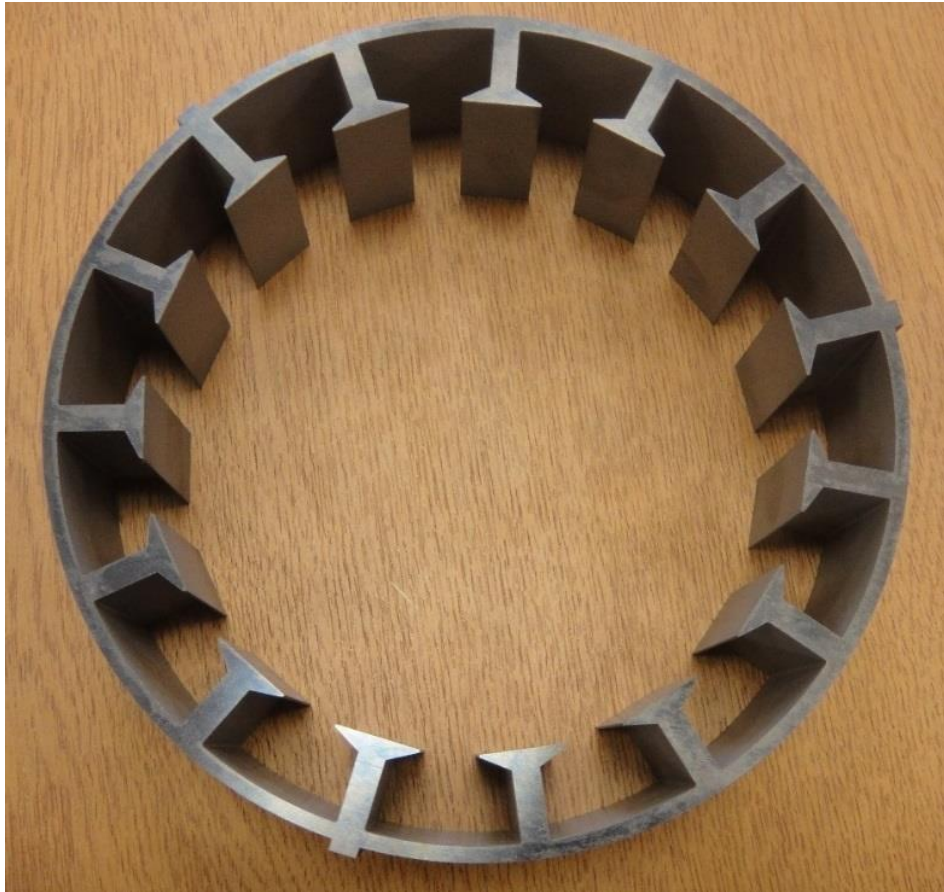


Figure 48 Stator core

The effective copper cross-sectional area required per turn was calculated to be 17.4mm^2 which corresponds to an equivalent single circular conductor of diameter 4.7mm. Manually winding conductors of this thickness in stator slots of the scale of the demonstrator machine is not possible, in particular if a packing factor of 0.5 is to be approached. In order to ease the difficulties of producing a practical winding with the desired cross-sectional area, the stator coils were wound by paralleling 49 strands of 0.67mm diameter circular. This combination of the number and size of individual wires was arrived at following windings trials, from which was observed that wire diameters greater than 1mm were too difficult to manoeuvre precisely to produce a neat and compact an in-situ winding. Each phase winding, which consists of 5 separate coils was wound in a single pass with no terminations between successive coils which make up the phase.

The use of 49 parallel strands also has the benefits of minimising any AC winding losses, which is a particular concern given the open-slot stator design. The skin depth at the rated fundamental frequency at 1.42 kHz is 1.75mm. The wire used was a double coated polyester C200 grade with temperature class of 200°C. The strands were taped together with a degree of transposition and wound in-situ with great degree of care. Figure 49 shows the stator part way through the overall stator winding process. The blue nylon mandrel shown in Figure 49 was used to prevent the coils from being displaced into the airgap region during the winding process, while temporary wooden forms were used within the slots to confine the coil being wound to occupy no more than half the available slot cross-sectional area. Nomex® aramid slot liner paper with a temperature range up 220°C was used to line the slots to insulate the coils from the stator core.



Figure 49 Stator winding part-way through manufacture

The machine was instrumented with 8 thermocouples at prescribed locations around the stator periphery and along the axial length as shown in Figure 50. The temperature measured by the thermocouples were logged using a National Instruments TC-2095 rack mount adapter link to Labview. It was anticipated that the type of flood cooling employed would give rise to varying temperature around the stator periphery due to gravity and non-uniform flow due to the asymmetric location of the coolant inlet and outlet. In addition, some axial temperature gradient would be expected.

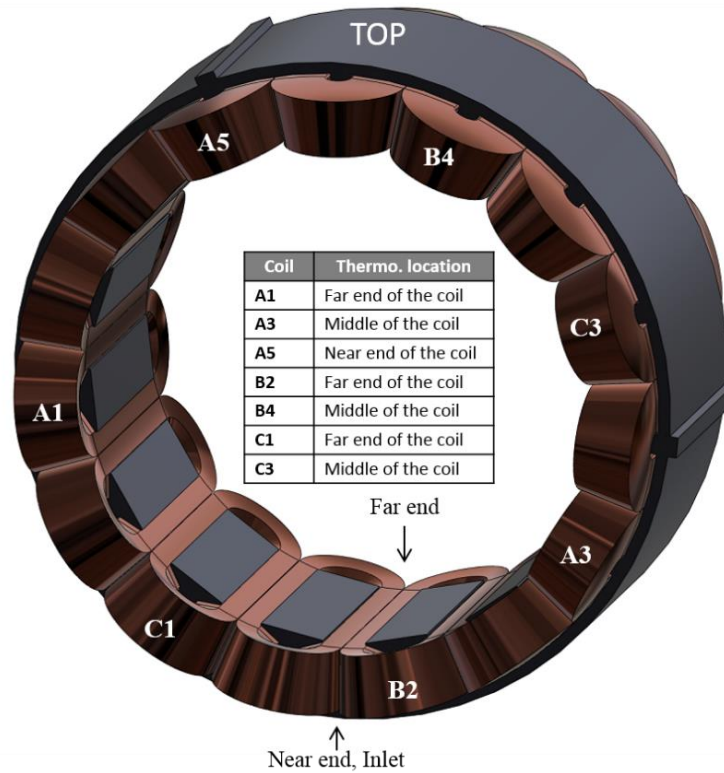


Figure 50 Location of thermocouples

3.4 FLOOD COOLING DESIGN

The stator annular void is completely flooded with Aeroshell turbine oil 3 [20], which acts as the coolant. This grade of oil is electrically insulating to all practical purposes and has a specific heat capacity of 1670 J/kg K at 15°C. This allows the coolant to be in direct contact with the individual conductors that make up the stator coils. A level of control can be exercised over the cooling and hence the temperature of the coils by adjusting the flow rate of the coolant using the existing oil-cooling system shown in Figure 69. This system includes a pump, an oil to water heat exchanger, manual flow control valves and instrumentation for measuring flow-rate and pressure.

The coolant is prevented from entering the airgap and the rotor void by a thin-walled cylindrical sleeve, which sits in the airgap. Since the thickness of the coolant sleeve increases the effective electromagnetic airgap, minimising its thickness is beneficial

in terms of electromagnetic performance. The sleeve was manufactured from PEEK, which is a high strength, high temperature and chemically resistant thermoplastic polymer [21]. The manufactured sleeve, which is shown in Figure 51, is 0.92mm at its thinnest but includes integral slot-wedges to add rigidity to the sleeve and provide location.

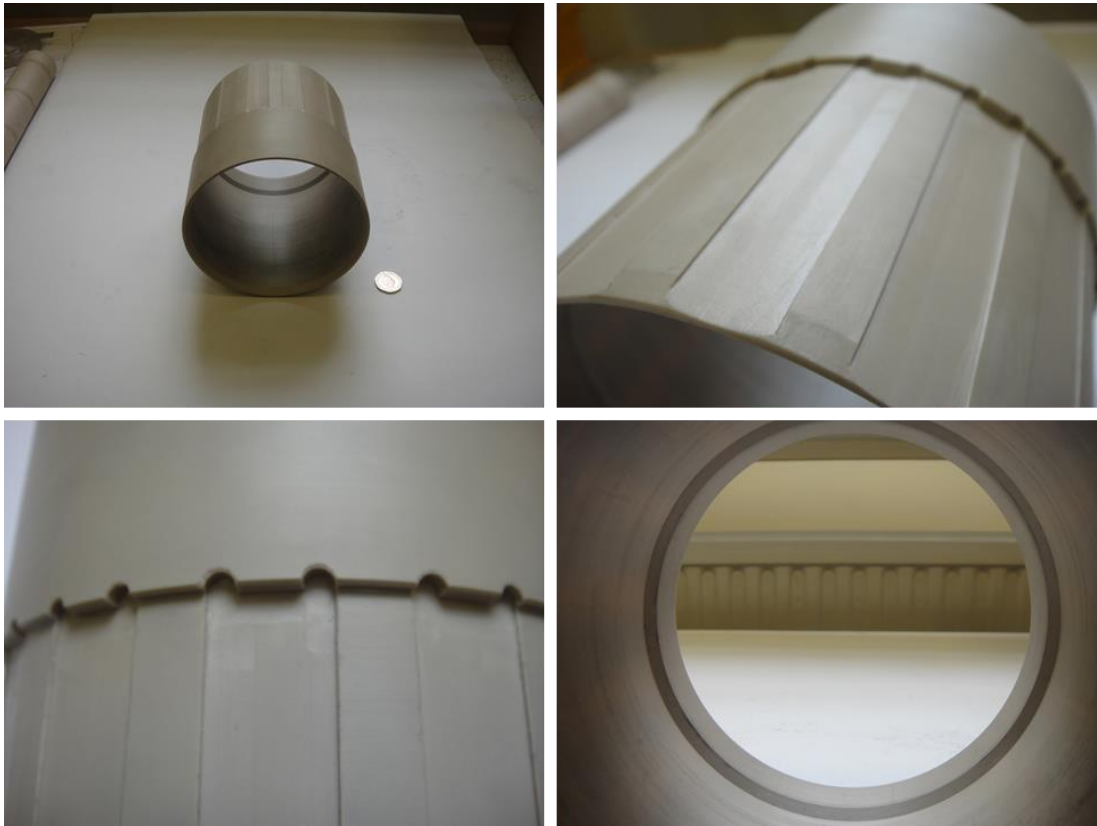


Figure 51 Photos of the finished PEEK air-gap sleeve

This integration of slot wedges into the sleeve is novel and is the subject of a patent application filed in 2015. The thickness of the ends of the sleeve beyond the region occupied by the rotor and stator core were increased to further increase mechanical rigidity. A CAD drawing of the assembly of the sleeve and casing to create the sealed region is shown in Figure 52. A total of four O-rings were used to seal the endplates to casing interface and the coolant sleeve to endplate interface.

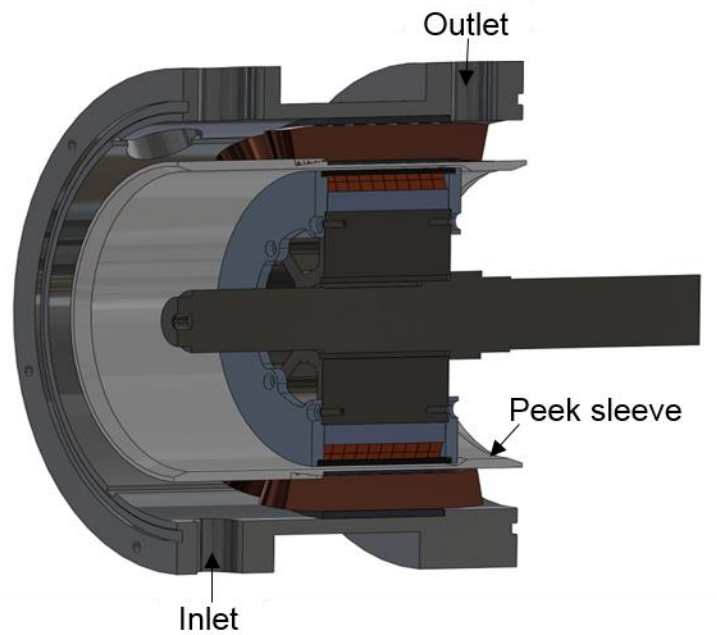


Figure 52 Cross-section of machine assembly

One consequence of flood cooling the entire stator void is the need to pass the electrical terminations of the stator winding through a liquid-tight seal connector. Given the high current involved and the limited space available on the casing, bespoke electrical connectors based on a design used on an earlier and smaller prototype were manufactured. The components which make up one electrical pass-through connector are shown in Figure 53. The brass-stud which serves as the electrical connector is fitted with a pair of Nitrile O-rings which seal on the bore of a PTFE insulating insert. This PTFE insert is fitted with a further pair of O-rings which seal onto a cylindrical surface produced by boring out a commercial sealed gland housing.

The various thermocouples which were incorporated into the stator were fed through a commercial pass-through connector (Model: MCH5-032-16-V manufactured by Conax Technologies). The connector, which is shown in Figure 54 employs a Viton insert with 16 holes to seal each of the wires from 8 thermocouples



Figure 53 Liquid-tight electrical feedthrough connectors

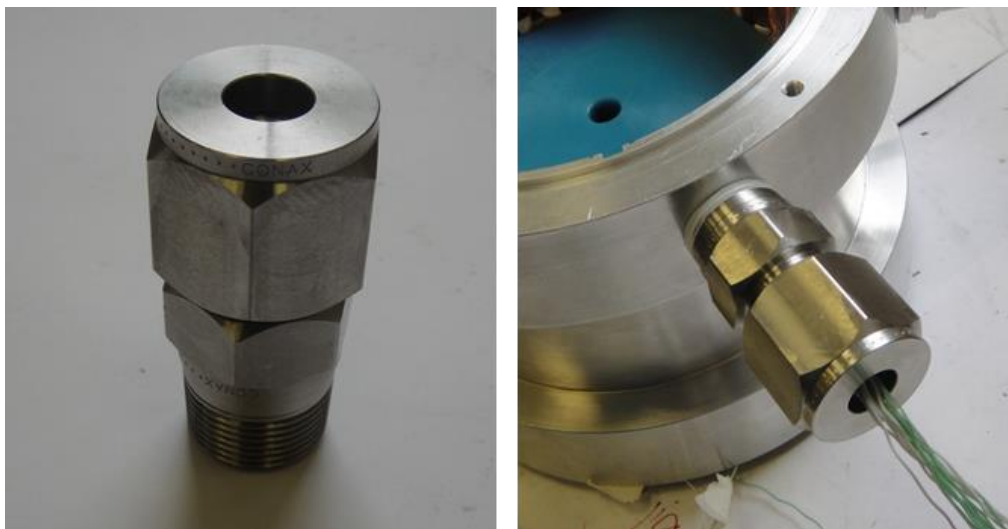


Figure 54 Liquid-tight thermocouple feedthrough gland

The coolant is supplied to and from the stator void via a pair of ½” BSP push-fit connectors. The coolant inlet was positioned at the base of the prototype and the outlet at the top in order to avoid air pockets in the flooded region of the machine. Figure 55 shows the complete assembly of the prototype.



Figure 55 Complete assembly of prototype generator

3.5 EXPERIMENTAL TESTING OF THE PROTOTYPE GENERATOR

Preliminary testing of the prototype was carried out at the University of Sheffield prior to it being taken to Rolls-Royce in Bristol to be integrated into ASTRAEA test-rig. These preliminary testing comprised measurements of open-circuit back-EMF, DC voltage at rectifier terminals under no load, resistance and inductance.

3.5.1 MEASUREMENT OF MACHINE PARAMETERS

The line-to-line DC winding resistances were measured using a Cropico D500 micro-ohmmeter and are summarised in Table 12. The predicted resistances used in the design stage (which consists of a summation of the individual coil resistance including their own end-windings) show a relatively good correlation with measured values, in all cases underestimating the measured values. The difference can be attributed in part to interconnects between coils, to the star-point and to the terminal

post, which were not accounted for in the design phase. As shown in Figure 56, which shows an end-on view of the various interconnects, these add a significant copper length to the phase windings, which is difficult to reliably predict during the design. The estimated additional length of these interconnects are 444.5mm per phase.



Figure 56 View of interconnections and star-point of completely wound stator

There is a slight difference in each phase additional length because of the relative location of the phases and the terminations, which is consistent with the slight differences in measured resistances of the three line-to-line resistances. The calculated additional resistance contributed by these interconnects are $0.89\text{m}\Omega$, which goes a considerable way to reconciling the differences between measured and predicted resistance.

Table 12 Measured and predicted line-to-line DC resistance

	Measured (mΩ)	Predicted during design (mΩ)
Phase A to B	9.56	8.22
Phase B to C	9.44	8.22
Phase C to A	9.43	8.22

The line-to-line inductance was measured at the maximum machine electrical frequency of 1.42 kHz (corresponds to 17,000rpm) using a Hioki 3522LCR meter. The measured line-to-line inductance consists of several components of self and mutual inductance as shown by Equation (9). The inductance measurements are summarised in the Table 13 along with the corresponding line-to-line values predicted at the design stage using magneto-static finite element analysis. There is a marked difference, which cannot be fully accounted for by interconnects. Potential sources of this discrepancy is due to the presence of the magnets on the rotor.

$$L_{AB} = L_A + L_B - 2M_{AB} = 2(L - M) \quad (9)$$

Table 13 Measured and predicted line-to-line inductance

	Measured (μH)	Predicted (μΩ)
Phase A to B	65.4	52.1
Phase B to C	65.4	52.1
Phase C to A	65.4	52.1

The prototype was driven at a series of constant speed set-point by an AVL APA 101/20 Dynamometer. This has a nominal power rating of 120kW, with a maximum speed of 20,000rpm and rated torque of 120Nm up to 10,000rpm (and constant power characteristic thereafter).

An existing custom-built uncontrolled rectifier, which is shown in Figure 57, was used in the measurements. This is based around Semikron SKKE330F bridge rectifier modules rated at 1700V and 450A and which was designed for frequencies up to 20 kHz. The diodes had a forward voltage drop of 1.8V at 300A at room temperature (25°C). The diode modules were cooled using a forced air-cooled heat sink.



Figure 57 1700V/450A uncontrolled bridge rectifier

3.5.2 EXPERIMENTAL NO-LOAD BACK EMF TEST

The line-to-line EMF waveform under open-circuit conditions was measured using the N2791A Agilent Technologies differential probes. The measured line-to-line EMF waveform at 17,000 RPM is shown in Figure 58. The peak value of the waveform shown is 230.4V. A comparison between the measured and finite element predicted emf waveforms at 17,000 RPM is shown in Figure 59. As will be apparent, there is a significant discrepancy in both the peak magnitude and shape of the two waveforms. As noted in section 2.5.1, the original FE simulated waveform is well

suites for a machine connected to an uncontrolled rectifier in which each phase conducts only over the central 60° of each 180° half-cycle. Hence, the significant reduction in the magnitude of the emf measured over this interval will inevitably result in a marked reduction in the power that can be delivered by the demonstrator machine. Given the extent of the discrepancy between the measured and predicted emf, a feature of machine performance which can normally be predicted to a good accuracy even with two-dimensional finite element analysis, a systematic study was undertaken to establish likely reasons for such a discrepancy.

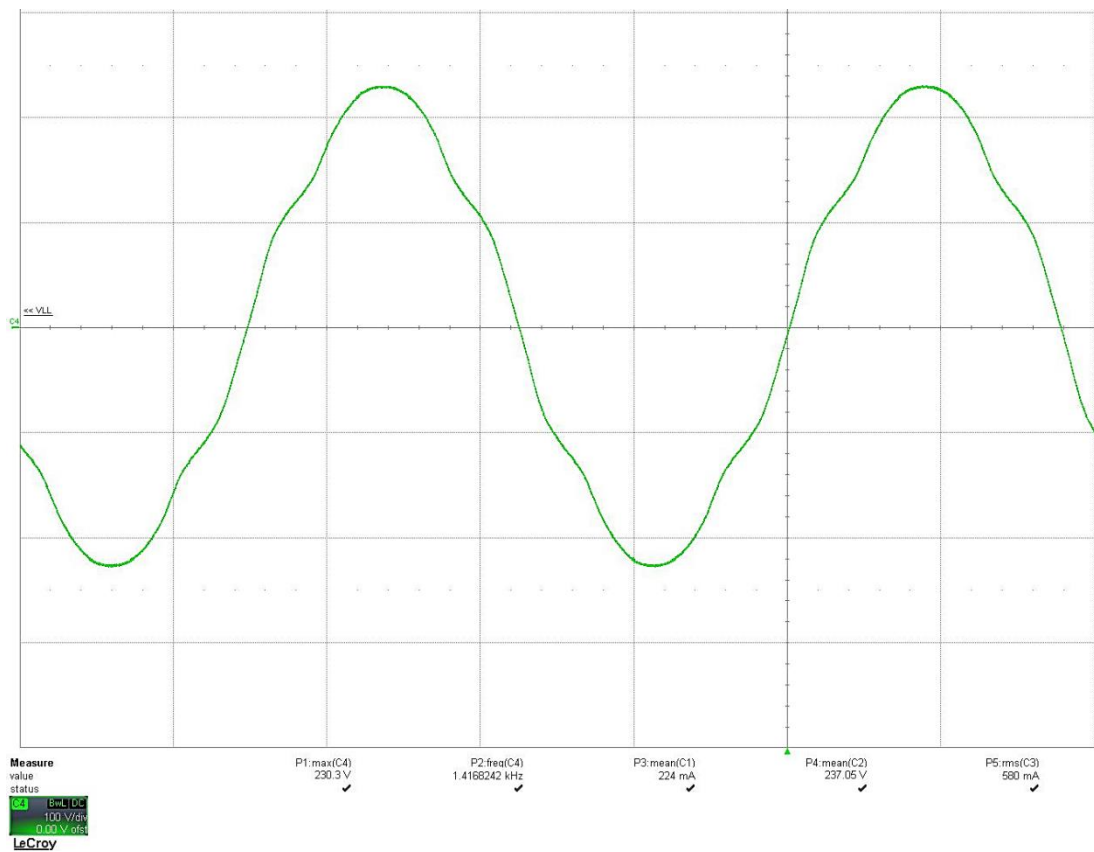


Figure 58 Measured line-to-line back EMF at 17,000 rpm

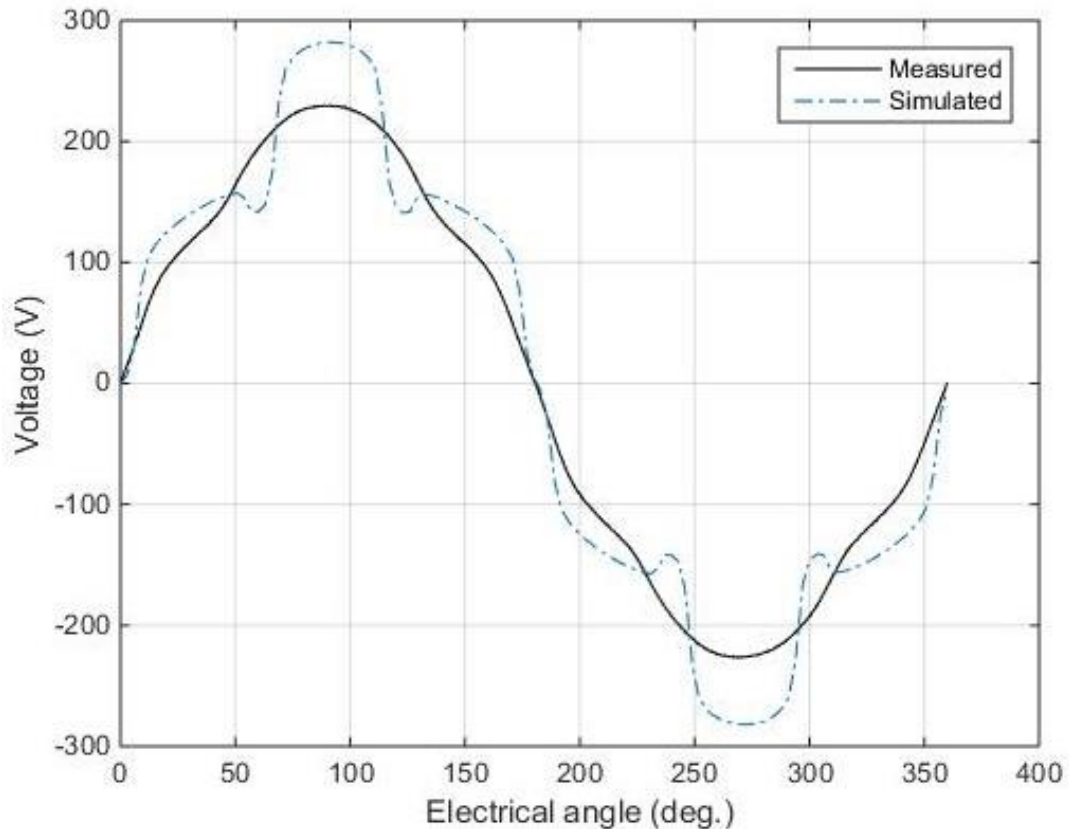


Figure 59 Simulated and measured line-line Back EMF at 17,000 rpm

The first factor investigated was the sensitivity of the two-dimensional finite element predictions to the properties of the rotor permanent magnets. In the case of the open-circuit back-emf, the property of most importance is the magnet remanence. In the specification of permanent magnets, manufacturers often quote a value of remanence and the energy product. In the case of the specific grade employed in the prototype these values are 1.07T and 30MGO respectively. Figure 60 shows the predicted variation in the back-emf waveform at 17,000rpm for remanence changes of 0.02T (in all cases for a fixed recoil permeability of 1.1) alongside the measured emf. As would be expected, in the absence of any significant saturation of the core, a factor would suppress the peak flux, the change in remanence simply results in a proportionate scaling of the emf with no change in form.

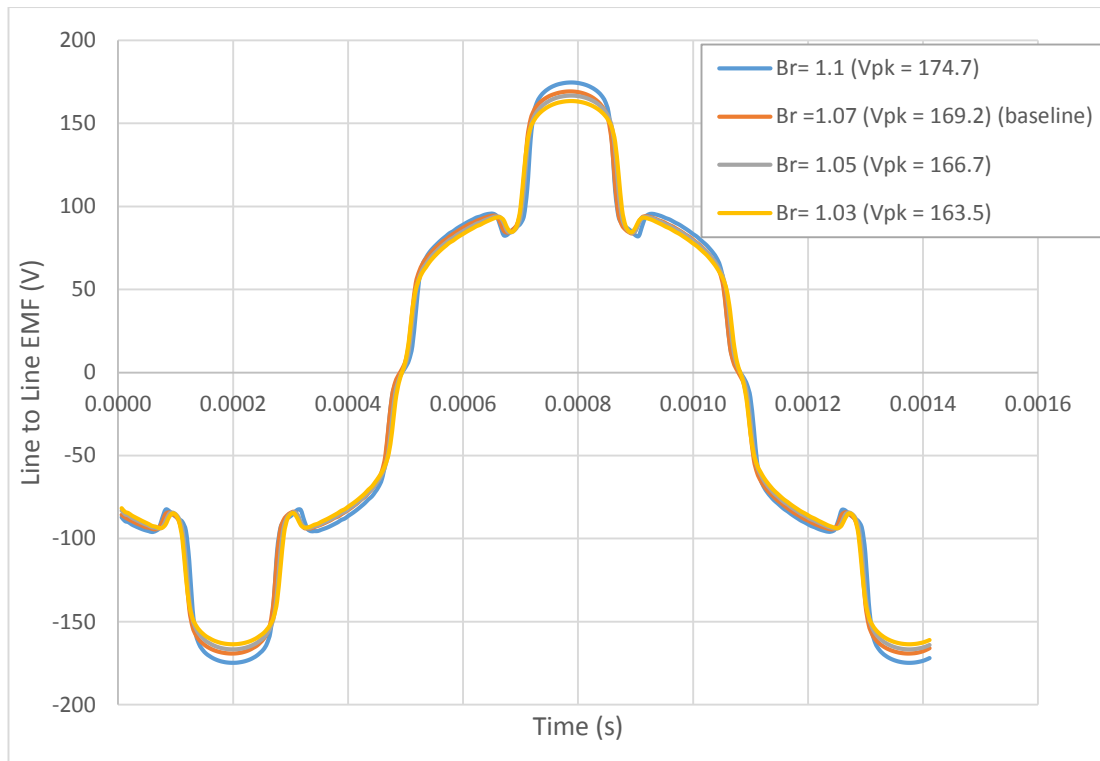


Figure 60 Predicted variation in the Back-EMF waveform at varying magnet remanence at 10195 rpm

Although the axial length of the core is not particularly short relative to the stator diameter, an assessment of whether significant end-effects were present was undertaken by predicting the back-emf waveform using a full three-dimensional model. The resulting waveforms are shown in Figure 61, from which it can be seen that there is little difference in form or magnitudes with peak values of emf of 163V and 164V for the two- and three-dimensional models respectively. A further set of two-dimensional finite element calculations were performed for increasing values of permeability of the magnet inter-pole regions (Hylomar ST724 filler), but with no appreciable sensitivity in the form of the emf waveform.

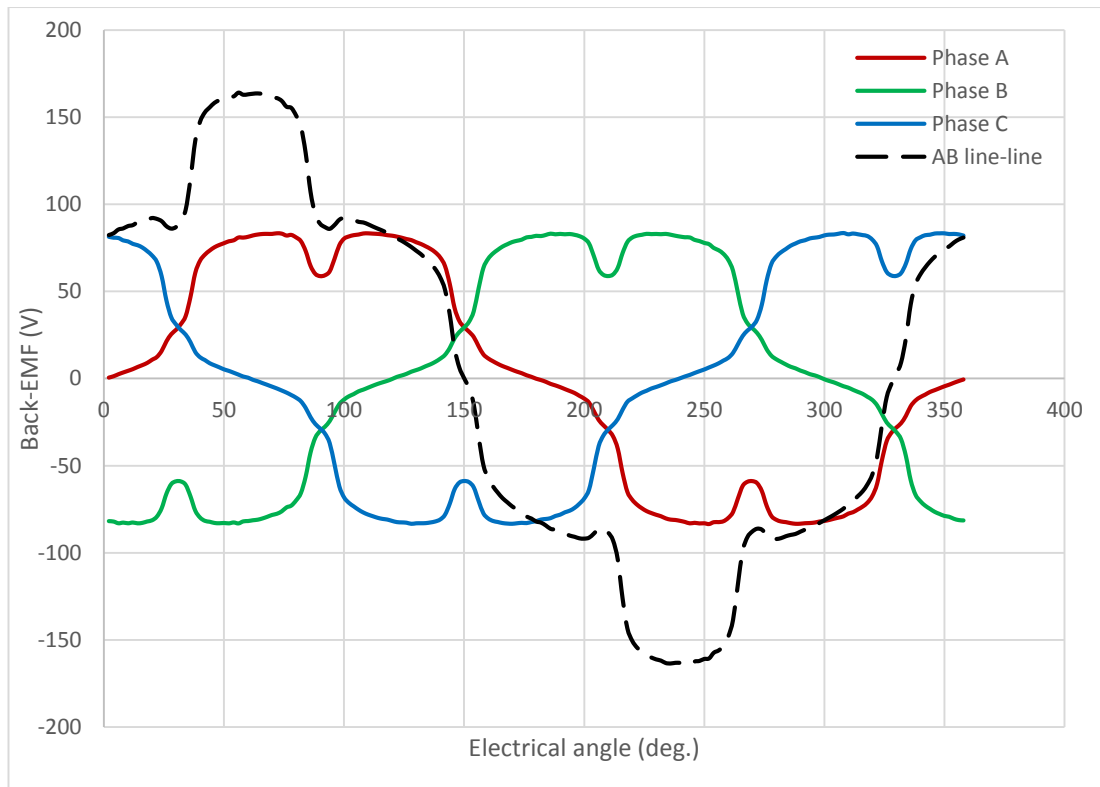


Figure 61 3D-FEA simulated back-EMF at 10195 rpm

Having explored all possible elements of the model of the nominal machine dimensions and included every minor geometrical feature, the role of the glue-line between the individual magnet segments was investigated systematically using a series of finite element models. As an example, Figure 62 shows a model in which the same overall magnet pole dimensions are maintained, but the glue-lines are represented as discrete 0.3mm wide non-magnetic regions.

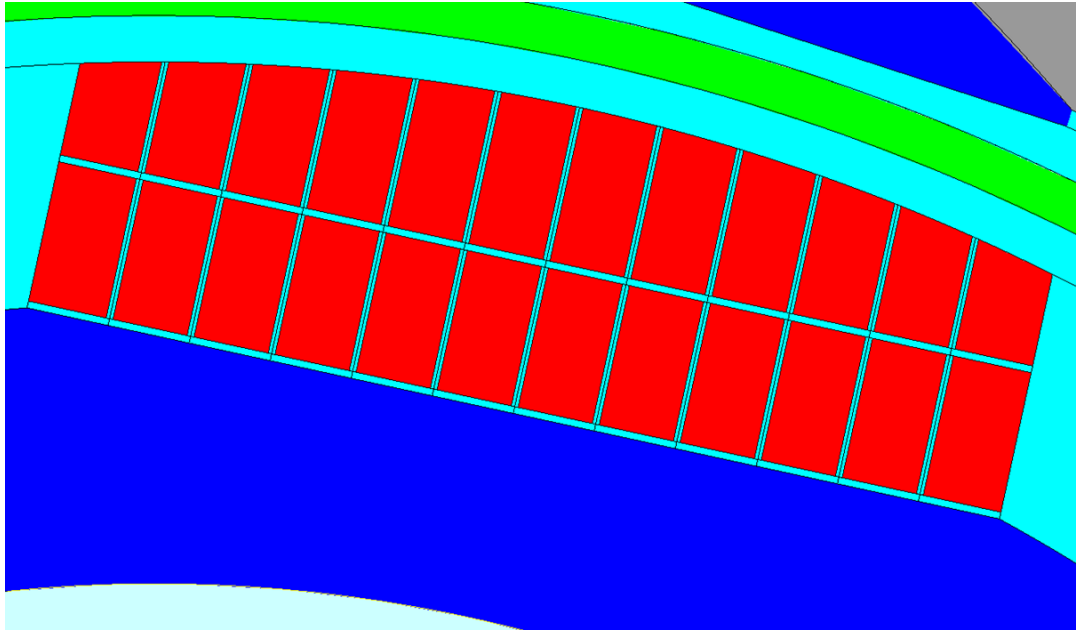


Figure 62 Magnet segmentation with glue-line width of 0.3mm

Using a series of models with increasing glue-line thickness, the line-to-line EMF waveform at 10,195 rpm was simulated. The resulting line-to-line emf waveforms for glue-line thicknesses between 0.1 and 0.3mm are shown in Figure 63.

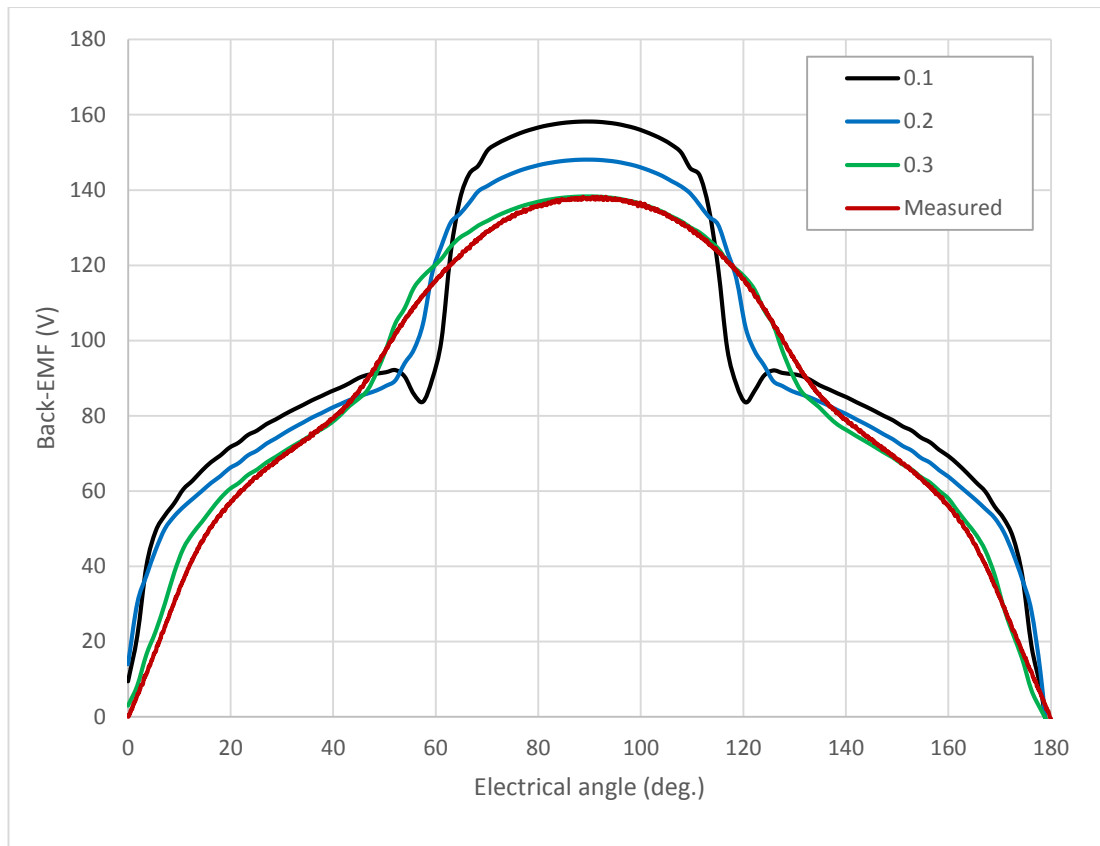


Figure 63 The EMF for varying adhesive thickness between segments compared with measured EMF waveform over 180 degrees electrical

It can be seen from Figure 63 that with a glue-line thickness of 0.3mm, there is a remarkably good correlation with the measured and predicted EMF waveform in both form and magnitude. With a glue-line as thick as 0.3mm, the net amount of magnet removed compared to a single piece pole is 15% by volume.

Although the rotor magnets could not be inspected in detail because of the carbon fibre sleeve which had been wound over the magnets, recourse to photographs taken during construction, such as that shown in Figure 64, did demonstrate some tolerance issues on the rotor. It can be seen from the close-up view that the magnets at the edge have been made noticeably narrower in order to accommodate the cumulative effect of glue-lines across the pole. Although it is recognised that the arrangement in Figure 64 is not the same as uniform width magnet segments spaced apart by 0.3mm (as is the case in the model of Figure 62) it is entirely possible that

glue-lines of the order of 0.3mm are present and contributing to the significant reduction in the emf.

This level of sensitivity of the EMF waveform to magnet discretisation and tolerances has not been observed in literature, and in part is a consequence of the careful refinement of the waveform in Chapter 2 to best meet the rather specific needs of an uncontrolled rectifier, i.e. the presence of a significant 5th harmonic as shown in the FFT analysis in Figure 65.

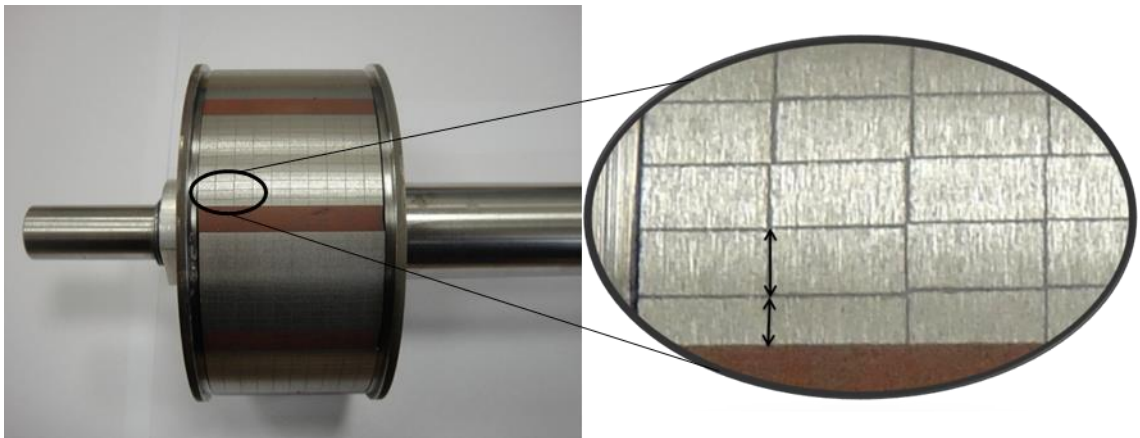


Figure 64 Photograph of rotor highlighting reduced width of segments at pole edge

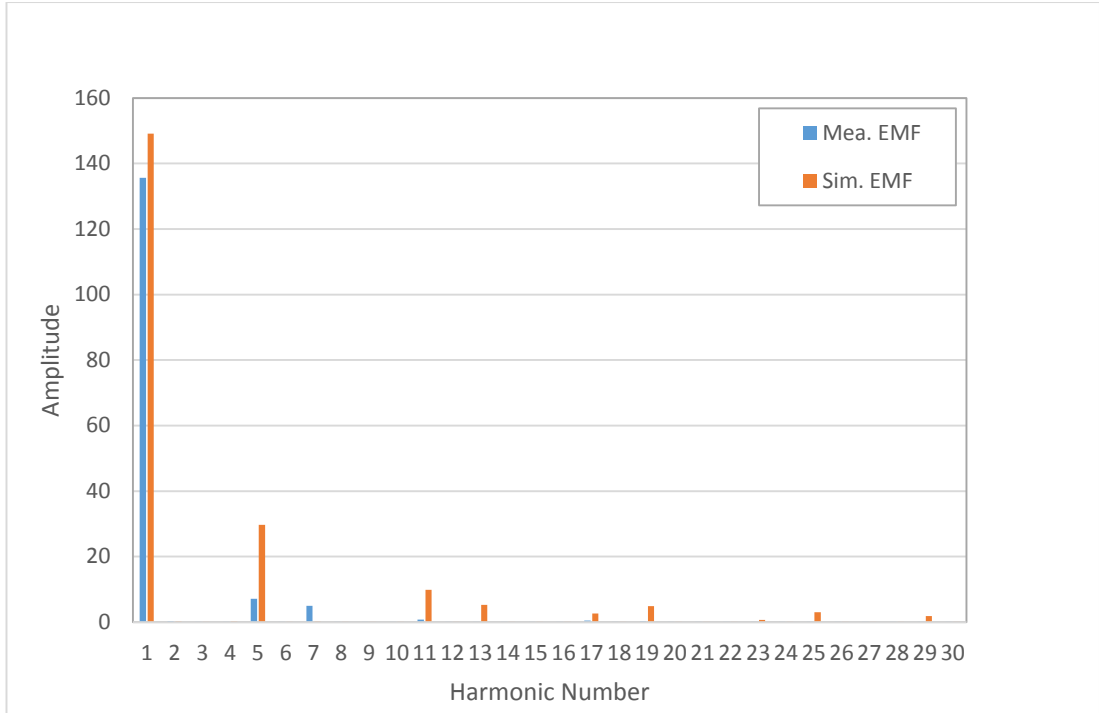


Figure 65 FFT analysis of the measured and simulated emf at 10195 rpm

3.5.3 ON-LOAD TESTING WITH DIODE BRIDGE RECTIFIER

The prototype machine was tested with several discrete values of load resistance connected to the rectifier output to measure some key points on the rectifier output V-I characteristics. Figure 66 shows the measured 6 points at 17,000 rpm along with predictions from electric circuit coupled finite element simulations using both the original design stage emf waveform and inductances (pre-build parameters) and the actual emf waveform and inductance (post-build parameters which includes end-winding inductances) . Also shown in Figure 66 are 30kW and 50kW constant power contours. The slope of the linear section of the V-I characteristic is governed by the impedance of the machine, cabling and rectifier, which is dominated by reactance at this frequency. The equivalent reactance that can be inferred from the measured characteristic is 0.30Ω , which is in reasonable agreement with the calculated value of 0.29Ω .

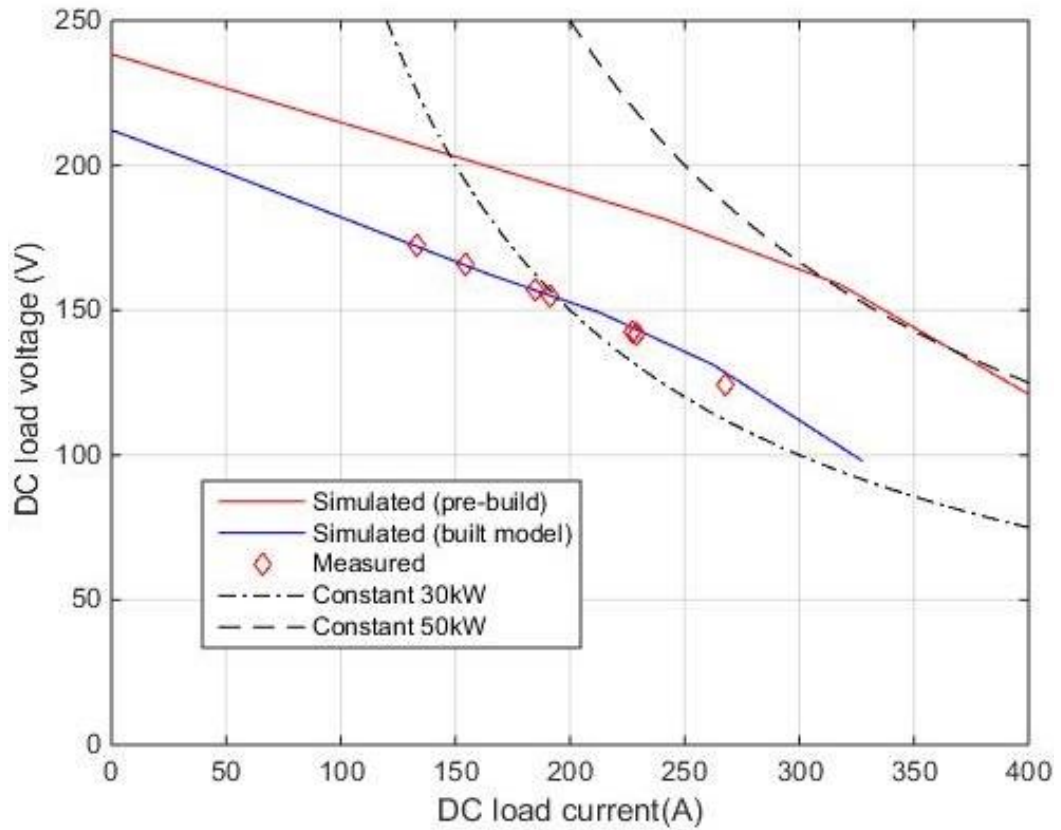


Figure 66 Comparison of the simulated and measured I-V curve of the machine at 17000 rpm

Figure 67 shows the rectifier output voltage and current waveforms along with machine phase-A current and phase A-to-B voltage at a load point corresponding to a rectifier output power of 30kW at 17,000rpm. Figure 68 compares the measured and simulated winding phase current at this 30kW operating point. The measured current corresponds to an rms current density in the stator coils of 8 A/mm².

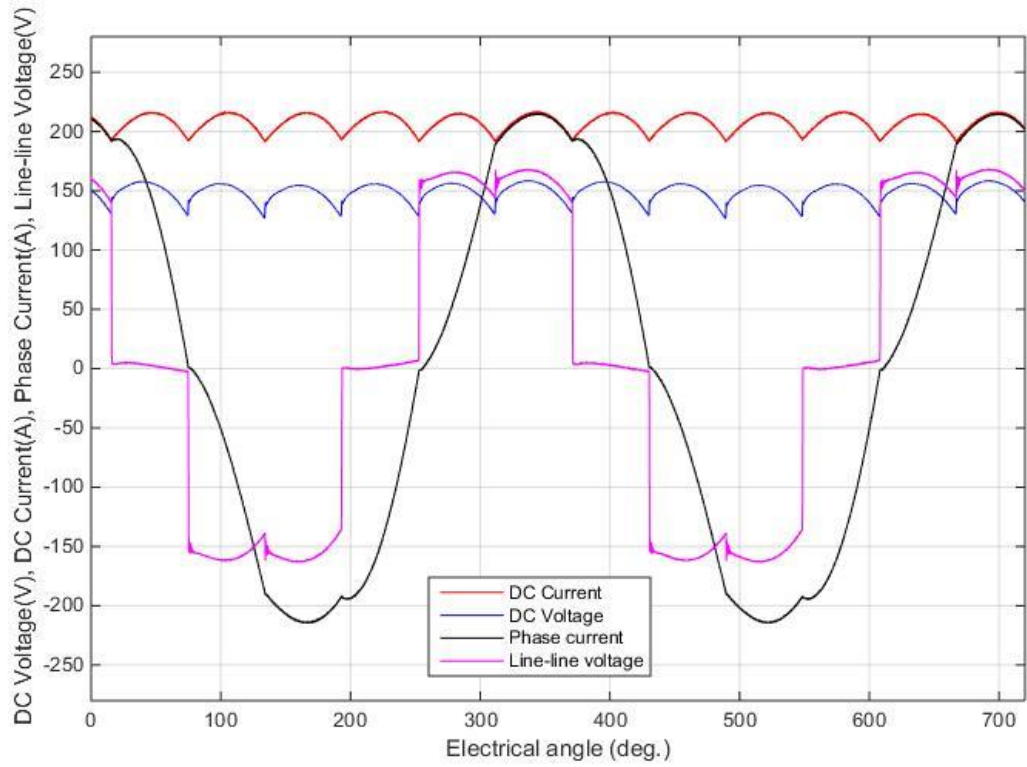


Figure 67 DC current and voltage, phase current and line-line voltage measurement at 30kW, 17,000 rpm operating point

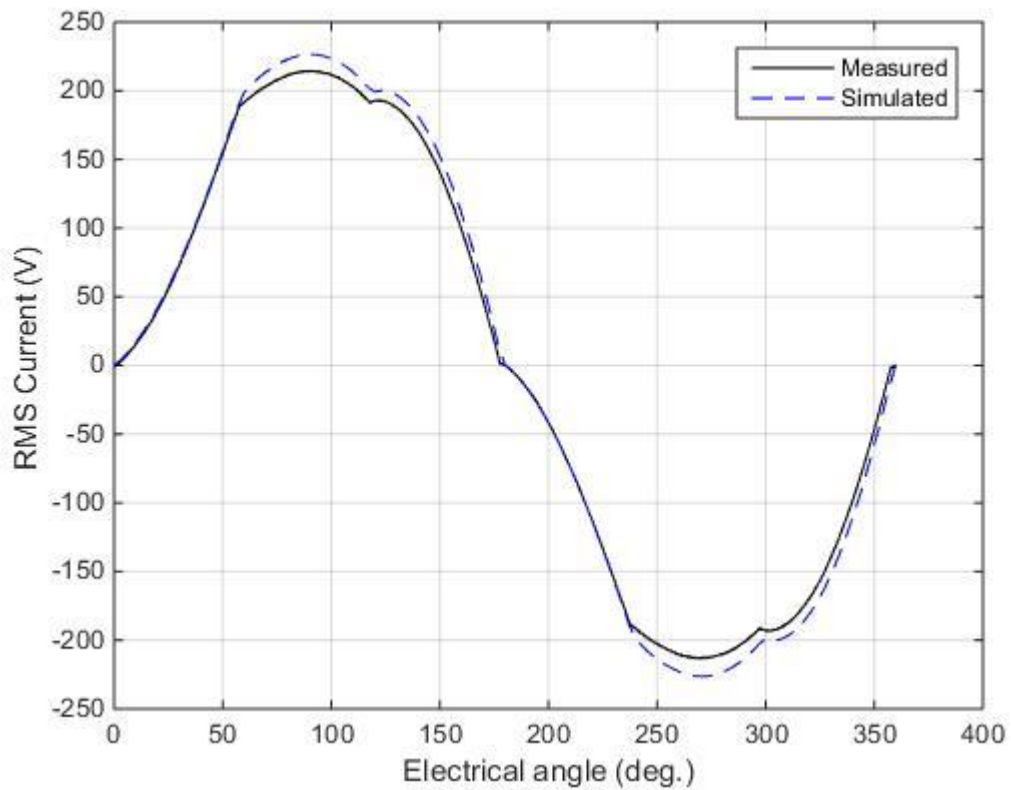


Figure 68 Comparison of simulated and measured winding current at 30kW, 17000 rpm

As will be apparent from the V-I characteristics, the significant reduction in emf arising from the gaps between magnets dictate that the machine cannot meet the 50kW specification test point and hence testing could not be performed at this operating point.

3.6 THERMAL MONITORING DURING TESTING AND ANALYSIS

A block diagram of the components and sub-system used for the thermal testing is shown in Figure 69. The main elements consist of the Control Techniques / Oswald dynamometer, the LP generator under test, an uncontrolled rectifier, resistive load banks, oil cooling unit and water chiller.

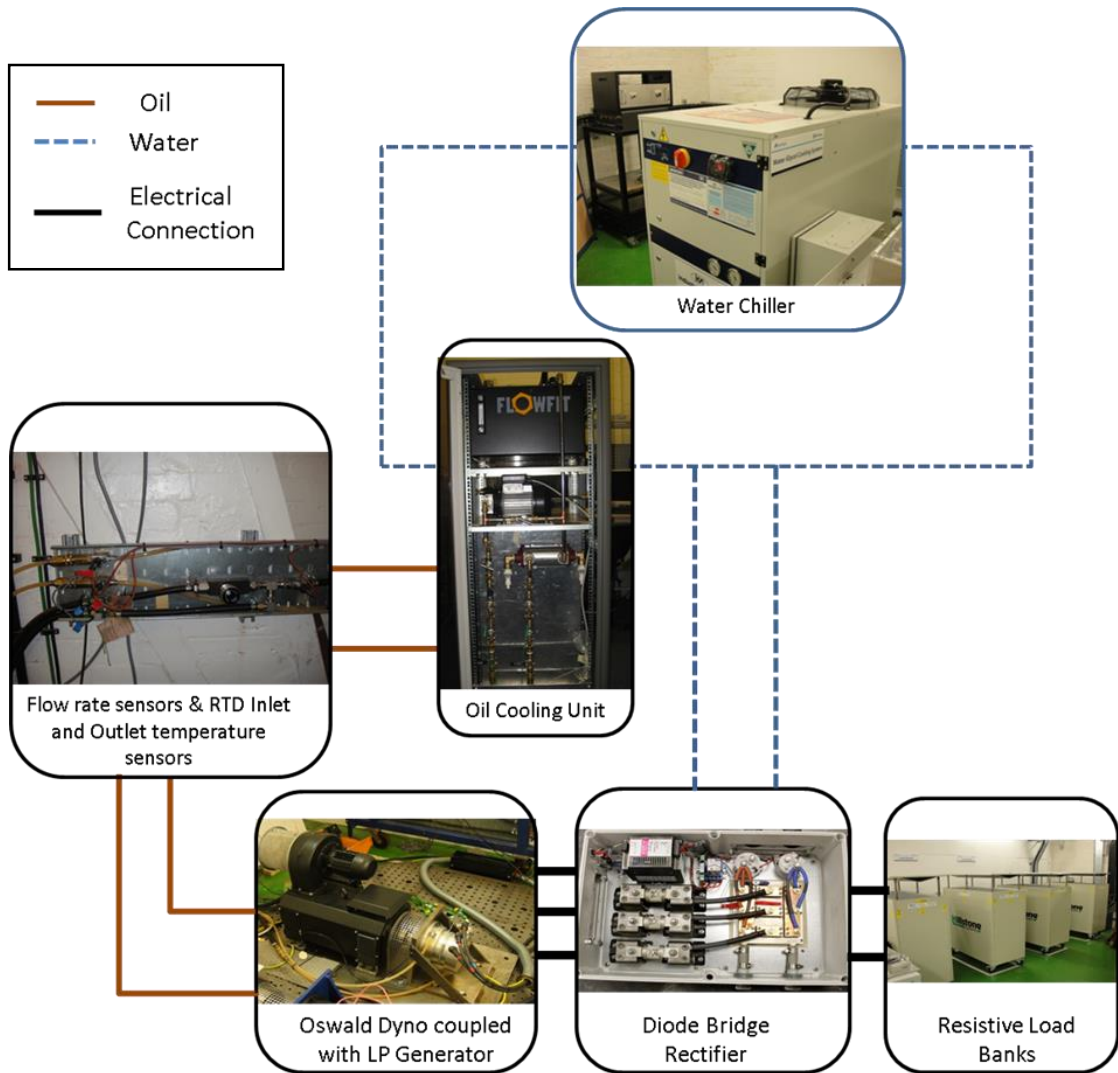


Figure 69 Generator thermal testing rig

All testing was performed with Aeroshell No. 3 turbine oil as the cooling oil. The temperature, flow, current and voltage sensors within the ASTRAEA rig are:

- **Machine winding temperatures:** The windings are instrumented with 7 K-Type thermocouples around the stator periphery at various positions in the coils of each phase as defined previously in section 3.3.
- **Machine casing temperatures:** A K-type thermocouple bonded on the machine outer aluminium casing at the 12 o'clock position, mid-way along the stator core.

- **Inlet and outlet oil temperatures:** RTD temperature sensors were used to measure the inlet and outlet temperatures of the oil. Due to the layout of the test-rig, this was at 2.3m away from the machine.
- **Oil flow rate:** Oil flow rates were measured using a turbine flow rate sensor which was located at the same distance away from the machine as the RTD temperature sensors.
- **Ambient air temperature:** The ambient temperature in the cell measured using a K-Type thermocouple. During the test period, the ambient temperature was typically $\sim 9\text{ }^{\circ}\text{C}$.
- **Water chiller set-point:** The water chiller was set to the ambient temperature $\sim 9\text{ }^{\circ}\text{C}$. This was controlled with a hysteresis band on the water outlet temperature with a maximum of 11°C and minimum of $7.5\text{ }^{\circ}\text{C}$.
- **Test-rig integrated DC current and voltage sensors:** The rig incorporates average DC voltage and current sensors, which were data-logged. Additional measurements of current and voltage were taken using a digital oscilloscope recording independently at a much higher sampling rate.

A series of test were carried out at a fixed speed of 17,000 rpm. For each test, the oil flow rate was set to a nominal value at the outset of the test by adjusting a manual by-pass valve in the oil cooler to a particular setting. However, the flow rate for a given valve setting changes during a test as the oil warms up due to significant changes in viscosity. The safety protocol for using the test rig precluded access to the test cell when the machine was rotating above 5000 rpm. As a consequence, for the test at 17,000 rpm, it was not possible to enter the cell to regulate the oil flow during a single test run, a process which normally involves manually adjusting a bypass valve on the oil cooler. This restriction on fine-tuning the valve setting when the

machine was near steady-state leads to oil flow rate being a measured quantity during the steady-state phase of test rather than being a precise set-point which is controlled during the test. This said, the drift in oil flow rate during a test due to changes in oil viscosity did not prevent a useful spread of oil-flow rates to be achieved. The maximum flow rate achieved during testing was ~6 l/min at an oil inlet temperature of 32 °C. The minimum oil flow rate of ~0.23 l/min was limited by the specification of the turbine type flow rate sensor in the test-rig.

The combination of the thermal mass of the machine and the change in flow-rate with oil temperature means that a typical tests takes ~30-45 mins to reach thermal steady-state. A test was deemed to have reached steady-state when there is less than 0.5% temperature rise in 5 minutes.

At the start of each test, the line-to-line voltage was measured along with the ambient temperature to provide an estimate of the magnet temperature. This voltage is proportional to the back-emf and hence magnet remanence. This provides a reference emf which can be used in combination with the magnet coefficient of remanence (-0.035% per °C for the grade of Sm₂Co₁₇ used in the demonstrator) to obtain an estimate of the average magnet temperature.

Digital oscilloscope measurements of the line-to-line voltages, winding current, DC voltage and DC current were logged every five minutes manually and recorded to a data file using the remote logging feature of the oscilloscope.

The maximum resistive load (minimum resistance) available during testing was 0.72Ω. This load corresponds to machine output power of 30 kW but ultimately limits the maximum current density in the windings to 8.9 A/mm² resulting in a predicted copper loss of 475W

3.6.1 THERMAL STEADY-STATE TEST RESULTS

A series of 19 test runs (TR) were completed at various current densities and flow rates, all at a fixed speed of 17,000rpm. Table 14 summarises the steady-state measurements at flow rates ranging from 0.27 to 6 l/min at current densities of 0 (i.e. rotation under open-circuit), 3, 7.7, 8.9 A/mm². Figure 70 shows the difference in temperature between the oil inlet and outlet as a function flow rate. Figure 71 shows the maximum coil temperatures (as inferred from the highest temperature reading of the array of 7 thermocouples) as function of flow rate at each of the designated current densities. To increase the maximum temperature in the machine windings at the current densities attainable, the flow rate was reduced to the minimum possible value of 0.23 l/min, a flow rate that is well below that anticipated in service.

Table 14 Summary of test run results at 17,000rpm

Test Ref.	Jrms (A/mm ²)	Flow rate (l/min)	Inlet temp. (°C)	Outlet temp. (°C)	ΔT of oil (°C)	Max. coil temp. (°C)
0 A/mm²						
TR1	0.0	0.27	29.9	44.4	14.5	51.6
TR2	0.0	1.75	23.8	30.8	7.00	29.8
TR3	0.0	3.61	23.9	28.5	4.60	26.9
TR4	0.0	5.33	23.9	27.1	3.20	25.8
3 A/mm²						
TR5	3.0	0.28	30.5	49.1	18.6	60.8
TR6	3.0	1.91	25.6	33.3	7.70	34.7
TR7	3.0	2.96	25.1	31.4	6.30	31.6
TR8	3.0	5.25	25.1	29.1	4.00	29.0
7.7 A/mm²						
TR9	7.7	0.88	31.3	57.0	25.7	71.8
TR10	7.7	2.23	31.5	46.1	14.6	55.3
TR11	7.7	3.56	31.3	41.5	10.2	48.6
TR12	7.7	5.90	31.6	38.6	7.00	44.0
8.9 A/mm²						
TR13	8.9	0.45	32.3	75.1	42.8	105
TR14	8.9	0.78	33.1	67.0	33.9	88.0
TR15	8.9	1.57	33.9	56.9	23.0	71.6
TR16	8.9	2.39	35.1	52.1	17.0	63.8
TR17	8.9	3.68	33.3	45.2	11.9	54.3
TR18	8.9	4.40	33.6	44.0	10.4	52.5
TR19	8.9	6.00	32.0	40.0	8.00	48.0

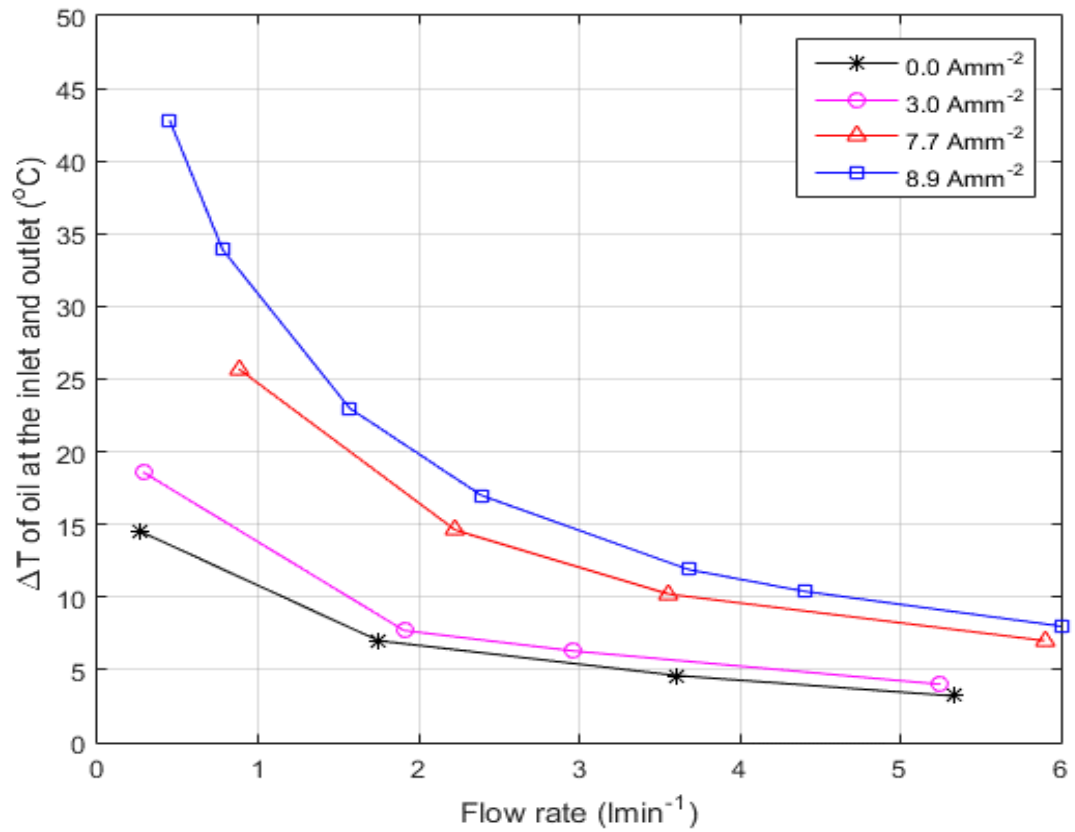


Figure 70 Temperature difference between oil inlet and outlet as a function of flow rate at a series of rms current densities

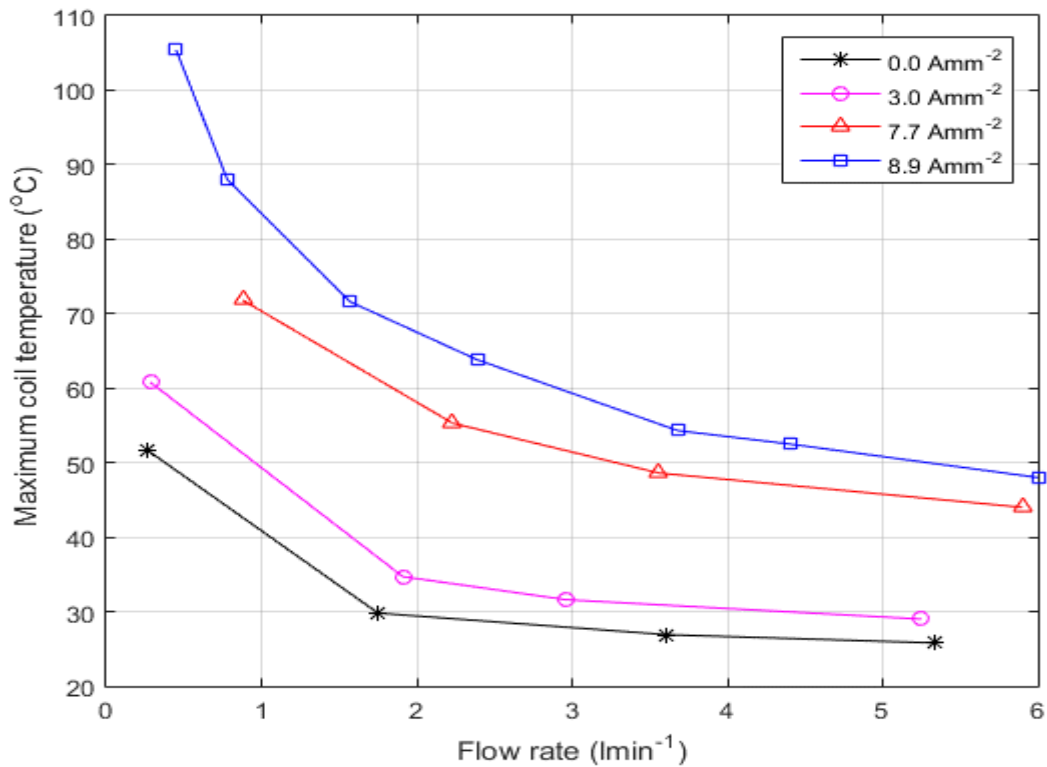


Figure 71 Maximum coil temperature as a function of flow rate for varying current densities (maximum taken at highest reading from the 7 thermocouples in the coils)

Figure 72 shows a typical temperature-time profile for the machine winding. This particular profile corresponds to maximum current density of 8.9A/mm² and a flow rate of 0.45 l/min (TR13). The speed was increased from 0 to 17000rpm starting at ~127s. The load step is applied at 243s following which the temperature rises to steady state by ~2365s, a period of essentially steady-state operation (from 2365s to 2920s) followed by the removal of the load and subsequent reduction of the speed back to standstill. In Figure 72 the designation of ‘Near’, ‘Mid’ and ‘Far’ in the thermocouple labelling indicates the axial location relative to the oil inlet. The coil labelling, e.g. C1, refers to the designation shown in Figure 73.

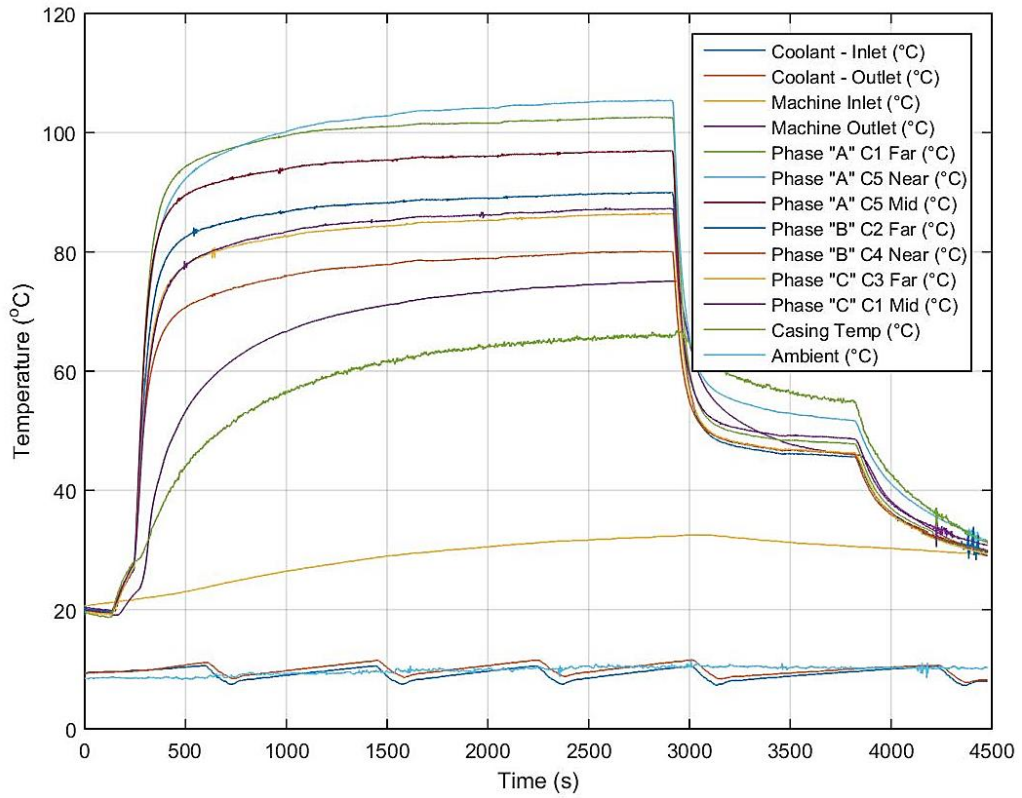


Figure 72 Measured temperatures within the machine for TR13 (see Table 14)



Figure 73 Location of the coils around the stator

There is quite a significant variation in the temperatures measured by the thermocouples that are buried in the stator coils. Under steady-state conditions, the thermocouple 'Phase A C5 Near' has the maximum temperature of 105°C which is 25°C higher than the lowest measured thermocouple temperature (Phase B C4 Near). This corresponds to a spread of 24% in the temperature rise from the nominal ambient of 19°C.

From the location of the thermocouples, it would be expected that there is some variation in the temperatures measured, e.g. thermocouples located closest to the inlet would be expected to measure lower than those nearer the outlet. Figure 74 shows the measured temperature of each thermocouple for varying flow rates. The spread in thermocouple temperature across the stator was more significant at low flow rates (i.e. below 1.5 or so) and gradually decrease as the flow rate increases.

On inspection of the measured results, there is no obvious and systematic logic to correlate location with measured thermocouple temperature. For example, Phase A-C5-Near is at a higher temperature than phase C-C3-Far despite being nearer the inlet.

This apparent lack of correlation may be a consequence of one or more of the following factors:

- The coils are manually wound and no two coils will be matched with any great precision.
- Flow imbalance due to various localised flow inhibitors, e.g. star-point connection and the interconnection between coils.
- Difference in volume of the voids at the inlet and outlet end-winding regions.

Although the above may contribute to some degree, the major difficulty in performing these measurements is that the localised temperature is likely to have a very high spatial gradient on a scale comparable with the sensing element of the thermocouple. As an example, there is likely to be a significant temperature difference between the flowing oil, which is close to the conductor surface, and the conductor surface. The exact location of the sensor element (on a scale of fractions of millimetres) will therefore have an effect on the temperature recorded, which may account for much of the variability between different thermocouples. These gradients will be much greater than the gradients present in a fully encapsulated coil where thermocouple measurements are far more representative of the entire local environment.

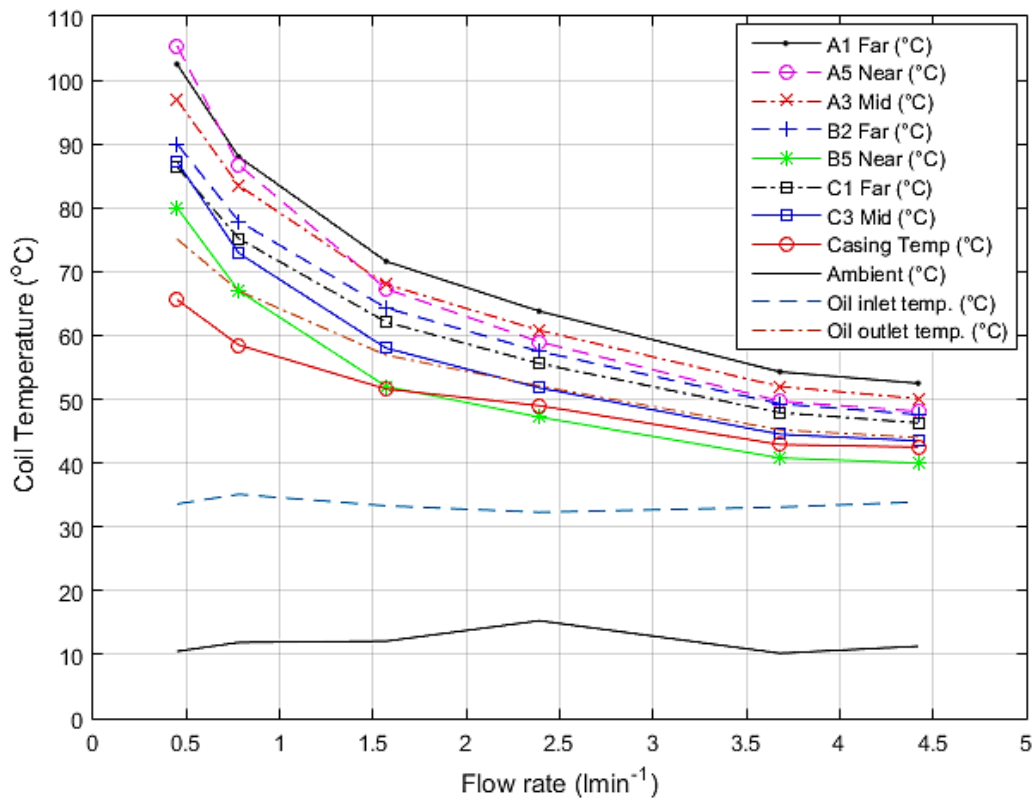


Figure 74 Coil temperature relative to flow rate at 8.9Amm⁻²

3.6.2 PREDICTION OF COIL TEMPERATURES AT HIGH CURRENT DENSITIES

Post processing analysis of the recorded temperature and flow rate measurements were carried out to predict the coil temperatures at a higher current density. An array of curve fitting techniques were used to derive equations for the curves, Figure 70 and Figure 71, the difference in maximum coil temperature and the oil inlet temperature as a function of flow rate. As mention above, there is a spread in the temperature rise of the coils measured and therefore the maximum was used as the worst-case value. Figure 75 shows the predicted temperature rise in the coil relative to the oil inlet temperature.

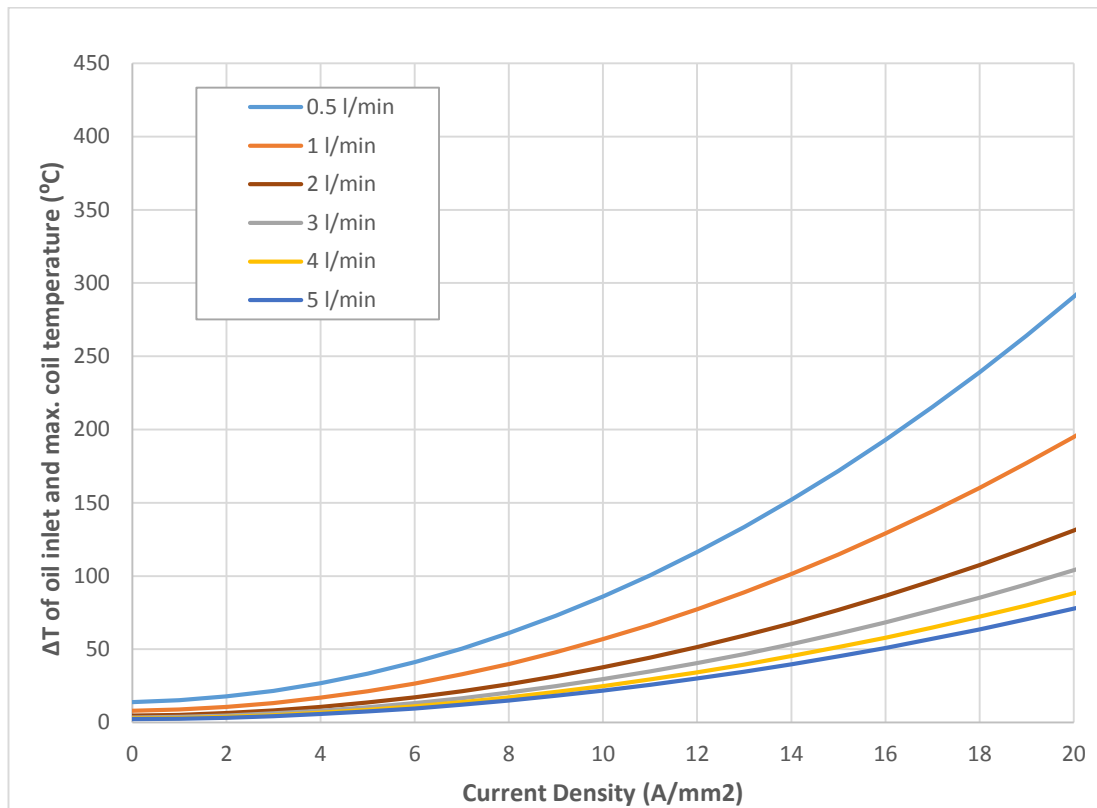


Figure 75 Predicted temperature difference of oil inlet and maximum coil as a function of current density for the prototype machine

Chapter 4 THERMAL CHARACTERISATION OF STATOR FLOOD COOLING METHOD

4.1 INTRODUCTION

High performance electrical machines which operate with current densities of $10\text{A}/\text{mm}^2$ or greater generally require some form of liquid-cooling to achieve sufficient levels of heat transfer to remove the heat generated by various components of losses. In high power density permanent magnet machines, the majority of these losses will be produced in the stator windings due to the characteristically high levels of RMS winding current. By way of example, at the rated 50kW operating point of the generator described in section 2.5.2, the copper losses comprise some 83% of the overall 1.4kW loss. As a consequence, liquid-cooling arrangements are primarily designed to extract losses from the stator coils in order to minimise localised temperature hot spots since such these often tend to be the limiting factor on achievable power density.

With regards to heating of the rotor, this can be caused by a combination of losses in the rotor itself or heat transferred from the stator. Losses in the magnets can be relatively high if preventative measures are not taken at the design stage, principally by segmenting the magnet pole. This was done in the design stage of the prototype as discussed in Chapter 3. Therefore, no additional cooling system was required for the rotor to maintain temperatures to sustainable levels.

There are several arrangements of liquid cooling and various strategies that have been investigated in literature. The most common approach of liquid cooling reported in literature is the use of a liquid-jacket [22-25]. This is effectively a liquid cooled heatsink integrated into the stator casing in close proximity to the outer

surface of the stator core. Liquid is circulated from one end, through a defined spiral path around the machine and exit at the other end. The liquid channels are optimised to maximise surface area in contact with the stator core. Some preliminary analysis was performed on this type of cooling for the reference generator design as previously described in section 2.6.1. This provides a straightforward means of confining the liquid and providing clear separation from the electrical parts of the machine, allowing the use of a wide range of liquids, e.g. water-glycol, oil etc. However, it does rely on conductive heat transfer across the winding and stator to the casing [23].

Refinements to this arrangement which allows the liquid to be in direct contact with the outer surface of the stator core is referred to as direct cooling [26]. Further improvements in the effectiveness of the cooling have been made to this approach by incorporating cooling channels in the back iron of the stator core as reported by [27]. However, this comes at a cost of reducing the flux carrying area of the stator core. This would not be feasible in the electromagnetic design proposed in chapter 2 because the back iron was, by design, thin and operating at its flux density limit.

A recently proposed strategy in literature, is to incorporate cooling channels within the slot between adjacent coils and at the top of the slot (close to the airgap) [28]. This provides a good approach for ensuring that the cooling medium passes close to the hottest regions of the coil. The channels are made of moulded thermoplastics produced by 3D printing. The authors report a significant improvement when compared to a conventional water-jacket cooling. However, the drawback of this type of cooling is that it significantly reduces the slot area available for the conductors and hence increases the current density.

In order to minimise the thermal resistance between the individual conductors and the coolant, thermally conductive potting compounds are often employed to fill voids within the coil, with typical thermal conductivities in the range of 0.2 - 0.6 W/m·K. Recent developments have resulted in new compounds with much higher thermal conductivity such as Durapot 865 and Thermoset SC-420 which have thermal conductivities of 1.7 and 3.2 W/m·K [29, 30] respectively. Increasing the thermal conductivities of potting materials is however achieved at the expense of diminishing other properties such as viscosity, temperature limit, durability and reduced dielectric strength. The analysis of the cooling-jacket in chapter 2 shows that this type of cooling is not adequate for this design at the rated power operating point.

The arrangement with cooling channels within the slot as shown in Figure 76 was investigated for this application. This approach was shown to be more effective but penalises the slot-fill factor which is undesirable as the current density increases.

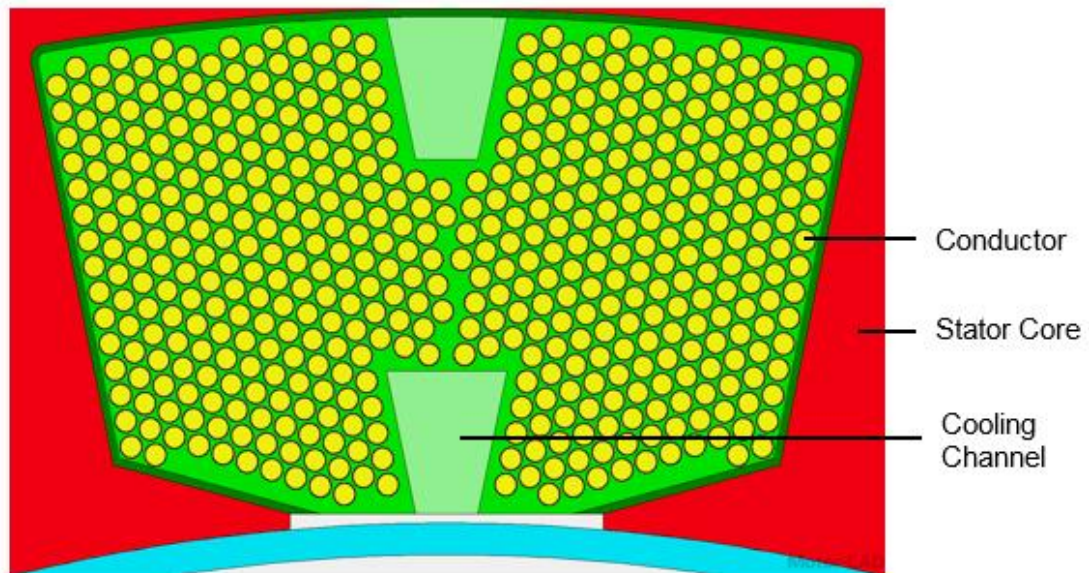


Figure 76 Liquid-cooling arrangement with cooling channels in the slot

Another approach reported in literature, is locating the coolant channels within the body of alternating teeth. It was reported that a 10% improvement in the cooling

performance in the slot region was achieved when compared with a standard cooling jacket [31]. The author also reported that the magnets were 50% cooler by flooding the airgap region with coolant. However, it was unsurprisingly noted that drag losses to the viscosity of the oil was a drawback, which could limit this latter approach to low-speed applications.

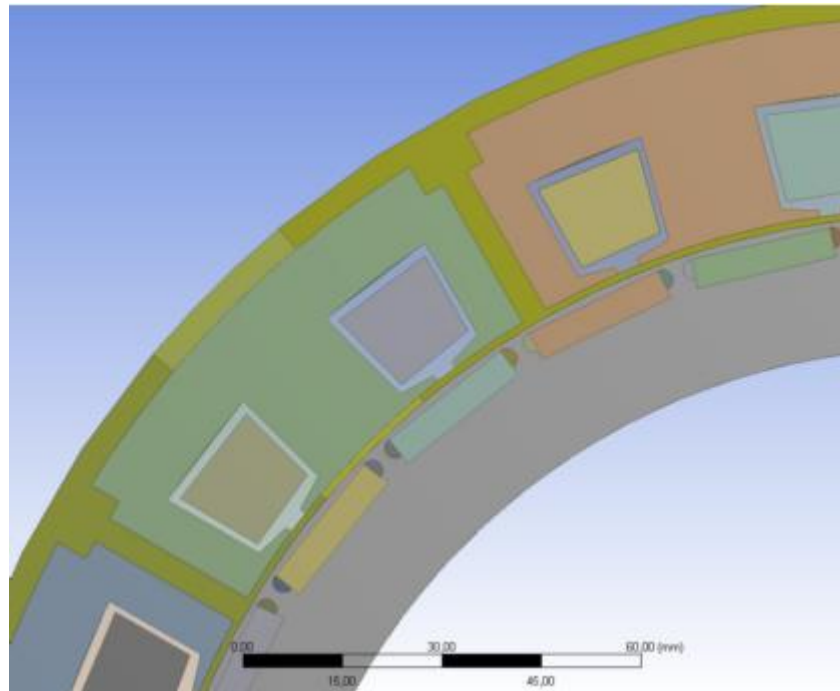


Figure 77 Cooling approach proposed by [31] with channels in alternating teeth and flooded airgap (yellow regions indicates fluid zone)

Spray-cooling of both the rotor and stator is common in high performance machine, and indeed it is the mainstream approach which is currently adopted in conventional wound-field aerospace generators [32, 33]. In this type of generator, it is necessary to both cool the stator coils and the rotor coils and rotating diodes. The oil spray is produced by an ‘oil-slinger’ on the rotor shaft.

In some machines, the individual solid conductors have sufficient cross-section enough to accommodate a cooling channel [34]. However, this approach is more suited to larger electrical machines on the MW scale with modest fundamental

frequencies rather than high frequency aerospace generators in the tens to hundreds of kW power range.

The liquid cooling approach that was adopted for this design, is to submerge the coils within a flow of coolant which passes through the stator from the non-drive end to the drive end. A brief analysis of the effectiveness of this type of cooling was described at the design stage in chapter 2 and a schematic of the arrangement is illustrated in Figure 39. The cooling channel was effectively the slot cross-sectional area remaining after achieving a coil packing factor of 0.5 and slot liner area. The end-winding are also subject to coolant flow. This type of arrangement is arguably the most effective type of liquid cooling in terms of maximising the direct surface contact between individual conductors and the coolant. However, when compared with the conventional approach of filling that unoccupied slot area with some form of potting or encapsulating compound, the mechanical performance of the coil may pose issues, particularly with vibration and abrasion of the insulation. The wire used for the coils has a double coat of polyamide-imide and polyesterimide, that is resistant to; chemicals, solvents and oil [35]. The drawback of directly exposing the coils to the coolant is that it limits the range of coolants that can be used, in particular it precludes the use of water/glycol.

4.2 ESTIMATION OF WINDING TEMPERATURES USING MOTOR-CAD

The geometry of an individual slot in the demonstrator machine is shown in Figure 16. The overall slot has a cross-sectional area of 348mm^2 and contains 490 conductors of 0.67mm diameter. This gives a net packing factor of 0.5. The heat transfer coefficients for this slot arrangement was calculated using the in-built functions in MOTOR-CAD which in turn are based on the correlation formulae

method proposed in [36] and by Schubert [22, 37]. The input parameters required for a given slot dimensions are the size and the number of conductors in the slot (which are assumed to be circular), ambient temperature, oil inlet temperature, volume flow rate, specific heat capacity, thermal conductivity, density, kinematic and dynamic viscosity and Prandtl number.

The total surface area of the conductors, stator tooth and stator slot bottom were 0.843, 0.012 and 0.016 m² respectively. The relative magnitudes of these surface areas demonstrate the potential for achieving very effective heat transfer from the coil by exposing the entire conductor surface area to the coolant as distinct from a small surface area with a coolant. Figure 78 shows the variation in the resulting calculated heat transfer coefficient as a function of flow rate for the demonstrator slot. The external surface of the casing was assigned a heat transfer coefficient of 6 W/m²·K, a value which is representative of natural convection.

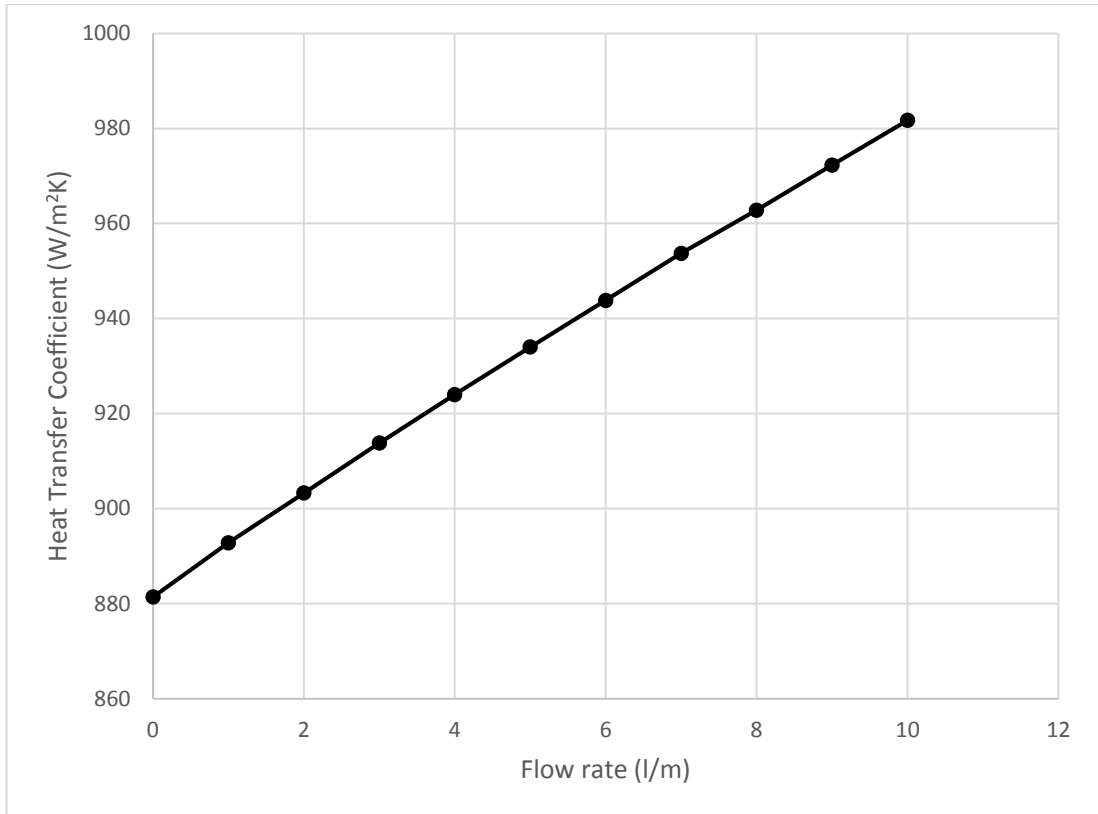


Figure 78 Calculated variation in HTC as a function of flow rate for the reference slot with a packing factor of 0.5 (490 conductors of 0.67mm diameter)

The fluid properties of the coolant used are summarised in

Table 10. The inlet temperature of the coolant was assumed to be at an ambient temperature of 25°C. The coolant was modelled as entering from the non-drive end and exiting at the drive end. This arrangement was selected on the basis that the non-drive end would have higher copper loss because of the contribution from the interconnections between individual coils and the start-point.

Table 15 Fluid properties of the oil

Properties	Value
Thermal conductivity	0.149
Density	986.9
Specific heat capacity	1926
Kinematic Viscosity	3.918e-5
Dynamic Viscosity	0.03867
Prandtl Number	499.8

In order to obtain a direct comparison with the experimental results, a specific operating point was simulated with a flow rate of 1.37l/min and copper losses of 1000W. The resulting predicted temperatures at locations within cross-sections of the machine are shown in Figure 79. The maximum winding temperature, which is predicted to occur, was 70.3°C in the end-windings with an average winding temperature of 63.3°C.

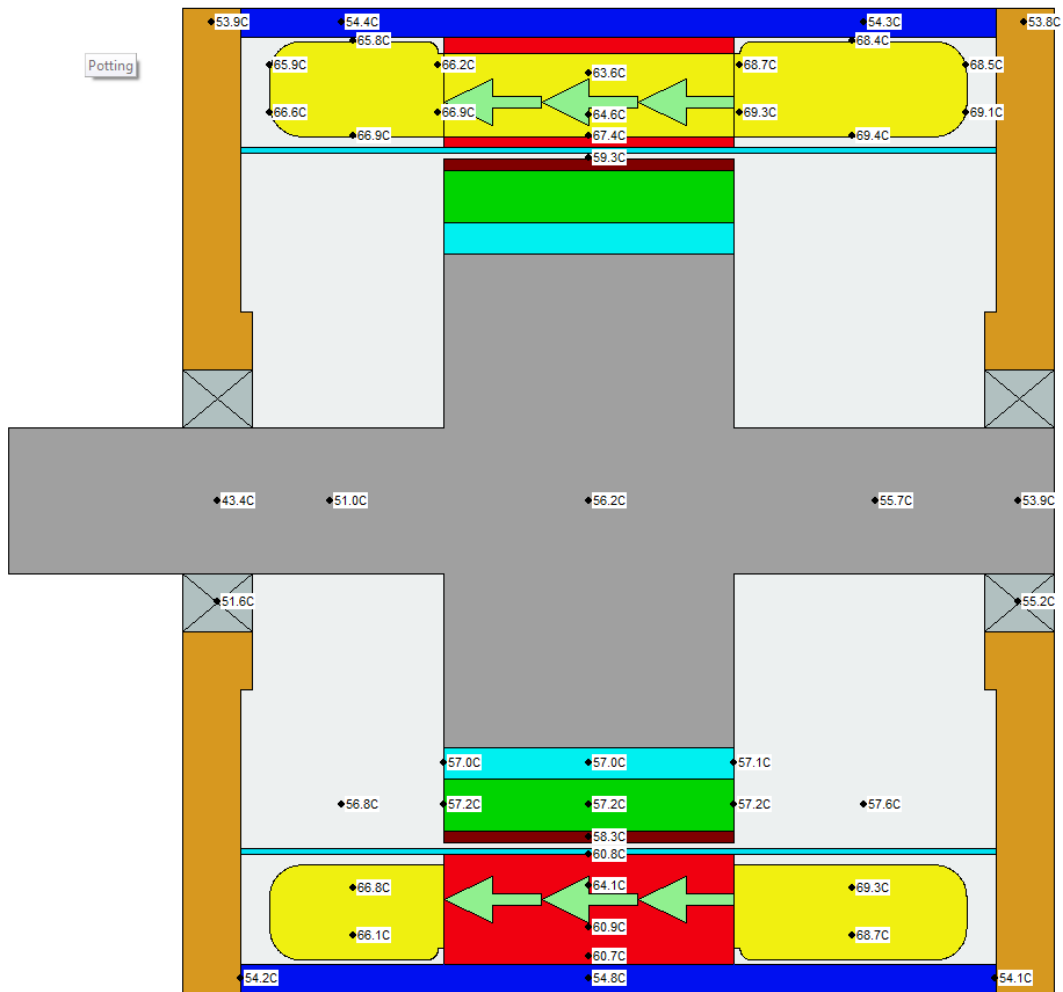


Figure 79 Temperatures across the machine at 1000W of copper loss only and a flow rate of 1.37l/min

4.3 THERMAL TESTING USING DC EXCITATION

A series of thermal measurements were described in detail in Chapter 3 with the machine operating at a series of load points. However, the exact overall losses present in the machine at these operating points had a degree of uncertainty, caused largely by the contribution of losses which are complex to quantify experimentally, viz. mechanical windage losses, bearing losses, core losses, and winding eddy-current losses.

In order to provide a more controlled loss in the machine for thermal characterisation, a series of further thermal experiments were performed with machine at standstill and with the windings supplied with precisely controlled DC

current. Under these conditions, the copper loss can be readily established to a high degree of precision by straightforward measurement of DC current and voltage. With this accurate measure of the overall losses, the thermal performance of the flooded stator design can be more accurately assessed.

The proportion of copper losses removed by the oil coolant can be established from the temperature rise in the oil at a given mass flow rate. This assessment of the effectiveness does not rely on the array of thermocouples in the winding.

Since the star-point was terminated inside the machine, it was not possible to independently set and control the current in the individual phases. The star connection requires that the controlled DC current passes through two phases at any given time. To ensure equal copper losses in each phase, the pairs of phases through which current flows were periodically rotated in sequence using a series of high current relays controlled by a programmable Arduino controller. Figure 80 shows the switching relay rig with four contactors and connections. These four contactors allow current to be cycled through all three possible combinations of phase pairs, i.e. A-B, A-C, and B-C.

The rate at which the current is cycled through the phase combinations is at a compromise because of low switching frequency rating of the contactors and the thermal time constant of the machine.

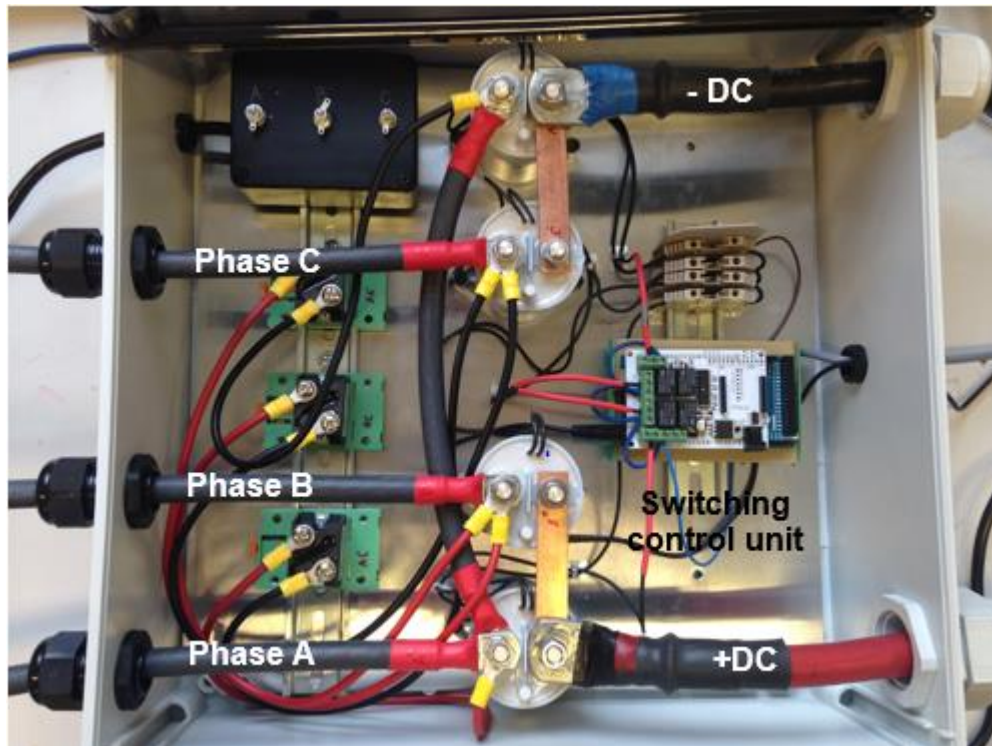


Figure 80 DC current switching rig

The motor was positioned in an upright orientation on a small wooden stand as shown in Figure 81. An additional flow-rate sensor was introduced into the oil system (recalling that previous on-load machine oil flow rates were measured by a sensor in the ASTRAEA test-rig). This was calibrated in-situ using a weighing scales and a timer.



Figure 81 Prototype machine during testing

4.4 EXPERIMENTAL RESULTS

Tests were carried out at a combination of 7 different oil flow rates and DC current levels. Figure 82 shows typical winding temperatures measurements, the specific case being for a DC supply of 200A and an oil flow rate of 2 l/min with current cycled between phases every 10 seconds. It is interesting to note that even with 10s cycling, there is a reasonable degree of ripple in the measured temperatures of the thermocouples as they respond rapidly to the change in localised power dissipation.

The results from 7 different tests (designated as T1 to T7) are summarised in Table 16. In all case, the measured DC voltage shown in Table 16 is the value when steady-state temperature was achieved. Steady-state temperature was met when there was less than 1°C rise over a 300s period. The temperature was taken as the average over the last few cycles.

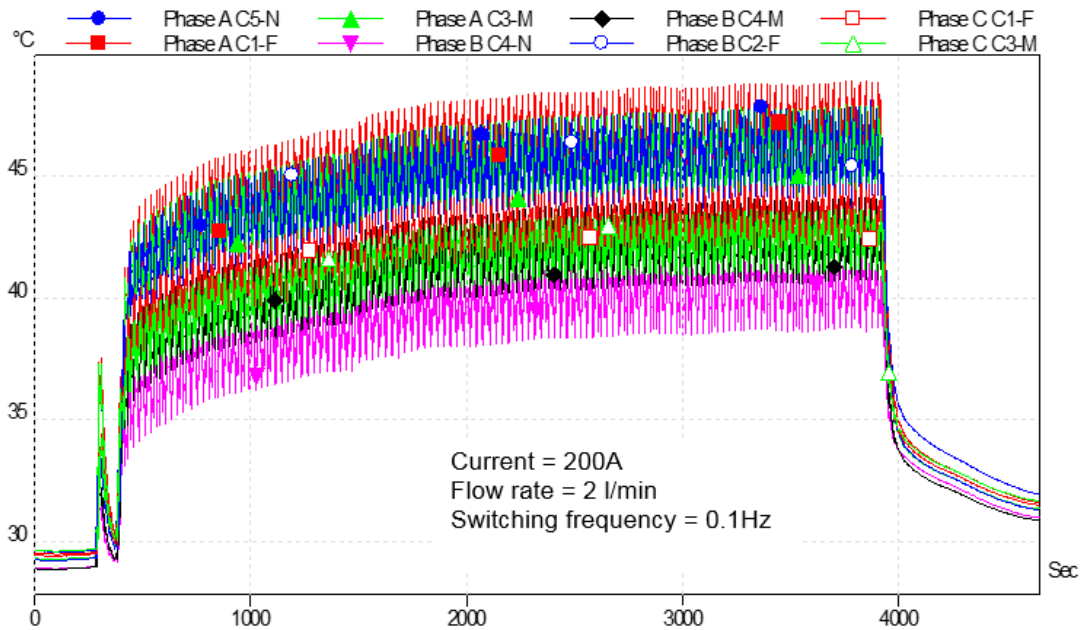


Figure 82 Winding temperatures with switching every 10s

Table 16 Experimental results for various currents and flow rates

	Test reference number						
	T1	T2	T3	T4	T5	T6	T7
DC Current (A)	100	200	100	200	100	200	300
DC Voltage (V)	1.00	2.06	1.00	2.05	0.99	2.03	3.33
Coil Losses (W)	100	412	100	410	99	407	999
Flow rate (l/min)	1.95	2.13	3.04	3.03	3.96	4.01	1.02
Oil inlet temperature (°C)	27.40	31.35	27.96	31.25	27.62	30.25	35.64
Oil outlet temperature (°C)	27.84	36.04	28.72	34.67	28.26	33.03	51.46
Oil ΔT (°C)	0.49	4.69	0.76	3.42	0.64	2.79	15.82
Max. Winding temp. (°C)	29.10	43.34	30.72	41.97	30.20	39.41	74.77

The measured temperature rise in the oil can be compared with the value obtained by assuming that all the losses were removed by the oil coolant. For the idealised case in which no loss leaves the machine through other means (e.g. via conduction and convection through the casing) then the temperature rise between inlet and outlet under steady-state conditions is given by:

$$\Delta T = \frac{q}{C_p \times \dot{m}} \quad (10)$$

The specific heat capacity of the Aeroshell oil used in the testing is temperature dependant as shown in Table 17. As will be apparent there is a difference of some 32% over a 0-145 °C temperature range. This was accounted for in the calculation of the temperature rise using equation 10.

The resulting predictions of temperature rise in the oil from equation 10 for the 7 test-points (T1-T7) are shown in Table 18. As would be expected, the calculated temperature rise is greater than that measured using equation (10) in all cases. Typically, these comparisons indicated that some 75% of the losses are removed directly by the oil coolant into the external heat exchanger with the remainder being dissipated from the casing (which could include transfer to the end-plates and tubular section of the casing via the oil).

Table 17 Specific heat capacity of Aeroshell turbine oil 3 for varying temperature at a density of 875 kg/m³ at 15°C – supplied by Shell Corporation

Temperature (°C)	Specific heat capacity (kJ/kg.K)	Temperature (°C)	Specific heat capacity (kJ/kg.K)
0	1.928	75	2.251
5	1.949	80	2.272
10	1.971	85	2.294
15	1.992	90	2.315
20	2.014	95	2.337
25	2.035	100	2.358
30	2.057	105	2.380
35	2.078	110	2.401
40	2.100	115	2.423
45	2.121	120	2.445
50	2.143	125	2.466
55	2.164	130	2.488
60	2.186	135	2.509
65	2.208	140	2.531
70	2.229	145	2.552

Table 18 Comparison of measured difference in outlet and inlet temperature and value calculated assuming that all the losses are removed by the oil

Test point	Mass flow rate (kg/s)	Specific heat (J/kg·K)	Losses (W)	Measured ΔT ($^{\circ}\text{C}$)	Calculated ΔT ($^{\circ}\text{C}$)
T1	1.71	2040	100	0.49	1.36
T2	1.86	2080	412	4.69	5.11
T3	2.66	2040	100	0.76	0.97
T4	2.65	2075	410	3.42	3.93
T5	3.68	2040	98.9	0.64	0.79
T6	3.69	2060	407	2.79	3.21
T7	1.37	2251	999	15.8	19.4

The first set of results showed a large margin of error and therefore a systematic check was carried out to verify the flow rate sensor readings. A calibrated sensor was installed in series to measure the actual flow rate. The findings show a mismatch in readings at the lower end of the range, which gradually converge as the flow rate increased. Figure 83 shows a plot of the actual flow rate against the old sensor measurements.

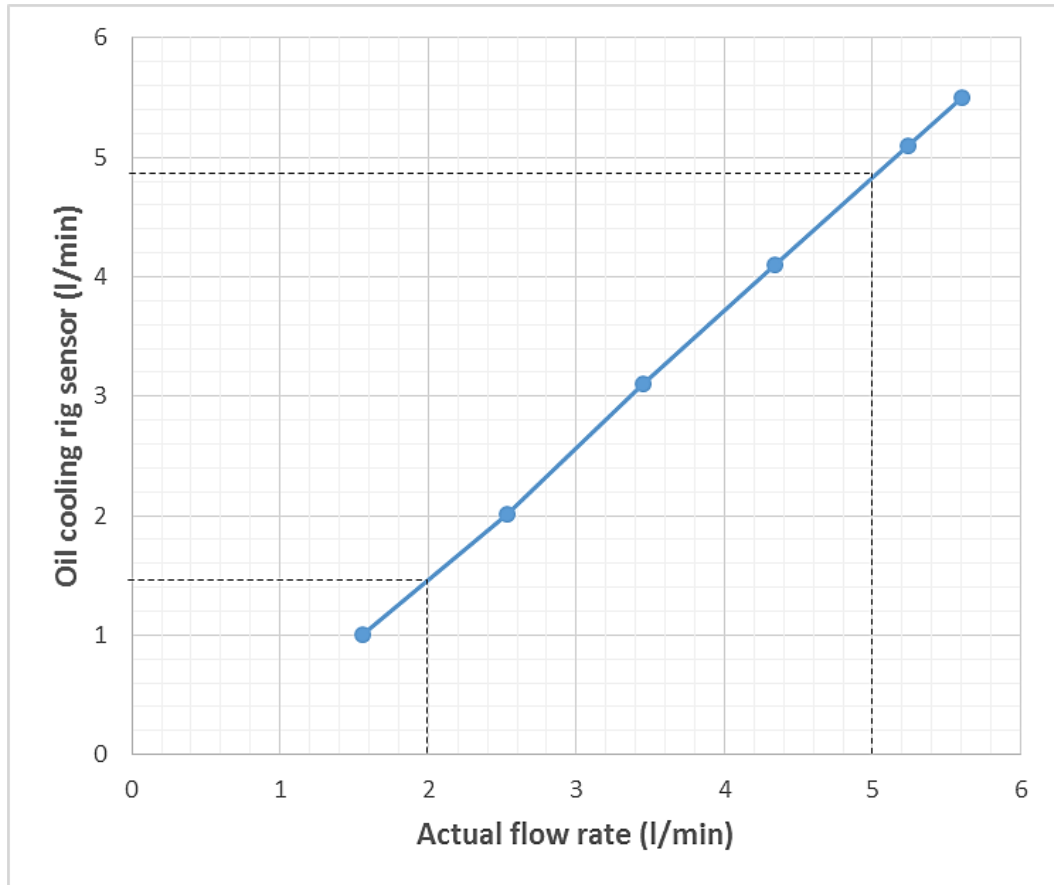


Figure 83 Verification of measured oil flow rate

4.5 COMPARISON OF EXPERIMENTAL AND PREDICTED TEMPERATURES

The results of test run no. 7 (T7) in Table 16 were used as a basis for verifying predictions from the Motor-CAD model. The model was simulated with the equivalent copper loss, flow rate, oil inlet and ambient temperature, and fluid properties of test run 7 (T7). Table 19 shows a comparison of the measured and predicted winding temperatures, in which the measured maximum corresponds to the highest temperature measured by any of the 7 thermocouples while the average measured coil temperature corresponds to 67°C.

Table 19 Comparison of predicted and measured temperatures for T7

Temperature	Predicted by MOTOR-CAD model	Measured
Max. Winding temperature (°C)	84.5	74.5
Average winding (°C)	78.1	66.9

There is some uncertainty to whether the thermocouples buried within the coils are measuring true copper temperature or the oil flow within the localised region. The temperature gradient over a small area can be large due to the dependency on the localised flow rate.

The change in coil resistance from a reference measurement taken at a known temperature provides an independent method for inferring the average coil temperature. For this purpose, the temperature coefficient of resistance for annealed copper of $0.0039\text{ }^{\circ}\text{C}^{-1}$ was used. The line-to-line resistance was derived from measurements of DC current and DC voltage, which were made to 3 significant figures. With a temperature coefficient of resistance of $0.0039\text{ }^{\circ}\text{C}^{-1}$, then the average temperature of the coil cannot be resolved below a resolution of $\pm 1.25^{\circ}\text{C}$, i.e. $0.005/0.0039$. Using Equation (6) and the values summarised in Table 20, the inferred average coil temperature was $59^{\circ}\text{C} \pm 1.25^{\circ}\text{C}$, which is in reasonable agreement with the value of 67°C inferred previously in Table 19 from the average of the thermocouple measurements.

Table 20 Summary of the values used to estimate the average winding temperatures from resistance (using T7 measurements)

Parameters	Values
Voltage at the terminals (V)	3.33 V
DC Current (A)	300 A
Resistance – calculated from measured current and voltage (Ω)	0.0111
Resistance measured at 20°C (Ω)	0.0096
Temperature coefficient of resistance (°C)	0.0039
ΔT – Calculated using Equation (6) (°C)	39.4
Average winding temperature (°C)	59 \pm 1.25°C

4.6 CONCLUSIONS

The liquid jacket, in-slot channel and flooded stator cooling approach were evaluated using Motor-CAD. The liquid-jacket and in-slot channel cooling were shown through these calculations to be insufficient in terms of maintaining localised peak coil temperatures below 200°C. The flooded stator approach proved very effective and provided adequate headroom to redesign a smaller machine for the same power requirements.

Chapter 5 COMPARATIVE ANALYSIS OF COPPER AND ALUMINUM WINDINGS FOR HIGH POWER DENSITY ELECTRICAL MACHINES

5.1 INTRODUCTION

Copper is by far the most widely used material for electrical machine winding conductors due to its high electrical conductivity. The only other material, which is sometime used, is Aluminum. Copper has an electrical conductivity that is 1.6 times greater than Aluminium. However, Aluminium only has a density of 2700 kg/m^3 as compared to 8900 kg/m^3 for Copper. Hence, Aluminum has a significantly higher specific conductivity than copper, with values of $12963 \text{ Sm}^{-1}/\text{kg}$ and $6517 \text{ Sm}^{-1}/\text{kg}$ respectively.

The prototype machine design described in chapters 2 and 3 was tailored to the requirements of an uncontrolled diode bridge rectifier and the resulting design has very small cross-sections of core with large slot areas. This was a result of the optimization to minimize the inductance as explained in more detail in chapter 2. Therefore, the majority of the stator mass and the machine as a whole was dominated by the weight of the conductors. For this reason, aluminum becomes attractive in this particular application where minimising weight is important. This chapter investigates the tradeoff between increased electrical resistance and weight savings to enhance the power density.

5.2 ALUMINUM AND COPPER CONDUCTORS

Although Aluminum is occasionally considered as an option to copper, in low cost, low performance motors [38], copper has remained by far the most popular selection for high performance machines. This is due to thermal management considerations

as copper produces less loss per unit volume of stator winding. Aluminum has also been explored as an alternative to reducing the AC winding loss where this is an issue at high frequencies [39, 40].

The disadvantages of Aluminum conductors in electrical machines are the lower electrical conductivity, higher thermal expansion and a more complex termination requirement. However, Aluminum has several advantages when compared with copper in electrical machines:

- More than 300% lighter than copper – This is attractive in applications where mass is critical.
- ~25-40% the cost of copper per unit volume.
- Double the thermal heat capacity of copper – This is important for transient overload conditions.

The authors of [41] has shown that a direct substitution of copper with aluminum while maintaining the same resistivity of the coil does not show improvement in weight savings. The study carried out in [41] was carried out using a more conventional design where the mass of the stator annular is dominated by the core.

Table 21 shows a comparison of the key material properties of Al and Cu. One of the major issues surrounding aluminum conductors was the integrity of the terminations

Table 21 Key material properties of copper and aluminum

Properties	Copper	Aluminium
Density (kg/m ³)	8900	2700
Resistivity ($\Omega/m \times 10^{-8}$)	1.72	2.83
Temperature coeff. (/°C)	0.0039	0.0043
Specific heat capacity (J/kg.K)	385	913
Thermal expansion coefficient	16.6	22

5.2.1 OXIDATION OF ALUMINIUM CONDUCTORS

Aluminum oxidises readily in air at room temperature and forms an electrically insulating oxide layer on exposed surfaces. This can significantly increase the localised resistance of any contacts between coils and terminations posts / connectors, which could lead to excessive localised heating. However, new techniques are emerging to terminate Aluminum conductors reliably, with two of the most promising being ultrasonic welding and cold pressure-welding [42] .

Although the uncontrolled oxidation of Aluminium is a problem in terms of terminations, there is considerable research and development directed at utilising precisely controlled oxidation to form a reliable and repeatable insulation layer. Although only capable of withstanding modest turn to turn voltages (typically 9.1-17.7 kV), this can be adequate for many machine applications and has the advantage of having high temperature capability. As an example, ANOFOL, has produced anodised aluminium strip coils that can operate up to 500 °C using the aluminium oxide insulation [42] with a typical breakdown voltage of up to 20kV. Another advantage of Aluminium oxide as an insulator is that it has a higher thermal conductivity than a polymer insulation such as polyesterimide, with typical values of ranging 16.6 - 36 and 0.15 - 0.5 W/m·K respectively [43].

5.3 MACHINE DESIGN OPTIONS USING ALUMINUM WINDINGS

Directly substituting copper conductors with aluminum windings has several implications to the design of the machine. The method in which these implications are dealt with or utilized can vary depending on the application and the design objective. There are two design choices that are available based on the application:

The copper and aluminum variant can be designed to have an equivalent resistance. This would require the aluminium variant to increase the volume of the slot area. Consequently, this increases the stator outer diameter and as a result, the stator core cross-sections.

This option would be necessary where efficiency is a vital design objective and will not be beneficial where both efficiency and volume are both constrained.

There is also the option of maintaining constant mass in both the copper and aluminum design. The weight saved by the aluminium variant can be redistributed to increase the performance and hence, power density. This option will be investigated to increase the power density of the prototype design.

There are two methods in which the active mass can be redistributed; by increasing the stator bore and outer diameter or by increasing the axial length. A trade study was carried out to investigate which approach is more beneficial for the prototype design.

5.3.1 AL DESIGN WITH INCREASED AXIAL LENGTH TO MAINTAIN EQUIVALENT MASS

An audit of the active mass of the prototype machine is shown in Figure 84. As is apparent, in this design, the windings accounts for large proportion of the active mass in comparison to many machine designs, due to a combination of employing Cobalt Iron and operating the core well into saturation in order to maximize power density (as discussed in detail in section 2.2).

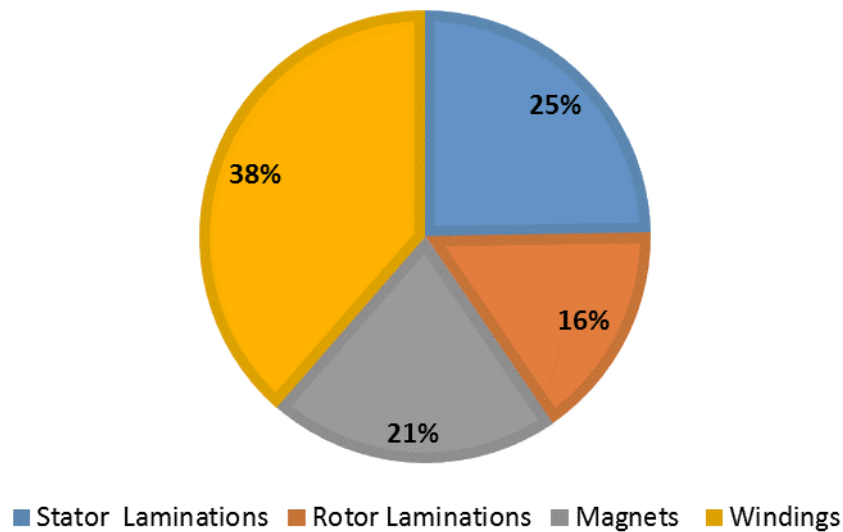


Figure 84 Proportions of the active mass component of the prototype

A simple direct substitution of Copper with Aluminum winding with all dimensions remaining fixed would reduce the mass of the winding by 70% and the overall mass by 27%. However, this would result in an increase in the ohmic losses in the winding by a factor of at least 54%. If the increased temperature rise were accounted for, then this would increase by an even higher factor.

An alternative substitution strategy is to replace the winding and increase the axial length of the stator core and rotor to yield the same overall mass as the original baseline Copper design. However, in order to do this consistently, the various contributions to the winding mass must be separated out as they scale differently with the stator core length. Furthermore, an increase in axial length of stator core

will result in a proportionate increase in the back EMF per turn. In this application, the open-circuit voltage produced by an extended axial length machine with the same number of turns would exceed the limit of 270V DC input to the DC-DC converter. The increase in axial length will therefore require an adjustment in the number of turns to remain within the 270V DC limit. A reduced number of turns offers the scope to increase the cross-sectional area of each individual turn if the same coil packing factor is to be achieved. Again, it is necessary to separate out the various contributions to the winding mass to establish the effect of changing the number of turns. Table 22 summarises the scaling factors of the mass and resistance of the various winding components with axial length and the number of turns.

Table 22 Scaling factors of the mass and resistance of the winding components with axial length and the number of turns

Component of winding	Scaling factor with stator core axial length		Scaling factor with number of stator turns (N_t)*	
	Mass	Resistance	Mass	Resistance
Section contained within stator slots	$\propto \frac{1}{L_{ax}}$	$\propto \frac{1}{L_{ax}}$	Remains fixed	$\propto \frac{1}{N^2}$
End sections of individual coils	Remains constant	Remains constant	Remains fixed	$\propto \frac{1}{N^2}$
Interconnects between coils	Remains constant	Remains Constant	$\propto \frac{1}{N}$	$\propto \frac{1}{N}$

* assumes cross-sectional area of each turn is adjusted to maintain the same coil packing factor

In order to scale the axial length to give the same overall machine mass, it is necessary to account for the various contributions from different sections of the windings. Let the proportions of the overall winding volume (and mass) contributed by the sections in the stator slots, end sections of each coil and the interconnects be k_{ss} , k_{ew} and k_{int} respectively. The axial length of the stator core in an Aluminium

design, which yields the same overall active machine mass as its copper counterpart, is given by:

$$L_{ax} = \frac{V_{cu}\delta_{cu}(k_{ss} + k_{ew} + k_{int}) + m_{mag} - V_{Cu}\delta_{Al}(k_{ew} + k_{int})}{\left(\frac{V_{Cu}\delta_{Al}k_{ss}}{L_{Cu}} + \frac{m_{mag}}{L_{Cu}}\right)} \quad (11)$$

The original Copper design has k_{ss} , k_{ew} and k_{int} values of 0.65, 0.24 and 0.11 respectively. Using these values, this approach to scaling the axial length results in the axial length of the stator core increasing from 50mm to 69mm to yield the same mass. It is recognised that this increase in stator core length would also increase the mass of the casing. This could be incorporated into the analysis by simply reflecting the casing mass in the quantity m_{mag} .

The mass audits for the original baseline Copper design and two Aluminium designs are shown in Table 23.

Table 23 Audit of the active mass components of the Cu and Al winding designs. All masses shown are in Kg

Component	Copper	Aluminium – maintaining the same core axial length	Aluminium – same overall active mass as the copper design
Axial length	50mm	50mm	69mm
Stator laminations	1.18	1.18	1.64
Rotor Laminations	0.75	0.75	1.04
Magnets	1.00	1.00	1.39
Windings	1.84	0.56	0.70
Total	4.77	3.49	4.77

5.4 PERFORMANCE OF ALUMINUM VERSUS COPPER WINDING DESIGN

As noted previously, increasing the axial length of the stator core will proportionally increase the flux-linkage per turn. This will require a reduction in the number of

series turns per coil in order to maintain the same output voltage under a prescribed set of conditions. However, as is the case in the baseline generator design considered in this thesis, the number of series turns per coil is low and hence only coarse adjustments can be made.

To explore the scope for adjusting the turns, a series of time-stepped, circuit coupled FE solutions was performed for three variations of the scaled axial length Al design with 5,4 and 3 series turns per coil. If the same coil, packing factor is retained then, as shown previously in Table 22, the resistance scales as $1/N^2$.

Table 24 Key parameters of alternative generator designs

	Prototype	Aluminium – maintaining the same core axial length	Aluminium – Same overall active mass as the copper design		
			5 turn	4 turn	3 turn
Design reference number	1	2	3	4	5
Winding	Cu	Al	Al	Al	Al
Stator core axial length (mm)	50	50	69.4	69.4	69.4
Overall machine active mass (kg)	4.77	3.49	4.77	4.77	4.77
No. of turns	5	5	5	4	3
Resistance at 22 ^o C (mΩ)	4.74	7.80	9.77	6.25	3.52

Figure 85 shows the FE predicted current-voltage characteristic of the four Aluminium designs alongside the original Copper based prototype. For the Aluminium design that retains 5 turns, the no-load DC output voltage increased from 238V to 327V due to the increase in axial length. Design 1 and 5 approached the

50kW operating point at an equivalent current loading but D5 was at a much lower no-load DC output voltage.

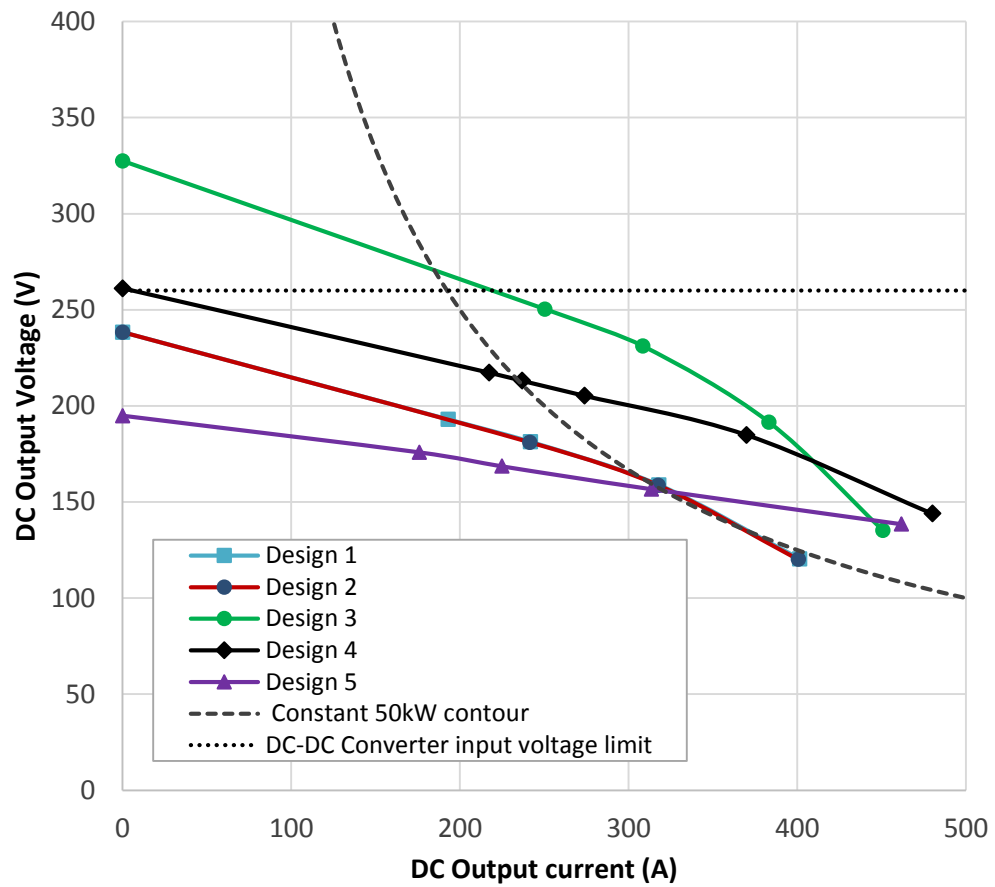


Figure 85 Simulated Current-Voltage characteristics of the various designs shown in Table 24

Table 25 summarises the performance of the five designs at the rated operating point of 50kW. The winding RMS current required by design 3 and design 4 to produce 50kW is much lower than the prototype because the magnitude of the back-EMF is larger.

Table 25 Performance comparison of designs 1 to 4 with the prototype at the rated 50kW operating point

	Design 1	Design 2	Design 3	Design 4	Design 5
No. of turns	5	5	5	4	3
Axial length	50.00	50	69.4	69.4	69.4
DC Voltage (V)	158	158	270.6	213.0	155.8
DC Current (A)	318	318	186.6	237.0	321.2
Winding Current (A_{rms})	237	236	145.0	183.0	247.3
Output Power (kW)	50.4	50.4	50.50	50.48	50.03
Ohmic losses at 22°C (W)	799	1303	615	628	645
Overall Active mass (kg)	4.77	4.77	4.77	4.77	4.77

5.5 CONCLUSIONS

Due to the mass distribution of the active components of the 50kW surface mounted PMSM prototype generator machine and its application, the use of Al coils has been investigated. There are two approaches to the electromagnetic design when substituting Aluminium with Copper winding. The first approach is to increase the slot area to maintain an equivalent value of resistance and the second approach is to maintain an equivalent mass whilst increasing the electromagnetic performance by increasing the axial length or stator bore diameter.

An Aluminium winding has the potential to improve the power density of machine designs, particularly machines that are constrained by an electromagnetic power limit rather than a thermal limit. Whether any benefits are derived, depends on the mass distribution of the active components and the objectives of the design. The prototype studied in this thesis is an example of a design, which can benefit from Aluminium coils because of its mass distribution and power density is the key design objective.

Chapter 6 NOVEL COIL WINDING METHODOLOGY USING ADDITIVE MANUFACTURING

6.1 INTRODUCTION

One of the main limiting factors on performance in high power electrical machines is the packing factor that can be achieved in the stator slots. As discussed in chapter 2, the packing factor is defined in this thesis as the fraction of the available slot cross-sectional area which is occupied by copper. Increasing the packing factor both reduces the loss generated to produce a given Ampere-turns in the slot and increases the effective cross-slot thermal conductivity. Hence, technologies that can increase the packing factor beyond the 50-60%, which cannot be achieved with coils wound with circular conductors, offer a route to further increases in power density.

Additive manufacturing (AM) is a manufacturing process which has the potential to enable innovative concepts for electrical machines windings, in terms of both electrical and thermal performance. AM covers a wide range of different processes which are classified according to the material, method of deposition and the heat source. For additive manufacturing of metals, selective laser melting (SLM) and electron beam melting (EBM) are the most established processes. Both methods are powder bed systems, in which a fine powder layer with a controlled thickness of 40-80 μ m is spread across the build area. The heat source, electron beam or laser, selectively melts localised regions of the powder to produce the desired geometry. This process is repeated layer by layer to build up a three-dimensional part. At present, SLM is the more widely used technology, particularly for cobalt chrome, stainless steel, aluminium and Titanium alloys, which are in high demand.

Whereas AM of Aluminium, Stainless Steel and Titanium is well developed and now a mainstream manufacturing process in high value product, AM of Copper is less well developed in part because of technical difficulties and the absence of potential applications. Due to the combination of its high melting point, high thermal conductivity and the optical reflectivity, EBM was identified as being more suitable for copper. Indeed, the very limited literature on AM of copper illustrates the limitations of SLM for Copper. EBM has a higher power capability and is does not suffer from difficulties with the optical reflectivity of copper. Therefore, higher power densities can be concentrated in the powder.

This chapter describes the AM process in the context of the requirements for AM copper coils for electrical machines. The research reported in this chapter, was performed using an existing EBM system at the Mercury Centre in the Department of Materials Science and Engineering in Sheffield, with the assistance and active involvement of Professor Ian Todd and his research team.

6.2 NOVEL COIL FEATURES ENABLED BY ADDITIVE MANUFACTURING

Additive manufacturing (AM) offers scope to incorporate far more intricate and novel geometrical features into a coil than traditional windings, which in turn may give rise to many opportunities to enhance coil performance.

In particular, AM offers the potential to exercise precise control over the localised geometry of the conductor at all points in the coil. This contrasts with a wound coil in which the cross-section remains fixed throughout the coil. Providing various practical challenges can be overcome, notably the ability to produce essentially fully dense copper of comparable electrical conductivity to the IACS standard, then this

degree of design freedom can be exploited to enhance several aspects of the performance of coils.

Arguably, the most significant factor in determining the performance of a coil is the packing factor that can be realised in the final device. The packing factor is the fraction of the overall coil cross-section which consists of the copper conductor, as distinct from the insulation layers, encapsulant and gaps between adjacent conductors. In a coil wound with circular cross-sectioned wire, packing factor can range from 30% in random wound coils in machine slots through to ~65% or so in precision wound solenoid coils. In high performance electrical machines wound with circular wire, it is often assumed at the design stage that some 45-50% of the overall slot area will consist of copper. The packing factor increases in coils wound with rectangular section wire, particularly in pre-formed coils wound ex-situ. This type of coil construction tends to be employed in large electrical machines. From the standpoint of AM, it is likely that packing factors of at least 65-70% would be required to be competitive with coils wound with rectangular section conductors.

AM offers the scope for exercising much greater flexibility on the geometry of the individual turns that make up the coil. In considering the scope for innovations and performance enhancements by employing AM to produce solid coils, it is useful to consider the regions of the coil which sit within the stator core separately from those regions which are commonly referred to as end-windings.

The overall cross-sectional area available within a stator slot is constrained by the dimensions of the stator core. The design of an electrical machine involves the careful apportioning of the stator volume between the core and the coil so as to meet some design objective, e.g. minimise loss, maximum power density. In a

conventional wound coil, either with circular or rectangular section wire, the current density in each successive series turn remains the same throughout the coil (it is recognised that paralleling of strands may give rise to some non-uniform distribution across those conductors that constitute one series turn). However, the effective thermal resistance from localised regions within the coil to the main heat sinking medium may well vary markedly across the coil cross-section due to the relatively modest thermal conductivity across the coil. This in turn can give rise to large temperature gradients within the coil. This thermal gradient is exacerbated by the positive temperature coefficient of resistance of copper ($\sim 0.4\%$ per $^{\circ}\text{C}$) as the hotter regions of the coil produce more loss for the same current density. If the machine power density was limited by a peak hot-spot winding temperature of say 200°C , then a significant fraction of the coil will be under-utilised, with considerable residual margin on operating temperature.

As well as under-utilisation of the coil, temperature gradients throughout the coil will give rise to differential thermal expansion. This is likely to be of little consequence in coils with polymeric insulation, but it could well be more problematic in high temperature coils in which significantly less compliant insulation systems based on ceramics are used.

By careful design of an AM coil, which would include a detailed consideration of the particular cooling mechanisms employed in the machine, it would be possible in most cases to achieve a near iso-thermal temperature throughout the entire coil, although that this may be somewhat specific to a range of operating points. This would be achieved by dividing the overall slot cross-section in proportions which reflects the relative difficulty of removing heat from different regions of the coil. An example coil based on exploiting this design freedom is shown in Figure 86. The coil

cross-section in Figure 87a comprises 16 turns, each 3.9x3.9mm with 0.05mm insulation thickness around each conductor, giving a net cross-sectional area of each turn of 15.2mm² at a packing factor of 0.92. The coil section shown in Figure 87b has the same overall cross-section with the same insulation thickness but has conductor cross-sections which range from 12.87mm² (3.3x3.9mm) to 20.25mm² (4.5x4.5mm). In a machine in which the majority of the loss generated in the coil passes into the stator core, it is likely that the largest cross-sectional area turns, which is located in the upper right hand corner of the coil shown, would sit furthest from the stator core, i.e. at centre of the slot nearest the working airgap. The smallest cross-sectional turn in the lower left corner would sit in the corner where the tooth body meet the stator core-back.

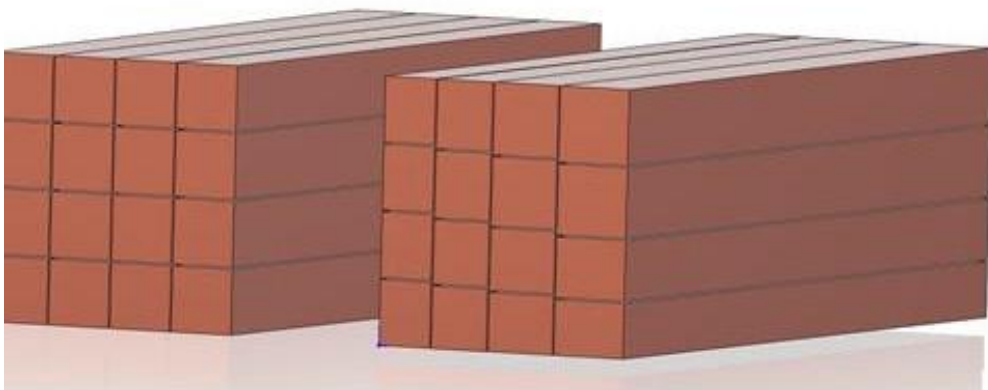
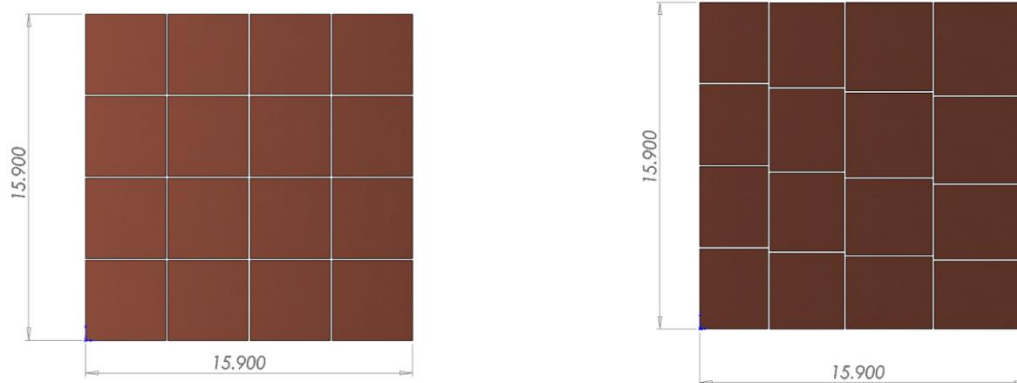


Figure 86 Model of AM Coils within the active region of a rectangular slot - uniform cross-section (left) and graded cross-section (right)



(a) Uniform cross-sectional area in each successive turn

(b) Graded cross-sectional areas of successive turns

Figure 87 Cross-section through the active region of an AM coil

The overall end-windings comprise the end-winding of the individual coils, the interconnections between successive coils and, in some cases, the star point. In this end-winding region, neither the geometry nor the net cross-sectional area of successive turns is constrained by the geometry of the stator slot. This said, in the majority of applications, there is often a desire to make the end-windings as compact as possible so as to minimise the overall casing axial length.

An AM coil offers scope to have very different cross-sections of individual conductors in the end-winding region as compared to the slots. This contrasts markedly with conventional coils wound from circular wire or rectangular bar that have the same cross-sectional area throughout the coil. This degree of design freedom could be exploited in a number of ways:

- To increase the machine efficiency, albeit at the expense of increased mass, by having a larger copper cross-sectional area in each turn throughout the end-winding region. The overall improvement in efficiency as a percentage of the total power will clearly be influenced by the relative proportions of the active

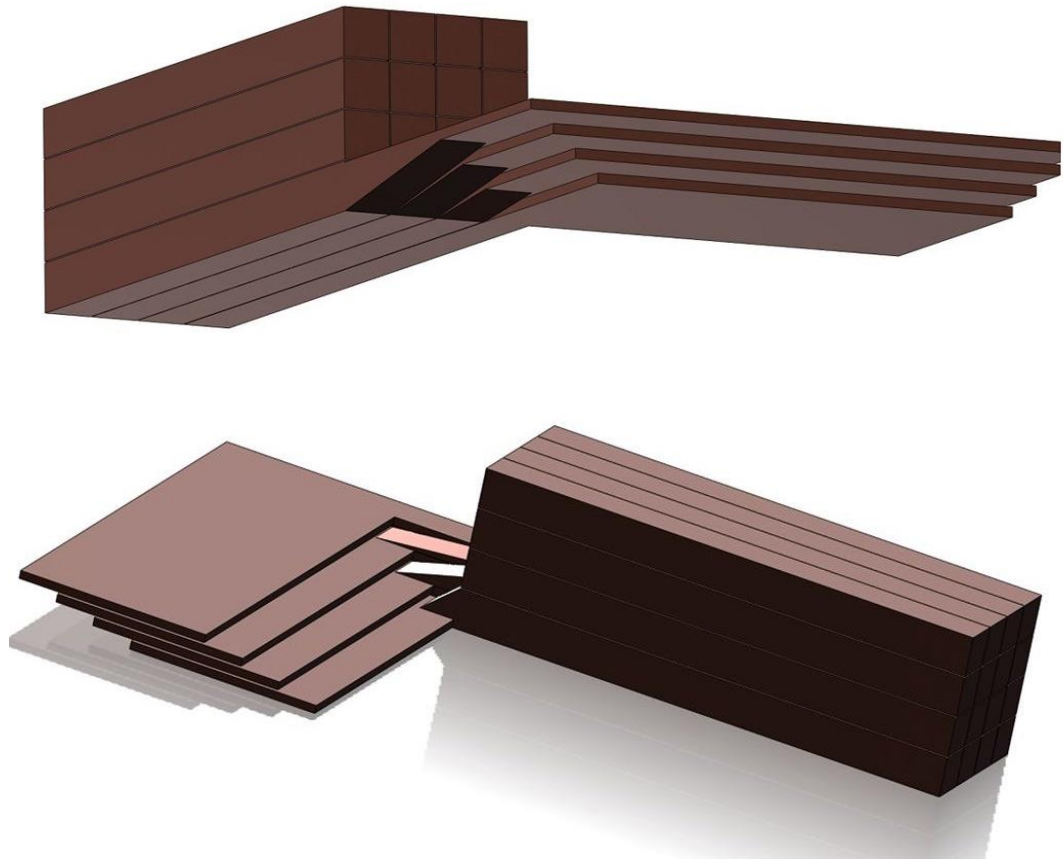
region copper (i.e. that enclosed within the stator core) and the end-winding copper. The greatest benefits will be derived in short axial length, low-pole number machines.

- Maintain the same cross-sectional area of the copper in each turn but increase the surface area to volume ratio of the individual turns to enhance heat transfer from the end-winding, e.g. morph square section copper in the slot region into flat thin plates in the end-winding region. To a first approximation, this would incur no mass penalty as the cross-sectional area remains the same. However, in practice the effective mean length of each turn is likely increase. Clearly within this overall approach, some compromise between mean length per turn, surface area, conductor cross-sectional area and mass could be arrived at.
- In cases where the end-windings are more favourably cooled, the regions contained within the stator slots (e.g. oil spray cooling of end-windings as is common in current aerospace generators), the cross-sectional area could be reduced compared to that in the stator slots since greater losses can be tolerated while remaining within the maximum temperature constraint. This would result in some mass saving, but at the expense of overall efficiency

In all of the above approaches, AM could offer scope to incorporate a series intricate and elaborate geometrical features to promote localised heat transfer, e.g. corrugations to promote turbulent flow, profiled ducts to control coolant flow (whether this be air or a liquid).

A small section of a coil showing one possible embodiment of such an end-winding concept is shown in Figure 88. The section shown consists of the same 4x4 arrangement of square sectioned conductors which sit in the stator core and a proportion end-winding. To aid clarity, the end-winding region is only shown for the

lower four turns in the coil (the general arrangement for successive layers would be very similar). Also shown in Figure 88 is one means, albeit rather rudimentary, of transitioning from a 3.9x3.9mm square section in the slot region to a 19mm x 0.8mm flat shaped end-windings (which nominally have the same cross-sectional area) without avoiding acute current density pinch-points. Even for this simplified arrangement, the advantages in terms of increasing the surface area for heat removal are readily evident.



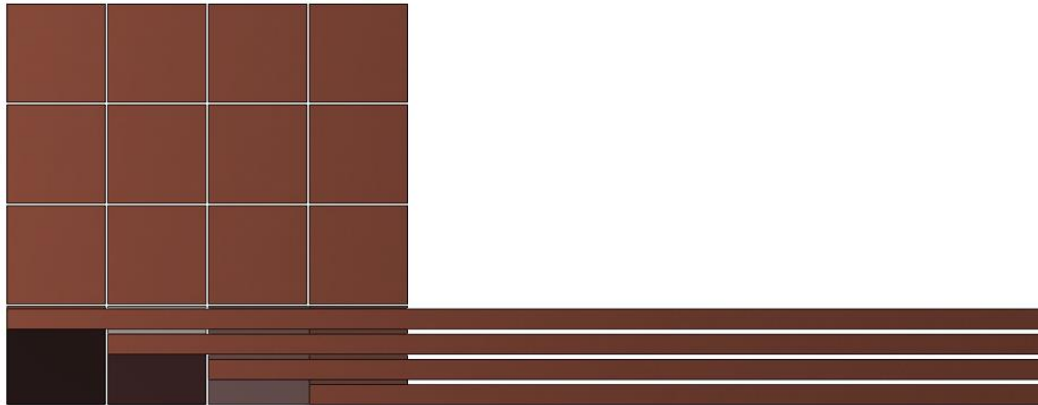


Figure 88 Example of an end-winding arrangement manufactured by AM

This section has described in board terms a few of the possible innovations that could be achieved with AM, providing the necessary electrical properties and geometric detail and tolerances could be realised in practice when forming complex coils.

6.3 ADDITIVE MANUFACTURING PROCESS

6.3.1 COPPER POWDER PROPERTIES

There are many grades of Copper powder produced commercially for various applications such as self-lubricating bearings, alloying with tin, zinc and nickel for structural parts and friction materials such brakes and clutches. These exhibit a range of properties in terms of electrical properties, particle shape and size distribution etc. The specific powder considered in this study is an oxygen free high conductivity (OFHC) grade manufactured by Sandvik Osprey Ltd. This was supplied in vacuum packed 5kg bags, subject to a minimum order of 20kg with a typical cost of £25/kg. The manufacturer supplied properties for the batches of powder supplied are summarised in Table 26. This is a general purpose copper powder product in terms of the particle size distribution, and not a bespoke powder manufactured against a tailored specification for EBM. It is worth noting that Sandvik Osprey has

the technical capability to produce specialist fine atomised powders with particle sizes less than 38µm.

Table 26 Copper powder batch properties

Particle Size Data		Percentages	
>106µm		0.1%	
<106µm and >38µm		97.7%	
<38µm		2.2%	
Powder Analysis (weight %)			
Element	Minimum	Actual	Maximum
Oxygen	0.000	0.060 %	0.150
Copper	BALANCE		

6.3.2 EBM MACHINE SPECIFICATIONS

EBM technology was pioneered by Arcam AB who remain the leading manufacturer of EBM systems and hold key proprietary rights. The two main industries they cater for are aerospace and medical devices, which are served by two different models of EBM machine. The model used in this investigation is the Arcam S12, which was the first commercially available EBM machine. There have been improvements to this model which is now rebranded as the A2 model. The specifications of the Arcam S12 machine is summarised in Table 27.



Figure 89 Arcam S12 EBM Unit

Table 27 Arcam EBM Machine specifications

Model designation	S12
Build tank volume	250 x 250 x 200 mm
Maximum build size	200 x 200 x 180 mm
Accuracy	± 0.4 mm
Melting speed	Up to 60 cm ³ /h (material dependant)
Layer Thickness	50 – 500 μm (material dependant)
Electron beam scan speed	20,000 mm/s
Electron beam positioning accuracy	± 50μm
Beam power	3500W

6.3.3 PROCEDURE FOR OPTIMISING PROCESS PARAMETERS

Figure 90 and Figure 91 shows a schematic and a photo respectively, of the Arcam S12 EBM machine used in this investigation. The first step in the EBM process involves setting the start plate such that it forms a level surface which is parallel to, and in intimate contact with, the powder rake. The height of the rake can be adjusted to establish the thickness of the powder layer that is spread across the start plate between successive layers. The powder is deposited across the bed or start plate by

the left and right traversal of the rake from one hopper to the other. The entire layer of powder on the start plate is pre-heated with a highly defocused E-beam. This pre-heat stage is not intended to melt the powder but to partially sinter the powder to provide support for successive layers and to reduce the effects of particle charging leading to 'smoking'. Smoking is the term given to a cloud of powder generated by the electrostatic interaction between the electron beam and the metal powder particles on the build plane.

The electron beam then raster scanned to deliver intense localised heating to the selective regions of the powder layer to melt the powder. The build platform is lowered into the build tank by an amount equal to the powder layer thickness and the process is repeated to build up the part. The excess partially sintered powder is usually removed at the end of the entire process by compressed air.

In order to achieve full density parts, there are three stages of the build process which need to be optimised; pre-heat, build temperature and the melting or hatching stage. There are standard build process parameters recommended by Arcam for the metal powders they have used commercially. Unfortunately, the portfolio of materials for which parameters are available did not include copper. It therefore proved necessary to undertake a series of trials to establish some machine settings which would realise complete but precise melting and therefore near full density components. This study was undertaken with significant input from Fatos Derguti and Everth Hernandez, who were familiar with the operating and set-up of the Arcam S12, hence operated the machine, and provided guidance on parameter selection.

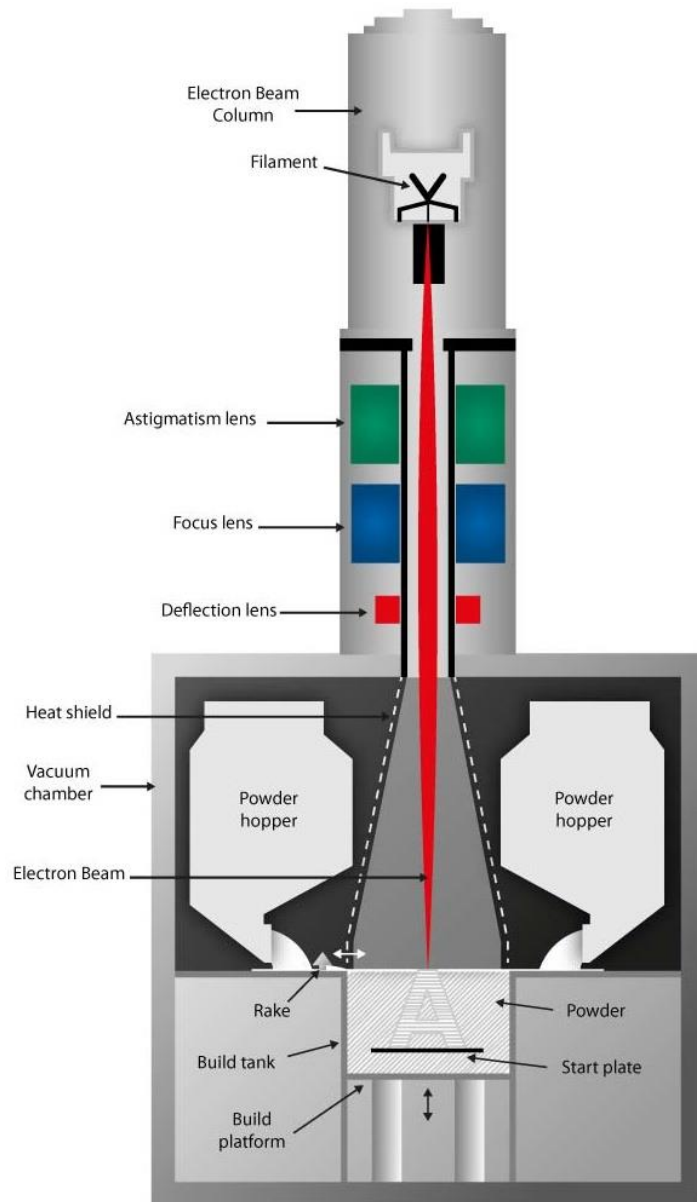


Figure 90 Schematic diagram of the Arcam EBM machine

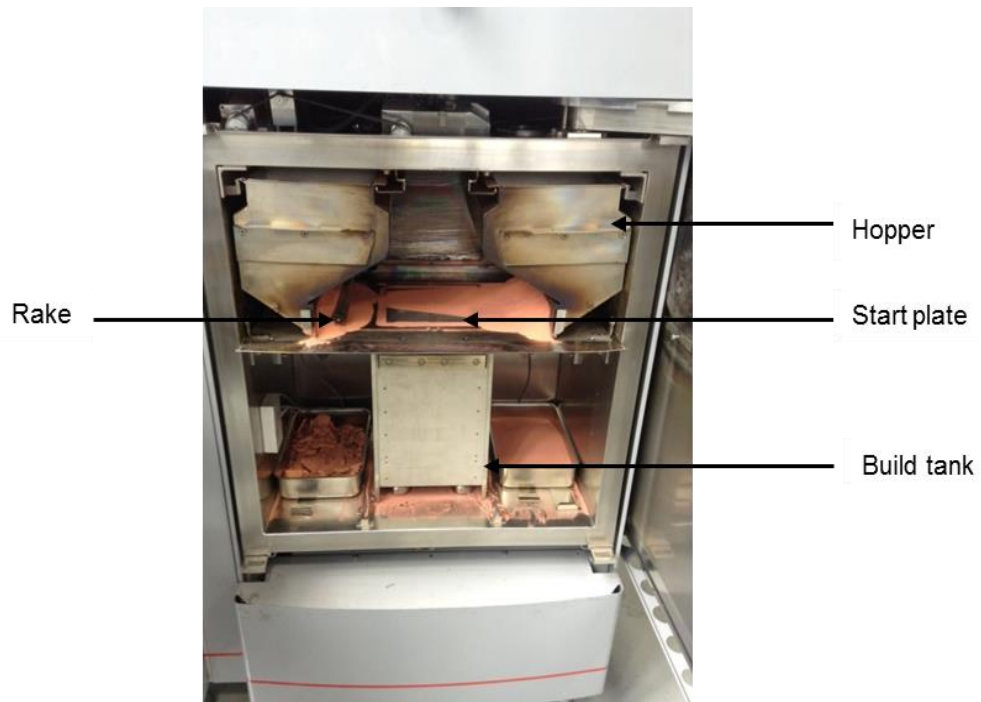


Figure 91 Photo of the build area Arcam EBM machine – shown with copper powder during trials

6.3.4 BUILD TEMPERATURE CONDITIONS

Prior to the start of any build, the start plate is preheated to a controlled temperature in order to prevent it from acting as a heat sink when a localised region is intensively heated by the electron beam. Indeed, when pre-heated it acts more like a heat source for the first few layers of powder. The build temperature is also important in minimising thermal gradients throughout the component being manufactured.

The optimum pre-heating temperature needs to be established from a series of trial runs. In these trials, a bed of powder is manually established in the build tank and the start plate is placed on top of this powder and levelled. The electron beam is used to heat the start plate and partially sinter the underlying powder. A thermocouple is located between the underside of the start plate and the underlying powder to monitor temperature. Several trial runs are required to determine the optimum temperature required. Previous preliminary investigations identified difficulties in establishing build temperature above ~ 550 °C due to the high thermal conductivity of

the copper. This problem was overcome by hindering heat flow out of the build tank by placing Zirconia tiles along the sides

6.3.5 PRE-HEAT CONDITIONS

The pre-heat conditions, which it will be recalled is applied across each successive layer to partially sinter the powder prior to melting of selected regions of the layer, must be tailored for each material because of differences in properties such as density, reflectivity, melting point and thermal conductivity. These material properties dictate the amount of energy required to partially sinter the powder. Figure 92 shows a schematic cross-section through a test-piece which illustrates the combination of melted and partially sintered regions. Excessive energy into the powder in the pre-heat stage (i.e. the blue regions in Figure 92) will cause the powder to melt or make it extremely difficult to remove from the finished part. Therefore, numerous trials were performed to optimise the preheat parameters for copper. Further investigations in this current phase of the programme were carried out to improve the build quality by improving the preheat stage. By way of example, Figure 93 shows a test-piece during build-up in which a large region of partially sintered powder is supporting relatively small square regions of fully-melted powder.

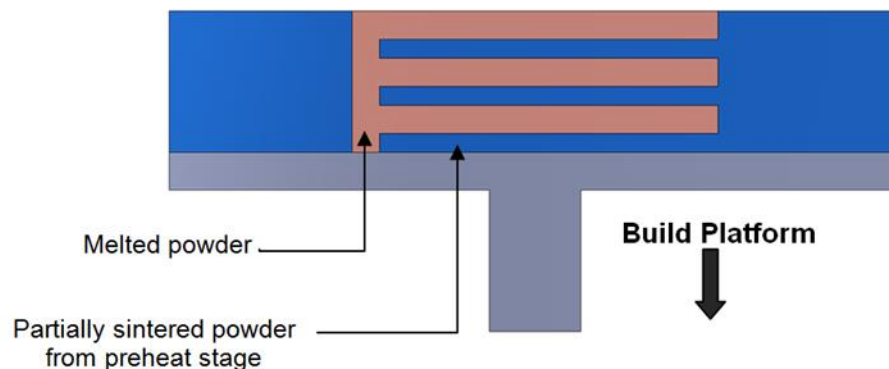


Figure 92 Schematic cross-section through a component during build showing melted and partially sintered regions

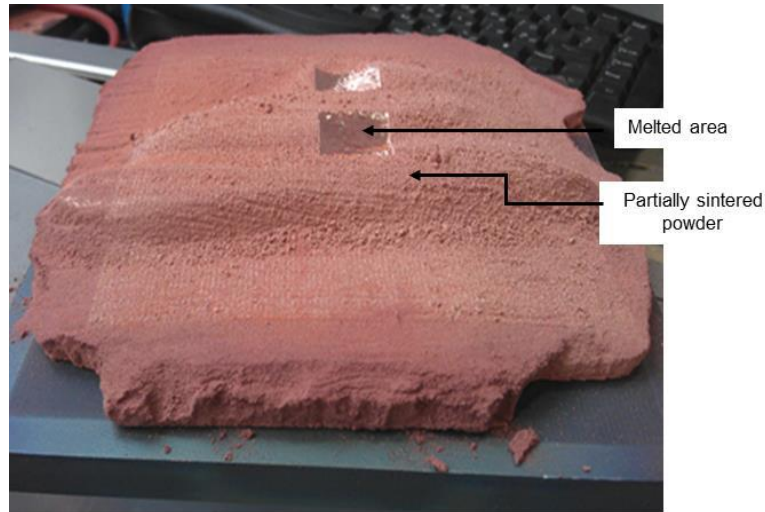


Figure 93 Typical sample during build-up showing preheated powder for support and fully melted regions

6.3.6 MELTING CONDITIONS

The so-called ‘hatching’ parameters controlled the localised melting of the powder. The parameters are the speed function (SF), beam speed, beam current, focus offset, line order and line offset. These parameters dictate how much energy is imparted into the powder, the rate at which this energy is input and the spatial resolution of the beam itself. It is critical to optimise these parameters in order to achieve both near full density parts and near precise control of geometry.

The so-called speed function attempts to provide a straightforward means for the user to specify a parameter which feeds into the automatic power calculation of the beam. It takes a discrete value ranging from -10 to 200. The relationship between the speed function, the beam current and speed of the beam has not been made available beyond Arcam for proprietary reasons, and recommended speed function parameters are only available for a limited set of materials, which at present does not include copper.

Figure 94 shows the line offset parameter which quantifies the distance between the electron beam lines of the raster pattern. The contour is defined by the perimeter of

the layer to be melted. There can be up to 5 contours offsets. The interior raster of electron beam melts the bulk of layer.

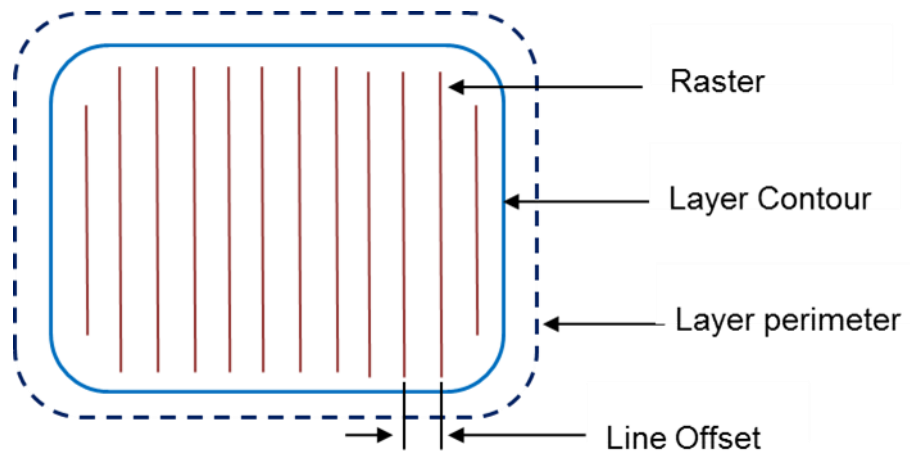
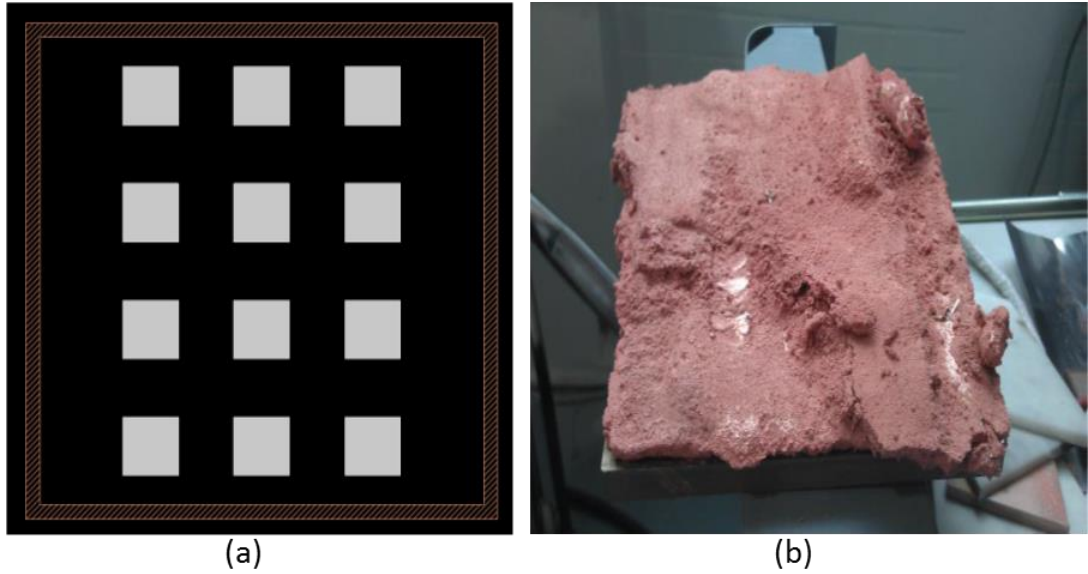


Figure 94 Electron beam scanning parameters

6.3.7 TRIAL RESULTS

The build parameters for Co-Cr were used as the starting point for fine-tuning the build parameters for copper. The initial plan was to build 12 cuboid specimens as shown in Figure 95(a) with variations in the speed function and preheat theme. As can be seen from Figure 95(b), good quality melting was not evident. This was believed to be due to the time spent melting each specimen being excessive and, as a result of the high thermal conductivity of copper, the heat escaping rapidly from the build envelope. This may well have caused the swelling and poor melting observed between the powder particles.



**Figure 95 (a) Specimen layout on start plate
(b) Start plate with attempted samples from the EBM machine**

The number of specimen was reduced from 12 to 2 in the second trial. A bespoke set of melting parameters were used for cube 1 and the Co-Cr standard parameters used for cube 2 as shown in Figure 96. Cube 1 showed swelling on the hatching surface of the sample. Cube 2 had a more uniform hatching surface but a rougher surface finish. The powder bed was heavily sintered, almost melted by the preheat stage. In the next series trials, the pre-heat parameters were modified systematically.

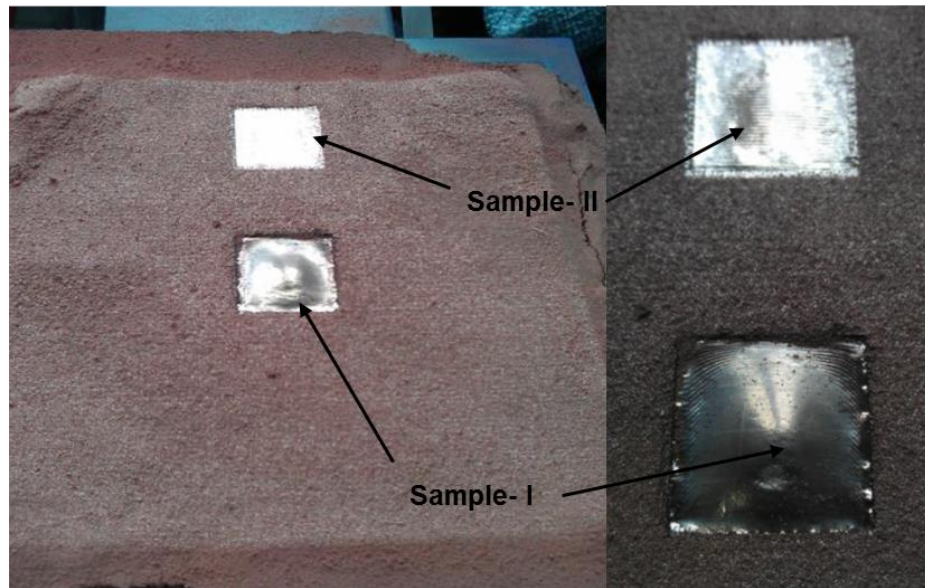


Figure 96 Cube sample I and sample II manufactured using LK and Co-Cr parameters respectively

In the subsequent set of trials, the speed function was the variable adjusted in an attempt to mitigate the swelling. The speed functions of sample- I and sample- II were set to 15 and 22 respectively. The lower the speed function, the slower the beam passes over the bed thus imparting more energy into the powder. There was no reduction in the swelling at the surface of the samples and therefore more trials were required at higher speed functions. Further modifications were required in the pre-heat stage, as this was also believed to be having an impact on the swelling. Further systematic trials were carried out to fine-tune the build parameters, using an approach similar to that reported above until a reasonable first-pass of parameters were established.

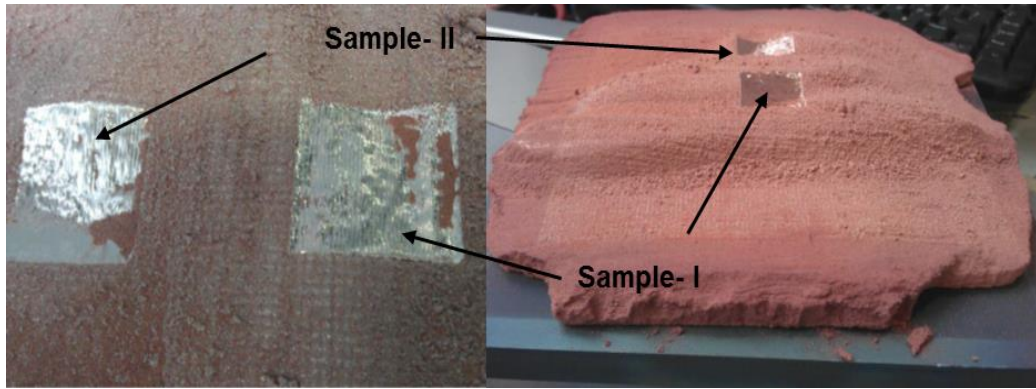


Figure 97 Sample-I and sample-II with SF of 15 and 22 respectively

Having established a satisfactory initial set of process parameters, an attempt was made at the more complicated geometry of a serpentine coil structure. The serpentine structure was chosen to give a path length of over 1.5m within the build envelope for subsequent resistivity measurements. Figure 98 shows the dimensions of the serpentine structure. The build parameters had to be modified slightly for the serpentine structure as optimum parameters are, to some degree, geometry dependant.

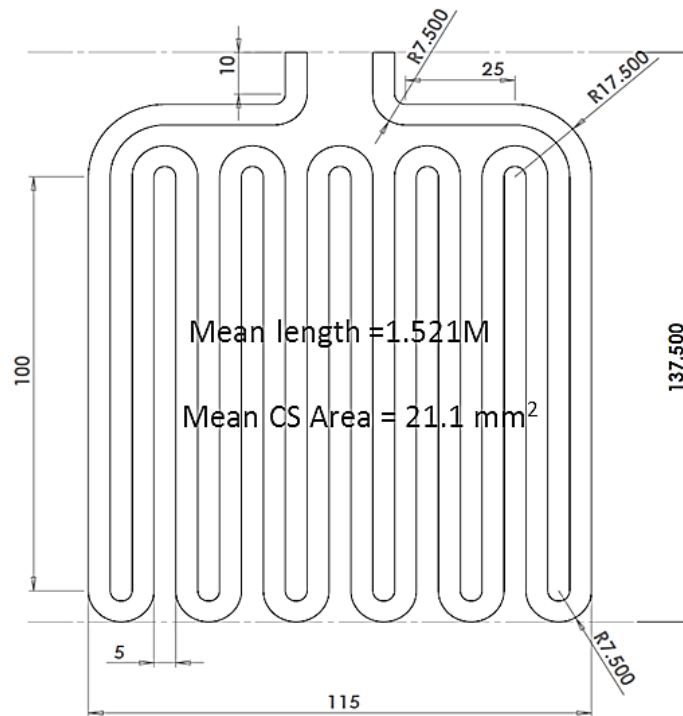


Figure 98 Dimensions of the serpentine sample (depth of 4.5mm)

Several trial builds were carried out in order to fine-tune the process and these highlighted several challenges. One of the problems encountered was incomplete interlayer fusion of the powder, which led to a delaminating type defect as shown in Figure 99. This was identified as being caused by non-uniform powder delivery by the raking system, with insufficient powder being delivered across the bed during the melting of a few of the layers. The powder was delivered by the rake colliding with the heap of powder at the foot of the hopper. The entire heap of powder which falls in front of the rake is then layered across the build area, with the excess pushed over to the other hopper. This process is then repeated from the other side of the hopper. Unfortunately, there is a tendency for the particular type and grade of copper powder used to agglomerate as the rake pushes up against it. This agglomeration prevents sufficient finely distributed powder from consistently falling in front of the rake, resulting in some incomplete filling of the layer and hence voids across the bed. This problem was temporarily overcome by completely filling up the hoppers with powder so as to increase the weight forcing down on the powder at the base of the hopper. This problem is consistent with the observations reported in [44]. It is believed that the copper powder used in this current set of trials has a high percentage of smaller 'satellite' particles. The work reported in [44] recommended using an electronic grade copper powder which provides a better flow of powder.

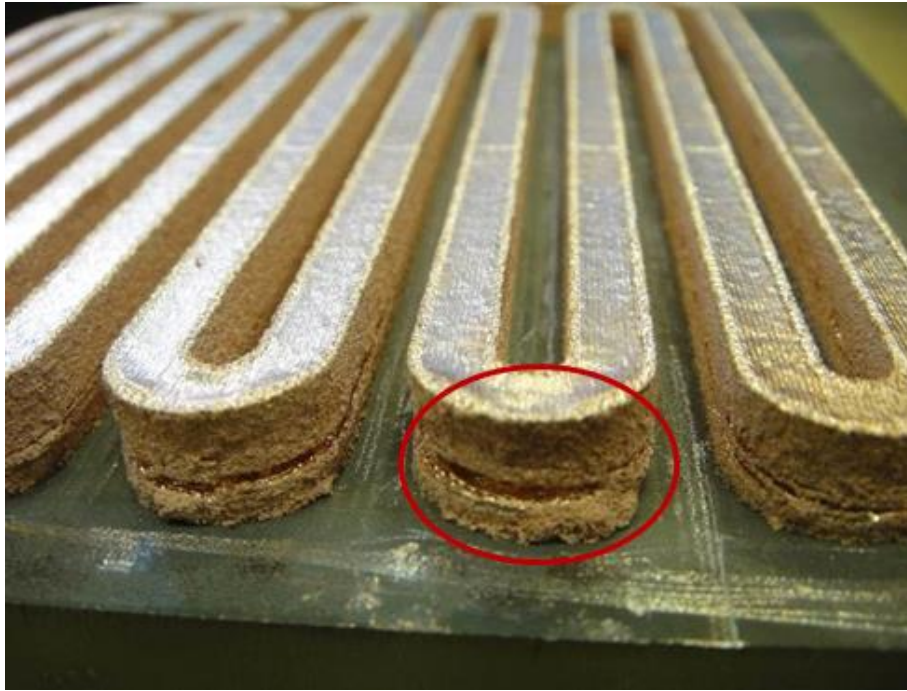


Figure 99 EBM serpentine structure with a de-laminating defect

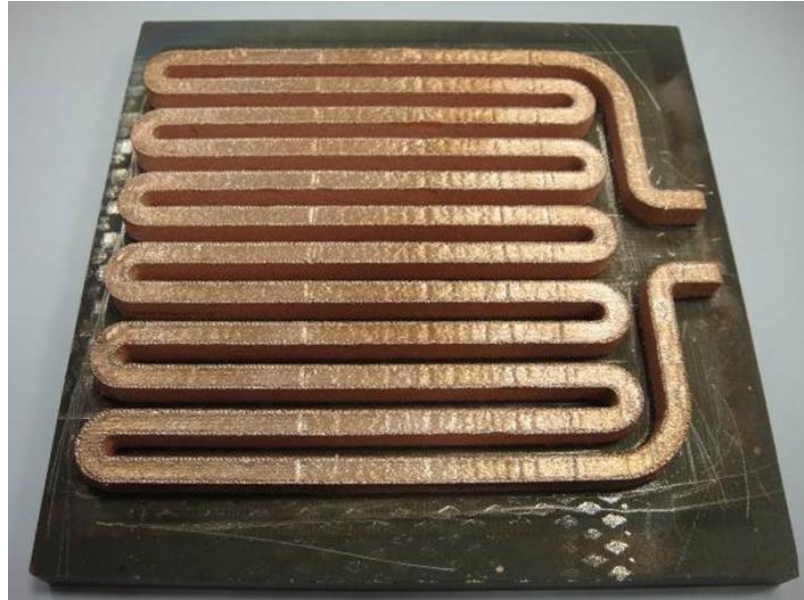
On a further trial build, the sample developed surface cracks as shown in Figure 100. This was ascribed to thermal cycling experienced by the sample as a result of the high aspect ratios of the individual limbs.



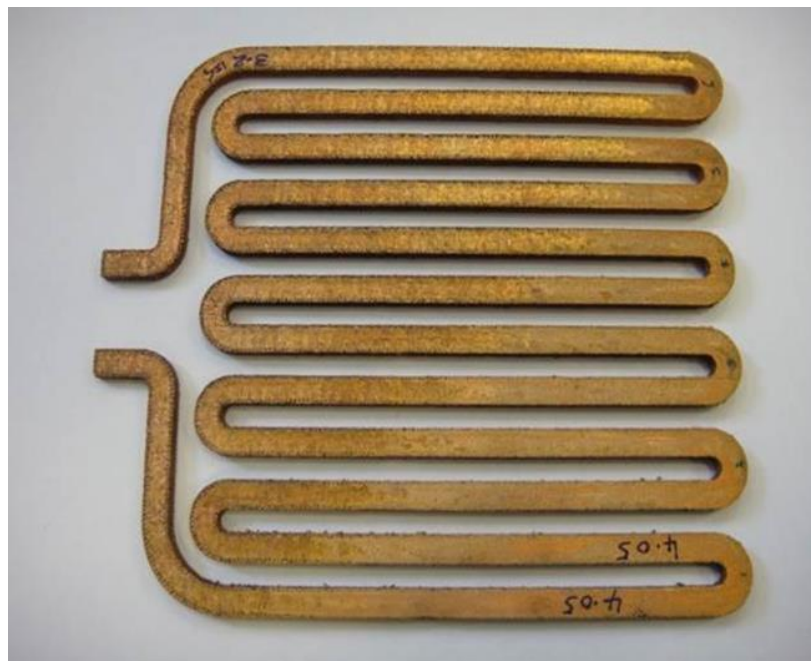
Figure 100 Surface cracks developed in test sample

Another trial run was performed which showed no cracks but some de-laminating towards the lower section of the build, i.e. near the start plate. The serpentine coil was cut away from the start plate by wire EDM. Since the region of de-lamination

was close to the base of the sample, the coil was cut away above this defect. The resulting sample, shown in Figure 101, was used to measure the electrical conductivity and density. Several close ups of the coil are shown in Figure 102 and Figure 103.



(a)



(b)

(a) Still attached to start plate (b) Removed from start plate

Figure 101 EBM Serpentine sample used for resistivity and conductivity measurements

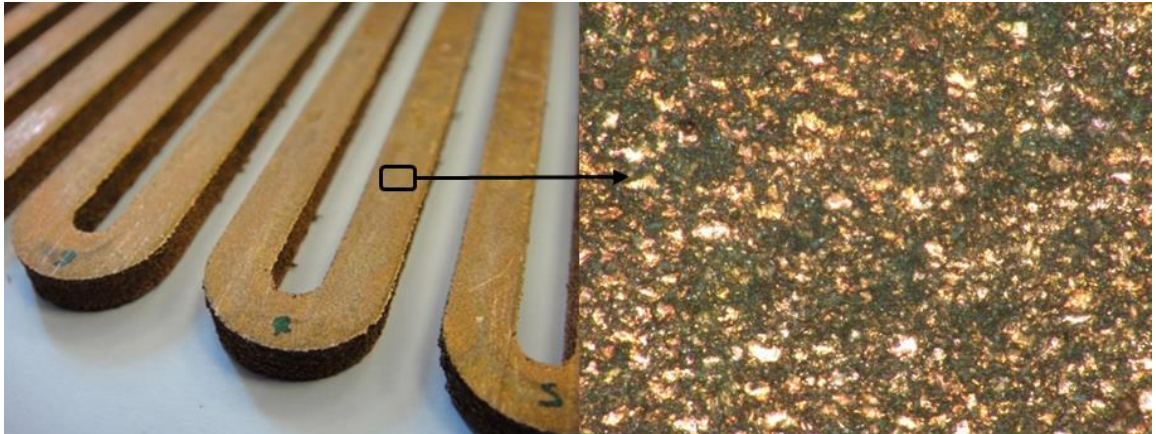


Figure 102 Surface after cutting using EDM.

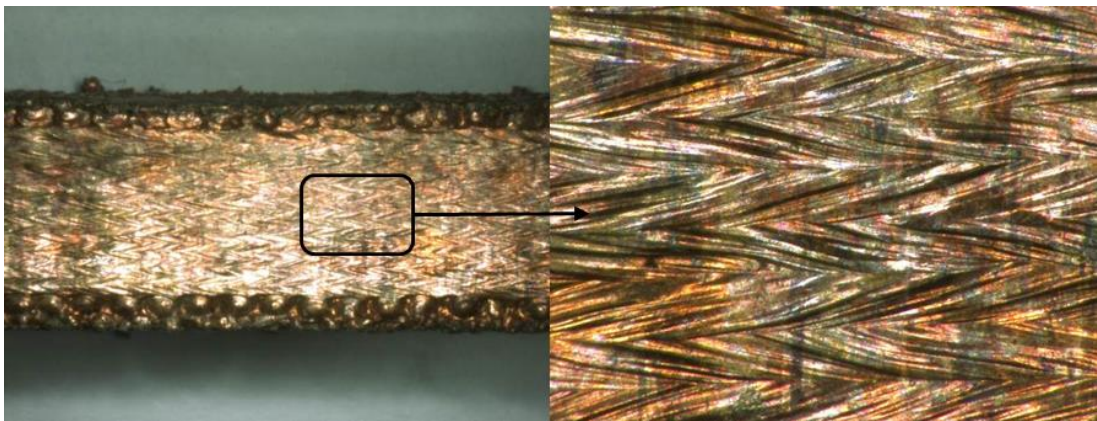


Figure 103 Surface finish from the EBM process

The set of build parameters which produced this sample are summarised in Table 28. Only one single preheat stage was used. The line offset is one of the most important parameters in ensuring that porosity is kept to a minimum, albeit there is some degree of trade-off with build time.

Table 28 Build parameters used to produce the sample in Figure 101

Start Plate Temp (°C)	680
Preheat	
Min. Beam Current	30Ma
Max. Beam Current	30Ma
Beam Speed	16000 mm/s
Average current	8.8 Ma
Hatching	
Speed function	18
Beam Speed	400 mm/s
Beam current	6mA
Line Offset	0.2mm
Line Order	1
Focus offset	22mA

The serpentine shown in Figure 101 had a measured density of 262.9 kgm^{-3} (92% of the theoretical full density of copper) based on its measured dimensions. The measured electrical resistance was $1.351 \text{ m}\Omega$, which corresponds to an effective mean electrical conductivity of $5.34 \times 10^7 \text{ Sm}^{-1}$ which is in turn is ~92% of the IACS value. As a first attempt, with limited access to the equipment to fine-tune and refine the process, these initial values of density and electrical conductivity were deemed very promising and already within the range in which the electrical conductivity is competitive with conventional drawn wire. Indeed, given that the same shortfall of 8% was observed in the density as is the conductivity, then the specific conductivity is already matching that of wire, indicating no first-order problems with the microstructure beyond porosity.

6.3.8 CONCLUSIONS OF THE ADDITIVE MANUFACTURING PROCESS

The trial builds reported in this chapter, although time constrained and reliant on significant input from others, demonstrated that even at this early stage, the material properties of the EBM copper with an electrical conductivity of 92% IACS and a density of 92% are competitive and do not present an obstacle to consideration of EBM for machine coil applications. Moreover, although there remains significant work to do to produce highly intricate and precise components, test-pieces with reasonable geometrical control were produced, although it should be recalled that the optimum build parameters are specific to the geometry of the sample.

One of the challenges yet to overcome is the intermittent delivery of the powder by the rake system which causes incomplete interlayer fusion. However, the root cause of this problem, as confirmed in [44], is due to a build-up of ‘satellite’ particles in the powder which leads to agglomeration. This could be minimised by using a so-called ‘electronic grade’ copper powder, albeit at increased cost.

Although competitive material properties have been demonstrated with EBM, there are two very significant challenges which must be overcome in order to make such coils a practical competitor to wound coils:

- The additional AC losses that are generated in large cross-section copper regions, as compared in particular to the use of multiple strands of small diameter.
- The ability to reliably insulate successive turns in the coil from each other.

6.4 AC LOSSES IN ADDITIVE MANUFACTURED COILS

Whereas the benefits of additive manufacturing coils in terms of flexibility of geometry and packing factor are recognised, one factor which may well limit their

use in many applications is that of AC losses in the coils themselves. These additional losses in the coil over and above the classical DC ohmic losses are the result of induced eddy currents flowing in the conductors. AC losses increase, albeit not in a straightforward manner, with frequency, electrical conductivity, conductor cross-sectional area and the proximity of other conductors and/or ferromagnetic regions.

All conductors which carry current and/or are subjected to time varying incident magnetic fields from other sources are susceptible to AC losses generated by induced eddy currents. This issue is usually addressed in conventional coils by selecting an appropriate individual wire diameter to minimise AC losses and making up the required overall coil cross-section with an appropriate number of individual wires in parallel, resulting in a so-called 'parallel stranded coils'. In many machines, particularly those operating with a combination of high frequency and high current, coils can be wound with tens of parallel strands of wire, e.g. 49 strands of 0.67mm wire in the case of the demonstrator discussed in chapter 3. For very high frequencies, so-called Litz wire is often used to reduce AC losses to a manageable level.

In the case of additive manufactured coils of the type described in above, although a given coil cross-section can in principle be subdivided into numerous parallel paths to reduce AC losses, the thickness of the gaps required to ensure some level of clearance as the coil is built up will increasingly impact on the achievable packing factor. This problem of diminishing packing factor with increasing sub-division is likely to be far more marked in coils produced by additive manufacturing than would be the case with a conventional wound coil where the insulation layer is generally

much thinner than the gaps required in an additively manufactured coil, particularly if the insulation is applied after the copper element is fully formed.

Although there are some standard formulae for predicting AC losses in isolated circular conductors, these have limited applicability to the losses that will occur in a practical coil which is located into a slot in a stator core. In a practical machine, proximity effects (i.e. the influence of other adjacent conductors) and the presence of the core and incident flux from other sources of excitation make it rather difficult to establish even estimates from analytical methods.

To quantify the extent of AC losses in a representative high performance machine design, a series of simulations were performed taking the prototype liquid cooled LP generator design described in chapter 2 and 3 as a baseline. This 3-phase machine has 10 rotor poles and 15 stator teeth, with each tooth being equipped with a concentrated coil with 5 series connected turn as described in chapter 2. The net cross-sectional area of each individual turn is 17.4mm^2 which yields an rms current density of $\sim 13\text{A}/\text{mm}^2$ at the rated current of 230Arms. In the existing prototype, the stator coils are wound with 49 parallel strands of circular wire of diameter 0.73mm (incl. double coated insulation). The net copper diameter of each strands is 0.67mm. The effective packing factor of the coil within the slots is 0.5. In addition to minimising AC losses, the wire diameter was selected predominantly to achieve the desired mechanical flexibility of the overall bundle so as to realise compact end-windings rather than from a detailed appraisal of AC losses. Indeed, the sub-division employed is such that AC losses are negligible in this machine.

The combination of a maximum rotational speed of 17,000rpm and 10 rotor poles gives rise to stator currents with fundamental electrical frequency of 1.42 kHz.

Although this is a high frequency when compared to many electrical machines, it is not untypical of the frequencies that might be encountered in starter-generators for aero-engines, in particular for smaller engines. At the operating point of 50kW (generating) at 17,000rpm, the phase current in the machine is 230Arms, which gives rise to a copper loss of 1.36kW assuming a mean coil temperature of 200°C (equivalent to 91W per coil). Of this total machine copper loss, 544W is contributed by the end-winding region. Hence, the copper loss contributed by the regions of the conductors within the stator slots is 816W.

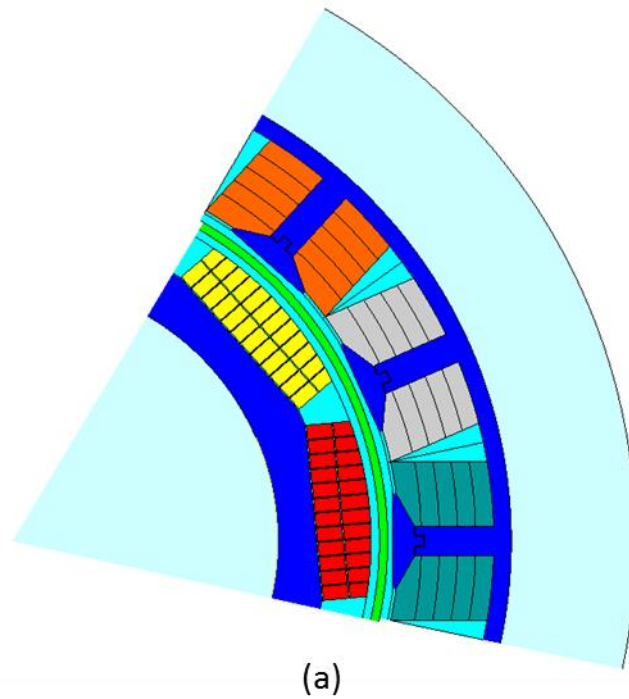
Against the backdrop of this baseline copper loss, several alternative additive manufactured coil variants were simulated using two-dimensional, transient, circuit coupled finite element analysis. In these simulations, the individual conductors which make up each coil were represented as so-called ‘solid regions’ in the finite element model, in which both imposed conduction currents and induced eddy currents can flow. It is important to note that this simulation, by virtue of its two dimensional nature, can only account for AC losses in the active region of the machine.

The first set of simulations were performed for the two conductor arrangements shown in Figure 104. In both cases, each successive series turn of the coil, of which are 5 per coil, consists of single solid conductor, i.e. there is no subdivision into parallel paths. Even a first order consideration of the AC resistance of an alone isolated conductor would suggest that a combination of a cross-sectional area of 26.3mm² and a frequency of 1.42kHz will give rise to significant difficulties.

The arrangement of conductors in Figure 104a has been designated as horizontally arranged. It can be seen from close inspection of Figure 104 that the stator tooth tips

in both cases is detachable. This is a pre-requisite for fitting pre-formed additively manufactured coils into stator slots with so-called ‘semi-closed slots’.

The conductor arrangements shown in Figure 104 achieve effective packing factors of 0.83 within the slots, c.f. the 0.5 achieved in the benchmark machine wound with conventional wire. This in turn would lead to a marked reduction in static copper losses (i.e. with no account for AC induced losses) for the same rms current of 230A rms, viz. from 1.36kW to 901W on the basis of simple scaling by the improved packing factor in both the active and end-winding regions.



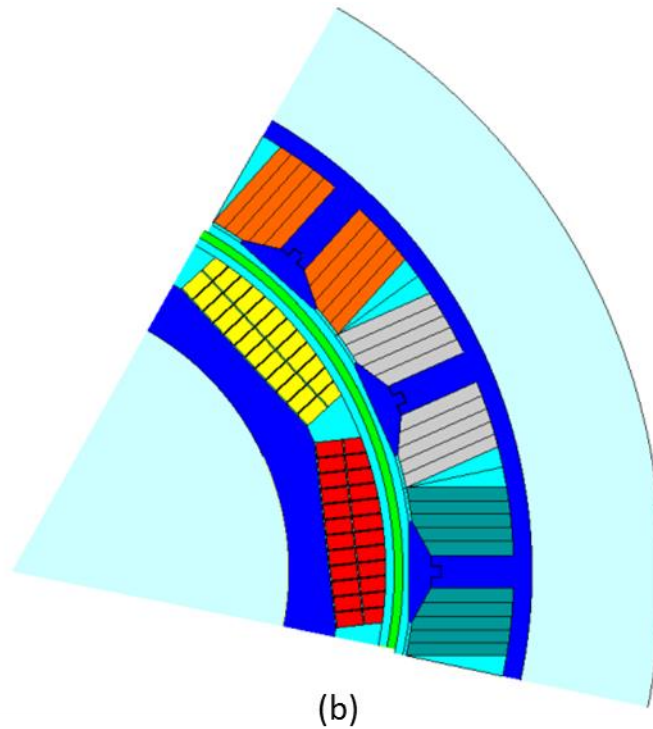


Figure 104 – Alternative additively manufactured conductor arrangements (one single conductor forming each successive turn of the coil) – (a) horizontal (b) vertical

A series of two-dimensional, fully transient finite element simulations were performed for both arrangements of conductors with a sinusoidal phase current which corresponds to 230Arms. As noted previously, these simulations can only account for the AC coil loss in the active region. From this point forward, for the purposes of this discussion, the comparison between the coil losses are based on the loss in the stator slot regions only, i.e. the baseline loss for the active region with the conventional stranded coil used in the demonstrator machine described in chapter 2 is 816W and not the full 1.36kW. The corresponding machine static ohmic losses in the active region for the additive manufactured coil with a packing factor of 0.83 is 541W at 200°C reducing to 330W at 20°C.

Rather than focus solely on the high speed operating point, at which AC losses will be most pronounced, machines equipped with the two winding variants were simulated over the full speed range up to 17,000rpm in eight increments, in each case at the rated coil current. The resulting variation in coil losses with speed are shown in Figure 105 and Figure 106. Several components of loss were identified separately through varying the excitation conditions at each speed via separate simulations, specifically:

Open-circuit coil losses – These losses are present when there is no externally driven current in the coil and its terminals are simply an electrical open circuit. These losses arise from eddy currents in the copper conductors which are induced as a result of exposure to the time varying field produced by the rotating permanent magnets, notably flux which is not shielded by the stator in the vicinity of the slot openings.

Coil losses due to winding mmf only - A series of simulations were repeated with the magnet excitation removed such that the only source of excitation in the machine was the rated stator currents. In these simulations, the rotor was still rotated in order to represent the modest level of saliency which is present.

Coil losses on rated load– In this series of simulations, both the rated stator mmf and the magnet excitation was present.

Summation of open-circuit and mmf only losses – This estimate of the loss on rated load was derived from a summation of the independently calculated losses due the magnet excitation and stator current. One would expect this to be broadly in line with the losses calculated from a full on-load simulation, but it should be recognised

that simple superposition does not capture the full effect of saturation in the stator and/or rotor core under true full-load conditions.

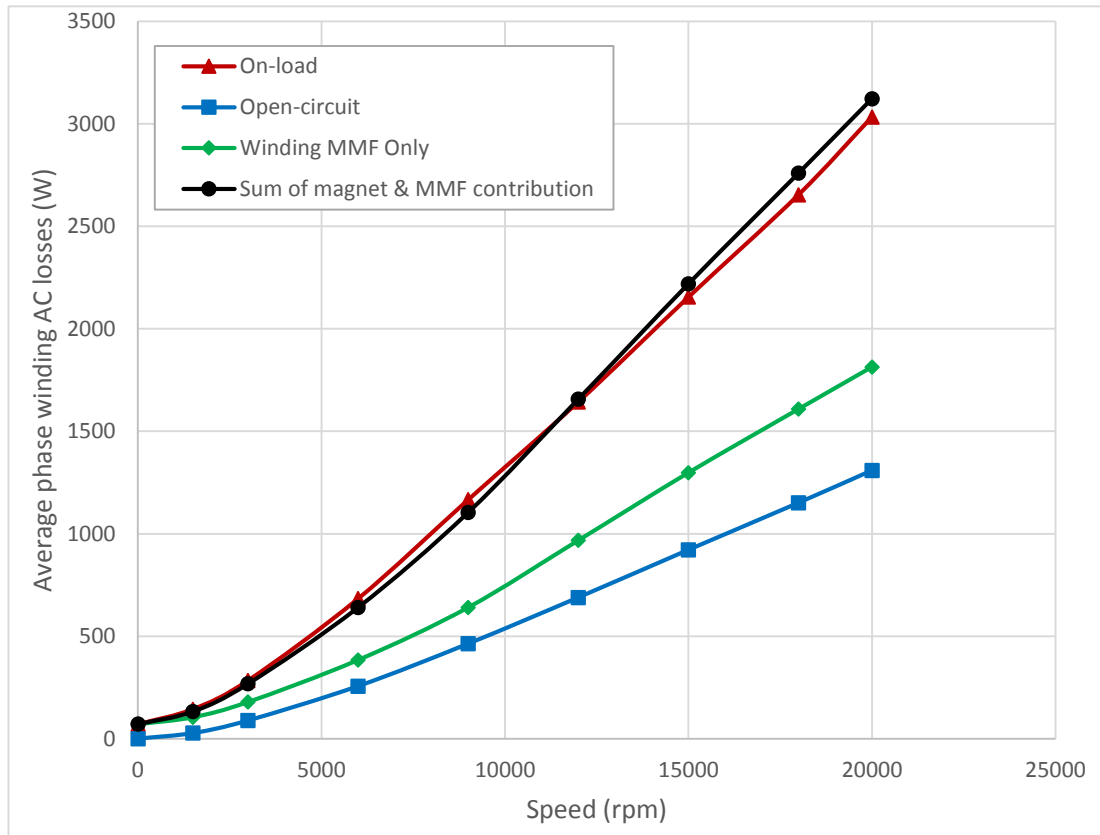


Figure 105 Finite element predicted coil losses for conductor arrangement shown in Figure 104a

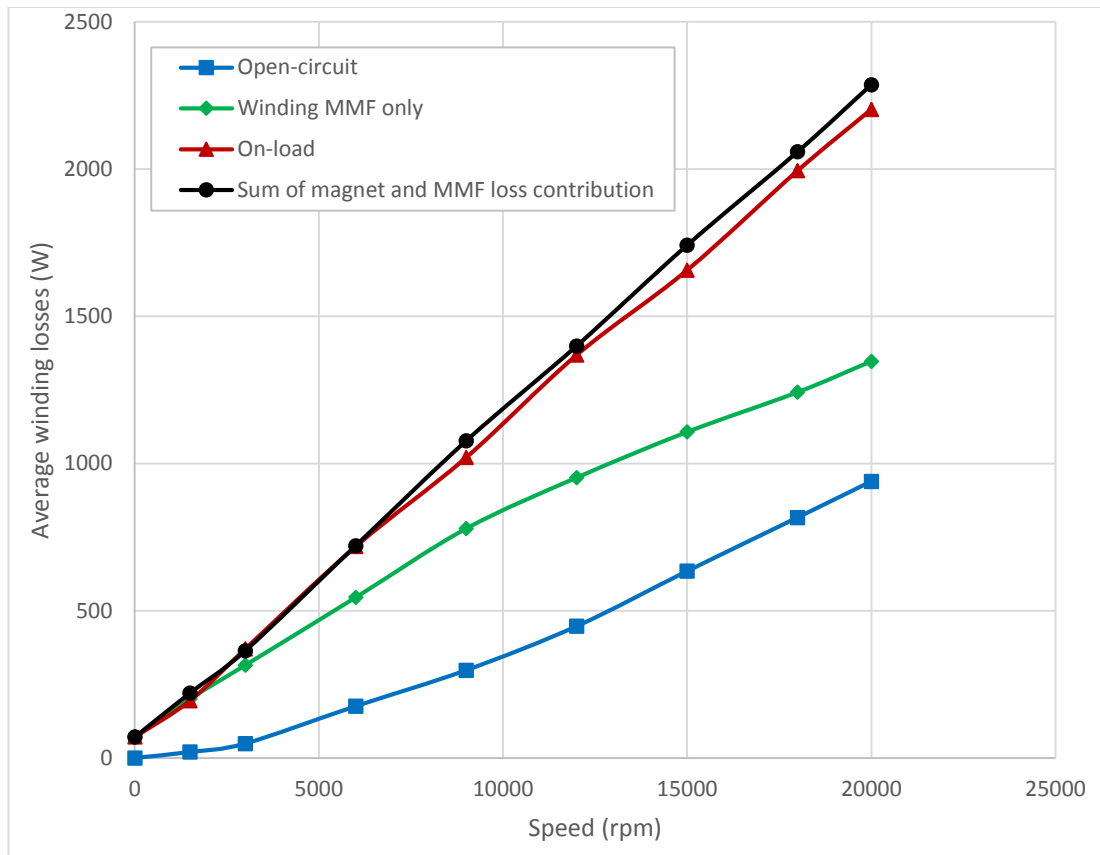


Figure 106 Finite element predicted coil losses (per phase) for conductor arrangement shown in Figure 104b

As will be apparent from the simulation results, for both conductor arrangements, the AC coil losses increase rapidly with speed to a point where they completely dominate over the static copper loss. Indeed, this level of additional AC loss in the coil would be unsustainable from a temperature rise perspective for the vast majority of the speed range, i.e. for speeds of ~1000rpm and above. It is also evident that open-circuit losses and the losses due to the mmf both contribute significantly to the overall loss. Of the two conductor arrangements shown in Figure 104, the losses are markedly lower with the conductor arrangement of Figure 104b than those for the conductor arrangement in Figure 104a.

As would be expected, the losses are particularly pronounced in the regions of the coil closest to the airgap due to a combination of the higher incident magnet flux and

the greater magnetic field strength across the slot (which can be inferred by a consideration of Ampere's Law). Furthermore, by the standards of most machines with semi-closed slots, the slot opening in this machine is relatively large, this being the result of the need to optimise the power delivered into an uncontrolled rectifier. This feature further compounds the difficulty in managing AC losses in the winding.

Although the losses for the simple arrangements of conductors shown in Figure 104 are well beyond the levels that could be sustained in practice, there are several remedial actions that can be taken in the design of the machine to reduce these AC losses:

- Incorporate semi-magnetic slot wedges to shield the regions of the coil near the airgap from the incident flux from the rotating permanent magnets
- Incorporate a series of additional slits into each individual conductor, in effect separating it into a number of parallel paths (at least in the active region of the machine).
- Reduce the slot opening to shield a greater proportion of the coil from the incident magnet flux. However, it should be noted that in this application, the resulting increase in the reactance would incur a penalty in terms of voltage regulation when connected to an uncontrolled rectifier.

A series of further transient simulations were performed for machine variants with 0.5mm thick semi-magnetic slot wedges with relative magnetic permeability value of 10, a value which is representative of those that can be realised in magnetically loaded composite wedges. A representative magnetic field distribution with these wedges in place is shown in Figure 107. As will be evident, the wedges are effective in providing some degree of shielding of the coil conductors which are nearest the

airgap, however, they are prone to saturation even with their modest permeability and hence their effectiveness will be limited.

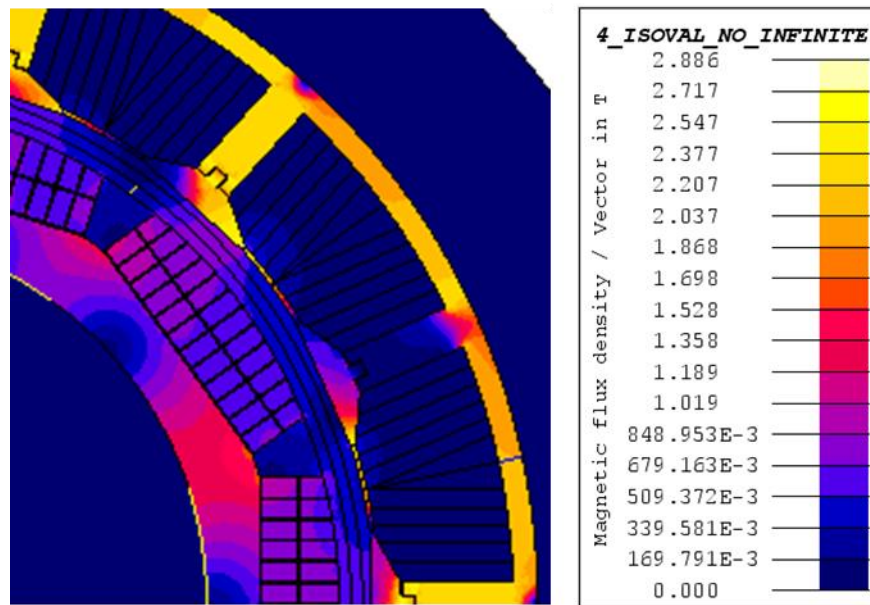


Figure 107 Representative magnetic flux density distribution demonstrating the effect of semi-magnetic slot wedges

The original rated on-load coil loss at 20,000rpm for the conductor arrangement of Figure 104b with no slot wedges was 2200W. This reduces, but only marginally to 1841W with semi-magnetic slot wedges. In order to gauge the sensitivity of this loss reduction to the relative permeability of the semi-magnetic wedge, further relative permeability values of 30 and 50 were simulated. These values were selected simply for the purposes of an electromagnetic sensitivity study rather than necessarily representing commercially available flexible slot wedges. For relative permeability values of 30 and 50, the corresponding predicted coil loss on rated load was 1800W and 1807W respectively, i.e. there is very little to be gained from higher relative permeability.

The other design feature which was investigated using transient finite element simulations was that of sub-dividing each individual series turns into a number of

parallel paths. It should be noted that there is considerable design freedom in how a given conductor can be divided with additive manufacture since the voids which separate individual regions within a given turn can be spaced flexibly. By way of illustration, Figure 108 shows one variant in which each individual turn of the conductor arrangement of Figure 104*b* is divided into 5 parallel paths, with the smallest cross-section path located in the region of highest loss in the single piece conductor. As would be expected, this sub-division yields some reduction in the overall on-load coil loss as shown in Figure 109, but falls far short of reducing the coil losses to an acceptable level. It is entirely possible to extend this basic principle of sub-division to more intricate and elaborate arrangements. However, it should be recognised that an increasing level of sub-division results in a progressive reduction in the effective packing factor as more gaps are introduced, thus eroding or indeed completely eliminating any advantage in packing factor over conventional wound coils.

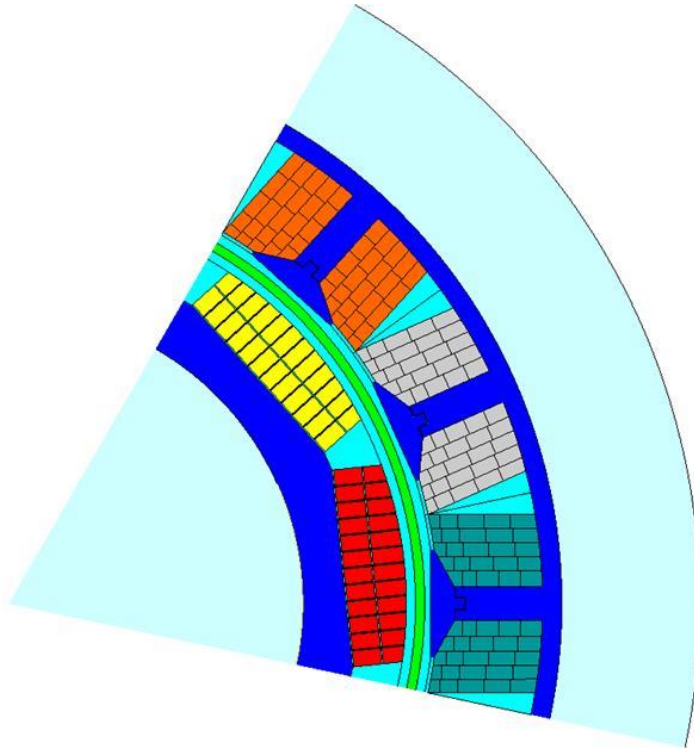


Figure 108 Conductor arrangement with each series turn divides into 5 parallel paths

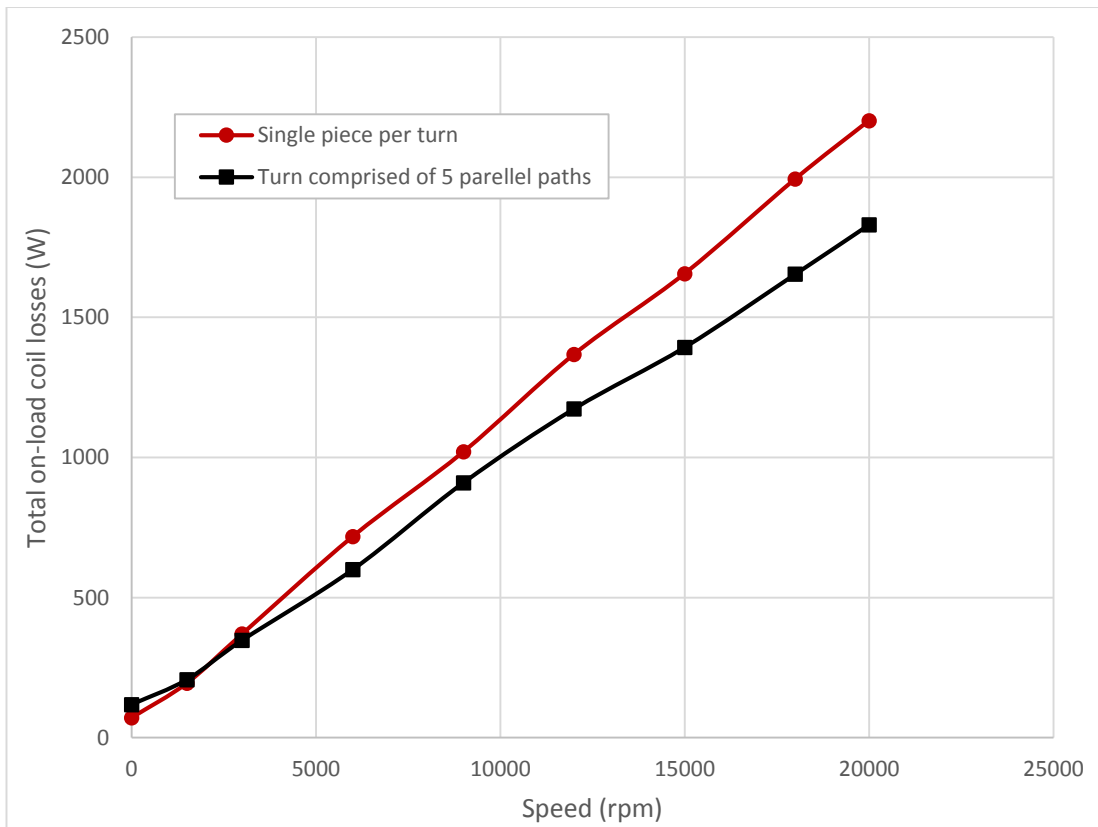


Figure 109 Predicted variation in coil losses with speed for a coil with a single conductor region per turn and a coil in which the cross-section of one turn is divided into 5 parallel paths as defined in Figure 108

In summary, this series of simulations has demonstrated the many difficulties in realising the potential of additive manufacturing coils in many aerospace electrical machine applications, particular high speed starter generators with ratings of many 10s of KWs to low 100s. This type of machine is characterised by high electrical frequencies and very low number of turns per coil.

Although some remedial features have been explored, albeit superficially, and demonstrated some scope to reduce losses, in this particular application they did not get remotely close to providing a competitive solution to highly stranded conventional conductors. There may be further reductions possible through a much greater level of sub-division and narrowing of the slot opening, but it is reasonable to contend that additive manufactured coils are not competitive in this type of machine. Their forte, is likely to be in lower speed machines with a higher number of series turns of much smaller overall cross-section.

6.5 PACKING FACTOR IN ADDITIVE MANUFACTURED COILS

6.5.1 REFERENCE COIL DESIGN

This section describes some practical aspects of producing a functional electrical machine coil using additive manufacturing techniques, in particular the clearance between turns to achieve competitive packing factors. One of the major cited benefits of using AM is increased packing factor. The packing factor is defined in this context as the ratio of copper cross-sectional area to the overall coil cross-section area. The outer surface of the coil would be dimensioned and profiled to closely match the shape of the slot.

A generic coil design with rectangular strands was selected as a starting point to verify the integrity of coils being manufactured by AM. The coil is made up of 5

turns with a cross-sectional area per turn which is consistent throughout at 17.4mm^2 , i.e. the same value as the demonstrator machine described in chapter 2. The key dimensions are shown in Figure 110 while Figure 111 shows a 3D CAD model of the coil.

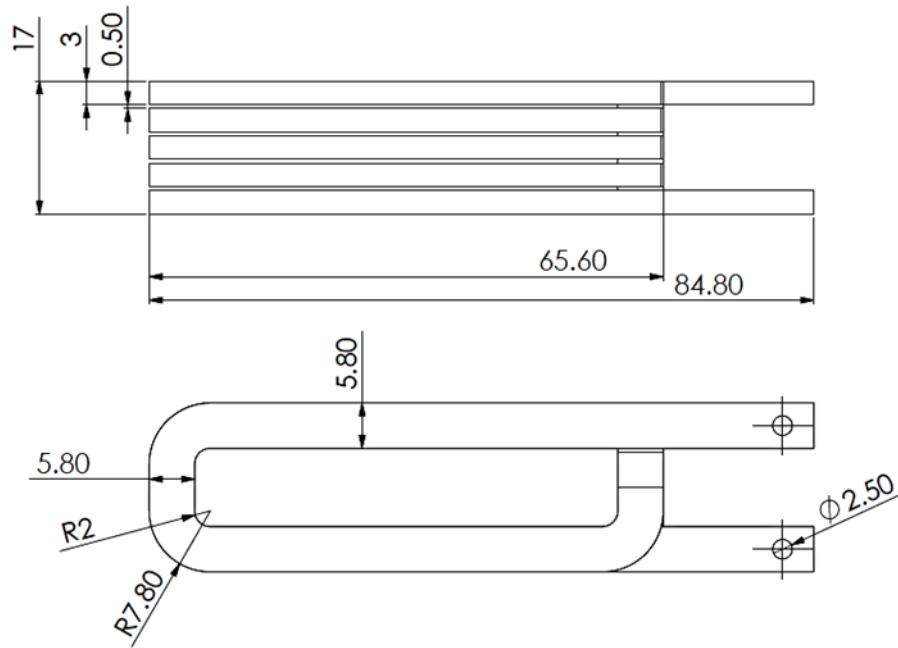


Figure 110 Coil dimensions

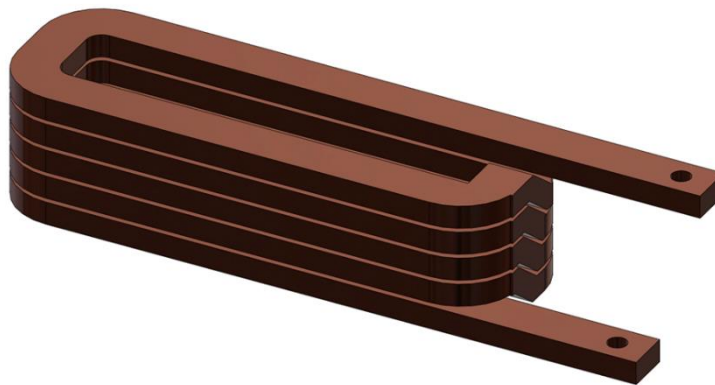


Figure 111 3D CAD drawing of the coil

6.5.2 MINIMUM COIL REQUIREMENTS

The clearance between successive turns of the coil must be maintained to ensure no short-circuiting between them. Figure 112 shows a cross-section through the coil in

which the proportions of the copper and insulation are evident. For the particular case shown, the packing factor is 0.73. A key requirement in the manufacture of a coil, is a post-build process of completely removing any copper powder in the gaps.

Figure 113 shows the calculated variation in effective packing factor as function of the thickness of insulation between turns. With conventional winding techniques, packing factors up to 0.6 or so can be achieved. As shown by Figure 113, the maximum insulation thickness which would still offer an enhancement would be 0.8mm. Conventional polyester insulated winding wires with a temperature range up to 220°C typically have thicknesses between 0.03 to 0.06mm. However, this range of insulation thickness is unlikely to be achievable with an AM coil because of the quality of the surface finish using current technology.

Although these packing factors look attractive, it is important to note that achievable packing factor is more or less proportional to the number of turns per coil for a given insulation thickness. For example, increasing the number of turns in the coil shown in Figure 112 from 5 to 20 would require an insulation thickness of 0.3mm in order to achieve a packing factor of 0.6.

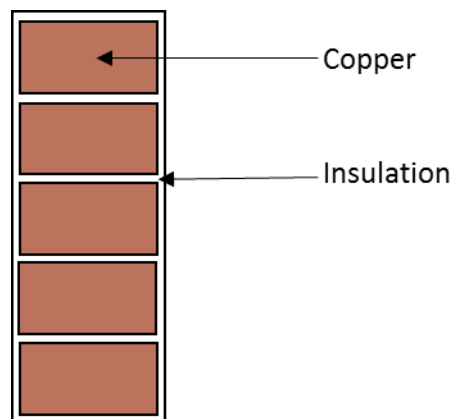


Figure 112 Cross-sectional view of coil in Figure 111, illustrating copper and insulation regions

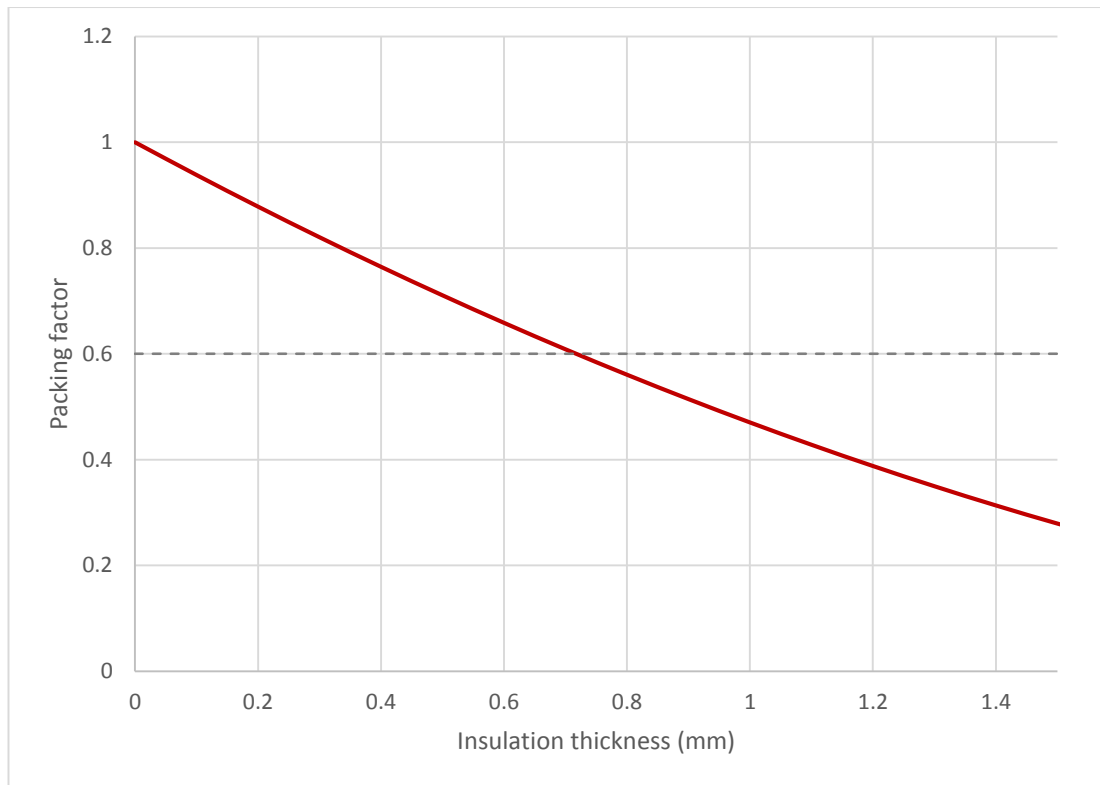


Figure 113 Packing factor against insulation thickness

6.6 CONCLUSION

AM coils can, in principle, provide an improvement to packing factor and thermal performance by incorporating novel geometrical features that are not possible with traditional means of winding. It has been shown that even with only preliminary process optimisation, that competitive electrical conductivities can be realised. However, there is a prohibitive increase in the AC losses when used in the type of electrical machine considered in this thesis, i.e. machines with a high fundamental frequency, large slot openings, and high phase currents, i.e. large cross-sectional area per turn. AM coils are likely to be suited to machines with low fundamental frequencies with lower cross-sectional area per turn and some level of shielding of the PM flux jumping across the airgap.

Chapter 7 CURRENT WAVEFORM OPTIMISATION FOR ENHANCING POWER DENSITY

7.1 INTRODUCTION

The generator design optimisation described in chapter 2 was performed within the context of connecting the generator to an uncontrolled rectifier as shown previously in the circuit diagram of Figure 10. The uncontrolled nature of the power converter means that there is no means of using control to enhance the electromagnetic power capability of the machine. As noted in detail in chapter 2, the power capability of the design is limited electromagnetically (to 50kW in the design which translated in to 36kW in the demonstrator, due principally to the influence of spacing between the magnet pieces within a pole). This chapter explores the additional power capability that could be realised from the demonstrator generator with an active controller and also assesses the capability of a variant on the design which employs a so-called interior permanent magnet (IPM) machine.

7.2 PREDICTED PERFORMANCE OF THE DEMONSTRATOR DESIGN WITH A FULLY CONTROLLER CONVERTER AND SINUSOIDAL CURRENT

The demonstrator design developed in chapter 2 had predicted maximum power capability of 50kW at 17,000rpm, although as discussed in chapter 3, the actual prototype fell short of this because of the sensitivity of the shape and magnitude of the back-emf to the gaps between individual magnet pieces. Taking the 50kW design performance at the baseline for operation with an uncontrolled rectifier and adopting the emf shape and magnitude predicted during the design phase (i.e. the waveform shown in Figure 29, then the power with a fully controlled converter can be established.

For the case of a sinusoidal phase current that is controlled to be aligned with the back emf of that phase, the maximum power was calculated in motoring mode by supplying sinewave currents. By following this procedure, an electromagnetic power envelope with a maximum value of 64kW was established, with a sinusoidal current of 236Arms, which corresponds to an rms current density of 13A/mm². It is worth recalling that the design was optimised for an uncontrolled rectifier, and hence the performance with a controlled converter could be further improved by revisiting the electromagnetic design, most likely resulting in a small increase in the tooth pitch to slot pitch ratio to capture more magnet flux and the expense of an increase in the reactance.

7.3 OPERATION WITH ARBITRARY CONTROLLED WAVEFORMS

Although significant improvements in power density were demonstrated in section 7.2 using a controlled converter, this was for the simple case of a sinusoidal current. A sinusoidal current produces the maximum possible output power per unit of winding loss for machines with a purely sinusoidal emf. As will be illustrated in section 7.4, this fundamental and straightforward relationship, provides a useful check for optimisation algorithms.

For other shapes of emf, there may be alternative non-sinusoidal current waveforms that result in an increased torque per unit winding loss, although the benefits may be small in many cases. In order to select the optimum current waveform (which in a practical system would provide the demand for the current control loop in the power converter) it is necessary to develop an optimisation algorithm for arbitrary waveforms. This is relatively straightforward if an isolated phase is considered since there are no constraints on the arbitrary instantaneous current other than the peak

rating of the converter. However, in a 3-phase star connected system, the instantaneous currents must always sum to zero, a condition that is intrinsically met by three 120° phase displaced sinewaves.

7.3.1 OPTIMISATION ALGORITHM

The starting point for any algorithm is an ability to predict the electromagnetic torque at any rotor angle for any given current. In its most basic form, this could be established from a single open-circuit emf waveform, although this would miss the influence of magnetic saturation. Alternatively, non-linear finite element modelling could be used to pre-characterise the machine, e.g. generate a look-up table of torque versus current at each angular increment at discrete values of current.

With this ability to calculate torque for any combination of rotor angular position and current, the total current available is divided up into a large number of small increments (typically several thousand in order to get a smooth waveform) and an electrical cycle is divided up into a number of discrete angular positions, e.g. 180 for 1° increments over half an electrical cycle etc.

A MATLAB algorithm was developed that sequentially progresses through each angular position, temporarily adding the small increment of current onto the existing current already assigned to that angular position (which all start at zero). On the nth pass through of the angles, the algorithm calculates the increase in torque and the increase in copper loss at angle (ang) using:

$$\frac{\Delta T_{ang(n)}}{(\Delta Ri^2)_n} = \frac{T_{ang(n)} - T_{ang(n-1)}}{Ri_{ang(n)}^2 - Ri_{ang(n-1)}^2} \quad (12)$$

Having swept through the full range of angular positions, the angle which has the highest value from equation (12) is permanently allocated that particular increment of current, and then the entire process repeats building up the waveform until the desired RMS value is reached. It is important to note that the number of increments of current added to reach a particular RMS value cannot be known in advance as it depends on the shape of the waveform. A flowchart of the algorithm is shown in Figure 114

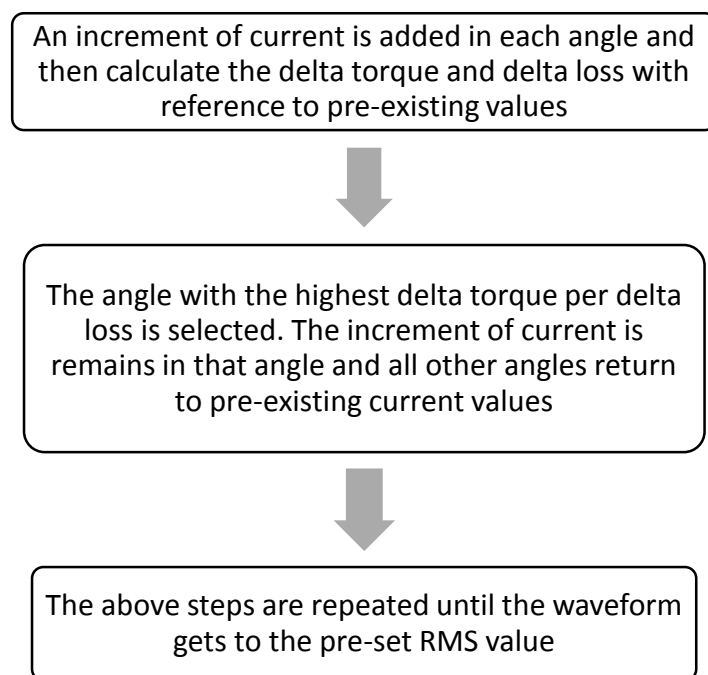


Figure 114 Flowchart of the optimisation process

The key to this algorithm is that the increment in loss is dependent on existing value of current already assigned to that angular position and hence the current naturally spreads out across the rotor angular positions rather than concentrating in the regions of highest torque per amp.

If each phase of the machine is considered separately, which in practice could be achieved with each phase being driven by an independent H-bridge, then this algorithm can be applied to a single phase. However, if significant saturation occurs,

then this single-phase module will not capture some mutual interactions caused by saturation from the currents in other phases.

If there is a need to perform the optimisation on all three phases at the same time, e.g. because they are star connected and/or to capture all saturation effects, then the complexity of the algorithm and the amount of pre-characterisation increases significantly. Fortunately, the constraint in a star-connection that the three currents sum to zero mean that there are only two degrees of freedom in terms of the values of current that need to be modelled, e.g. torque at each angular position for combinations of values of I_a and I_b with I_c being implied through the zero sum constraint. Hence, for a three-phase star-connected machine, it may be necessary to pre-characterise the torque producing capability for all-inclusive combinations of the following three degrees of freedom: rotor angular position, magnitude of current in phase A and the magnitude of current in phase B. Even with relatively coarse increments in each, this will require a large number of static finite element calculations to be performed in advance in order to populate the look-up tables, e.g. 180 rotor angles at 15 values each if I_a and I_b requires 40,500 calculations, i.e. $(180 \times 15 \times 15)$.

7.4 OPTIMISATION STUDIES

7.4.1 VERIFICATION OF THE OPTIMISATION ALGORITHM

The waveform optimisation algorithm for a three-phase star-connected machine was first tested by populating a full torque look-up table from a pure sinusoidal EMF with no saturation effects. Using this data, set, the algorithm should build up current waveforms in all 3 phases that are a balanced set of sinusoids. Figure 115 shows the the optimum current waveform, as expected a series of three sinusoids.

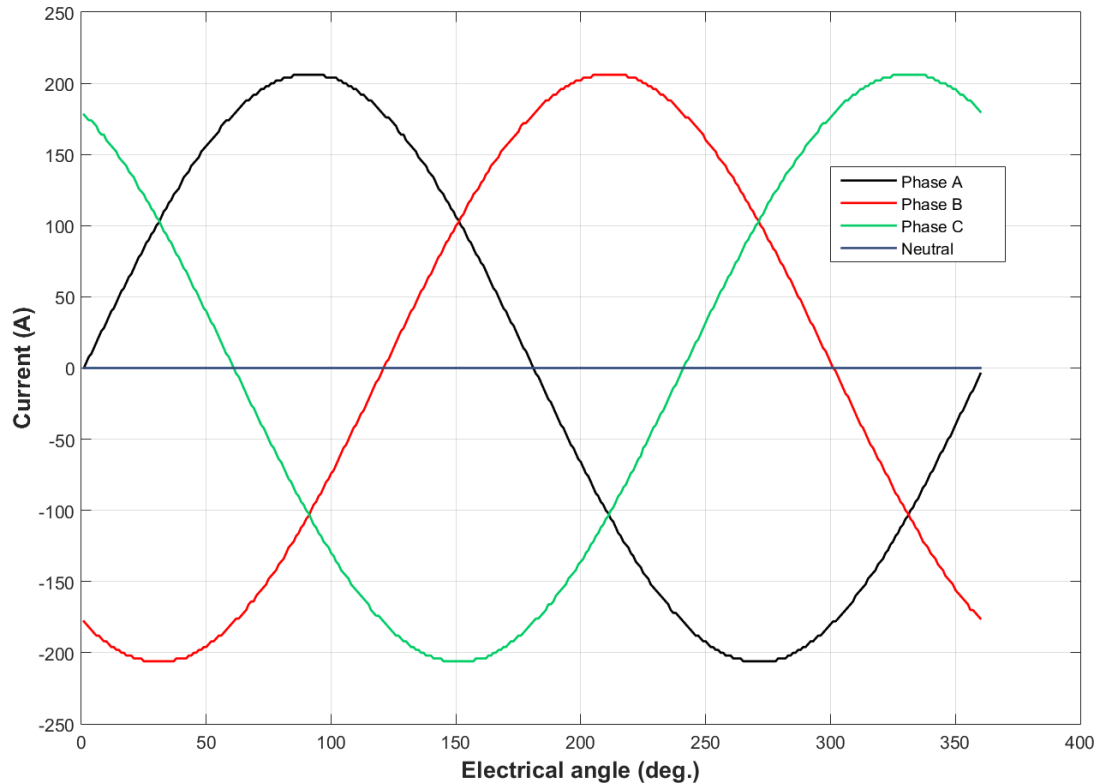


Figure 115 Optimised current waveforms generated by the optimisation algorithm for torque look up tables populated from an idealised sinewave back-emf

7.5 OPTIMISATION OF CURRENT WAVEFORM FOR THE DEMONSTRATOR DESIGN

The variation in output torque of the demonstrator design was incorporated into a series of look-up table and the current waveform optimised to produce maximum torque for a copper loss equivalent to an rms current density of 8.4A/mm^2 (i.e the baseline for the demonstrator design). The optimised current waveforms are shown in Figure 116. As will be apparent, these are several small inflections and dips in the current waveforms, notably near zero crossings which are likely to be the result of the interpolation between discrete data points and the need to satisfy the constraint that the currents must sum to zero. The average torque produced by these optimised current waveforms is 23.6Nm as compared to an average of 22.3Nm with 3 sinusoids producing the same copper loss (assuming the coils are at the same temperature and

hence resistance). The torque waveforms for the original sinusoid and the optimised current waveforms are shown in Figure 117.

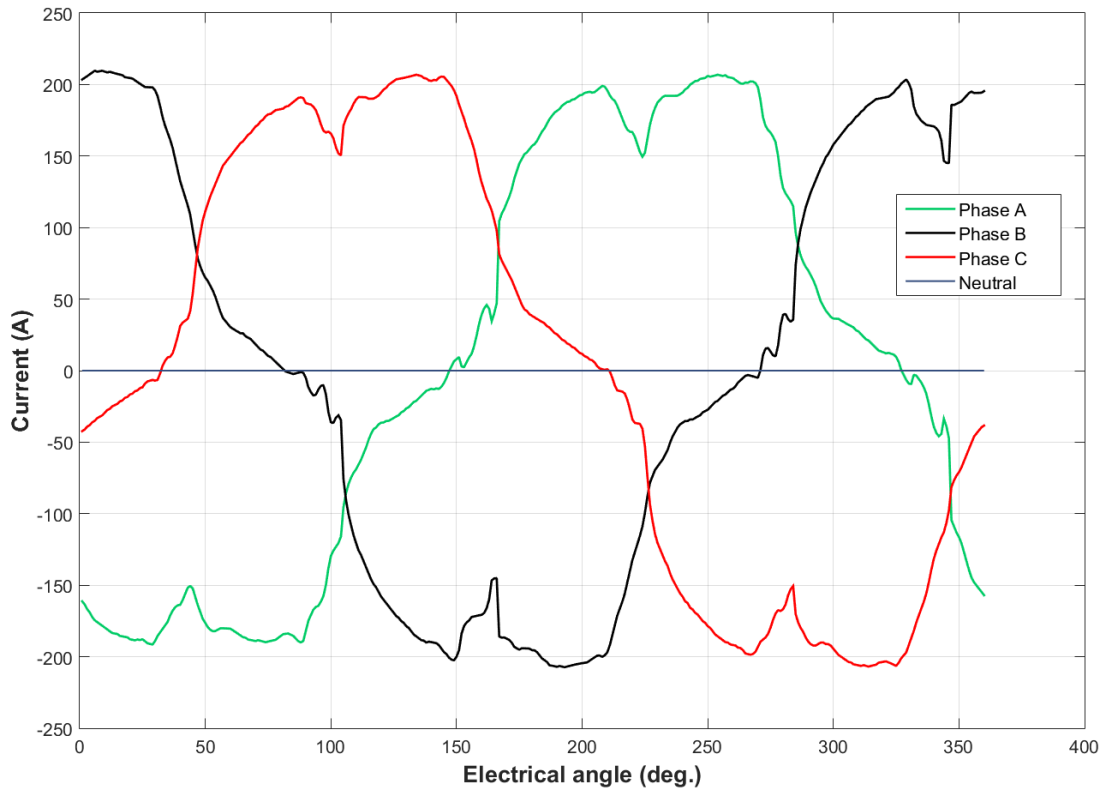


Figure 116 Optimised current waveform generated for the prototype machine described in chapter 2 and 3

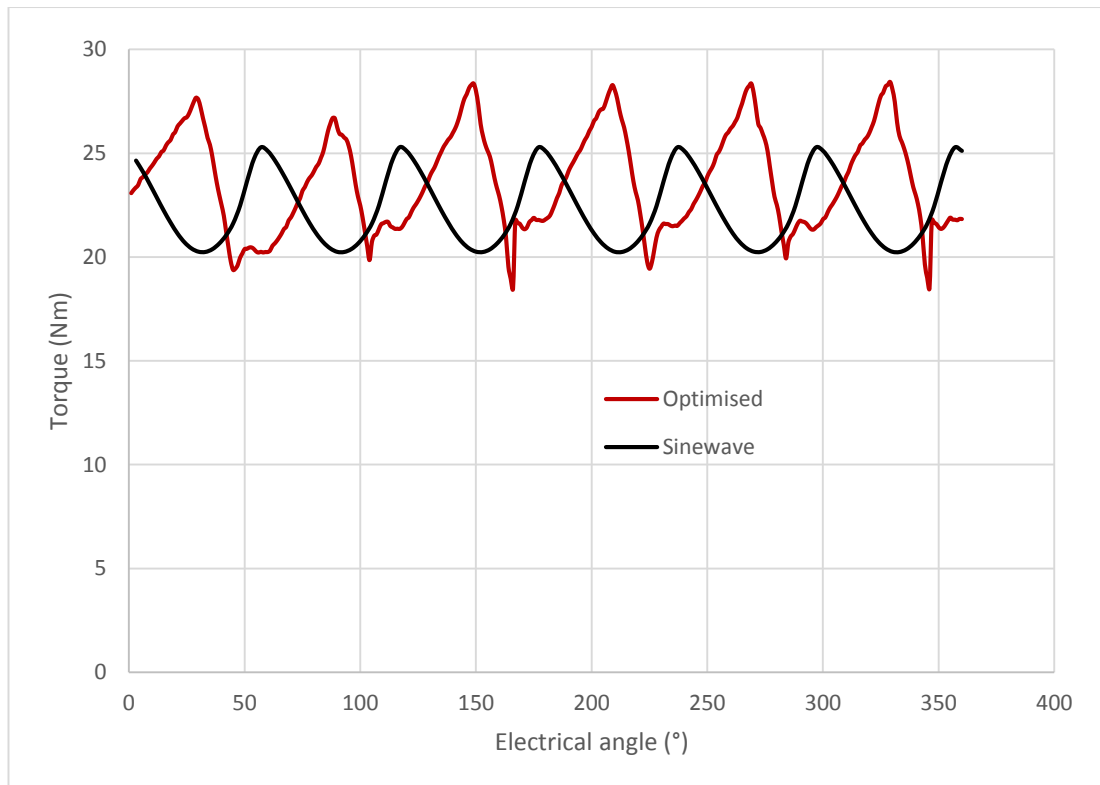


Figure 117 Torque waveform for the pure sinusoid and the optimised current at 8 Amm⁻² when supplied to the demonstrator

The optimisation algorithm has shown some dividends in terms of enhancing the torque capability compared to a sinusoid. This is to be expected given the non-sinusoidal emf and the likelihood of magnetic saturation being present on some regions of the current waveform. However, this is a rather simple case as there is little saliency in the rotor (beyond the non-circular geometry of the rotor hub which consists of ten flats). Machines with more saliency might benefit more from a move away from sinusoidal currents, and to investigate this, a variant on the original design was considered with a so-called interior permanent magnet (IPM) rotor.

7.6 INTERIOR PERMANENT MAGNET MACHINES

7.6.1 ROTOR GEOMETRY AND TORQUE PRODUCTION

Interior permanent magnet (IPM) machines rotors incorporate the array permanent magnet within apertures in the rotor core rather than mounting them on the surface of

the core. This arrangement give rise to some degree of saliency in the rotor and hence IPMs are able to produce an extra component of torque from reluctance torque. IPMs have gained popularity in the automotive industry since the saliency increases the flux-weakening capability and hence, the constant power speed range achievable from a given converter VA [45-47]. The reluctance torque is directly proportional to the saliency ratio, i.e. the ratio of the maximum to minimum inductance, and is dependent on several factors: the geometrical positioning of the magnets on the rotor, level of saturation in the core and the stator winding layout. A higher saliency ratio can be achieved using distributed winding than concentrated windings [48].

The case considered in this chapter, is limited to a replacement of the rotor into the similar existing 15 slot, 3-phase stator, a topology that will have a lower saliency ratio as a fully re-designed IPM, e.g. the adoption of a distributed winding in say a 30 slot design. It is worth noting that some authors [48, 49] have reported on the optimisation of the saliency ratio for fractional-slot concentrated winding.

The presence of reluctance torque provides an opportunity to increase the average torque produced by the conventional sinewave current excitation by maximising the summation of the reluctance torque and the excitation torque. This is traditionally achieved by phase shifting a sinusoidal current as the magnitude of the current increases to optimise the contribution from the reluctance component, i.e. gradually increasing the contribution of the direct-axis current.

The magnitude of the reluctance torque is proportional to the square of the current, as shown in Equation (13) and hence the reluctance torque has greater scope to make a contribution at higher current levels. High current loading may cause magnetic

saturation which reduces the saliency ratio [48] but this behaviour is likely to occur at a significantly lower rate than the current squared.

$$T = \frac{3}{2}n_p[\psi_{pm}i_q + (L_d - L_q)i_d i_q] \quad (13)$$

Maximum torque per amp (MTPA) optimisation is achieved in general by tuning the relative magnitudes of the d and q axes currents using various methods [50-53]. Relatively few authors have focus on optimising the shape waveform or profiling of the current [54-57]. An estimation of the optimised current waveform using mathematical expressions using Lagrange has been proposed by [56]. It takes into account, the star connection constraint and any asymmetry in the back emf but does not take into account any non-linearity that may arise from saturation. In a method proposed in [57], the optimum current waveform is generated using the harmonics in the back-EMF. However, at high current density, the optimal waveform deviates from the harmonics present in the back-EMF as the reluctance torque becomes more significant.

The optimisation algorithm described in section 7.3.1 provides an alternative method of enhancing the torque produced, in particular by placing current asymmetrical across the cycle to enhance the useful contribution from reluctance torque.

7.6.2 REFERENCE IPM DESIGN

The optimisation process was performed on the IPM design shown in Figure 118 and whose leading dimensions are summarised in Table 29. The stator core is almost identical to the demonstrator, except the slot pitch-to-tooth pitch ratio and the tooth body values was increased and the stator coils have the same 5 turns per coil. The rotor design follows a reasonably standard approach to magnet geometry and orientation, although would be expected the degree of saliency is only modest.

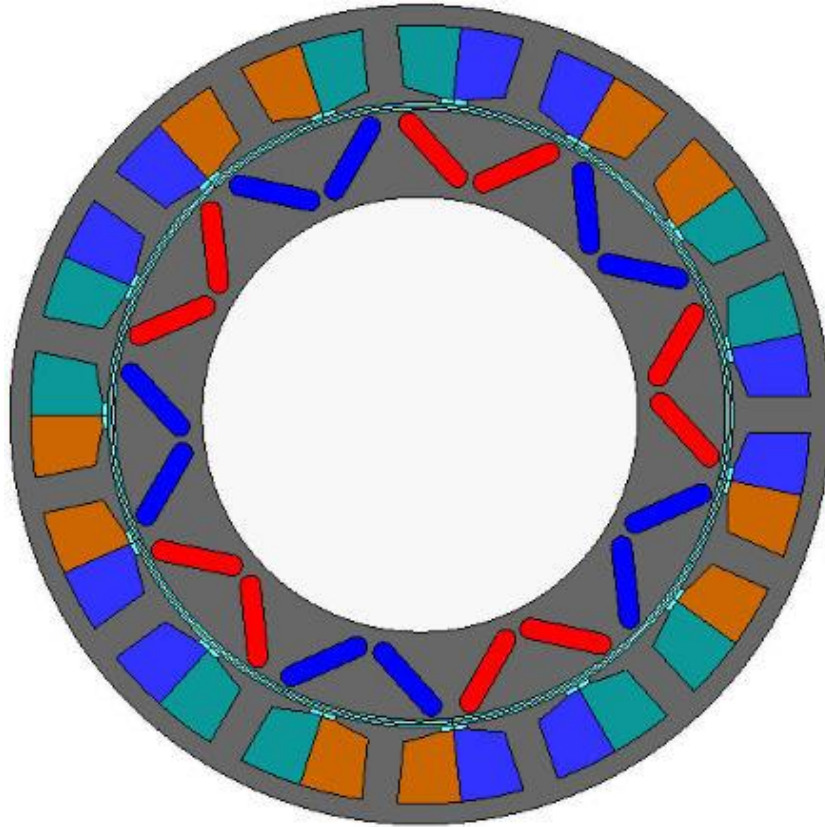


Figure 118 Cross-section of IPM FEA model

Table 29 Key dimensions of the IPM machine in Figure 115

Key dimensions	Value (mm)
Stator outer diameter	160
Stator bore	120
Stator back iron thickness	4
Tooth body	7
Rotor outer diameter	118
Rotor inner diameter	85
Magnet length	14
Magnet V-shape angle (°)	104

7.7 SINGLE PHASE OPTIMISATION

7.7.1 TORQUE PRE-CHARACTERISATION

The torque was calculated with a magneto-static FE model for a range of current densities from -30 to 30 A/mm² (corresponds to currents of -876 A – 876 A) at 1°

electrical degree steps across 360° electrical of rotor angular displacement. The model was solved using DC currents, in increments of $29.2A_{DC}$ in one phase only for the isolated phase optimisation, i.e. optimise one phase without regard to the star-point connection constraint. For each value of current, the torque at every angle was stored in a three dimensional array. The total number of FE calculations performed for this analysis was 625. Figure 119 shows representative examples of the torque waveforms generated.

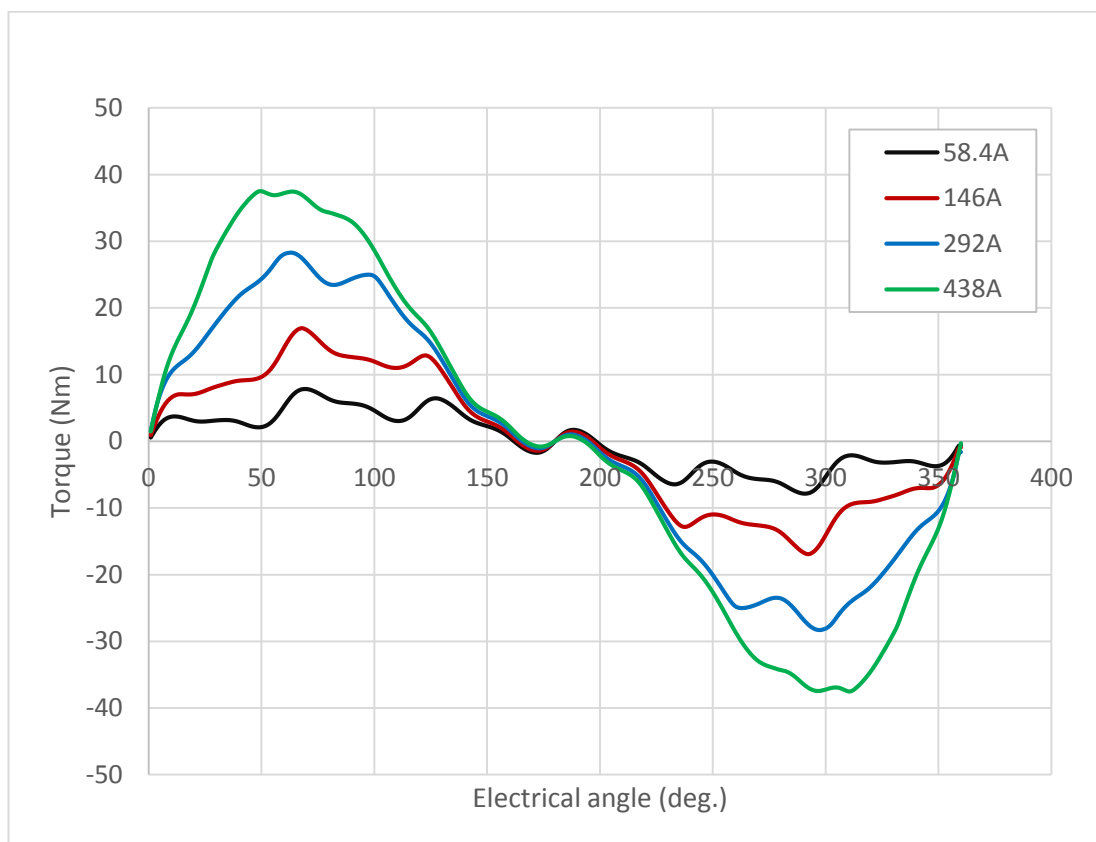


Figure 119 Torque waveform for a range of DC currents at a speed of 17,000 rpm

The complete set of torque data was fed into the algorithm. A spline interpolation was then carried out to produce a grid which could be reliably interpolated to predict the torque at any angle for any given value of current. The accuracy of the interpolation was verified by comparing the torque and produced by FEA and the

Matlab algorithm for the same current waveform. One such example is shown in Figure 120.

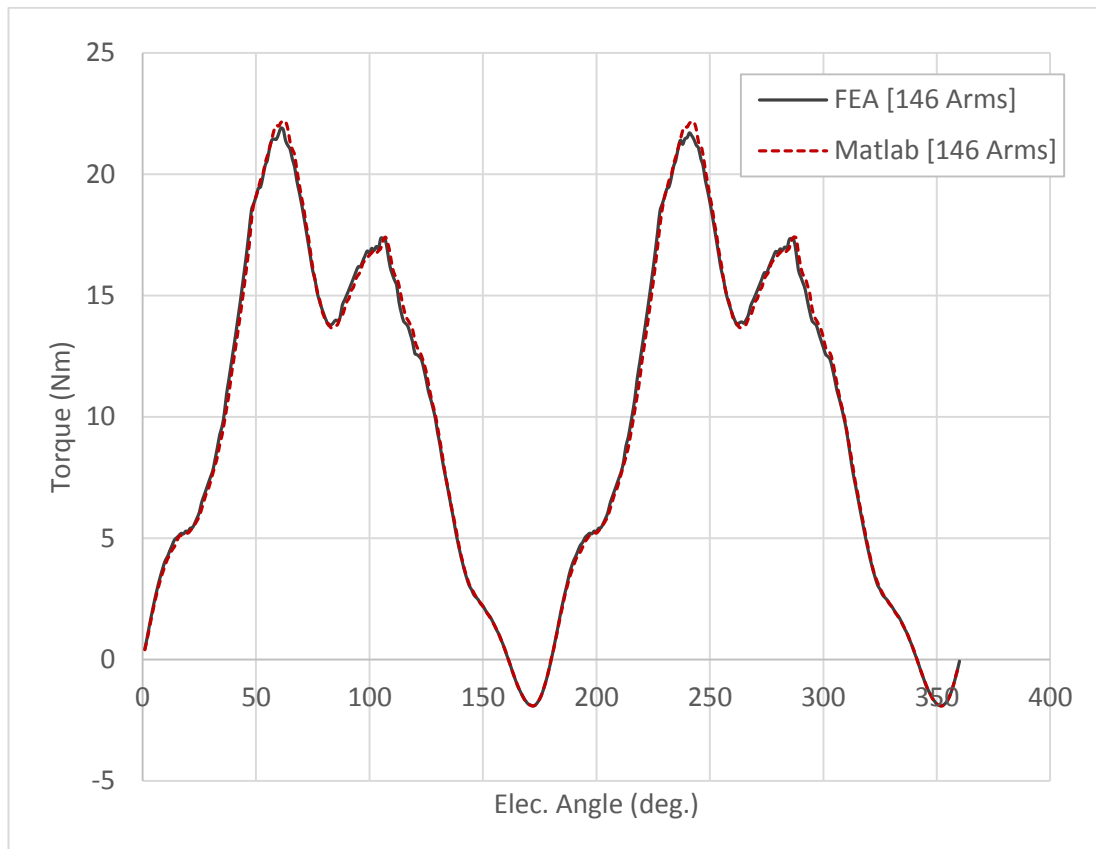


Figure 120 Verification of the spline interpolation prediction

7.7.2 RESULTS FOR SINGLE PHASE OPTIMISATION

At low current densities, the optimised current waveform will tend to approach the shape of the back-emf waveform. This is because optimising the current waveform using back-emf will generate a current waveform consisting of identical harmonics present in the emf [55, 56]. However, as the current density increases the optimum waveform deviates from back-EMF profile as non-linearity due saturation and cross-coupling become more pronounced. Figure 121 shows a plot of the optimum waveform for an RMS current of $292A_{rms}$.

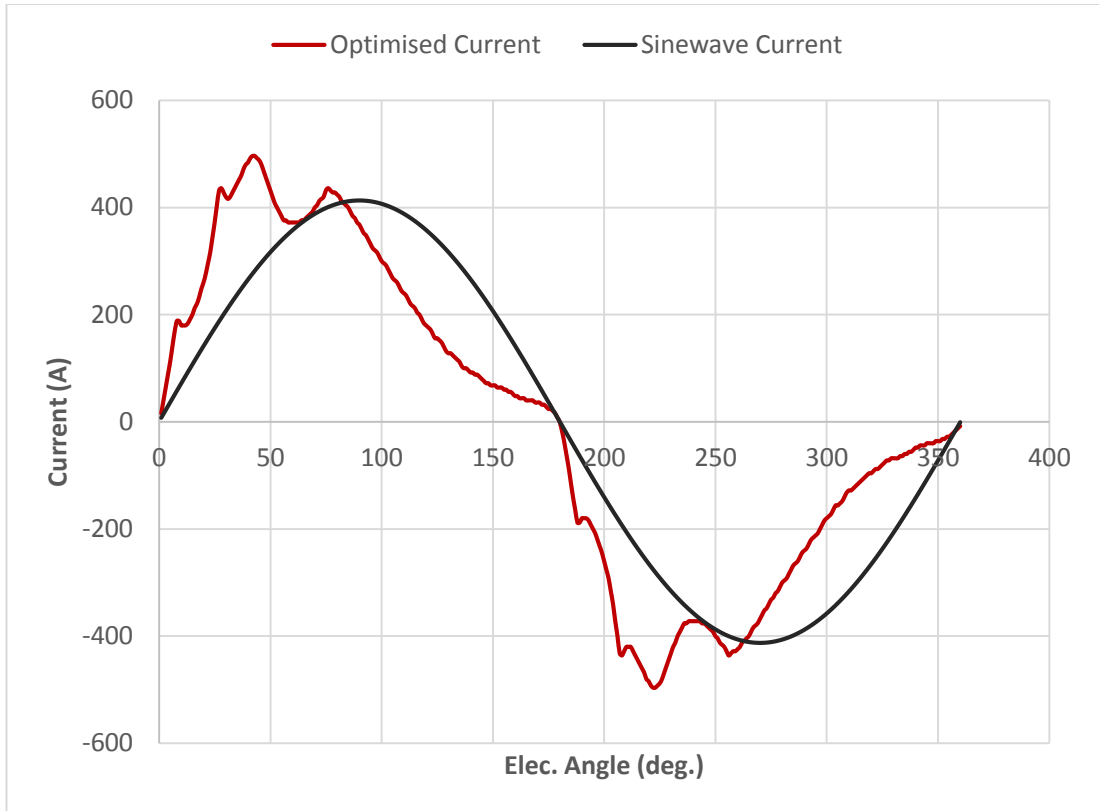


Figure 121 Comparison of optimised and sinewave current of the same RMS value of $292A_{rms}$

The finite element predicted torque produced by the optimised current waveform was compared with the torque produced by a sinewave of an equivalent RMS magnitude as shown in Figure 122.

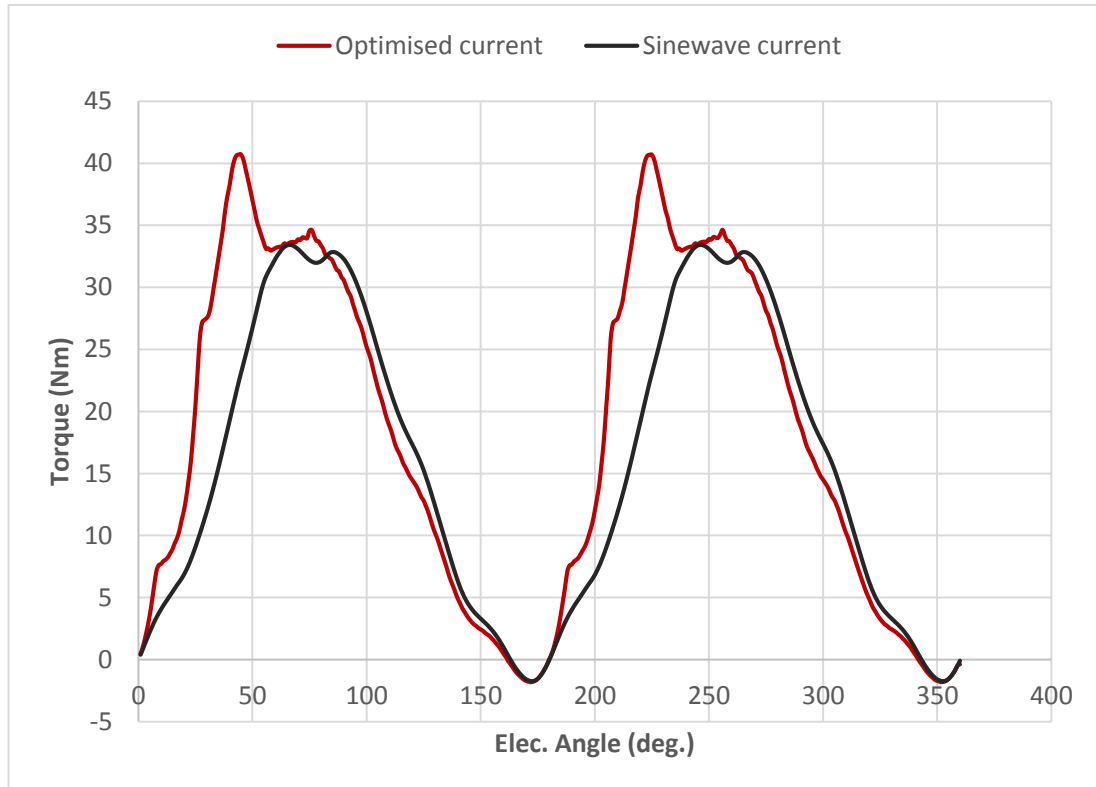


Figure 122 Comparison of torque produced by phase A when excited with a sinewave current (in phase with back-EMF) and the optimised current waveform of the same RMS value

The improvement in torque produced by the optimised waveform compared to an equivalent sinewave increases as the magnitude of current increases, at least up to a point. Beyond a certain point, the level of saturation reduces the saliency and little discernible further improvement is achieved for any higher current loading. A summary of the findings is shown in Figure 123 and Table 30, from which it can be seen that the optimised current waveform can increase the torque (and hence power providing the converter can deliver the demand waveform).

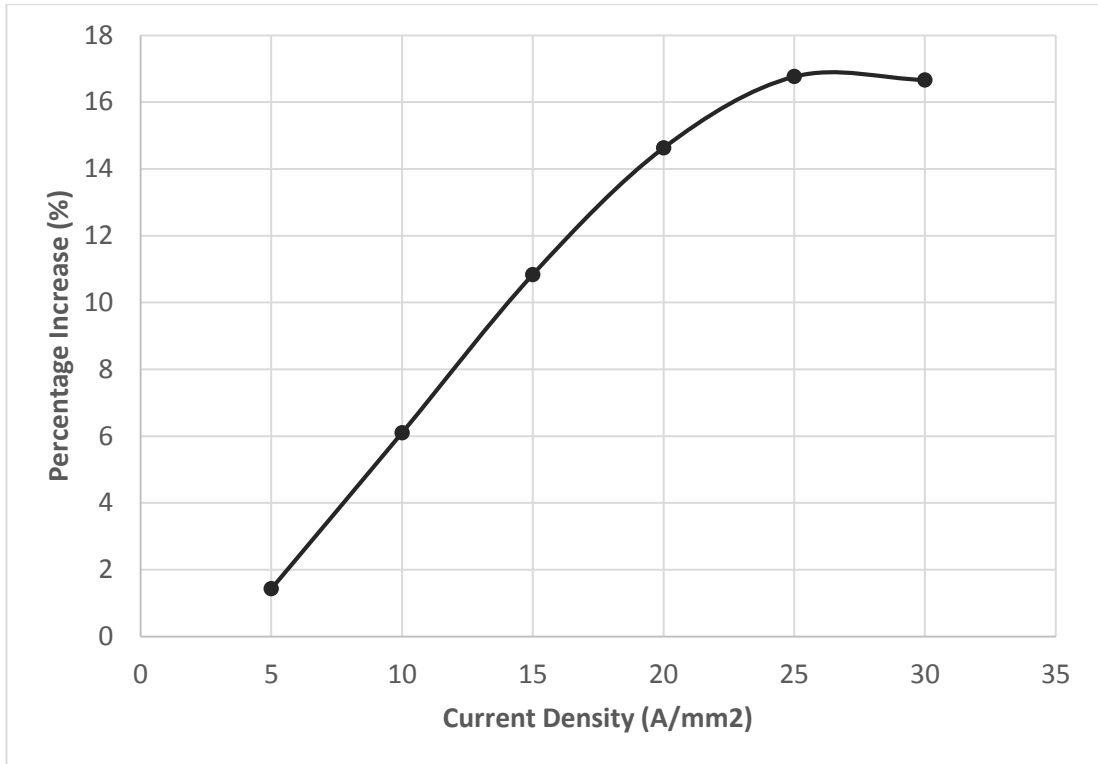


Figure 123 Percentage increase in torque produced by the optimised current waveform for a range of current densities

Table 30 Comparison of torque produced by sinewave (in phase with back-emf) and optimised current waveform for varying current densities

Current Density (A/mm ²)	Torque (Nm)	
	Sinewave ($\alpha=0^\circ$)	Optimised waveform
5	4.94	5.01
10	9.34	9.92
15	12.97	14.38
20	15.94	18.27
25	18.38	21.46
30	20.41	23.81

It is important to note that the benefits shown in Table 30 were comparisons against a sine-wave with no phase shift, whereas it may be possible to exploit some of the reluctance torque capability by phase advancing the sine-wave. The torque produced

by phase advancing the sinewave current was simulated using FEA for a range of angles as shown in Figure 124. The reluctance torque contribution increases and the magnet excitation torque begins to decrease but at a much lesser rate and hence the overall torque is increased up to a maximum at $\sim 20^\circ$ in this case.

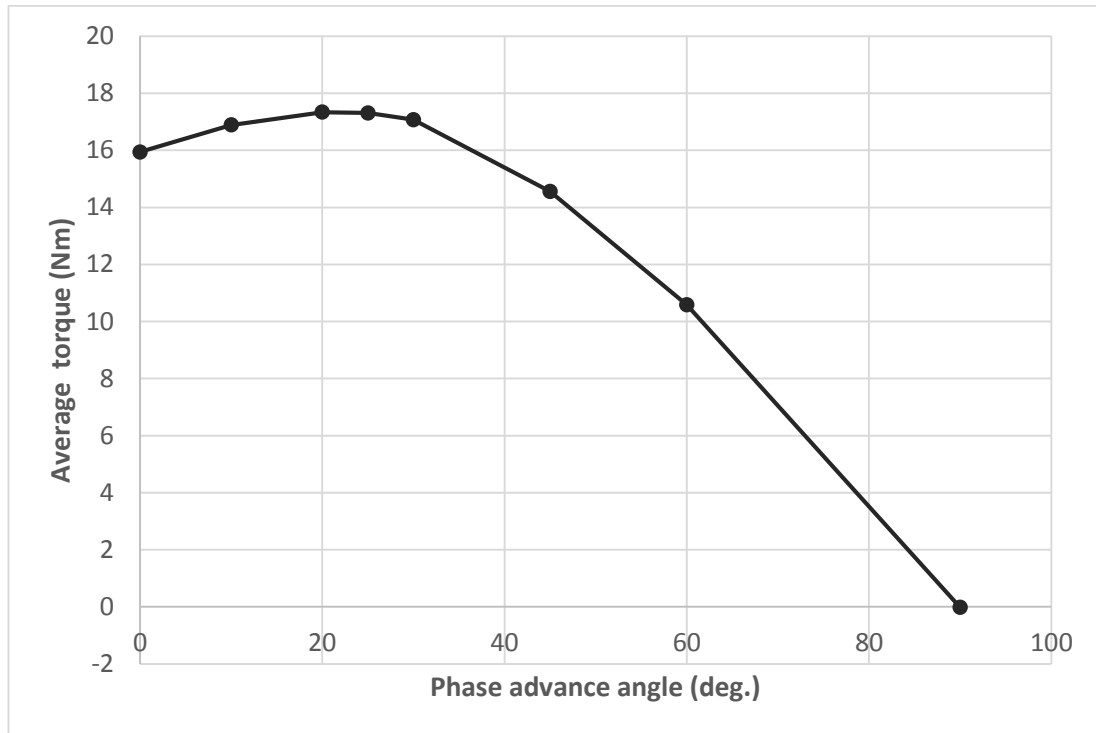


Figure 124 Plot of average torque for varying phase advance angle at current density of $20\text{A}/\text{mm}^2$

This technique is relatively simple to implement, therefore it is only a fair analysis to compare the maximum torque using the phase advancing technique with the torque produced by the optimised current waveform. This comparison is shown in Figure 125, which still shows an improvement in torque with the optimised current, but the benefit has decreased from 14.6% to 5.4%.

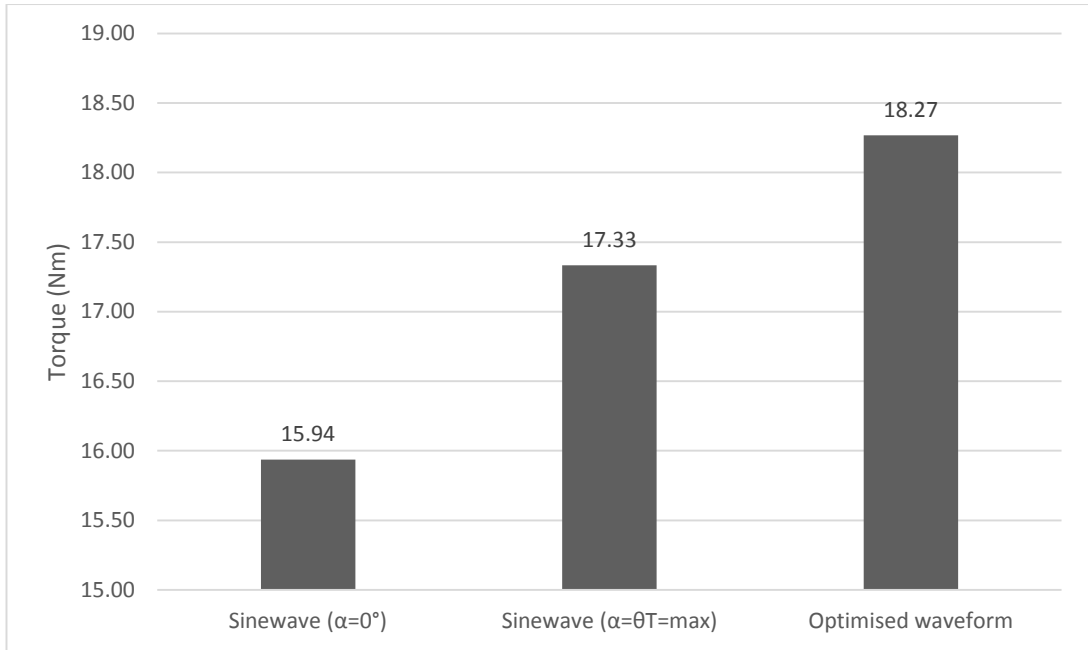


Figure 125 Comparison of average torque for the same RMS current of 292 A_{rms} ($20 A/mm^2$)

Figure 126 shows the changing shape of the optimised current waveforms (notably its increasing asymmetry) as the current density increases. This is due to saturation and the reluctance torque.

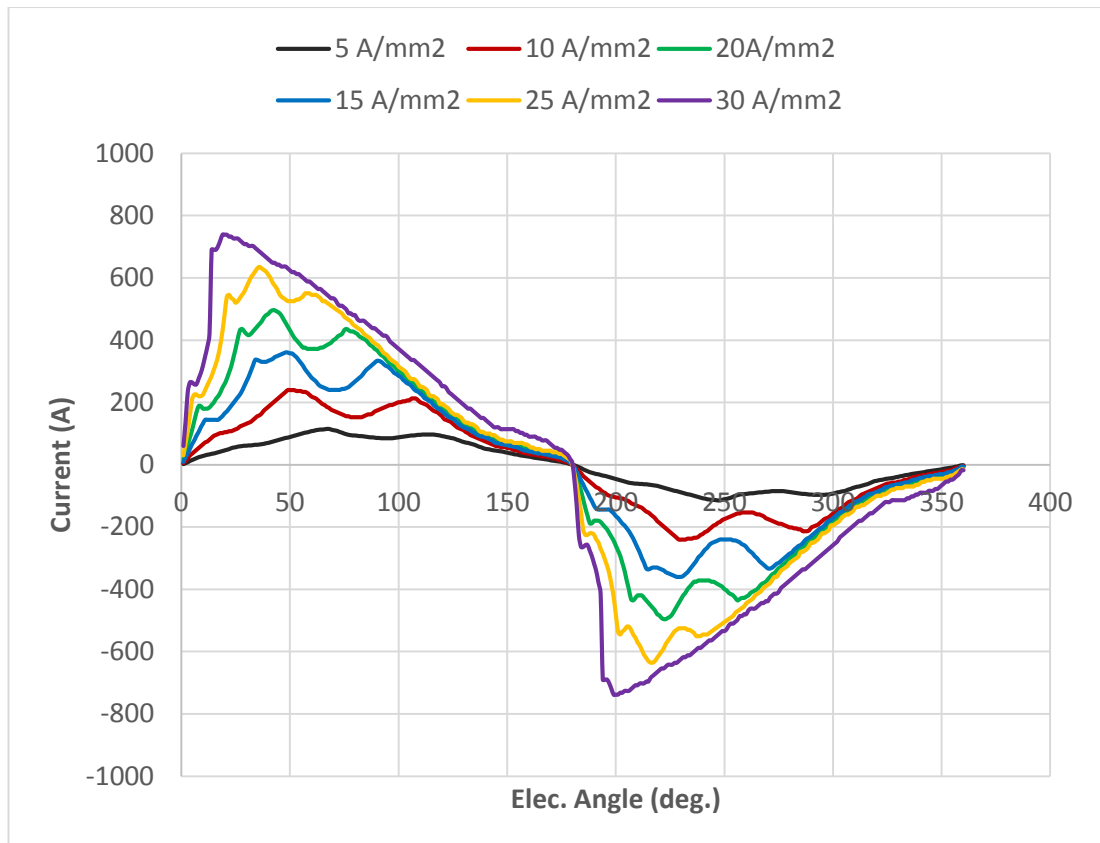


Figure 126 Optimised single phase current for a range of current densities

7.8 THREE PHASE OPTIMISATION

This is the more complex case with less degree of freedom, since the star-connection forces a relationship between the phase currents. It also fully captures the effect of mutual saturation effects that are not present in the single-phase model, which relies on superposition.

7.8.1 TORQUE PRE-CHARACTERISATION

The FE model was used with DC currents in all three phases and the sum of these currents was forced to be zero. Therefore, all-inclusive combinations of the Phase A and Phase B currents between -700.2A and 700.2A in increments of 58.4A were simulated, with the current in phase C set to satisfy the star-point constraint in each case. The four variables: phase-*a*, phase-*b*, angle and torque (phase-*c* is determined by phase-*a* and phase-*b*) were arranged in a 3D grid.

7.8.2 OPTIMISATION ALGORITHM

The complete set of torque-current data (comprising 225,000 separate data points) was loaded into the algorithm and arranged into a 3D grid of torque against phase-*a* and phase-*b* current for each angle. A spline interpolation was carried out using the 3D grid. From Figure 127, it can be observed that the original FEA torque data and the data generated by interpolation of the look-up table have good correlation. Figure 128 shows 1 of the total of 360 contour map representation of the torque data, in this specific case for angle 35°.

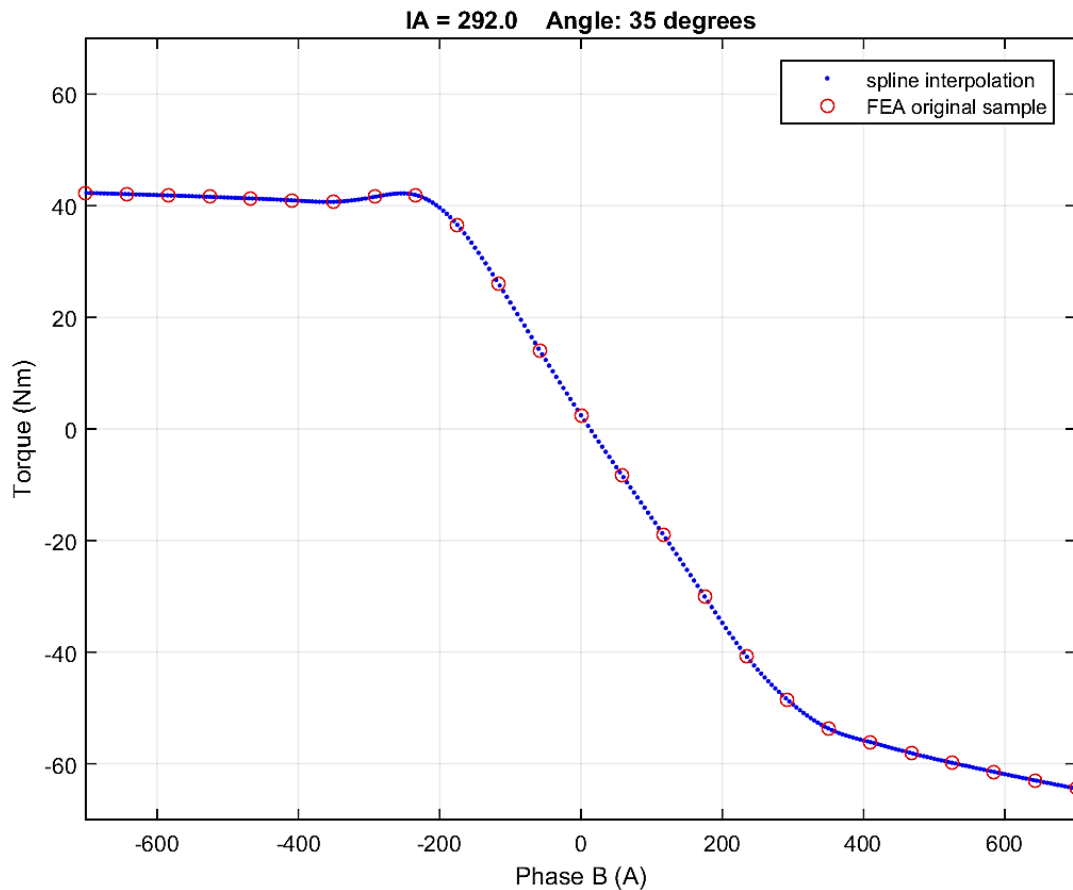


Figure 127 Plot of torque against phase-*b* current using FEA and gridded-interpolation for a phase-*a* current of 292A at angle 35°

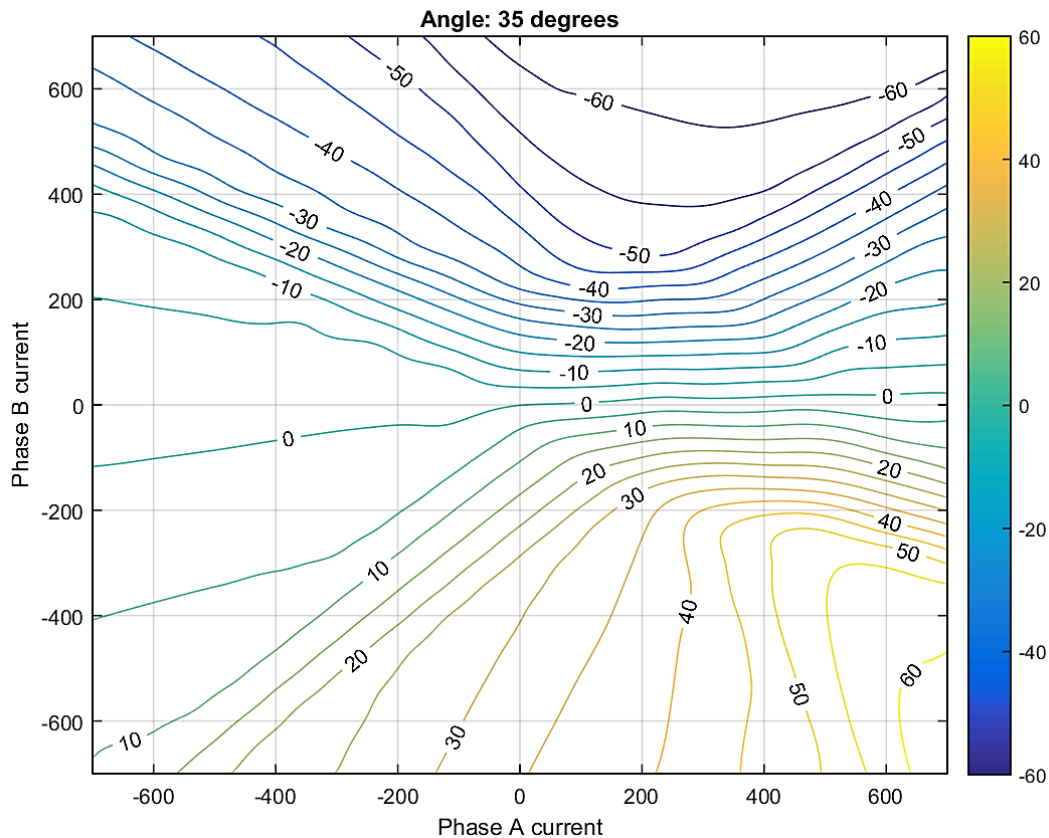


Figure 128 Contour map of the torque produced by interpolation at angle 35°

The optimisation decision process operates in a similar manner as the single phase case. The angle to which a particular combination of phase-*a*, phase-*b* and phase-*c*, increments of current was selected, are based on the total change in torque per unit change in copper loss.

7.8.3 ASSESSMENT OF THE OPTIMISED THREE PHASE CURRENT WAVEFORMS

Figure 129 and Figure 130 shows the optimised current and torque waveforms respectively at a current density of 5A/mm^2 . There is 0.8 Nm (5%) increase in torque when compared with a sinewave with no phase advance (i.e. the current and the emf are in phase). Figure 131 and Figure 132 shows the current and torque waveform at a higher current density of 20Amm^{-2} . The torque produced by the sinewave current with no phase advance has increase by 10.9Nm (29%) using the optimised currents. There is a greater improvement in the torque due to the optimised

currents as the current density increases. It is worth noting that there are some minor imbalances in the current waveforms, with small features that are not present to the same degree in all phases. Detailed inspection of the algorithm and the data tables indicate that these may be due to some interpolation effects in the very intricate multi-dimensional data tables.

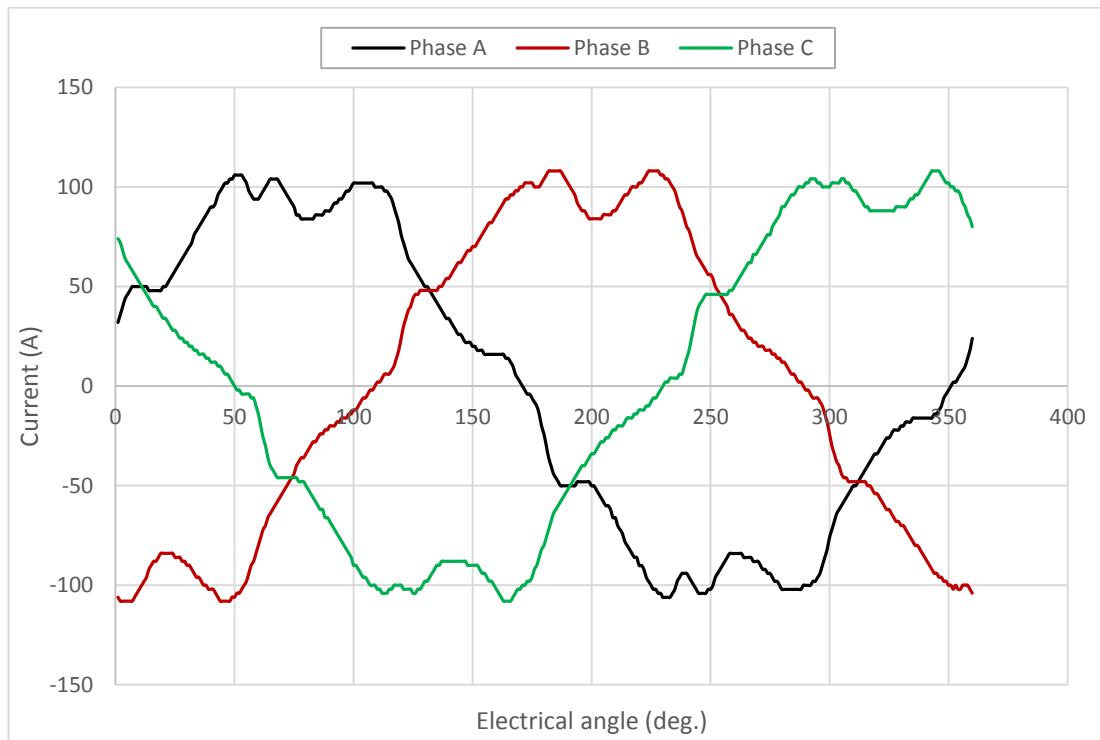


Figure 129 Optimised current waveform at a current density of 5Amm^{-2} (73A_{rms})

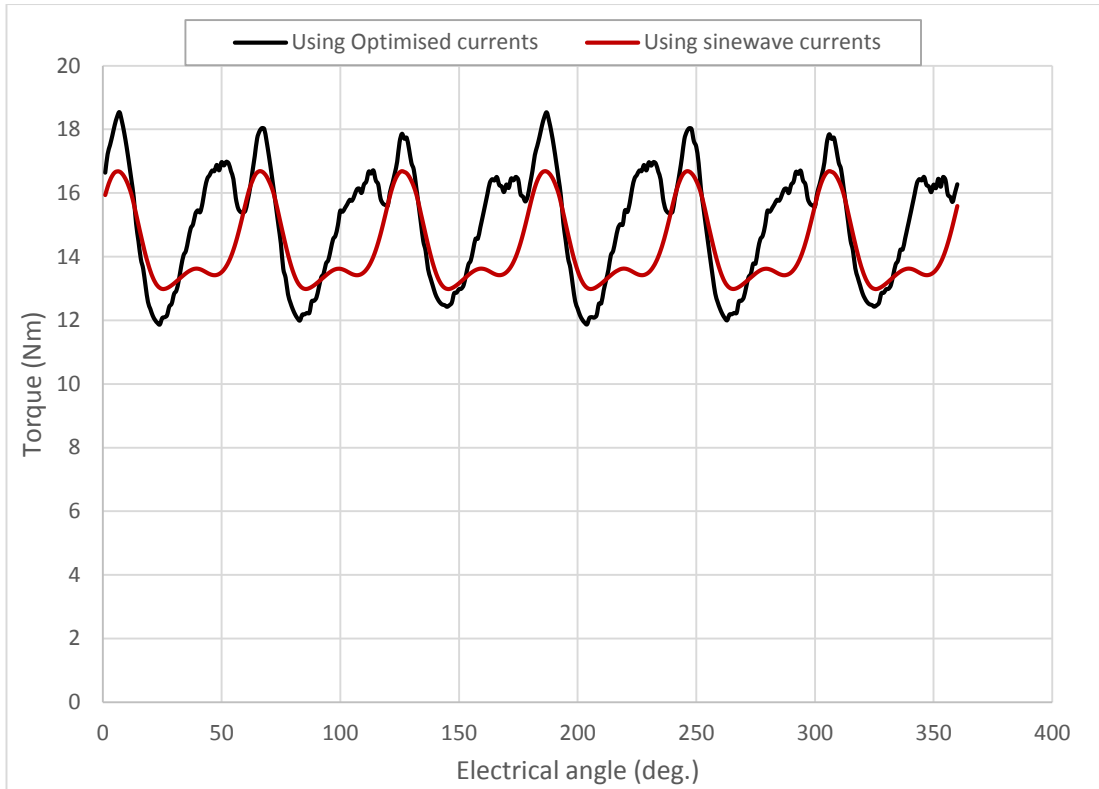


Figure 130 Torque comparison of the optimised (Figure 129) and sinewave current of the same RMS value at a current density of 5Amm^{-2} (73A_{rms})

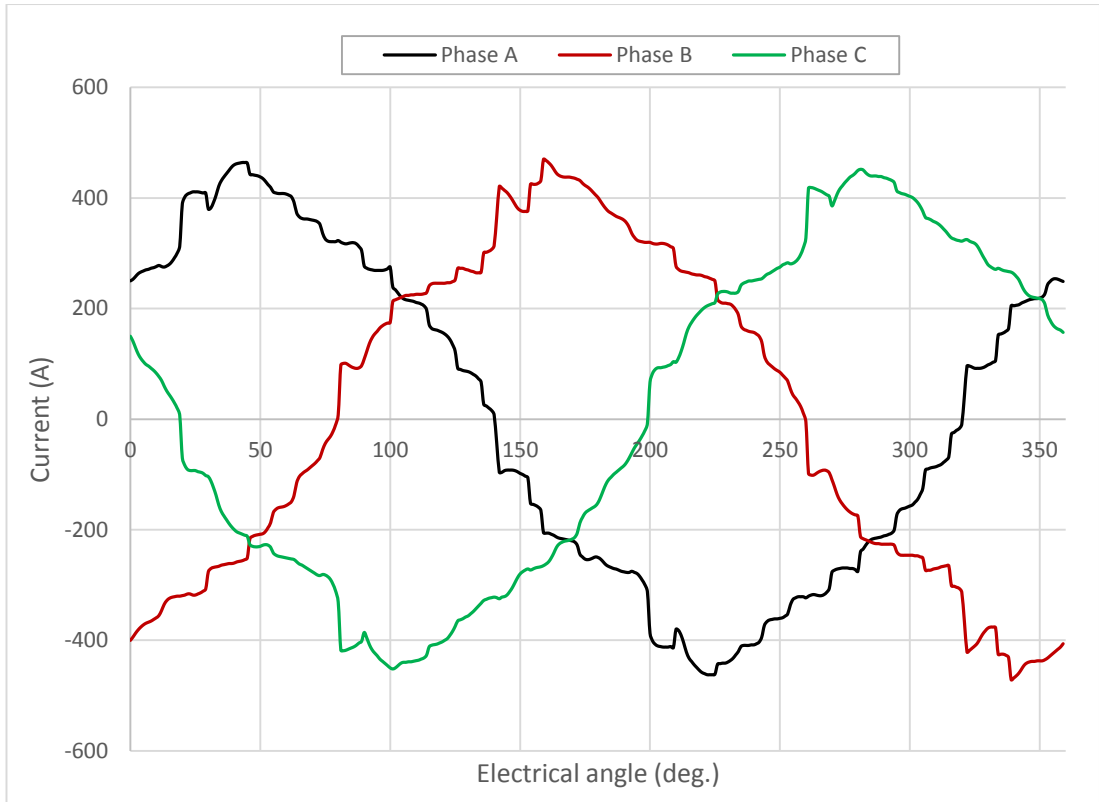


Figure 131 Optimised current waveforms at a current density of 20Amm⁻² (292A_{rms})

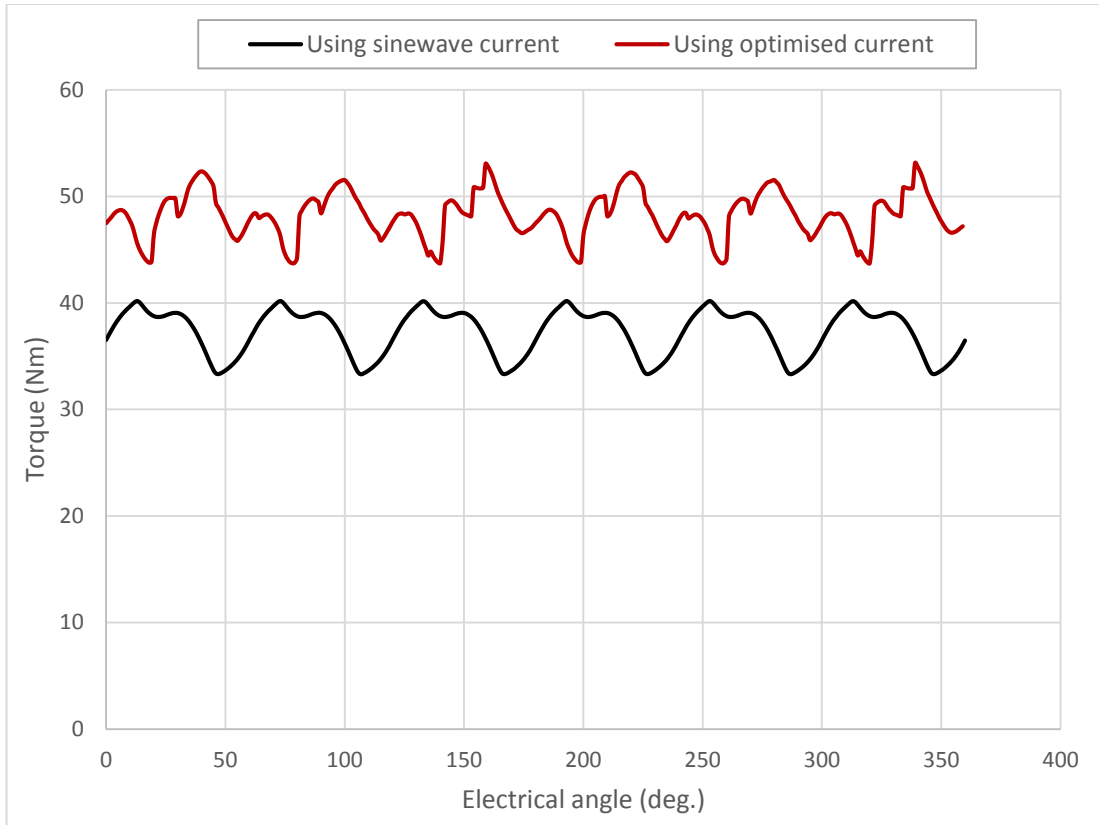


Figure 132 Torque comparison using optimised (Figure 131) and sinewave current (no phase advance) at current density of 20Amm^{-2} (292A_{rms})

However, as would be expected, phase advancement of a sine-wave current narrows the advantage of the optimised current waveform. Table 31 shows a comparison of the torque generated using the optimised currents, sinewave with no phase advance and sinewave with phase advance. The optimum angle of phase advance varies with the current loading. The optimum angle for each current density is shown in Table 31.

Table 31 Comparison of the average torque produced by sinewave and the optimised currents

	Torque (Nm)			
Current density (Amm ⁻²)	5	10	15	20
Sinewave with no phase advance	14.3	24.7	31.9	37.3
Sinewave with phase advance	14.9	28.8	40.2	47.6
Optimum phase advance angle	20	30°	40°	40°
Optimised	15.1	29.0	40.4	48.2

This chapter has illustrated the potential benefits of optimising current waveforms to exploit non-sinusoidal emfs and reluctance torque, and some useful improvements demonstrated.

Chapter 8 GENERAL CONCLUSION

Many factors that determine the power density of a high speed PM synchronous generator have been explored in this thesis. The research demonstrated that high power density could be achieved by using the high performance materials and optimising the design to operate at its electromagnetic limit.

The key role that effective cooling plays in determining power density was clearly illustrated by the design study of the generator. The design study also highlighted the opportunities and challenges for further improving the power density beyond that achieved in the demonstrator. The constraint that the machine reactance imposes on the output power that can be extracted with an uncontrolled bridge was demonstrated, and a means proposed for maximizing this power was illustrated. This included dimensioning the magnetic core such that it was operating well into magnetic saturation, arguably much higher than would be the case with a more conventional approach to core sizing.

The sensitivity of the airgap flux density due to the thickness of adhesive joints between the magnet pieces of a heavily segmented pole was demonstrated. This had a significant impact on the open-circuit back-EMF and as a result, the output power of the demonstrator fell surprisingly short of the target performance. In addition, the thickness of the magnet containment and the requirement of the sleeve in the airgap to contain the oil on the stator side was shown to have a considerable effect on the magnetic loading of the design due to the consequently large electromagnetic airgap.

The flood cooling of the stator shown to be a very effective means of cooling and provided more than adequate cooling of the prototype, indicating potential to even further reduce its size. More specifically, the experimental results showed a current

density greater than 12 A/mm² can be sustained. However, the measured performance of the machine illustrated the difficulties in both measuring and calculating localised temperatures with random wound coils. The cooling method adopted allowed the oil coolant to be in intimate contact with the entire surface of the individual conductors. Although very effective for cooling, this approach may raise some concerns around damage to the insulation caused by friction induced by vibration. However, the coil wire used in constructing the prototype has a doubled coat and oil has excellent lubricating properties to reduce the effects of friction.

The optimisation of the electromagnetic design resulted in a stator core cross-section dominated by the conductor slot area, and hence the majority of the stator mass was contributed by Copper. Therefore, the use of Aluminium conductors were investigated with the objective of reducing the overall weight. In this case, the comparison showed that the use of Aluminium conductors could significantly reduce the weight and increase the power density of the generator. However, this outcome is a consequence of the design having a stator mass dominated by the winding.

In an attempt to increase the slot fill factor and reduce winding temperatures through improved heat transfer within the coil cross-section, additive manufactured copper coils were explored. At this time, there was little research published on electron beam melting or sintered laser melting of copper. Therefore, the preliminary phase of the investigation was to establish whether the electrical conductivity of additive manufactured copper could reach values that would make such coils competitive with normal drawn copper wire. It was shown in Chapter 6 that electrical conductivities of 92% of IACS could be achieved with limited parameter optimisation. Finally, slot fill factors greater than 80% could be achieved in some coil. However, for the electrical frequency in the target application, the skin effect

and proximity losses at high frequencies were, by some distance, unsustainable. In the correct applications, e.g. low speed machines or linear actuators, additive manufactured coils offers great flexibility and an ability to add novel intricate features to further enhance performance.

The opportunity to increase the torque for the same given RMS current and hence, losses, was examined by optimising the waveform of the current. An algorithm was developed to generate the optimised waveform. For the single-phase optimisation, 10% more torque was produced when compared with the torque of produce by a sinewave. This benefit was reduced for the case of three-phase optimisation where the additional constraint of the zero instantaneous sum of currents was applied.

Summary of novel contributions are:

- The discovery of the benefits of operating heavily in magnetic saturation in terms of current density reduction and the opportunity of employing a less dense winding material to minimize weight.
- Findings on the benefits that can be realised by using Aluminium conductors as an alternative to copper conductors.
- The effectiveness of flood cooling the stator with quantitative characterisation of its effectiveness.
- Novel method of manufacturing high slot fill factor coils with the flexibility to add novel features to increasing performance.
- Optimisation process for the current waveform to increase output torque for the same RMS current when compared with a sinewave current.

8.1 SCOPE FOR FUTURE WORK

This thesis has highlighted that there are aspects of machine design that can be further investigated to enhance performance:

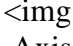
- Further optimisation of the thickness of the magnet containment in close cooperation with composite manufacture to minimise the safety factor.
- Further characterisation of the flooded stator cooling by computer fluid dynamics analysis is required to establish a generalized heat transfer coefficient for predicting winding temperatures of all types of machines.
- The key stage of establishing the electrical conductivity of additively manufactured copper was investigated and reported. The next step is to manufacture a functional coil and to apply novel features identified in this thesis. This project has been taken on internally by Rolls-Royce to continue exploring the flexibility of manufacturing coils additively.

REFERENCES

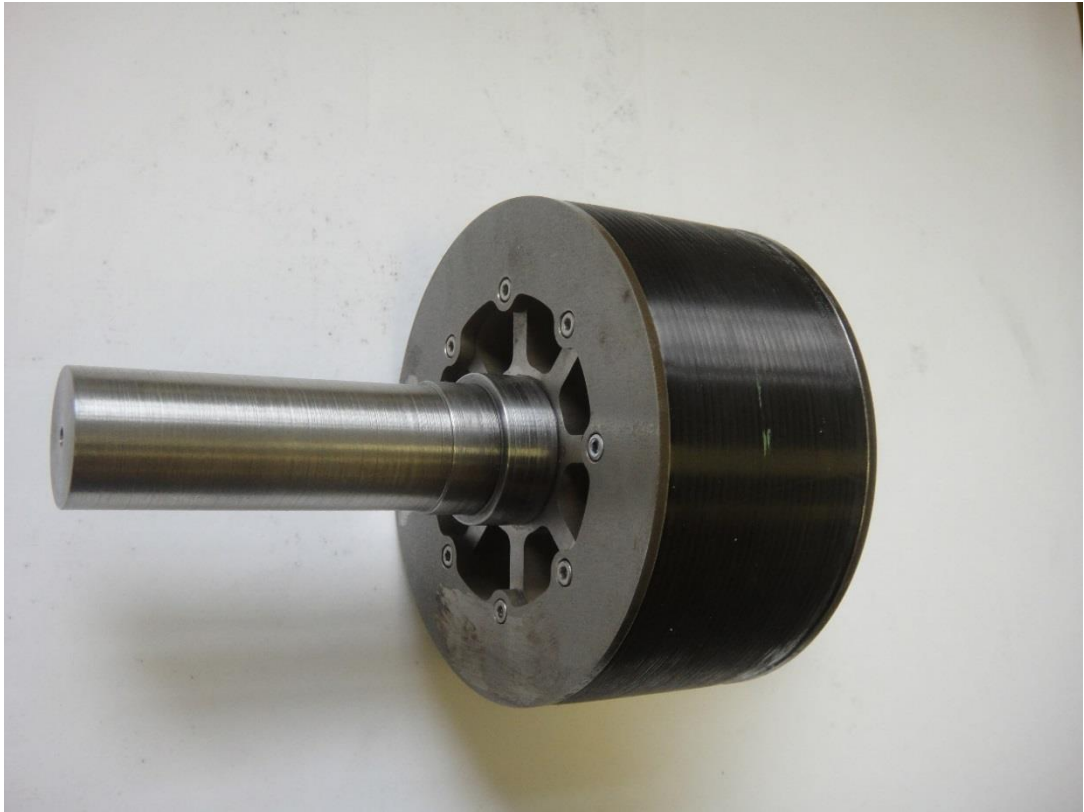
- [1] A. Boglietti, A. Cavagnino, A. Tenconi, and S. Vaschetto, "The safety critical electric machines and drives in the more electric aircraft: A survey," in *Industrial Electronics, 2009. IECON '09. 35th Annual Conference of IEEE*, 2009, pp. 2587-2594.
- [2] I. Moir, "More-electric aircraft-system considerations," in *Electrical Machines and Systems for the More Electric Aircraft (Ref. No. 1999/180), IEE Colloquium on*, 1999, pp. 10/1-10/9.
- [3] M. Hirst, A. McLoughlin, P. J. Norman, and S. J. Galloway, "Demonstrating the more electric engine: a step towards the power optimised aircraft," *Electric Power Applications, IET*, vol. 5, pp. 3-13, 2011.
- [4] A. Boglietti, A. El-Refaie, O. Drubel, A. Omekanda, N. Bianchi, E. Agamloh, *et al.*, "Electrical Machine Topologies: Hottest Topics in the Electrical Machine Research Community," *Industrial Electronics Magazine, IEEE*, vol. 8, pp. 18-30, 2014.
- [5] T. J. Woolmer and M. D. McCulloch, "Analysis of the Yokeless And Segmented Armature Machine," in *Electric Machines & Drives Conference, 2007. IEMDC '07. IEEE International*, 2007, pp. 704-708.
- [6] N. Bianchi and E. Fornasiero, "Impact of MMF Space Harmonic on Rotor Losses in Fractional-Slot Permanent-Magnet Machines," *Energy Conversion, IEEE Transactions on*, vol. 24, pp. 323-328, 2009.
- [7] K. Yamazaki and K. Kitayuguchi, "Teeth shape optimization of surface and interior permanent-magnet motors with concentrated windings to reduce magnet eddy current losses," in *Electrical Machines and Systems (ICEMS), 2010 International Conference on*, 2010, pp. 990-995.
- [8] K. Yamazaki, Y. Fukushima, and M. Sato, "Loss Analysis of Permanent Magnet Motors with Concentrated Windings - Variation of Magnet Eddy Current Loss Due to Stator and Rotor Shapes," in *Industry Applications Society Annual Meeting, 2008. IAS '08. IEEE*, 2008, pp. 1-8.
- [9] V. I. Patel, W. Jiabin, W. Weiya, and C. Xiao, "Six-Phase Fractional-Slot-per-Pole-per-Phase Permanent-Magnet Machines With Low Space Harmonics for Electric Vehicle Application," *Industry Applications, IEEE Transactions on*, vol. 50, pp. 2554-2563, 2014.
- [10] M. Galea, C. Gerada, T. Raminosa, and P. Wheeler, "A Thermal Improvement Technique for the Phase Windings of Electrical Machines," *Industry Applications, IEEE Transactions on*, vol. 48, pp. 79-87, 2012.
- [11] J. R. Hendershot and T. J. E. Miller, *Design of brushless permanent-magnet machines*. Venice, Florida: Motor Design Books, 2010.
- [12] A. A. Qazalbash, S. M. Sharkh, N. T. Irenji, R. G. Wills, and M. A. Abusara, "Rotor Eddy Current Power Loss in Permanent Magnet Synchronous Generators Feeding Uncontrolled Rectifier Loads," *Magnetics, IEEE Transactions on*, vol. 50, pp. 1-9, 2014.
- [13] J. J. H. Paulides, "High performance 1.5MW 20,000 rpm permanent magnet generator with uncontrolled rectifier for 'more-electric' ship applications," Ph.D., The University of Sheffield, 2005.
- [14] F. Magnussen and H. Lendenmann, "Parasitic Effects in PM Machines With Concentrated Windings," *Industry Applications, IEEE Transactions on*, vol. 43, pp. 1223-1232, 2007.

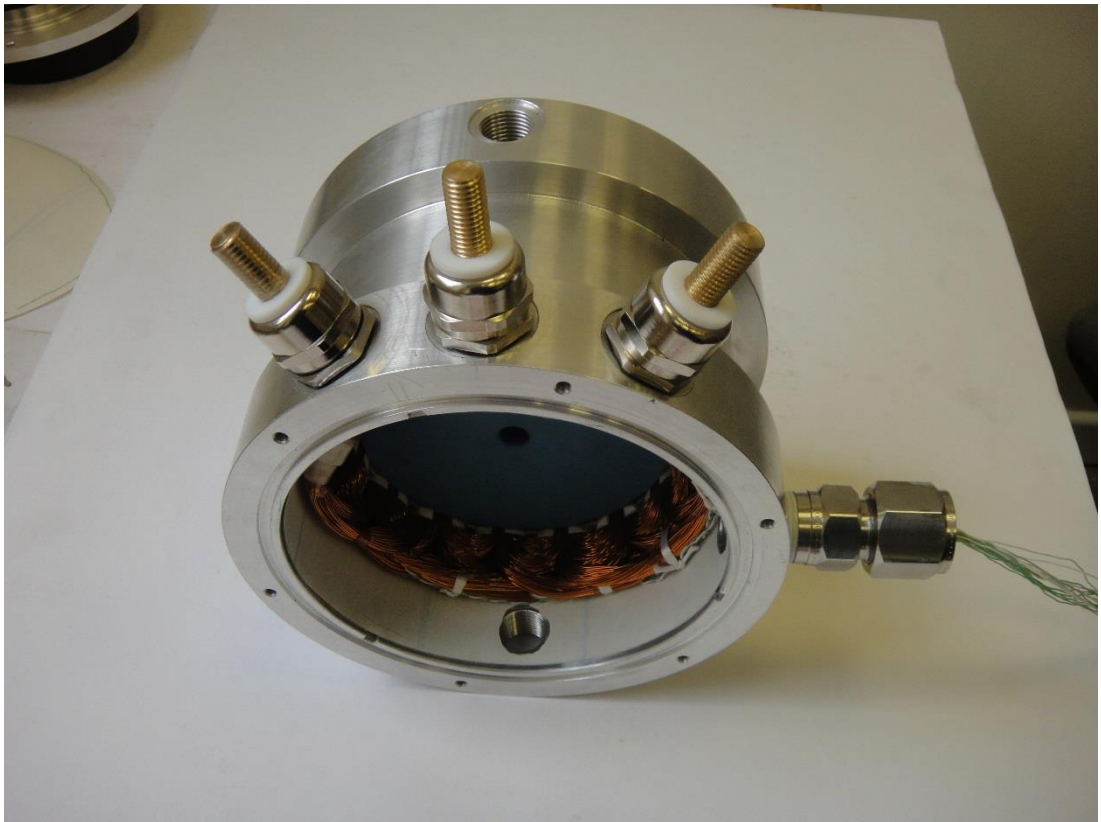
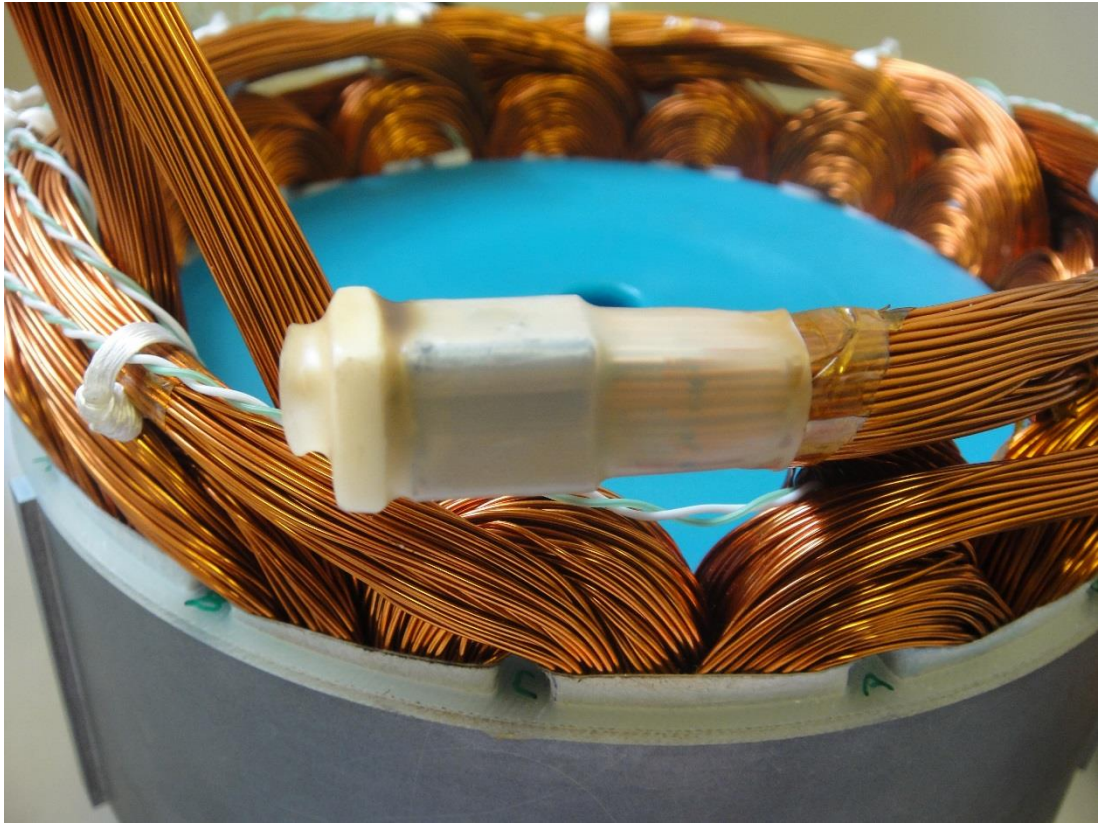
- [15] B. Aslan, E. Semail, and J. Legranger, "Analytical model of magnet eddy-current volume losses in multi-phase PM machines with concentrated winding," in *Energy Conversion Congress and Exposition (ECCE), 2012 IEEE*, 2012, pp. 3371-3378.
- [16] K. Yamazaki, M. Shina, Y. Kanou, M. Miwa, and J. Hagiwara, "Effect of Eddy Current Loss Reduction by Segmentation of Magnets in Synchronous Motors: Difference Between Interior and Surface Types," *Magnetics, IEEE Transactions on*, vol. 45, pp. 4756-4759, 2009.
- [17] G. Vacuumschmelze GmbH & Co., Susanne. (2009, Soft magnetic CoFe alloys for electric motors and generators. *Vacuumschmelze GmbH & Co.KG (Apr 2009)*, 15.
- [18] C. Corporation, "Specialty High Temp. Adhesives - 500F Duralco NM25," C. Corp., Ed., ed.
- [19] H. Ltd, "Electrical grade epoxy putty," Hylomar, Ed., ed. Wigan, UK, 2004.
- [20] S. Corporation, "Aeroshell Turbine Oil 3," F. s. Inhibitors, Ed., ed. 11/10/99: Shell Corporation, 1999.
- [21] D. P. Ltd. (2012, 06/02/2012). *PEEK Material Data Sheet*. Available: <http://www.directplastics.co.uk/pdf/datasheets/PEEK%20Data%20Sheet.pdf>
- [22] D. A. Staton and A. Cavagnino, "Convection Heat Transfer and Flow Calculations Suitable for Analytical Modelling of Electric Machines," in *IEEE Industrial Electronics, IECON 2006 - 32nd Annual Conference on*, 2006, pp. 4841-4846.
- [23] D. P. Kulkarni, G. Rupertus, and E. Chen, "Experimental Investigation of Contact Resistance for Water Cooled Jacket for Electric Motors and Generators," *Energy Conversion, IEEE Transactions on*, vol. 27, pp. 204-210, 2012.
- [24] A. M. El-Refaie, J. P. Alexander, S. Galioto, P. B. Reddy, H. Kum-Kang, P. de Bock, *et al.*, "Advanced High-Power-Density Interior Permanent Magnet Motor for Traction Applications," *Industry Applications, IEEE Transactions on*, vol. 50, pp. 3235-3248, 2014.
- [25] M. Polikarpova, P. M. Lindh, J. A. Tapia, and J. J. Pyrhonen, "Application of potting material for a 100 kW radial flux PMSM," in *Electrical Machines (ICEM), 2014 International Conference on*, 2014, pp. 2146-2151.
- [26] Z. Huang, F. Marquez, M. Alakula, and J. Yuan, "Characterization and application of forced cooling channels for traction motors in HEVs," in *Electrical Machines (ICEM), 2012 XXth International Conference on*, 2012, pp. 1212-1218.
- [27] A. Nollau and D. Gerling, "A new cooling approach for traction motors in hybrid drives," in *Electric Machines & Drives Conference (IEMDC), 2013 IEEE International*, 2013, pp. 456-461.
- [28] M. D. Schiefer, M., "Indirect Slot Cooling for High-Power-Density Machines with Concentrated Winding," presented at the Electric Machines & Drives Conference, 2015. IEMDC '15. IEEE International, 2015.
- [29] C. Corporation. *Durapot Epoxies - High performance casting, Embedding and Encapsulating Compounds*. Available: http://www.cotronics.com/vo/cotr/ea_encapsulants.htm
- [30] L. Corporation, "Thermoset SC-420 Thermally Conductive Silicone Encapsulant," ed, 2014.

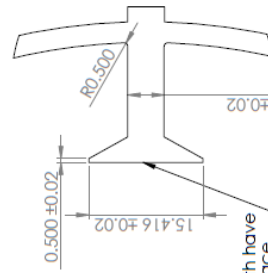
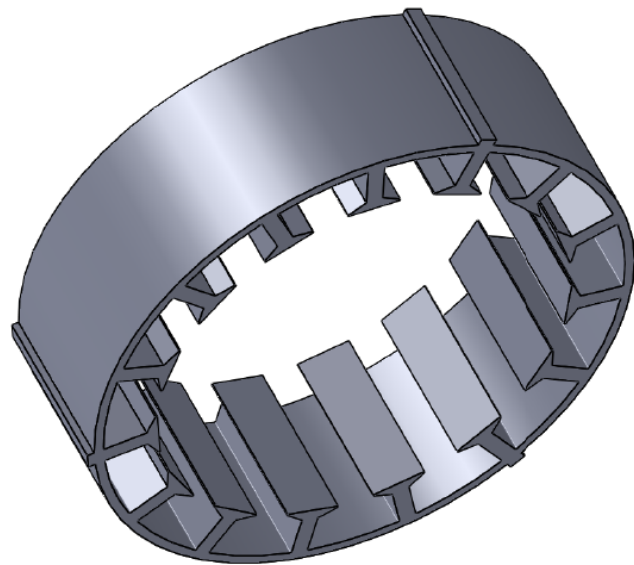
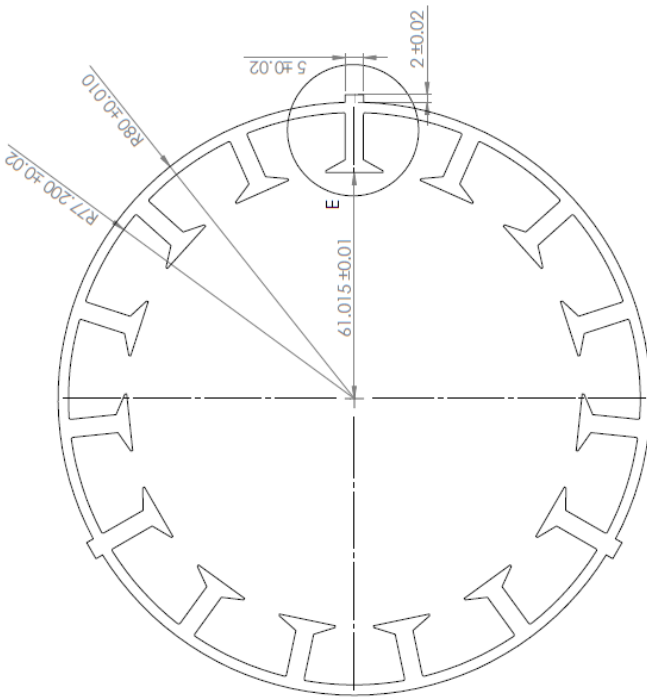
- [31] A. Nollau and D. Gerling, "Novel cooling methods using flux-barriers," in *Electrical Machines (ICEM), 2014 International Conference on*, 2014, pp. 1328-1333.
- [32] "Electrical system with integrated drive generator," *Aircraft Engineering and Aerospace Technology*, vol. 46, pp. 7-8, 1974.
- [33] J. F. Gieras, *Advancements in Electric Machines*: Springer, 2008.
- [34] Y. Alexandrova, S. Semken, M. Polikarpova, and J. Pyrhonen, "Defining proper initial geometry of an 8 MW liquid-cooled direct-drive permanent magnet synchronous generator for wind turbine applications based on minimizing mass," in *Electrical Machines (ICEM), 2012 XXth International Conference on*, 2012, pp. 1250-1255.
- [35] P. A. R. I. W. Ltd, "Polyester C200 Round - High temperature enamelled copper wire," ed.
- [36] A. F. Mills, *Heat Transfer*: Prentice Hall, 1999.
- [37] E. Schubert, "Heat transfer coefficients at end winding and bearing covers of enclosed asynchronous machines," *Elektrie*, vol. 22, 1968.
- [38] H. Pil-Wan, C. Yon-Do, C. Jae-Hak, K. Mi-Jung, K. Dae-Hyun, and L. Ju, "The study to substitute aluminum for copper as a winding material in induction machine," in *Telecommunications Energy Conference, 2009. INTELEC 2009. 31st International*, 2009, pp. 1-3.
- [39] R. Wrobel, D. Salt, N. Simpson, and P. H. Mellor, "Comparative study of copper and aluminium conductors - Future cost effective PM machines," in *Power Electronics, Machines and Drives (PEMD 2014), 7th IET International Conference on*, 2014, pp. 1-6.
- [40] L. Del Ferraro and F. G. Capponi, "Aluminium Multi-Wire for High-Frequency Electric Machines," in *Industry Applications Conference, 2007. 42nd IAS Annual Meeting. Conference Record of the 2007 IEEE*, 2007, pp. 89-93.
- [41] M. Peter, J. Fleischer, F. S. L. Blanc, and J. P. Jastrzembski, "New conceptual lightweight design approaches for integrated manufacturing processes: Influence of alternative materials on the process chain of electric motor manufacturing," in *Electric Drives Production Conference (EDPC), 2013 3rd International*, 2013, pp. 1-6.
- [42] O. Zimmermann, "ANOFOL, Coils from Anodised Aluminium, the Alternative to copper," in *3rd International Electric Drives Production Conference (EDPC)*, Nuremberg, Germany, 2013, pp. 212-216.
- [43] W. Gitzen, *Aluminas as Ceramic Material*. Columbus: American Ceramic Society, 1970.
- [44] P. Frigola, R. Agustsson, L. Faillace, R. Rimmer, W. Clemens, J. Henry, *et al.*, "Development of a CW NCRF photoinjector using Solid Freeform Fabrication (SFF)," 2010, pp. 3804-3806.
- [45] R. Dutta and M. F. Rahman, "Design and Analysis of an Interior Permanent Magnet (IPM) Machine With Very Wide Constant Power Operation Range," *Energy Conversion, IEEE Transactions on*, vol. 23, pp. 25-33, 2008.
- [46] P. Huang, C.-y. Miao, H.-q. Li, and C. Zhang, "Maximum-Torque-Per-Ampere Control of Interior Permanent Magnet Synchronous Machine Applied for Hybrid Electric Vehicles," in *Control, Automation and Systems Engineering (CASE), 2011 International Conference on*, 2011, pp. 1-3.

- [47] S. Liwei, J. Daqian, C. Shumei, and S. Shan, "Reluctance torque analysis and reactance calculation of IPM for HEVs based on FEM," in *Vehicle Power and Propulsion Conference (VPPC), 2010 IEEE*, 2010, pp. 1-4.
- [48] J. K. Tangudu, T. M. Jahns, and A. El-Refai, "Unsaturated and saturated saliency trends in fractional-slot concentrated-winding interior permanent magnet machines," in *Energy Conversion Congress and Exposition (ECCE), 2010 IEEE*, 2010, pp. 1082-1089.
- [49] L. Chong and M. F. Rahman, "Saliency ratio optimization in an IPM machine with fractional-slot concentrated windings," in *Electrical Machines and Systems, 2008. ICEMS 2008. International Conference on*, 2008, pp. 2921-2926.
- [50] R. Antonello, M. Carraro, and M. Zigliotto, "Towards the automatic tuning of MTPA algorithms for IPM motor drives," in *Electrical Machines (ICEM), 2012 XXth International Conference on*, 2012, pp. 1121-1127.
- [51] Z. Ping, L. Dingsheng, G. Wimmer, N. Lambert, and Z. J. Cendes, "Determination of $\langle \text{formula formulatype="inline"} \rangle$  Axis Parameters of Interior Permanent Magnet Machine," *Magnetics, IEEE Transactions on*, vol. 46, pp. 3125-3128, 2010.
- [52] H. Shoudao, C. Ziqiang, H. Keyuan, and G. Jian, "Maximum torque per ampere and flux-weakening control for PMSM based on curve fitting," in *Vehicle Power and Propulsion Conference (VPPC), 2010 IEEE*, 2010, pp. 1-5.
- [53] L. Zheng and L. Hongmei, "MTPA control of PMSM system considering saturation and cross-coupling," in *Electrical Machines and Systems (ICEMS), 2012 15th International Conference on*, 2012, pp. 1-5.
- [54] L. Parsa, H. Lei, and H. A. Toliyat, "Optimization of average and cogging torque in 3-phase IPM motor drives," in *Industry Applications Conference, 2002. 37th IAS Annual Meeting. Conference Record of the*, 2002, pp. 417-424 vol.1.
- [55] W. Wang, B. Fahimi, and M. Kiani, "Maximum torque per ampere control of Permanent Magnet Synchronous Machines," in *Electrical Machines (ICEM), 2012 XXth International Conference on*, 2012, pp. 1013-1020.
- [56] A. P. Wu and P. L. Chapman, "Simple expressions for optimal current waveforms for permanent-magnet synchronous machine drives," *Energy Conversion, IEEE Transactions on*, vol. 20, pp. 151-157, 2005.
- [57] L. Guo and L. Parsa, "Torque ripple reduction of the modular Interior Permanent Magnet machines using optimum current profiling technique," in *Electric Machines and Drives Conference, 2009. IEMDC '09. IEEE International*, 2009, pp. 1094-1099.

APPENDIX A: CONSTRUCTING PROTOTYPE



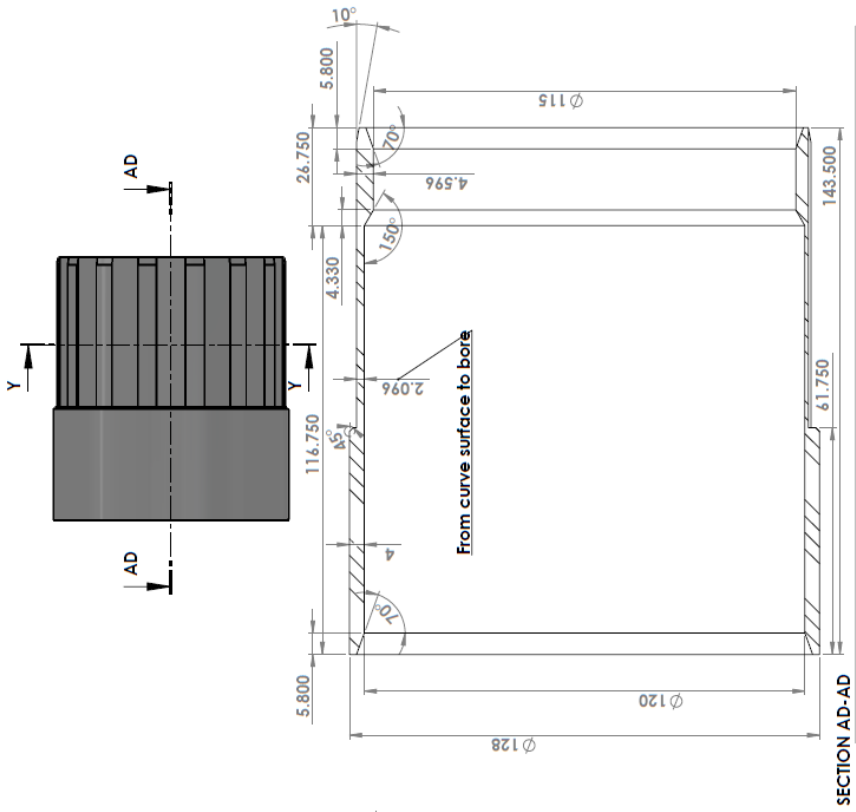




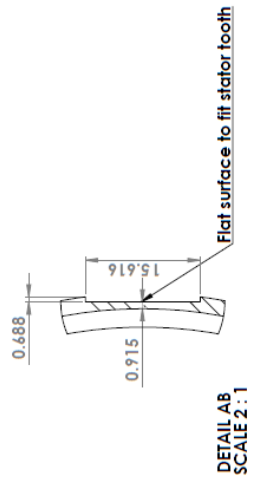
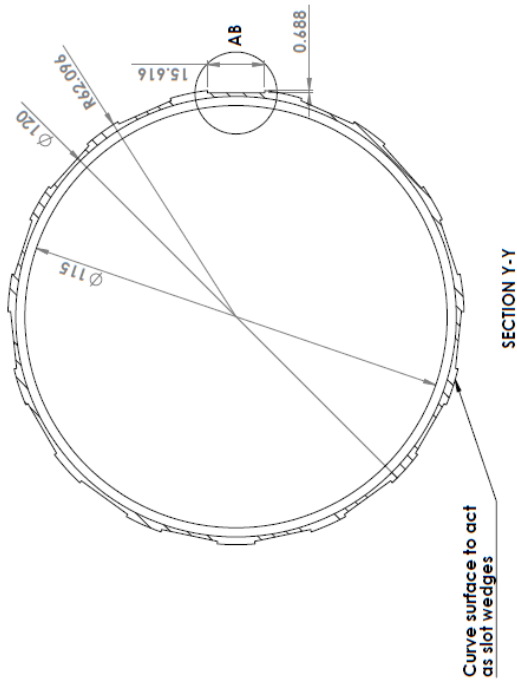
FILE E
SCALE 2:1

NAME:	DATE:	REVISION:
Axial stack length = 50mm +/- 0.2mm	12/01/2012	V.1
Material VACOFLEX 50	Created by:	Maurice Shortie & Keir Wilkie
Unless specified tolerance required is +/- 0.02mm	TITLE	Liquid Cooled LP Gen - Stator LAM
Finalised - 18/01/2012 Sent for manufacture - 18/01/2012	DWG NO.	LPGEN2/TD/001
EMPHASIS USE IN MILLIMETERS	SCALE:	SHEET 3 OF 8
DO NOT SCALE DRAWING		A3

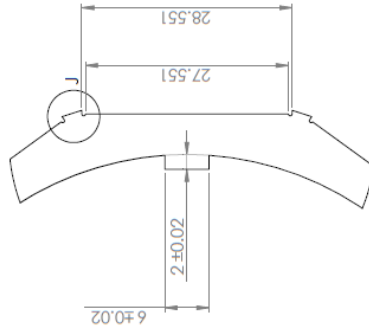
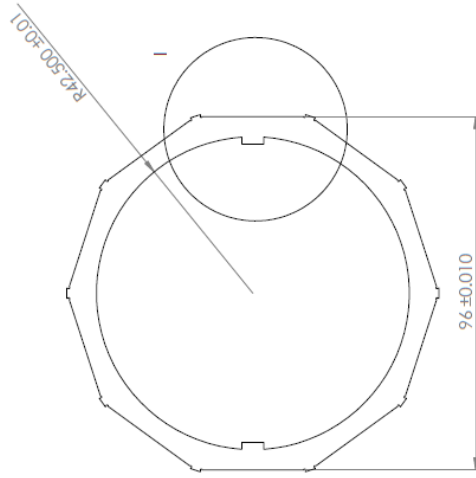
SolidWorks Educational Edition
For Instructional Use Only.



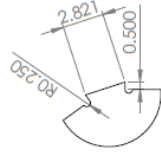
Date:	16/04/2012	Revision:	V.1
Created by:	Maurice Shortle		
Title:	PEEK Sleeve		
DWG NO.:	LPGEN2/TD/001		A3
SCALE:1:1		DO NOT SCALE DRAWING	SHEET 12 OF 24



**SolidWorks Educational Edition.
For Instructional Use Only.**



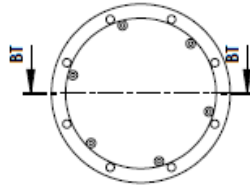
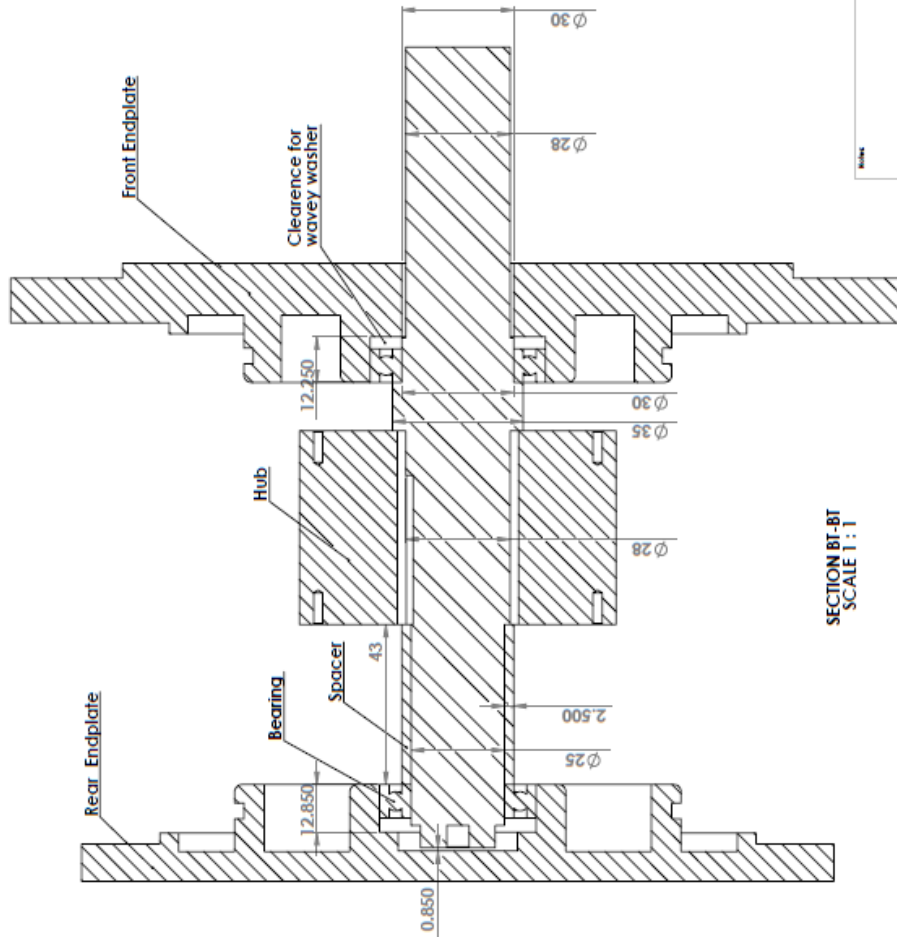
DETAIL I
SCALE 2 : 1



DETAIL J
SCALE 4 : 1

**SolidWorks Educational Edition.
For Instructional Use Only.**

DATE	17/01/2012	REVISION	V.1
CREATED BY	Maurice Shortle		
TITLE	Liquid Cooled LP Gen - Rotor LAM		
DWG NO.	LPGEN2/TD/001	SHEET # OF 16	
NUMBER: Axial stack length = 50mm +/- 0.2mm Material: VACOFLUX 50 Unless specified tolerance required is +/- 0.02mm Finalised - 18/01/2012 Sent for manufacture - 18/01/2012		DIMENSIONS ARE IN MILLIMETERS DO NOT SCALE DRAWING SCALE 1:1	



Bearing Details

- Front Endplate Bearing OD: 47 ID: 30 W: 9
- Rear Endplate Bearing OD: 42 ID: 25 W: 9

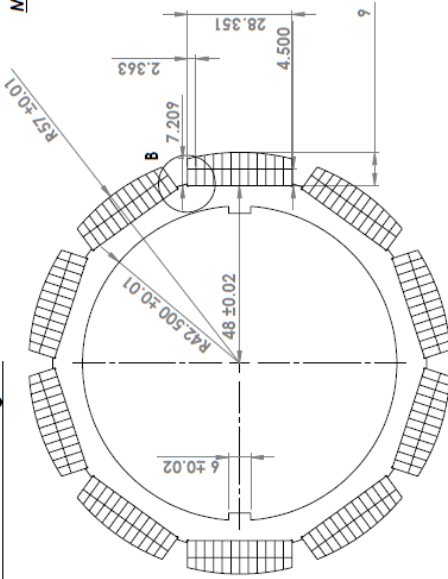
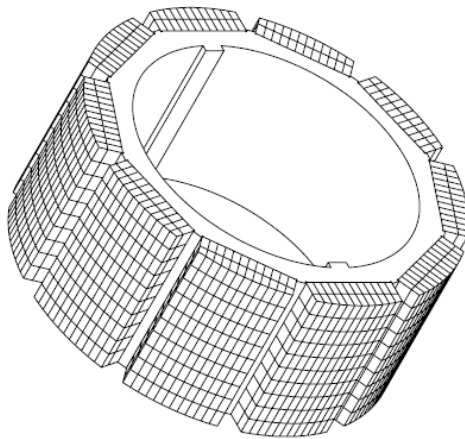
Shaft must be inserted from the rear end due to Peek sleeve.

SECTION BT-BT
SCALE 1:1

DATE	8/06/12	REVISION	V.1
CREATED BY	Maurice Shortle		
TITLE	Shaft & Bearing Details		
DWG NO.	LPCGEN/TD/001		
SCALE	A3		
DO NOT SCALE DIMENSIONS		SHEET 22 OF 23	

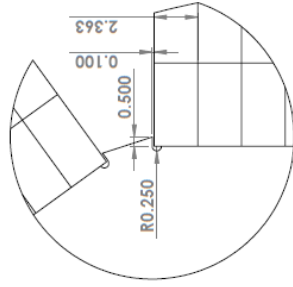
**SolidWorks Educational Edition.
For Instructional Use Only.**

Rotor Lamination & Magnets



Final Axial Length = 50mm

Magnet Location Detail



DETAIL B
SCALE 5 : 1

Magnet Segmentation

- 12 segments circumferentially (dimensions shown)
- 2 Radial segments
- 10 axial segments
(with segment length of 5mm to achieve 50mm total length)
- 10 Poles in total
- 2400 total number of magnet blocks

Magnet Material

- Sm2Co17
- Grade required 30MGOe
- Remanent flux density range 1.08 - 1.10

Operating Conditions

- Maximum speed 17000rpm
- Maximum operating temperature 150degC
- Maximum temperature 177degC

The lamination adhesive and inter pole infill must be rated to achieve a maximum temperature of 177degC which occurs during the carbon fibre cure process. Our preference is for (these can be free issued if required)

- Duralco NM25 - Lamination adhesive
- Hylormar s1574 - in-fill between poles

Magnet should be ground to a final diameter of 114mm

DATE:	12/01/2012	REVISION:	V.1
CHECKED BY:	Keir Wilkie & Maurice Shortte		
TITLE:	Liquid Cooled 50kW LPGEN - Magnet Details		
DWG NO.:	LPGEN2/TD/010	A3	
DIMENSIONS ARE IN MILLIMETERS		DO NOT SCALE DRAWING	
SCALE: 1:1		SHEET 13 OF 22	
NAME: Finalised - 13/01/2012 Sent for manufacture - 13/01/2012			

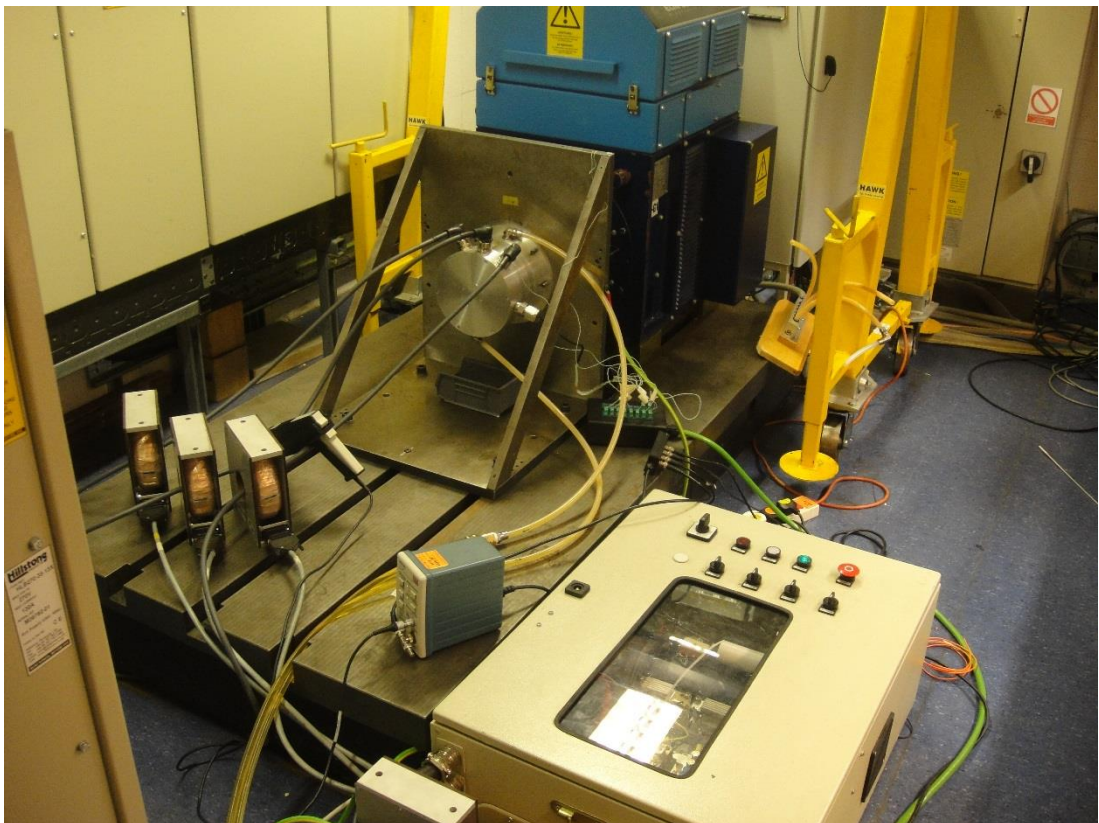
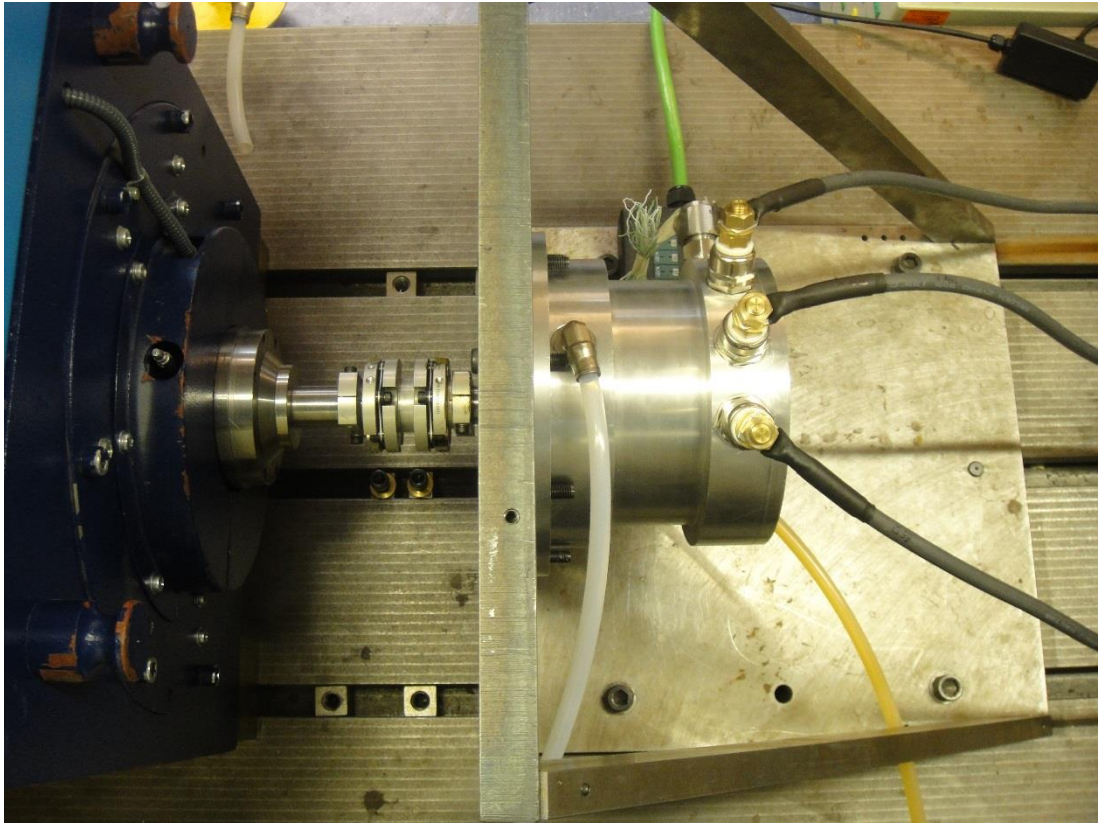
**SolidWorks Educational Edition.
For Instructional Use Only.**



DATE:	5/2/2012	REVISION:	V.1
CREATED BY:	Maurice Shortle		
TITLE:	Liquid Cooled 50kW LPGEN - Rotor Assembly		
DWG NO.:	LPGEN/TD/009		A3
SCALE:	1:1	SHEET 11 OF 22	
NOTE: DIMENSIONS ARE IN MILLIMETERS DO NOT SCALE DRAWING			

**SolidWorks Educational Edition.
For Instructional Use Only.**

APPENDIX B: PROTOTYPE TESTING



APPENDIX C: CURRENT OPTIMISATION

		Phase A																								
		-48	-44	-40	-36	-32	-28	-24	-20	-16	-12	-8	-4	0	4	8	12	16	20	24	28	32	36	40	44	48
Current Density	-700.8	-700.8	-642.4	-584	-525.6	-467.2	-408.8	-350.4	-292	-233.6	-175.2	-116.8	-58.4	0	58.4	116.8	175.2	233.6	292	350.4	408.8	467.2	525.6	584	642.4	700.8
	-700.8	1401.6	1343.2	1284.8	1226.4	1168	1109.6	1051.2	992.8	934.4	876	817.6	759.2	700.8	642.4	584	525.6	467.2	408.8	350.4	292	233.6	175.2	116.8	58.4	0
	-642.4	1343.2	1284.8	1226.4	1168	1109.6	1051.2	992.8	934.4	876	817.6	759.2	700.8	642.4	584	525.6	467.2	408.8	350.4	292	233.6	175.2	116.8	58.4	0	-58.4
	-584	1284.8	1226.4	1168	1109.6	1051.2	992.8	934.4	876	817.6	759.2	700.8	642.4	584	525.6	467.2	408.8	350.4	292	233.6	175.2	116.8	58.4	0	-58.4	-116.8
	-525.6	1226.4	1168	1109.6	1051.2	992.8	934.4	876	817.6	759.2	700.8	642.4	584	525.6	467.2	408.8	350.4	292	233.6	175.2	116.8	58.4	0	-58.4	-116.8	-175.2
	-467.2	1168	1109.6	1051.2	992.8	934.4	876	817.6	759.2	700.8	642.4	584	525.6	467.2	408.8	350.4	292	233.6	175.2	116.8	58.4	0	-58.4	-116.8	-175.2	-233.6
	-408.8	1109.6	1051.2	992.8	934.4	876	817.6	759.2	700.8	642.4	584	525.6	467.2	408.8	350.4	292	233.6	175.2	116.8	58.4	0	-58.4	-116.8	-175.2	-233.6	-292
	-350.4	1051.2	992.8	934.4	876	817.6	759.2	700.8	642.4	584	525.6	467.2	408.8	350.4	292	233.6	175.2	116.8	58.4	0	-58.4	-116.8	-175.2	-233.6	-292	-350.4
	-292	992.8	934.4	876	817.6	759.2	700.8	642.4	584	525.6	467.2	408.8	350.4	292	233.6	175.2	116.8	58.4	0	-58.4	-116.8	-175.2	-233.6	-292	-350.4	-408.8
	-233.6	934.4	876	817.6	759.2	700.8	642.4	584	525.6	467.2	408.8	350.4	292	233.6	175.2	116.8	58.4	0	-58.4	-116.8	-175.2	-233.6	-292	-350.4	-408.8	-467.2
	-175.2	876	817.6	759.2	700.8	642.4	584	525.6	467.2	408.8	350.4	292	233.6	175.2	116.8	58.4	0	-58.4	-116.8	-175.2	-233.6	-292	-350.4	-408.8	-467.2	-525.6
	-116.8	817.6	759.2	700.8	642.4	584	525.6	467.2	408.8	350.4	292	233.6	175.2	116.8	58.4	0	-58.4	-116.8	-175.2	-233.6	-292	-350.4	-408.8	-467.2	-525.6	-584
	-58.4	759.2	700.8	642.4	584	525.6	467.2	408.8	350.4	292	233.6	175.2	116.8	58.4	0	-58.4	-116.8	-175.2	-233.6	-292	-350.4	-408.8	-467.2	-525.6	-584	-642.4
	0	700.8	642.4	584	525.6	467.2	408.8	350.4	292	233.6	175.2	116.8	58.4	0	-58.4	-116.8	-175.2	-233.6	-292	-350.4	-408.8	-467.2	-525.6	-584	-642.4	-700.8
	58.4	642.4	584	525.6	467.2	408.8	350.4	292	233.6	175.2	116.8	58.4	0	-58.4	-116.8	-175.2	-233.6	-292	-350.4	-408.8	-467.2	-525.6	-584	-642.4	-700.8	-759.2
	116.8	584	525.6	467.2	408.8	350.4	292	233.6	175.2	116.8	58.4	0	-58.4	-116.8	-175.2	-233.6	-292	-350.4	-408.8	-467.2	-525.6	-584	-642.4	-700.8	-759.2	-817.6
	175.2	525.6	467.2	408.8	350.4	292	233.6	175.2	116.8	58.4	0	-58.4	-116.8	-175.2	-233.6	-292	-350.4	-408.8	-467.2	-525.6	-584	-642.4	-700.8	-759.2	-817.6	-876
	233.6	467.2	408.8	350.4	292	233.6	175.2	116.8	58.4	0	-58.4	-116.8	-175.2	-233.6	-292	-350.4	-408.8	-467.2	-525.6	-584	-642.4	-700.8	-759.2	-817.6	-876	-934.4
	292	408.8	350.4	292	233.6	175.2	116.8	58.4	0	-58.4	-116.8	-175.2	-233.6	-292	-350.4	-408.8	-467.2	-525.6	-584	-642.4	-700.8	-759.2	-817.6	-876	-934.4	-992.8
	350.4	350.4	292	233.6	175.2	116.8	58.4	0	-58.4	-116.8	-175.2	-233.6	-292	-350.4	-408.8	-467.2	-525.6	-584	-642.4	-700.8	-759.2	-817.6	-876	-934.4	-992.8	-1051.2
	408.8	292	233.6	175.2	116.8	58.4	0	-58.4	-116.8	-175.2	-233.6	-292	-350.4	-408.8	-467.2	-525.6	-584	-642.4	-700.8	-759.2	-817.6	-876	-934.4	-992.8	-1051.2	-1109.6
	467.2	233.6	175.2	116.8	58.4	0	-58.4	-116.8	-175.2	-233.6	-292	-350.4	-408.8	-467.2	-525.6	-584	-642.4	-700.8	-759.2	-817.6	-876	-934.4	-992.8	-1051.2	-1109.6	-1168
	525.6	175.2	116.8	58.4	0	-58.4	-116.8	-175.2	-233.6	-292	-350.4	-408.8	-467.2	-525.6	-584	-642.4	-700.8	-759.2	-817.6	-876	-934.4	-992.8	-1051.2	-1109.6	-1168	-1226.4
	584	116.8	58.4	0	-58.4	-116.8	-175.2	-233.6	-292	-350.4	-408.8	-467.2	-525.6	-584	-642.4	-700.8	-759.2	-817.6	-876	-934.4	-992.8	-1051.2	-1109.6	-1168	-1226.4	-1284.8
642.4	58.4	0	-58.4	-116.8	-175.2	-233.6	-292	-350.4	-408.8	-467.2	-525.6	-584	-642.4	-700.8	-759.2	-817.6	-876	-934.4	-992.8	-1051.2	-1109.6	-1168	-1226.4	-1284.8	-1343.2	
700.8	0	-58.4	-116.8	-175.2	-233.6	-292	-350.4	-408.8	-467.2	-525.6	-584	-642.4	-700.8	-759.2	-817.6	-876	-934.4	-992.8	-1051.2	-1109.6	-1168	-1226.4	-1284.8	-1343.2	-1401.6	
SET-->	1	2	3	4	5	6	7	8	9	10	11	12	13	14	15	16	17	18	19	20	21	22	23	24	25	

Current waveform optimisation algorithm

```
Clear all %#ok<CLSCR>

d=360; %degrees
j=25; %input current density (A/mm2)
iph=14.6*j;%RMS current limit
%iph=;
l_inc=10;
n=91;

I_RMS_A=0;
I_RMS_B=0;
I_RMS_C=0;
I_RMS_AVG=0;

% TORQUE DATA REARRANGED INTO NGRID structure
torq_data=importdata('IPM_meshgrid_torq_030715.mat');
%torq_data(:, :, 360)=[]; %delete the data in angle 361, because its a
repeat of 1.
TORQ=torq_data;

TORQ_NGRID =permute(TORQ, [2,1,3]);

%CORRESPONDING NGRID Structure OF THE CURRENT DATA
ia=(-700.8:58.4:700.8);
ib=(-700.8:58.4:700.8);
ang=(1:d);

[IA,IB,ANG]=ndgrid(ia,ib,ang);
% Preloaded cogging torque
%preload_cogg_torq = load ('torq_with_cogg_preload.mat');

%PREALLOCATED ARRAYS for speed improvement
best_ang_rslt= zeros(d,7);

I_FINAL_A(:,1)= zeros(d,1);
I_FINAL_B(:,1)= zeros(d,1);
I_FINAL_C(:,1)= zeros(d,1);

Ia_exs= zeros(d,1);
Ib_exs= zeros(d,1);
Ic_exs= zeros(d,1);

Ia_new= zeros(d,1);
Ib_new= zeros(d,1);
Ic_new= zeros(d,1);

T_FINAL= zeros(d,1);
cogg = zeros(d,1);
cogg(:) = TORQ (13,13,:);

T_exs=cogg;
```

```

net_delta_T_per_loss =zeros(n,1);

% Applying the grid interpolant (spline) function to the torq data
grid_torq_interp=griddedInterpolant(IA,IB,ANG,TORQ_NGRID,'spline');

% the possible proportions of incremental currents in a look up
table
load('delta_i_inc.mat');

tic
while (I_RMS_AVG <= iph )

    for ang=1:d

        com_rslt=zeros(n,7); % preallocating array to store the
results of all possible combinationsof current

        % updates the current existing in an angle
        Ia_exs(:,1)=(I_FINAL_A(:,1));
        Ib_exs(:,1)=(I_FINAL_B(:,1));
        Ic_exs(:,1)=(I_FINAL_C(:,1));

        for m=1:n % Runs through the possible combinations of
current increments (91 possible solutions)

            delta_ia=(l_inc*delta_i_sols(m,1));
            delta_ib=(l_inc*delta_i_sols(m,2));
            delta_ic=(l_inc*delta_i_sols(m,3));

            % Adds the incremental currents to the existing
current in the
            % angle
            Ia_new(ang,1)=((Ia_exs(ang,1))) + (delta_ia);
            Ib_new(ang,1)=((Ib_exs(ang,1))) + (delta_ib);
            Ic_new(ang,1)=((Ic_exs(ang,1))) + (delta_ic) ;

            % Calculates the existing loss
            L_exs_a =((Ia_exs(ang,1))^2);
            L_exs_b= ((Ib_exs(ang,1))^2);
            L_exs_c= ((Ic_exs(ang,1))^2);

            % Calculate the new loss
            Loss_new_a = Ia_new(ang,1).^2;
            Loss_new_b = Ib_new(ang,1).^2;
            Loss_new_c= Ic_new(ang,1).^2;

            % Calculate the delta loss
            delta_loss_a= (Loss_new_a-L_exs_a);
            delta_loss_b= (Loss_new_b-L_exs_b);
            delta_loss_c= (Loss_new_c-L_exs_c);

            net_delta_loss= delta_loss_a + delta_loss_b +
delta_loss_c;

            % Calculate existing torque using existing current

```

```

net_torq_exs= T_exs(ang,1);

% Calculate new torque using new current
net_torq
grid_torq_interp(Ia_new(ang),Ib_new(ang),ang);

% Calculates the delta torque
net_delta_torq= (net_torq)-(net_torq_exs);

% Calculates the delta torque per delta loss
net_delta_T_per_loss(m,1)
(net_delta_torq/(net_delta_loss));

%Stores the net delta torque per net delta loss for
all possible combinations of
%incremental current for an angle.

com_rslt(m,1)= (ang);
com_rslt(m,2)= (delta_ia);
com_rslt(m,3)= (delta_ib);
com_rslt(m,4)= (delta_ic);
com_rslt(m,5)= (net_delta_T_per_loss(m,1));
com_rslt(m,6)= (net_delta_loss);
com_rslt(m,7)= (net_delta_torq);

% Makes the possibility of having a negative
delta_loss
% invalid and replace the delta_torq per delta loss
as a NaN
if net_delta_loss<0
    com_rslt(m,5)= NaN;
end

% At this point, the delta_torq per delta loss for all
possible
% current combinations is stored in the array com_rslt for
this particular angle

% Selects the best combination of currents for this angle
[max_val,row] = max((com_rslt(:,5)));

% the best combination for each angle (1-360) is stored in
this array 'best_ang_result'
best_ang_rslt(ang,:)=com_rslt(row,:);

end %....Continues to the next angle (1-360) and repeat

end

%Selects the angle which has the best delta_torq per delta loss
result
[max_val1,indx1] = max((best_ang_rslt(:,5)));
[rol,col1]=ind2sub(size(best_ang_rslt(:,5)),indx1);

% the values of the best results are assigned a name here
max_angle= best_ang_rslt(rol,1);

```

```

max_ia = best_ang_rslt(rol,2);
max_ib = best_ang_rslt(rol,3);
max_ic = best_ang_rslt(rol,4);
max_dT = best_ang_rslt(rol,7);

% The current waveform array is updated with the new value of
current
I_FINAL_A(max_angle,1) = Ia_exs(max_angle,1)+ max_ia;
I_FINAL_B(max_angle,1) = Ib_exs(max_angle,1)+ max_ib;
I_FINAL_C(max_angle,1) = Ic_exs(max_angle,1)+ max_ic;
T_FINAL(max_angle,1)= T_exs(max_angle,1)+ max_dT ;

T_exs(max_angle,1) = T_FINAL(max_angle,1);

% Calculates the RMS value of the current waveforms
I_RMS_A = sqrt((sum(I_FINAL_A.^2)/d));
I_RMS_B = sqrt((sum(I_FINAL_B.^2)/d));
I_RMS_C = sqrt((sum(I_FINAL_C.^2)/d));

I_RMS_AVG = (I_RMS_A+ I_RMS_B+I_RMS_C)/3

end
% ***** END OF THE OPTIMISATION *****

% PLOTTING OF THE RESULTS

%calculates the torque waveform using the optimised current
waveforms
for w=1:d
ang_tq=TORQ(:, :, w);
NET_TORQ_FINAL(w,1) =grid_torq_interp(I_FINAL_A(w),I_FINAL_B(w),w);
I_NEU(w,1) = I_FINAL_A(w,1) + I_FINAL_B(w,1) + I_FINAL_C(w,1);
end

AVG_TORQUE = (sum(NET_TORQ_FINAL))/d;

ang=1:d;
subplot(2,1,1);
plot(ang,I_FINAL_A,'b',ang,I_FINAL_B,'k',ang,I_FINAL_C,'r',ang,I_NEU
,'g')
title ('Optimised Phase Currents')
legend ('Phase A','Phase B','Phase C','Neutral')
xlabel('Elec. Angle (deg.)')
ylabel('Current (A)')
grid on

subplot(2,1,2); plot(ang,T_FINAL,'b',ang,cogg,'r')
title ('Optimised Net Torque')
legend ('Opt.Torque','Cogging Torque')
xlabel('Elec. Angle (deg.)')
ylabel('Torque (Nm)')
grid on

%filename = 'testdata.xlsx';
%xlswrite(filename,I_FINAL_A,I_FINAL_B,I_FINAL_C,T_FINAL)

```